

Low-mass dielectron measurement in Pb–Pb collisions at $\sqrt{s_{\text{NN}}} = 2.76$ TeV with ALICE at the LHC

Meting van de productie van elektronparen met lage invariante massa in Pb–Pb botsingen met $\sqrt{s_{\text{NN}}} = 2.76$ TeV met ALICE bij de LHC

(met een samenvatting in het Nederlands)

Proefschrift

ter verkrijging van de graad van doctor aan de Universiteit Utrecht op gezag van de rector magnificus, prof.dr. G.J. van der Zwaan, ingevolge het besluit van het college voor promoties in het openbaar te verdedigen op dinsdag 4 april 2017 des ochtends te 12.45 uur

door

Alberto Calivà
geboren op 22 december 1984
te Palermo (Italië)

Promotor: Prof. dr. T. Peitzmann

This thesis was accomplished with financial support from the Foundation for Fundamental Research on Matter (FOM), which is now part of the Netherlands Organisation for Scientific Research (NWO).

To my wife and daughter, the most precious treasures of my life. I love you.

*A new scientific truth does not
triumph by convincing its opponents
and making them see the light,
but rather because its opponents eventually die,
and a new generation grows up
that is familiar with it.*

Max Karl Ernst Ludwig Planck

Acknowledgements

The accomplishment of my research project and the completion of this manuscript have been possible also thanks to the support, encouragement, and supervision of some people that here I would like to thank.

Foremost, I would like to express my deepest thanks to Prof. Dr. Thomas Peitzmann, my supervisor and promotor, who has enriched me hugely, not only scientifically but personally too. I have enormously benefited from his advice, suggestions, comments and critical observations about my work. I've learned a lot from his lectures and from our long and stimulating discussions thanks to his wide and deep knowledge of many different aspects of our research field. He has been always present and available to help, encourage and support me in many situations. I would like to thank him for the great opportunities and for the immense trust he gave me throughout my time as PhD. His attitude has been fundamental for my development as an independent scientist. I have been extremely lucky to have a supervisor who cared so much about my work, who carefully read my manuscript and who responded to my questions and queries so promptly.

I would like to thank Dr. Hongyan Yang, my former co-supervisor during the first two years of my PhD, for her patient guidance, especially in the first few months, and for her contribution to the development of my different mental attitude. I've learned how to solve all kind of technical issues and inconveniences related to the software and the analysis framework by myself, without invoking other people's help.

I would like to thank Prof. Dr. Harry Happelsauer, Dr. Torsten Dahms, and Dr. Taku Gunji, the members of my working group, for their careful and scrupulous review of my analysis, for their interest and support, and for their comments and suggestions during our meetings. They gave a substantial contribution to the development and improvement of my analysis techniques.

I wish to express my most sincere gratitude to Andrea Dubla and Sandro Bjelogrljic, my paranymphs and my dear friends, for the role they had in my professional and private life. Andrea, with his pragmatism and rude sincerity, and Sandro, with his immense calm and positive attitude, have been very important references in many aspects of my life.

I would like to thank them also for their support and help in many difficult moments. I would like to thank Davide Lodato, my dear Sicilian friend and colleague, for his immense and kind availability, and for his nearness in many circumstances. He has been very helpful with his experience of the analysis framework and the operating system. I would also like to thank all the staff members at the institute of Subatomic physics of the Utrecht university and at Nikhef. In particular I wish to thank Marco Van Leuween, for his help and technical support with the computer cluster at the University, Alessandro Grelli, for his gags and useful tips, Mike Sas and Tuva Richert, my officemates, for the nice and funny moments we shared together and Emilia Leogrande, my former officemate, for her help and for the possibility I had to discuss with her about many aspects of our research activities.

I would like to thank all my friends in Utrecht for all the moments we shared together. I would like to thank Dr. Silvia Masciocchi, the ALICE group leader at the GSI, for the interest she expressed in my work and for the great opportunity she gave me for the future prosecution of my scientific career.

I would like to thank Dr. Mischa Bonn, the lecturer who gave the course on "how to get funded" organized by FOM, for the contribution he gave in opening unexpected perspectives and opportunities to continue my activity in the Academia.

For my family and relatives, I would like to express my deep gratitude and heartfelt thanks to Morena, my wife, for her love, her continued support, and encouragement. She stayed next to me in the most difficult and frustrating moments and she gave me her precious help in overcoming them. She had a fundamental role in the accomplishment of my PhD.

Special thanks go to my little daughter, Gaia, for cheering me up on some bad days with her joyful smiles, and for helping me to distract from some stressful moments with the game. I would like to thank Luciano, Giovanna, Teresa and Maria, my family members, for their support and the deep interest they have always expressed for my work and my life.

Abstract

In ordinary matter, quarks and gluons are confined inside hadrons by the strong interaction. At extreme conditions of temperature and energy density, a new state of matter is formed, called quark-gluon plasma (QGP). This is made of deconfined quasi-free quarks and gluons. Based on the current cosmological picture, the quark-gluon plasma was the state of our universe few μs after the Big Bang. Moreover, there is evidence that a degenerate state of matter with similar properties to the QGP exists in the inner core of neutron stars and other compact astrophysical objects.

Microscopic and extremely short-lived quantities of such a nuclear plasma can be created in ultra-relativistic heavy ion collisions. Its properties can be studied through several experimental probes using dedicated detectors installed around the collision region. This interesting branch of research is part of the experimental program of the Large Hadron Collider (LHC) at CERN, where lead ion beams are accelerated to unprecedented energies.

The QGP properties, in principle, can be described by Quantum-Chromodynamics (QCD), the quantum field theory of the strong interaction. However, a description of the system based on QCD first principles is extremely complicated due to the relatively low energy scale involved (compared to Λ_{QCD}), which does not allow to solve the QCD equations using the perturbative approach. Further complications arise from many-body properties of QCD which are anyhow extremely interesting to explore.

The deconfined medium created in heavy-ion collisions rapidly evolves, passing through several thermodynamic stages. According to the overall picture of the space-time evolution of the collision, the system quickly approaches local thermal equilibrium. This phase is followed by a rapid expansion, which is usually described by relativistic hydrodynamics. During the system expansion, its temperature and density decrease until quarks and gluons recombine into hadrons. After hadronization, the interactions in the hot and dense gas of hadrons are described using phenomenological transport models. In this stage, the particle density further decreases until all interactions cease at the so-called freeze-out, after which the particles produced propagate freely into the vacuum.

Photons and dileptons are unique tools to study the properties of heavy-ion collisions.

These particles are continuously emitted by the expanding system, and they cross the medium with negligible final state interaction, thus carrying undisturbed information on their production source. Electromagnetic probes provide complementary information to hadronic probes, which are mostly sensitive to late stages of the collision, thus allowing to constrain the theoretical models used for the description of the system in the early stages. Thermal photons and dileptons carry information on the system temperature. Moreover, in-medium effects of short-lived vector mesons can be studied through their dilepton decay channels. Modifications of the electromagnetic spectral functions of low-mass mesons are expected in a high-temperature and high-density hadronic environment. These modifications, which are reflected in the resonance mass or width, have since long been proposed as signatures of chiral symmetry restoration. Dileptons are also sensitive to heavy-flavor production, which gives a significant contribution to the intermediate mass region of the dilepton spectrum ($m_\phi < m_{l+l-} < m_{J/\psi}$).

In this thesis, the dielectron production in Pb–Pb collisions at $\sqrt{s_{\text{NN}}} = 2.76$ TeV with the ALICE experiment at the LHC has been studied. ALICE is the detector at the LHC dedicated to the study of heavy-ion collisions. Its excellent tracking and particle identification capabilities, over a wide range of particle momenta, make this experiment well suited for dielectron measurements. A large effort has been dedicated to the suppression of the main sources of background through innovative and efficient techniques. The main focus has been the study of the low-mass region of the dielectron invariant mass spectrum, where contributions from thermal dileptons and from in-medium modified low-mass vector mesons are expected. The fraction of virtual direct photons has been measured, which is compatible with real direct photon measurement from ALICE and existing dielectron measurements from RHIC at lower center-of-mass energy. Moreover, the measured dielectron spectrum has been compared to the expected contributions from hadron decays, thermal dileptons and in-medium modified ρ^0 and ω mesons, resulting in good agreement within the experimental uncertainties. The future perspectives for the dielectron measurement and the predicted scenario after the upgrade of the main ALICE sub-detectors are also presented.

Table of contents

1	The Quark-Gluon Plasma (QGP) and its Experimental Signatures	1
1.1	Introduction	1
1.2	Quantum ChromoDynamics (QCD)	5
1.2.1	Asymptotic Freedom And Confinement	7
1.2.2	Chiral Symmetry	11
1.3	The Limiting Temperature	13
1.4	Deconfinement And Phase Transition	15
1.4.1	The MIT Bag Model	16
1.4.2	The QCD Phase Diagram	18
1.4.3	Results From Lattice QCD Calculations	19
1.5	Heavy-Ion Collisions and Evolution of the Hot and Dense Matter	21
1.5.1	Space Time Evolution of Heavy-Ion Collisions	22
1.5.2	Thermal Models of Particle Production	25
1.6	Experimental Signatures of the QGP	26
1.6.1	Collective Flow	27
1.6.2	Strangeness Enhancement	29
1.6.3	Quarkonium Suppression	30
1.6.4	In-medium Parton Energy Loss	32
1.7	Summary of the main Global Properties of the QGP	36
2	Electromagnetic Probes	39
2.1	Introduction	39
2.2	Photon Sources	40
2.3	Prompt Photon Production	41
2.3.1	Drell–Yan Process	43
2.4	Thermal Emission Rate	44
2.5	Photon Production in the Early Stages	47
2.6	Real Photon Measurements	47

2.7	Dilepton Measurements	52
2.7.1	Dielectron Spectrum	53
2.7.2	Thermal Dileptons	54
2.7.3	Quasi-real Virtual Photons	55
2.7.4	In-Medium Effects of Vector Mesons	56
2.8	Review of Experimental Results on Dileptons	57
2.8.1	The First Dilepton Measurements: the SPS Era	58
2.8.2	Dilepton Measurements at RHIC: PHENIX and STAR	62
2.8.3	Dilepton Measurements at the LHC	67
3	The Experimental Setup and the Analysis Framework	71
3.1	Introduction	71
3.2	The Large Hadron Collider (LHC)	71
3.3	The ALICE Detector	73
3.3.1	Inner Tracking System (ITS)	74
3.3.2	Time Projection Chamber (TPC)	75
3.3.3	Time-Of-Flight (TOF)	77
3.3.4	Forward Detectors (FWD)	78
3.3.5	Other Detectors	79
3.4	Particle Identification (PID)	80
3.4.1	PID Based on Energy Loss Measurements	81
3.4.2	PID Based on Time-Of-Flight Measurements	82
3.5	Analysis Framework	83
3.6	Monte Carlo Simulations	84
4	Data Acquisition and Event Reconstruction	87
4.1	ALICE Data Acquisition (DAQ)	87
4.1.1	The ALICE Trigger System	88
4.1.2	The High Level Trigger	89
4.2	Offline Event Selection	90
4.2.1	Machine Induced Background (MIB)	90
4.2.2	Physical Background	92
4.3	Reconstruction And Data Format	92
4.4	Collision Centrality	94
4.5	Reaction Plane	97
4.6	Central Barrel Tracking	99
4.6.1	Preliminary Vertex Determination	100

4.6.2	TPC Seed Finding	100
4.6.3	Track Reconstruction	101
4.6.4	Final Vertex Determination	104
4.6.5	ITS Standalone Tracking	104
4.6.6	Tracking Performances	104
4.6.7	Secondary Tracks	106
4.7	Monte Carlo Sample	108
4.8	Event And Run Selection	109
5	Track Selection and Photon Conversion Rejection	113
5.1	Track Quality Cuts	113
5.2	Particle Identification	119
5.2.1	TPC post-calibration	121
5.2.2	Electron Identification Strategy	123
5.3	Photon Conversion Rejection	127
5.3.1	Conversion Rejection on a Single Track Basis	128
5.3.2	Conversion Rejection Using Pair Cuts	133
5.3.3	Comparison Between Single-track and Pair Rejection Methods	139
6	Background Estimation and Signal Extraction	141
6.1	Introduction	141
6.2	Background Components	141
6.2.1	Charge Asymmetry	143
6.2.2	Acceptance Correction: the R-factor	144
6.3	Hadronic Background	147
6.4	Signal Extraction	152
6.5	Impact of the Non-Uniformity in the <i>kCentral</i> Trigger Efficiency	155
7	Efficiency Calculation and Hadronic Cocktail Simulation	159
7.1	Introduction	159
7.2	MC Simulations	159
7.3	Correction of the Input Spectra	160
7.3.1	Electrons from HIJING Sources	160
7.3.2	Electrons from the Enriched Sample	163
7.4	Efficiency Calculation and Detector Effects	163
7.4.1	Detector Response Matrices	165
7.5	Reconstruction Efficiency of Single Electrons	167

7.6	Pair Reconstruction Efficiency	171
7.6.1	Heavy-Flavor Electrons	171
7.6.2	Pre-filter Correction	173
7.6.3	Random Rejection Probability	173
7.6.4	Residual Conversion Contribution	175
7.6.5	Pair Efficiency Correction	177
7.7	Hadronic Cocktail	179
7.7.1	Light-Flavor Component: Resonance Decays	179
7.7.2	Heavy-flavor Decays	180
8	Systematic Uncertainties	183
8.1	Introduction	183
8.2	Systematic Uncertainties Estimation	183
9	Results and Discussion	187
9.1	Introduction	187
9.2	Cocktail Comparison	187
9.3	Virtual Direct Photon Measurement	190
9.4	Comparison with Theoretical Predictions	195
10	Perspectives for Dielectron Measurements after the ALICE Upgrade	197
10.1	Introduction	197
10.2	Upgrade of the ITS and TPC	197
10.3	Physics Performance Study	200
10.4	Expected Scenario for Dielectron Measurements	201
11	Summary and Conclusions	207
Appendix A Reconstruction of Secondary Tracks: Features of the Tracking Algorithm		213
A.1	Shift in the Track Momentum	213
A.2	Mass and Opening Angle Shift	214
Appendix B Upper Limit Estimation		219
B.1	Confidence Belts: Neyman's Construction	219
B.2	Extraction of Confidence Intervals	221
References		223

Chapter 1

The Quark-Gluon Plasma (QGP) and its Experimental Signatures

1.1 Introduction

The Standard Model (SM) of particle physics describes elementary particles and their interactions. Developed in the early 1970s, it is a very rich scientific theory which has been tested to an incredible level of precision. It has successfully explained many experimental results and provided precise predictions for a wide variety of phenomena.

Elementary particles can be classified into two main categories, according to their spin, i.e. intrinsic angular momentum: *matter particles* (half-integer spin) and *field mediators* (integer spin). These categories play different roles in the realm of particle physics. Matter particles represent the fundamental building blocks of matter in our universe and they include three generations of quarks, three of leptons and the same number of generations of corresponding antiparticles. Field mediators, also called gauge bosons, are the messengers of the fundamental forces, which are exchanged by the interacting particles, according to the description provided by modern quantum field theories [1]. The Standard Model includes also the Higgs boson, which is involved in the mechanism that generates the mass of elementary particles [2]. The elementary particles included in the Standard Model and some of their properties are summarized in Fig. 1.1.

Three of the four fundamental interactions are relevant in particle physics: the strong interaction, responsible for binding together quarks inside hadrons, the weak interaction, responsible for nuclear β -decay and the interaction of neutrinos with ordinary matter, and the electromagnetic interaction, governing all electromagnetic processes. These interactions are described by relativistic quantum field theories, called *gauge theories*, which are incorporated in the Standard Model. A unified description of the electromagnetic

mass →	$\approx 2.3 \text{ MeV}/c^2$	$\approx 1.275 \text{ GeV}/c^2$	$\approx 173.07 \text{ GeV}/c^2$	0	$\approx 126 \text{ GeV}/c^2$
charge →	$2/3$	$2/3$	$2/3$	0	0
spin →	$1/2$	$1/2$	$1/2$	1	0
	u up	c charm	t top	g gluon	H Higgs boson
QUARKS	$\approx 4.8 \text{ MeV}/c^2$	$\approx 95 \text{ MeV}/c^2$	$\approx 4.18 \text{ GeV}/c^2$	0	
	$-1/3$	$-1/3$	$-1/3$	0	
	$1/2$	$1/2$	$1/2$	1	
	d down	s strange	b bottom	γ photon	
	$0.511 \text{ MeV}/c^2$	$105.7 \text{ MeV}/c^2$	$1.777 \text{ GeV}/c^2$	$91.2 \text{ GeV}/c^2$	
	-1	-1	-1	0	
	$1/2$	$1/2$	$1/2$	1	
	e electron	μ muon	τ tau	Z Z boson	
LEPTONS	$< 2.2 \text{ eV}/c^2$	$< 0.17 \text{ MeV}/c^2$	$< 15.5 \text{ MeV}/c^2$	$80.4 \text{ GeV}/c^2$	
	0	0	0	± 1	
	$1/2$	$1/2$	$1/2$	1	
	ν_e electron neutrino	ν_μ muon neutrino	ν_τ tau neutrino	W W boson	
					GAUGE BOSONS

Fig. 1.1 : Fundamental matter particles and gauge bosons (field mediators) included in the Standard Model of particle physics.

and weak interactions, the electroweak theory, has been developed by Weinberg, Salam, and Glashow in 1967. A large effort to include also the strong interaction into a unique theoretical framework has led to the development of Grand Unified Theories (GUT), which predict the unification of electroweak and strong interactions at very large energy scales. The experimental test of these theories is however out of reach in the present days due to the relatively limited energy reachable in the existent particle accelerators. Gravity is not relevant at the typical energy scales of elementary particles and their aggregates (hadrons or nuclei) due to the weakness of its strength compared to the other fundamental interactions. Only when the matter is in bulk, at the scale of the planets or stars, for example, does the effect of gravity dominate. Moreover, a quantum theory of gravity is not available yet since fitting general relativity and quantum theory into a unique theoretical framework has proven to be an extremely challenging task.

Table 1.1 summarizes the four fundamental forces at work in our universe and some of their properties, such as their typical ranges and strength relative to the strong force.

The general scope of research of this thesis is the study of strongly interacting matter – i.e. quarks, gluons and their bound states – at extreme conditions of temperature and energy density. In ordinary matter quarks and gluons are confined inside hadrons by the strong interaction. Quantum Chromo Dynamics (QCD), the theory of strong interaction, predicts a phase transition from hadronic phase to a deconfined phase of quarks and gluons, called *quark-gluon plasma* (QGP), at temperatures and energy densities exceeding some critical thresholds. The interest in this particular phase of matter comes from the need to understand the structure of our universe in the early stages of its evolution. In

Force	Strength relative to strong force	Range (fm)	Mediators
Strong	1	~ 1	gluons
Electromagnetic	$\sim 10^{-2}$	∞	photons
Weak	$\sim 10^{-16}$	$\sim 10^{-3}$	W^\pm & Z^0
Gravitational	$\sim 10^{-41}$	∞	graviton (?)

Table 1.1 : Fundamental forces in our universe and their main features. The mediator of gravitational force, called graviton, is a hypothetical particle which has not been discovered yet.

fact, it has been established that few μs after the Big Bang the quark-gluon plasma was the state of our universe. Moreover, the physical conditions in the inner core of neutron stars and other compact and massive astrophysical objects are believed to be suitable for the existence of the QGP as a stable phase of the matter. The study of the QGP properties is thus a common interest of Astrophysics, Cosmology, as well as Particle Physics. Since it is not possible to access the inner parts of a neutron star or to look back in time when our universe was opaque, the only way to study the quark-gluon plasma is to create it in the laboratory. Violent collisions of heavy ions, pushed to ultra-relativistic energies by powerful accelerators, create small drops of this matter, which have typical lifetimes of few tens of fm. They rapidly expand, undergoing several ephemeral thermodynamic states before quarks and gluons recombine again to form hadrons (hadronization).

Several experiments performed at the Super Proton Synchrotron (SPS) at CERN and Relativistic Heavy-Ion Collider (RHIC) at Brookhaven National Laboratory, New York, have provided a significant evidence of the formation of this novel state of matter. The exploration of its physical properties now continues at higher energies with the LHC, within its heavy-ion experimental program.

The study of the transition to a deconfined phase of quarks and gluons is not only relevant to understand and characterize the beginning of our universe, but it has a deep impact on the theoretical aspects of the QCD. In physics, a phase transition is usually accompanied by a symmetry restoration. An analogy with the ferromagnetic phase transition can be made, where the isotropy symmetry is broken at low temperature when all dipole magnetic moments are aligned, giving a macroscopic magnetization. This

symmetry is however restored at high temperatures, where the thermal motion of the particles impedes a preferred orientation of the magnetic dipole moments.

Chiral symmetry is an approximate symmetry of the QCD Lagrangian which is spontaneously broken at low temperatures and it is expected to be restored at high temperatures and energy densities. Lattice QCD calculations indicate that the transition which leads to restoration of chiral symmetry (chiral transition) and the deconfinement phase transition occur at the same critical temperature, providing strong evidence that these two different transitions might actually coincide. The understanding of the conditions for the restoration of chiral symmetry is crucial not only for theoretical reasons, but also for its impact on the structure of our universe: chiral symmetry breaking is, in fact, responsible for $\sim 99\%$ of the proton and neutron masses, hence most of the visible mass of our universe, i.e. excluding dark matter. Many open questions still remain which need to be addressed, such as the order of the phase transition, the characterization of the QCD phase diagram, the equation of state of the QGP, its evolution and the exact mechanism of hadronization.

Several experimental probes can be used to study the QGP, which are sensitive to different properties. Electromagnetic probes, i.e. photons and dileptons, are unique tools to study the space-time evolution of the QGP. These particles are continuously emitted during the system evolution and they interact with the surrounding medium only through the electromagnetic force. Their mean free path in the created matter is much larger compared to its typical size so that they travel through it essentially undisturbed, thus carrying unaffected information on the properties of their production sources.

In this thesis, the study of the dielectron invariant mass spectrum measured in Pb–Pb collisions at $\sqrt{s_{\text{NN}}} = 2.76$ TeV is presented, with particular focus on the low-mass region ($m_{ee} < 900$ MeV/ c^2). This region of the dielectron spectrum is particularly interesting to study the production of quasi-real virtual direct photons (in the kinematic domain $p_{\text{T}}^{ee} \gg m_{ee}$) produced during the expansion of the hot system. This provides a complementary measurement to real direct photons, using calorimetry or the Photon Conversion Method (PCM). Moreover, the low-mass region contains a significant contribution from thermal dileptons emitted in the hadronic phase, whose production is largely mediated by the ρ^0 resonance ($q\bar{q} \rightarrow \rho^0 \rightarrow e^+e^-$), due to its large $\pi - \pi$ coupling. Since the ρ^0 lifetime is small compared to the average lifetime of the hot and dense matter, this particle lives its entire life in a high-density and high-temperature hadronic system. In medium modifications of the spectral properties (mass and width) of ρ^0 and other light vector mesons are expected in these conditions and they have since long been proposed as signatures of chiral symmetry restoration.

The first part of this chapter contains a general overview of the theory of strong interaction and its properties, a description of the QCD phase diagram, a discussion of the deconfinement phase transition and the illustration of the current picture about the space-time evolution of heavy-ion collisions. In the second part, a review of the most important experimental signatures of the QGP is presented. Chapter 2 is dedicated to the electromagnetic probes. Their importance in the study of the evolution of heavy-ion collisions and their advantages compared to other probes are highlighted. The main experimental results on dileptons and real photon measurements are presented in order to provide a broader picture of the research topic into which this thesis work is inserted. Chapter 3 provides a description of the particle accelerator and of the experimental apparatus. The following chapters contain a detailed description of the analysis strategy and the results are discussed in Chapter 9. To conclude, the perspectives for the dielectron measurement and the expected scenario after the ALICE upgrade are presented in Chapter 10, while Chapter 11 contains a brief summary of this work.

1.2 Quantum ChromoDynamics (QCD)

The nuclear force – which holds protons and neutrons together inside atomic nuclei – and, more generically, the force between hadrons are not fundamental forces. They can be described by an effective theory, the Yukawa theory [3], in terms of exchange of pseudoscalar mesons¹, which are not fundamental particles. Hadronic interaction is, in fact, a more complex manifestation of an underlying fundamental interaction, the *strong interaction*, similarly to the atomic or Van der Waals interactions between molecules, which can be ultimately brought back to QED. Strong interaction is described by a non-abelian gauge theory, called *Quantum ChromoDynamics* (QCD), based on the $SU(3)_C$ symmetry group. The QCD Lagrangian is given by:

$$\mathcal{L}_{\text{QCD}} = \sum_f \bar{q}_f (i\gamma^\mu D_\mu - m_f) q_f - \frac{1}{4} G_a^{\mu\nu} G_{\mu\nu}^a \quad (1.1)$$

where $q_f \equiv (q_f^1, q_f^2, q_f^3)$ is the vector notation for the quark field of flavor f , in which the three components indicate the three different color states, γ^μ are the Dirac matrices, and D_μ is the covariant derivative defined by:

¹A pseudoscalar quantity behaves like a scalar, except that it changes sign under parity inversion. In high-energy physics, a pseudoscalar meson is a meson with total spin 0 and odd parity (usually noted as $J^P = 0^-$). Pions are pseudoscalar mesons and their existence has been predicted by Yukawa in 1935, before their actual discovery (the charged pions in 1947, and the neutral pion in 1950).

$$D_\mu \equiv \partial_\mu - ig \frac{\lambda^a}{2} G_a^\mu \quad (1.2)$$

here λ^a ($a = 1, 2, \dots, 8$) are the generators of the fundamental representation of the $SU(3)_C$ algebra, G_a^μ are the gluon fields and g represents the coupling strength.

The second term in the Lagrangian is the gauge-invariant gluon field strength tensor:

$$G_a^{\mu\nu} \equiv \partial^\mu G_a^\nu - \partial^\nu G_a^\mu + gf^{abc} G_a^\mu G_b^\nu \quad (1.3)$$

where f^{abc} are the structure constants of the symmetry group.

The first part of the Lagrangian $\sum_f \bar{q}_f (i\gamma^\mu D_\mu - m_f) q_f$ contains three terms:

$$\sum_f i\bar{q}_f \gamma^\mu \partial_\mu q_f - m_f \bar{q}_f q_f + g\bar{q}_f \gamma^\mu \frac{\lambda^a}{2} G_a^\mu q_f \quad (1.4)$$

The first term describes the free quark propagation in the vacuum, the second is the mass term of quarks and the last one describes the quark-gluon vertex, represented by the Feynman diagram shown in Fig. 1.2. This part of the Lagrangian is similar to QED.

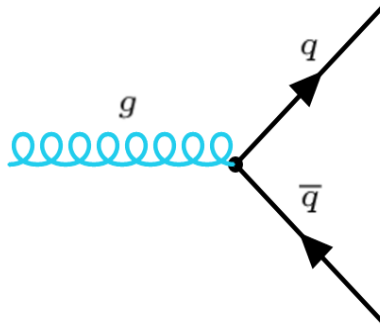


Fig. 1.2 : Feynman diagram representing the quark-gluon vertex.

The second part of the Lagrangian can be written in the symbolic form:

$$G^2 + gG^3 + g^2G^4 \quad (1.5)$$

The first term describes the free gluon propagation, while the last two terms describe the interaction between gluons, giving three-gluon and four-gluon vertices (Fig. 1.3).

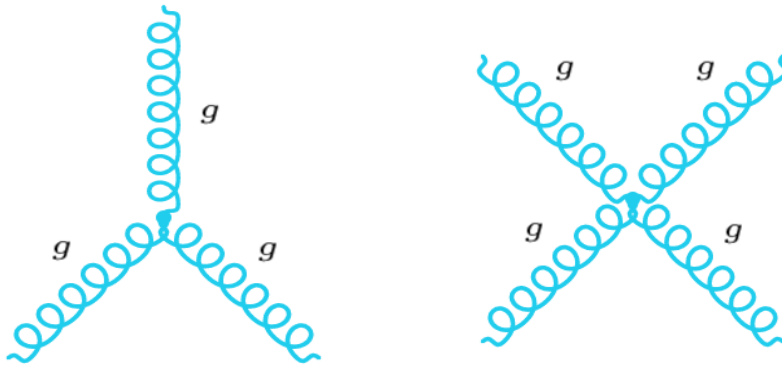


Fig. 1.3 : Feynman diagrams representing the three-gluon (left) and four-gluon coupling (right).

Gluons carry unbalanced color charge² and, differently from photons, they can interact among themselves. This unique aspect of the theory makes QCD a lot more complicated than QED, and it has deep implications on the features of the strong interaction and on the properties of the QCD vacuum.

1.2.1 Asymptotic Freedom And Confinement

The quark model was introduced by Murray Gell-Mann and Zweig in 1964 [4] to provide a plausible explanation of the curious patterns of the *Eightfold Way*, i.e. the classification of hadrons according to their hypercharge and strangeness. According to this model, hadrons are bound states of quarks, more specifically baryons are made of three quarks (anti-baryons are made of three antiquarks) and mesons are made of a quark and an antiquark. Despite the success of the quark model in explaining the hadron multiplets and predicting new particles that had indeed been discovered (like the Ω), there was a diffuse skepticism by many physicists due to the lack of observation of free quarks. The notion of *confinement* was introduced in order to explain the failure of experiments to produce isolated quarks. A more comprehensive understanding of the mechanism responsible for quark confinement came in 1964 when Greenberg introduced the color quantum number to save the quark model from a deep inconsistency related to the Pauli exclusion principle: each quark has an additional degree of freedom, expressed by an additive quantum number called *color*, which can assume three possible values: *red*, *blue* and *green*. Quarks bind together to give colorless hadrons, i.e. hadrons with no net color. This can be expressed using the analogy between the color states and

²Gluons carry one unit of color and one unit of anti-color.

2-dimensional vectors: the three color states correspond to three vectors, all starting from the point $(0, 0)$ and forming angles of 120° with the neighbor (Fig. 1.4). The color quantum number of a composite object is given by the vector sum of the colors of its constituents. According to this geometrical analogy, a baryon is made of three quarks with different color states, and a meson is made of a quark with a given color and an antiquark with the corresponding anticolor.

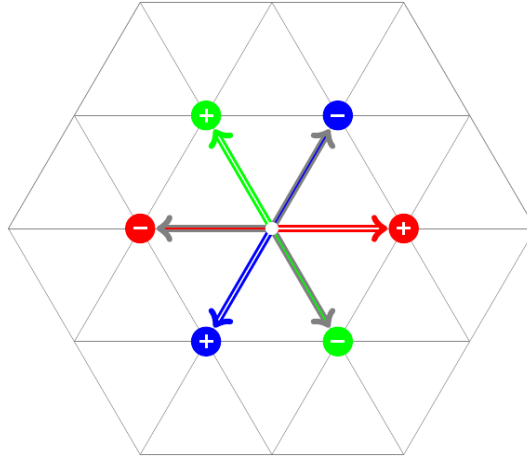


Fig. 1.4 : Geometrical analogy between color states and 2-dimensional vectors. The color of the bound state is given by the vector sum of the colors of its constituents.

Another important and peculiar feature of strong interaction was revealed by J. Friedman, H. Kendall, R. Taylor and their collaborators at the Stanford Linear Accelerator (SLAC) in their experiments using high energy photons to study the internal structure of protons. They discovered that protons are indeed made of three quarks. More surprisingly, they found that when quarks are hit hard they seem to move (more accurately: to transport energy and momentum) as if they were free particles. Before the experiment, most physicists had expected that whatever caused the strong interaction of quarks would also cause quarks to radiate energy abundantly, and thus rapidly to dissipate their motion, when they got violently accelerated, but this was not the case. This behavior of quarks is known as *asymptotic freedom*: high energy quarks, with large momentum transfer in their interactions with other quarks, behave asymptotically as free particles. Since high momentum transfer corresponds to short range interactions, this means that quarks interaction gets weaker at short distances.

Since the source of the strong field is the color charge, this implies that the bare color charge of quarks is in fact very small. The magnitude of the color charge, and hence the resulting strong field, is enhanced by the *anti-screening* effect of virtual gluon loops, created by quantum fluctuations of the QCD vacuum, which prevails over the screening

effect of quark-antiquark pairs. The gluon anti-screening effect is a direct consequence of gluon-gluon interactions, described by the QCD Lagrangian, and provides a simple argument to explain the absence of free quarks. The "effective" color charge of an isolated quark should grow to infinity as virtual gluon pairs gather around the cloud of color charge. This is impossible since this process would require an infinite amount of energy. The mechanism to compensate this infinite growth of color charge is the presence of an antiquark, which produces an anti-field, or the presence of two more quarks with different color states, which produce color fields that cancel the field of the initially isolated quark. The field is not canceled everywhere since this would require the total superposition of the three quarks (or quark and antiquark) and this is not possible since quarks are quantum particles, which cannot be localized within a too narrow wave packet. This would, in fact, broaden very quickly as a consequence of the Heisenberg uncertainty principle. The compromise between the minimization of the field energy and localization energy is represented by hadron states.

The concept of asymptotic freedom is expressed in a mathematical way by the dependence of the strong coupling constant on the momentum transfer in the interaction between two (anti-)quarks [5]:

$$\alpha_s(|q^2|) = \frac{12\pi}{(11n_C - 2f) \ln(|q^2|/\Lambda_{\text{QCD}}^2)} \quad (1.6)$$

where n_C is the number of colors, f the number of quark flavors and $\Lambda_{\text{QCD}} \approx 200$ MeV is the scale parameter of the theory. In nature $11n_C > 2f$, in consequence, the strength of the coupling constant decreases at high momentum transfer, i.e. short distances (Fig. 1.5).

Asymptotic freedom represents a huge advantage for theoretical calculations. In the high-energy regime ($|q^2| \gtrsim 1 \text{ GeV}^2$) in fact, when the strength of the interaction is weak, QCD can be treated perturbatively, thus enormously simplifying the calculations of cross sections and decay rates. The perturbative approach, however, cannot be applied in the domain where $\alpha \gtrsim 1$ ($|q^2| \lesssim 1 \text{ GeV}^2$), since higher order Feynman diagrams give increasing contributions which cannot be neglected in the calculations. The difficulty in solving QCD equations in the low-energy regime has led to the development of many effective models to obtain predictions, to explain phenomena and hadron properties at low energy, such as hadron masses, the hadronization mechanism and the coupling strength. Nowadays the application of QCD in the low-energy domain is based on lattice QCD, where the QCD equations are solved numerically in a finite space-time lattice, with the usage of computers.

In many phenomenological models of hadronization, baryons are treated as made of a

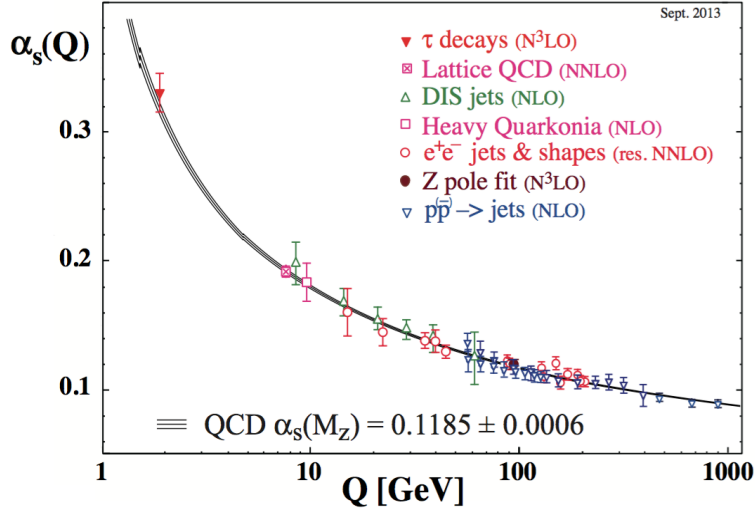


Fig. 1.5 : Strong coupling constant as a function of the momentum transfer in the interaction [5].

quark and diquark³, which is a bound state of two quarks. The interaction between a quark and a diquark in a baryon or between a quark and an antiquark in a meson can be expressed by the effective potential:

$$V(r) = -\frac{\alpha_s}{r} + k \cdot r \quad (1.7)$$

the first term, which is dominant at short distances ($r \ll 1$ fm), is a "Coulomb-like" potential, which expresses the fact that in the perturbative regime QCD becomes similar to QED. For short distances, Feynman diagrams with only one-gluon exchange are sufficient for the calculation of the interaction cross sections.

The strong field lines connecting the two interacting particles (quark–antiquark or quark–diquark) concentrate within a tight cylindrical region due to the interactions among gluons (Fig. 1.6 left). The second term in Eq.(1.7), linearly increasing with the distance where $k \simeq 1$ GeV/fm, is obtained assuming a constant linear energy density of the color field. This term describes quark confinement: when energy is supplied to a quark, which is pulled away from its partner inside a hadron, their potential increases until the energy threshold for a quark–antiquark (or diquark–anti-diquark) pair production is reached. This results in the creation of one more hadron, which is again in a color-neutral state (Fig. 1.6 right). This mechanism is used to explain hadronization in the Lund string fragmentation model [6] and is observed in dijet events where the two quarks produced

³This is a hypothetical state which is used to simplify the calculations.

in the collision fragment generating a large number of particles in the final state, flying back-to-back in the center-of-mass system within the jet cones.

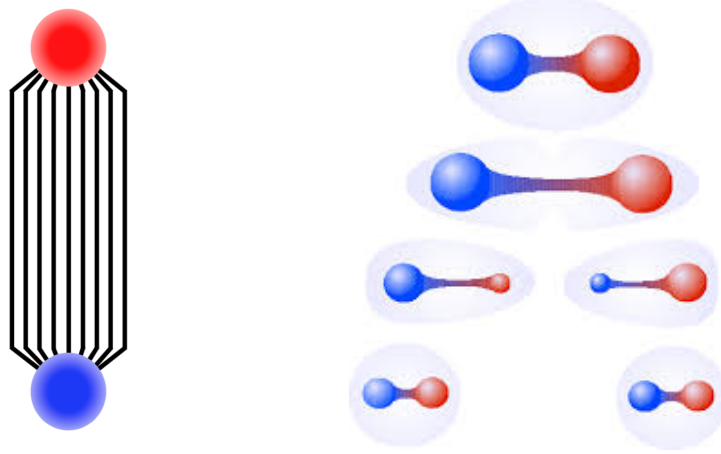


Fig. 1.6 : Strong field lines connecting two interacting quarks (or di-quarks) (left) and illustration of hadron formation by string fragmentation (right).

1.2.2 Chiral Symmetry

The QCD Lagrangian for massless quarks is symmetric under the following transformations, called *chiral transformations*:

$$\Lambda_V : q \rightarrow e^{-i\frac{\tau}{2}\theta} q$$

$$\Lambda_A : q \rightarrow e^{-i\gamma_5\frac{\tau}{2}\theta} q$$

When the mass term for quarks $-m_f(\bar{q}_f q_f)$ is also considered, the Lagrangian is still symmetric under the *vector transformation* Λ_V , but it is no longer symmetric under the *axial transformation* Λ_A :

$$\Lambda_A : m_f \bar{q}_f q_f \rightarrow \bar{q}_f q_f - 2i\theta \left(\bar{q}_f \frac{\tau}{2} \gamma_5 q_f \right)$$

Most of the mass of the visible universe originates from the lightest quarks, the u and d quarks, whose masses are $m_u = 2.3 \pm 0.7 \pm 0.5 \text{ MeV}/c^2$ and $m_d = 4.8 \pm 0.5 \pm 0.3 \text{ MeV}/c^2$ [7]. These values are considerably smaller than the scale parameter of QCD, $\Lambda_{\text{QCD}} \approx 200 \text{ MeV}$, hence the chiral symmetry can be regarded as an approximate symmetry of the QCD Lagrangian, in the sense that the predictions based on the exact

symmetry are close to the actual results.

The vector transformation Λ_V can be identified with the rotations in the isospin space and the symmetry of the Lagrangian under this transformation implies the isospin conservation by the strong interaction. The axial transformation Λ_A transforms particles with opposite chirality, named chiral partners, such as pion and σ -meson or the ρ and a_1 , into each other.

The (approximate) symmetry of the Lagrangian under the Λ_A transformation would imply that states which are rotated into each other by this transformation have the same mass. This is however not the case, as for example $m_\rho = 770 \text{ MeV}/c^2$, while $m_{a_1} = 1260 \text{ MeV}/c^2$. The large difference in mass between chiral partners cannot be explained by the small (*explicit*) symmetry breaking introduced by the tiny masses of u and d quarks. It is rather a consequence of the *spontaneous* breakdown of chiral symmetry, which occurs when the symmetry of the Lagrangian does not correspond to the symmetry of its ground state.

This can be better illustrated by the classical analogy depicted in Fig. 1.7. The potential shown in (a) and its state of minimum energy (ground state), realized at the point (0,0), are both symmetric under rotation. The potential shown in (b) is also symmetric under rotation, but its ground state is realized at finite distance from the geometric center of the potential, thus a ball on top of the hill, which is an unstable local maximum, will roll down towards the ground state breaking the rotational symmetry.

Assume that the effective QCD potential has the shape depicted in Fig. 1.7 (b), where the x and y coordinates are replaced by the σ and π fields. The axial transformation Λ_A corresponds to space rotations. In this picture, excitations in the π -direction, i.e. along the valley, do not cost energy and the pion is massless. Excitations in the σ -direction correspond to radial movements, which require energy and hence are massive. The pion mass is actually not zero as a consequence of the explicit symmetry breaking. In the previous picture, this would correspond to a slight deformation of the potential shape, such that some small amount of energy would be required also for excitations along the valley. The chiral symmetry is expected to be restored at high temperatures and, in consequence, the effective QCD potential is expected to become similar to Fig. 1.7 (a). In this limit, chiral partners are expected to be degenerate in mass. The chiral symmetry restoration is however only partial since the explicit breaking due to small but finite quark masses cannot be avoided. However, if the temperature at which chiral symmetry is restored coincides with the deconfinement temperature, the notion of hadron becomes meaningless (see Section 1.4.3).

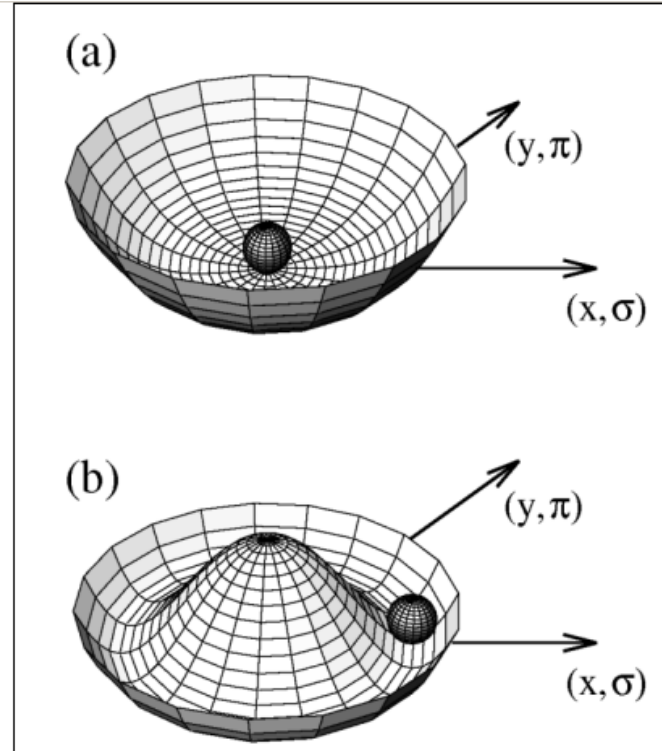


Fig. 1.7 : Illustration of spontaneous symmetry breaking. In (a) the potential and its ground state are symmetric under rotation. In (b) rotational symmetry is spontaneously broken by the ground state.

1.3 The Limiting Temperature

Curiously, the prediction of a critical behavior of hadronic matter at high temperature, done by Rolf Hagedorn in 1965 [8], came before the formulation of QCD and the discovery of partons. Hagedorn studied the mass distribution of the known hadronic species (Fig. 1.8) and described it using the following function:

$$\rho(m) = \frac{A}{m^2 + m_0^2} \exp(m/T_H) \quad (1.8)$$

where $\rho(m)$ is the density of hadron species per mass unit and T_H is a parameter, called *Hagedorn temperature*, whose value obtained from the fit was $T_H \approx 180$ MeV. The exponential behavior of the density of states created divergences in the partition function describing the statistical properties of a hadron gas when the temperature exceeded T_H . In consequence, the Hagedorn temperature T_H was interpreted as a limiting temperature of the hadronic matter: any additional energy supplied to the system at the Hagedorn temperature results in the creation of new hadron species. Hagedorn's conclusion was however based on the assumption that hadrons are elementary particles, while we know

that they are actually composite and extended objects whose typical size is ~ 1 fm. Close to the Hagedorn temperature, the hadron density increases reaching values of ~ 1 hadron per fm^3 , and for $T > T_H$ hadrons start to overlap. Under these conditions, hadrons can no longer be regarded as point-like objects since their mean free path is of the same order of magnitude as their typical size, which invalidates Hagedorn's conclusion. However, he deserves the credit for predicting the existence of a critical behavior of hadronic matter happening at a temperature which, according to the current estimates, is very close to Hagedorn temperature.

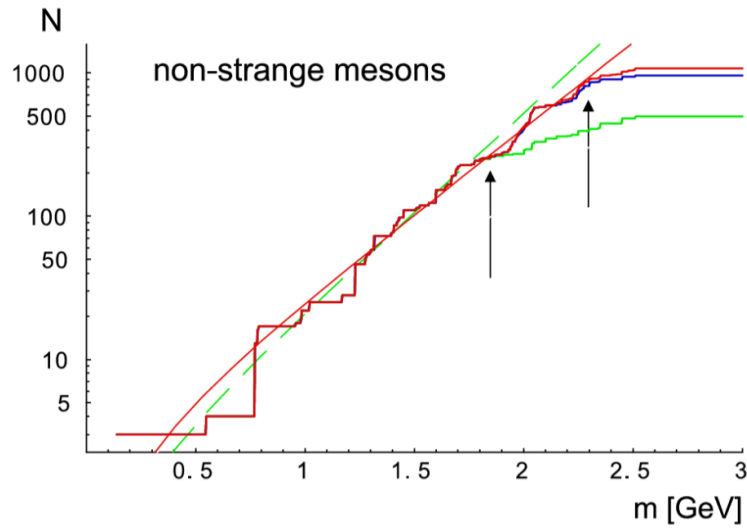


Fig. 1.8 : Number of non-strange mesons as a function of their mass [9]. The lower curve at high mass (solid green line) corresponds to particles listed in the Particle Data Tables of Ref. [10], the middle curve (solid blue line) includes the states listed in Refs. [11, 12], while the top curve (solid red line) includes in addition the states with hidden strangeness ($s\bar{s}$). The thin dashed (solid) line corresponds to the exponential fit to the spectra of the old (new) data. The arrows indicate the approximate upper values in mass of the validity of the Hagedorn hypothesis for the old and new data, respectively.

1.4 Deconfinement And Phase Transition

After the discovery of the asymptotic freedom by Frank Wilczek, David Gross, and independently by David Politzer in 1973 [13, 14] – for which they shared the Nobel Prize in 2004 – the existence of a deconfined phase of quarks and gluons was predicted at high temperature and/or pressure [15, 16]. The deconfined state was later called *quark-gluon plasma* (QGP) [17]. A first pioneering phase diagram of hadronic matter was imagined (Fig. 1.9), using two independent variables: temperature T and baryon density ρ_B .

The energy of thermal agitation of quarks inside hadrons increases with temperature, thus their interactions become weaker due to asymptotic freedom, till the point in which they behave as free particles and are no longer confined. At high-temperature, the hadronic matter essentially melts liberating its constituents, i.e. quarks and gluons. Alternatively, a transition to a deconfined phase can be obtained by increasing the pressure of hadronic matter, and hence its density. Hadrons are pushed against each other until the distances between quarks belonging to different hadrons become smaller than the hadron's typical size ($R \sim 1$ fm): hadrons are no longer distinguishable and they essentially merge.

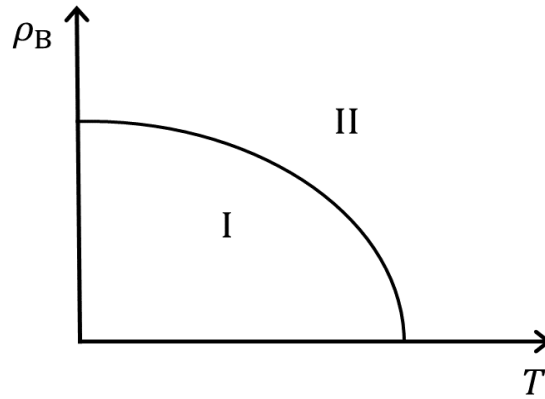


Fig. 1.9 : First phase diagram of hadronic matter. T is the temperature, ρ_B the baryon density, (I) is the confined phase while (II) is the deconfined phase [16].

The study of the QCD phase diagram is one of the primary goals of high energy nuclear physics. Much work has been done in the last decades, scanning different regions of the phase diagram, corresponding to different center-of-mass energies of colliding nuclei. The precise determination of the phase boundaries and the characterization of the nature of the phase transition for different regions of the phase diagram are important aspects which still need to be addressed. The latter is a crucial point since the existence of a

phase transition is strictly connected to the intrinsic symmetries of the QCD Lagrangian.

In the following sections the modern version of the phase diagram of the hadronic matter is presented and some results from lattice QCD, regarding the order of the phase transition and its connection to chiral symmetry restoration, are illustrated.

1.4.1 The MIT Bag Model

The transition from ordinary nuclear matter to a deconfined phase of quarks and gluons can be understood using the phenomenological *bag model*, developed at the MIT in the 1970s to describe the structure of hadrons [19]. In this model, hadrons are represented by spherical *bags*, containing massless and non-interacting quarks and gluons. Confinement results from the balance between the outward pressure arising from the kinetic energy of quarks and gluons and the inward pressure of the bag B . For a system with $N = 3$ quarks inside a bag of radius $r = 0.8$ fm, the equilibrium condition gives:

$$B^{1/4} = 206 \text{ MeV} \quad (1.9)$$

According to this model, deconfinement occurs when the pressure of quarks and gluons exceeds the bag pressure. This happens either by increasing the temperature or the density of quarks inside the bag. The latter can be explained by the Pauli exclusion principle, which states that fermions cannot populate states with the same set of quantum numbers. Increasing the number of quarks inside the bag implies the occupation of higher momentum states and, in consequence, the pressure arising from the average kinetic energy of quarks increases.

The bag model can be used to extract quantitative estimates of the critical temperature and the critical baryon density for the deconfinement. Usually, in high-energy nuclear physics, the baryon density is expressed in terms of the *baryochemical potential* μ_B , defined as the energy increase of a system when the number of baryons is increased by one unit. The baryochemical potential of a quark has the opposite sign of that of the corresponding antiquark. In this paragraph, the estimates of the critical values corresponding to two limiting cases are considered, which correspond to $\mu_B = 0$ and $T = 0$.

Case $\mu_B = 0$:

Assuming the same number of quarks and antiquarks ($\mu_B = 0$), it can be shown (see Ref. [20]) that the total pressure of quarks, antiquarks and gluons is given by:

$$P_{\text{tot}} = P_q + P_{\bar{q}} + P_g = \left[g_g + \frac{7}{8}(g_q + g_{\bar{q}}) \right] \frac{\pi^2}{90} T^4 \quad (1.10)$$

here g_q , and $g_{\bar{q}}$ and g_g are the number of degrees of freedom of quarks, antiquarks and gluons, respectively. Assuming two quark flavors, $g_q = g_{\bar{q}} = 2$ (flavors) \times 2 (spin states) \times 3 (colors) = 12. For gluons, $g_g = 8$ (gluons) \times 2 (polarization). From Eq.(1.10) it is possible to estimate the critical temperature, at which the pressure of quarks and gluons is equal to the bag pressure:

$$T_C = \left(\frac{90}{37 \pi^2} \right)^{1/4} B^{1/4} \quad (1.11)$$

For $B^{1/4} = 206$ MeV, the above equation gives $T_C = 144$ MeV. This value is very close to more recent and precise estimates based on lattice QCD calculations, which give $T_C = 175$ MeV [21].

Case $T = 0$:

It can be demonstrated (see Ref. [20]) that the pressure due to a degenerate gas of quarks at $T = 0$ is given by:

$$P_q = \frac{\epsilon}{3} = \frac{g_q}{24\pi^2} \mu_q^4 \quad (1.12)$$

where ϵ is the energy density of the system and μ_q is the quark chemical potential. The critical pressure is reached when:

$$\mu_q = \left(\frac{24\pi^2}{g_q} B \right)^{1/4} \quad (1.13)$$

which corresponds to a critical quark number density:

$$n_q = 4 \left(\frac{g_q}{24\pi^2} \right)^{1/4} B^{3/4} \quad (1.14)$$

and a critical baryon number density:

$$n_B = \frac{4}{3} \left(\frac{g_q}{24\pi^2} \right)^{1/4} B^{3/4} \quad (1.15)$$

For a bag pressure $B^{1/4} = 206$ MeV, $n_B = 0.72/\text{fm}^3$, which is almost 5 times larger compared to the density of ordinary nuclear matter $n_B = 0.14/\text{fm}^3$.

Using the bag model, it is possible to find the critical temperature corresponding to any value of the baryo-chemical potential, thus finding a relation between T and μ_B which defines the phase boundary. However, the results provided by the bag model

are not accurate enough due to the simplistic assumptions which completely ignore the complex and rich features of the strong interaction.

1.4.2 The QCD Phase Diagram

The phase diagram of hadronic matter, based on the current knowledge, is illustrated in Fig. 1.10. Thermodynamic states are represented by space points with coordinates (μ_B, T) and lines represent the boundaries between different phases.

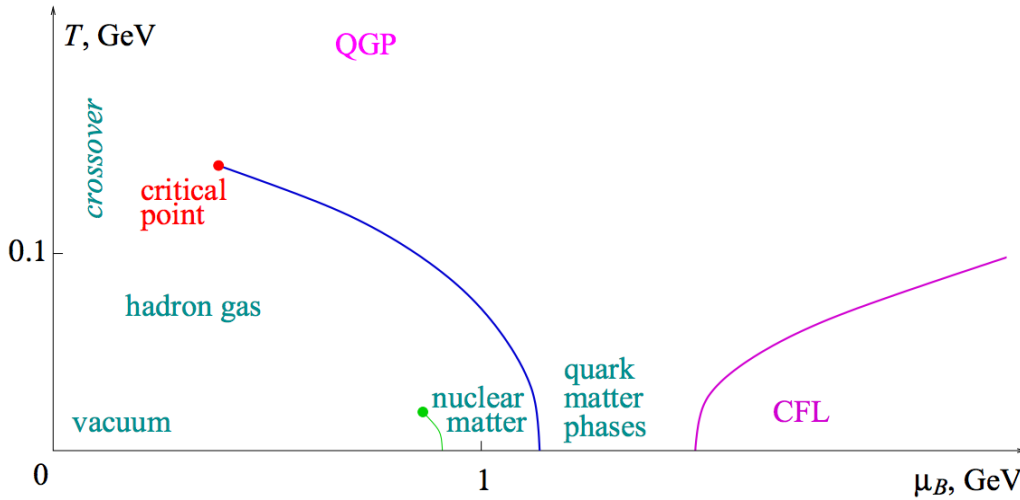


Fig. 1.10 : Semiquantitative sketch of the phase diagram of hadronic matter, based on present-day knowledge [18].

Ordinary nuclear matter exists at temperature close to zero, and $\mu_B \approx 940$ MeV. At low temperature and higher baryochemical potential (corresponding to pressures above $1 \text{ MeV}/\text{fm}^3$), the matter can be described as a degenerate gas of neutrons. This phase is expected to exist in neutron stars. In these stellar objects a mass slightly larger than that of our Sun is confined within a spherical volume of radius ~ 10 km, such that densities as high as $10^{17} \text{ kg}/\text{m}^3$ are reached. For higher pressures (larger than $1 \text{ GeV}/\text{fm}^3$), the repulsive force of the degenerate gas of neutrons cannot compensate the pressure and the matter becomes a degenerate gas of quarks, which are no longer confined inside hadrons. High-density and low-temperature matter is expected to be a color superconductor [22], which is a degenerate Fermi gas of quarks with a condensate of Cooper pairs near the Fermi surface that induces color Meissner effects. At the highest densities, where the QCD coupling is weak, rigorous calculations are possible, and the ground state is a particularly symmetric state, the color-flavor locked (CFL) phase. The CFL phase is a superfluid, an electromagnetic insulator, and breaks chiral symmetry.

The degenerate gas of neutrons, at temperatures above 10 MeV, is expected to become a gas of nucleons. The nucleon-nucleon interaction has some similarities to the Van der Waals force between molecules, thus a liquid-gas phase transition is expected. The nucleon gas at higher temperatures, $T > 100$ MeV, becomes a hadron gas. In this phase, several hadronic species which are not present in nuclear matter, such as pions of excited states of nucleons (like Δ), are in equilibrium. For higher values of temperature and baryochemical potential, the matter is in the quark-gluon plasma state.

The exact location of the line in the phase diagram defining the phase boundary and the existence of a critical point are not known. The exploration of the QCD phase diagram, the localization of the phase boundary and the characterization of the phase transition are interesting aspects which are at the center of the research program of heavy-ion physics.

1.4.3 Results From Lattice QCD Calculations

Recent progress of fast computers and the development of more efficient discretization algorithms, have contributed to the make Lattice QCD an extremely powerful tool to solve QCD equations in the non-perturbative regime. This approach is used to investigate the phase transition from ordinary hadronic matter to the deconfined phase of free quarks and gluons, the Quark-Gluon Plasma. The primary goal is to characterize the features of the phase transition and link them to the intrinsic symmetries of the QCD Lagrangian.

Results of lattice QCD calculations, for a system of massless quarks at $\mu_B = 0$ and finite temperature, indicate a phase transition at $T = 173 \pm 15$ MeV, corresponding to an energy density of $\epsilon = 0.7 \pm 0.3$ GeV/fm³ [23]. This is illustrated in Fig. 1.11, which shows the temperature dependence of the energy density of a system including two or three quark flavors.

For massless quarks, the energy density displays a rapid increase at the critical temperature. This is due to the abrupt change in the number of degrees of freedom of the system in the phase transition. While the masses of u and d quarks can be neglected, being much smaller than the QCD typical scale, $\Lambda_{\text{QCD}} \approx 200$ MeV, the mass of the *strange* quark ($m_s = 95 \pm 5$ MeV [7]) cannot be neglected. In the case of massless u and d quarks, and physical mass for the s quark, the calculations indicate that the phase transition fades away, becoming a cross-over. In this case, the transition is smooth and no critical behavior is observed [23].

The order of the phase transition depends on the number of quark flavors and their mass. Fig. 1.12 shows the criticalness of the phase transition as a function of quark masses, obtained from lattice QCD calculations. In the study presented here, the masses

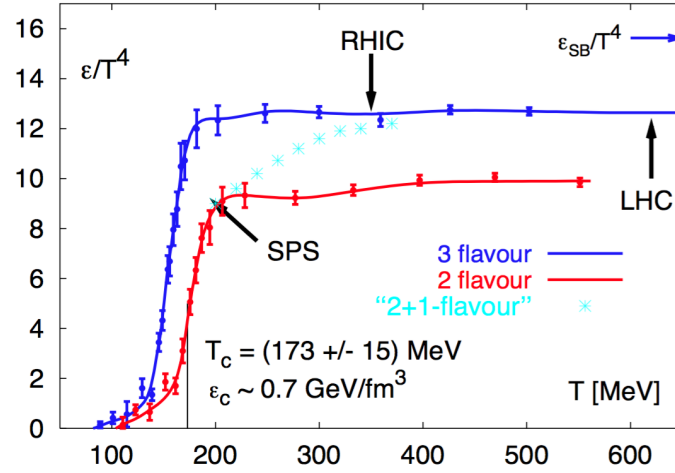


Fig. 1.11 : Temperature dependence of the energy density of a system of two or three quark flavors at $\mu_B = 0$ obtained from QCD calculations on the lattice [23].

of the u and d quarks are assumed to be identical and $\mu_B = 0$. The transition is of the first-order for very small or extremely large quark masses, while it is a cross-over for intermediate masses. A second-order phase transition occurs at the borders between first-order transition and cross-over. There is a broad consensus that a rapid cross-over occurs at the LHC energies [23, 24].

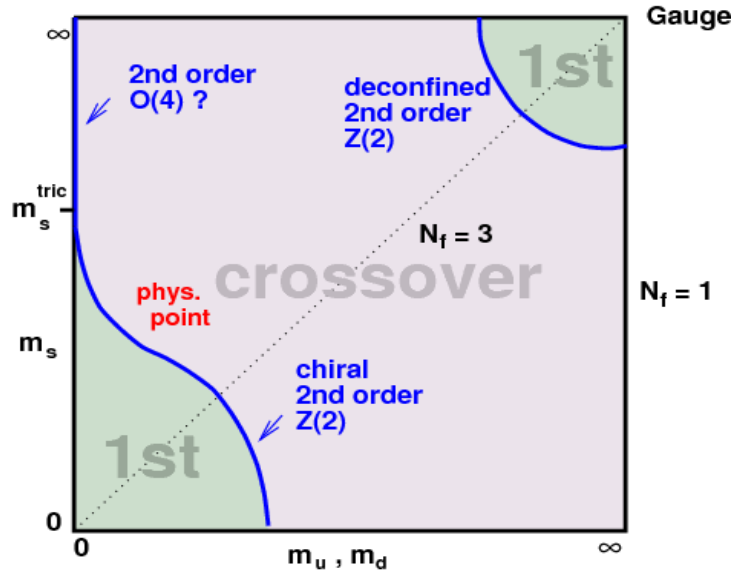


Fig. 1.12 : Results of lattice QCD on the criticalness of the phase transition for three quark flavors, $\mu_B = 0$, and assuming that the masses of the u and d quarks are identical [23, 24].

Finally, the order parameters of the chiral and deconfinement transitions have been studied using lattice QCD (see Fig. 1.13). The results of these studies interestingly show that both transitions occur at the same critical temperature, suggesting that deconfinement and chiral symmetry restoration might be two different features of the same transition.

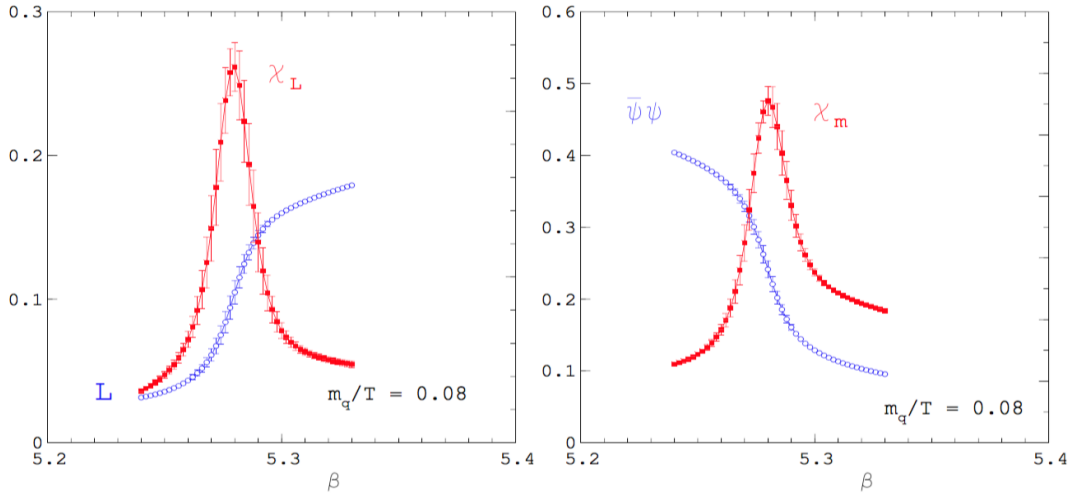


Fig. 1.13 : Critical behaviour for massless quarks and $\mu_B = 0$ of the order parameters of the deconfinement (left) and of the chiral (right) transitions as predicted by lattice QCD calculations. The order parameters are the Polyakov susceptibility (χ_L) and the chiral susceptibility (χ_m) [23].

1.5 Heavy-Ion Collisions and Evolution of the Hot and Dense Matter

Colliding heavy-ions at ultra-relativistic energies represents a unique experimental technique to create the quark-gluon plasma in the laboratory and to study its properties. Large detectors are used, installed around the collision region, to intercept the particles produced, which carry direct or indirect information on the system properties. High energy densities, above the limit of $\epsilon_c = 1 \text{ GeV}/\text{fm}^3$, are required to create a deconfined medium of quarks and gluons. In high energy nuclear collisions, only a fraction of the total center-of-mass energy of the colliding nuclei is dissipated, due to the limited stopping power of the nuclei. The amount of energy dissipated is deposited in the collision region and, if the energy density is above the limit, it is converted into internal energy of the quark-gluon plasma. Considering the limited fraction of the available energy that can be

converted into degrees of freedom of free quarks and gluons, it was an open question to establish the minimum energy of the colliding nuclei required to reach the critical energy density. Bjorken provided an estimate for the energy density reached in the collision region [25], which is given by:

$$\epsilon = \frac{1}{\pi R^2 \tau_{\text{form}}} \left[\frac{dE_{\text{T}}}{dy} \right]_{y=0} \quad (1.16)$$

where τ_{form} is the QGP formation time, i.e. the (proper) time needed to reach local thermodynamic equilibrium and $[dE_{\text{T}}/dy]_{y=0}$ is the transverse energy distribution of the produced particles per unit of rapidity, measured at midrapidity ($y=0$). The QGP formation time is not known exactly and cannot be directly measured in the experiments. It is a free input parameter of the theoretical models based on relativistic hydrodynamics that are used to describe the space-time evolution of the QGP. The formation time, as well as the time where hydrodynamic simulation is stopped, are usually varied within some time ranges. This reflects our limited knowledge of the space-time evolution of the deconfined medium. The QGP formation time can be reasonably assumed to be $\tau_{\text{form}} \lesssim \tau_{\text{strong}} \sim 1 \text{ fm}/c$ ⁴. Based on this estimate, the energy densities reached in heavy-ion collisions at the SPS energies were already above the critical value for the deconfinement phase transition.

In 2000, the analysis and interpretation of the obtained experimental results from several fixed-target experiments at the SPS at $\sqrt{s_{\text{NN}}} = 17 - 19 \text{ GeV}$ was completed and a press released was organised where it was announced a compelling evidence that a new state of matter had been formed, in which quarks, instead of being bound up into more complex particles such as protons and neutrons, were liberated to roam freely. The new state of matter found in heavy-ion collisions at the SPS featured many of the characteristics of the theoretically predicted quark-gluon plasma.

The space-time evolution of the created matter was described by Bjorken in [25] and it is illustrated in the following paragraph.

1.5.1 Space Time Evolution of Heavy-Ion Collisions

The two incoming nuclei appear as two almost flat disks to an observer in the laboratory frame, due to the strong Lorentz contraction in the direction of motion (Fig. 1.14). The crossing time of the two nuclei is given by:

⁴The QGP formation time, based on hydrodynamic model calculations, is shorter for higher energy density reached in the collision. At the LHC it is expected to be $\tau_{\text{form}} \sim 0.1 \text{ fm}/c$, while it was $\tau_{\text{form}} \sim 1 - 2 \text{ fm}/c$ at the SPS energies.

$$\tau_{\text{cross}} = \frac{2R}{\gamma} \quad (1.17)$$

where R is the nucleus radius and $\gamma = 1/\sqrt{1 - v^2/c^2}$ is the Lorentz factor.

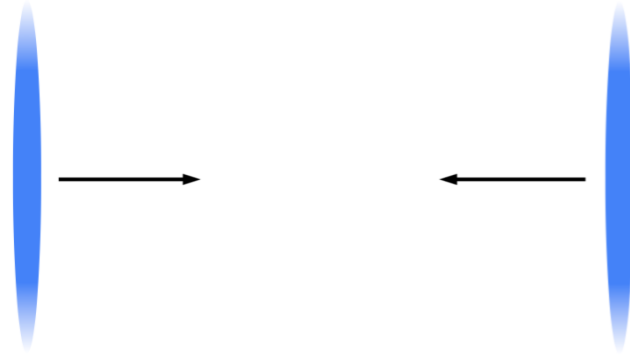


Fig. 1.14 : Incoming nuclei appear stretched in the laboratory frame due to the strong Lorentz contraction.

In the Bjorken picture, the multiplicity distribution as a function of pseudorapidity is assumed to be uniform and the crossing time is assumed to be shorter than the typical time scale of processes governed by the strong interaction, $\tau_{\text{strong}} \sim \Lambda_{\text{QCD}}^{-1} \sim 1 \text{ fm}/c$. Under the latter assumption, the particles produced by the strong interaction, in the initial hard parton-parton scattering, are created once the two nuclei have already crossed each other. The stages of the space-time evolution of the system created in the collision, illustrated schematically in Fig. 1.15, can be summarized as follows:

- **Initial state:** High energy nuclei are strongly compressed in the laboratory frame of reference by the Lorentz factor γ . Moreover, the time scale of quantum fluctuations happening inside nucleons, which produce many virtual gluons, are dilated by the same factor. The density of gluons thus increases with energy, until the *saturation* limit is reached, due to the competing gluon-fusion process $g + g \rightarrow g$ which limits the increase in the gluon density. Nuclei in the ultra-relativistic limit appear as dense clouds of gluons. These systems can be treated as classical fields, which are described by the model of *Color Glass Condensate* (CGC) [26].
- **Pre-equilibrium:** After the collision, the particles produced in the collision region interact among each other until local thermodynamic equilibrium is reached. Theoretical models based on relativistic hydrodynamics assume fast thermalization

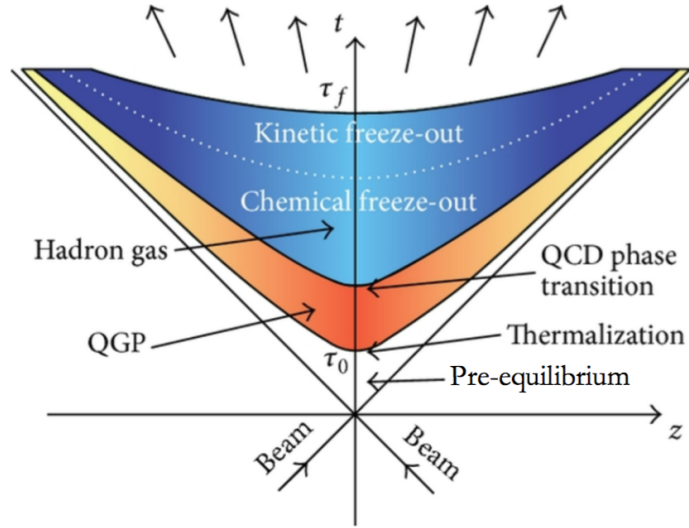


Fig. 1.15 : Schematic illustration of the space-time evolution of a collision between two high energy nuclei.

($\tau_{\text{therm}} \lesssim 1 \text{ fm}/c$). Although experimental data are well described by these models, the theory has not been able to explain the exact mechanism which leads to thermal equilibrium in such short time scales.

Thermal-like distributions have also been observed in elementary collisions (e^+e^- , K^+p , π^+p , ...) [27]. The thermalization process, described in terms of the semi-classical picture in which thermal equilibrium is reached by binary collisions among particles, is ruled out in elementary collisions due to the long mean free path of the produced particles compared to the length scale of thermalization. Yet, the agreement between data and theoretical models which assume thermalization is surprisingly accurate in elementary collisions, even more accurate than in heavy ion collisions. Hadrons, somehow, "*must be born into equilibrium*" as Hagedorn first pointed out [28]. The idea, that is shared by many [29], is that the thermal-like behavior is of genuine quantum-mechanical origin and not related to semi-classical collision processes.

In nucleus-nucleus collisions, the classical color fields, produced by saturated systems of gluons, remain coherent for a brief amount of time after the collision, forming a state known as *Glasma*. This approach seems to be the best theoretical tool to study the pre-equilibrium stage of heavy-ion collisions.

- **Hydrodynamical expansion:** When local thermal equilibrium is reached, the extremely hot and dense system undergoes a dramatic expansion against the vacuum

due to the extremely large pressure gradient. The system evolves like a "perfect" fluid, i.e. with shear viscosity close to ideal lower limit [30]. The evolution is described by the laws of relativistic hydrodynamics [31], in which small viscous corrections are included. A longitudinal expansion takes place first, due to the larger pressure gradient along the beam direction, and it is followed by a 3-dimensional expansion, driven by the pressure arising from thermal motion of the particles in the system. During the expansion, the energy density and the system temperature decrease.

- **Hadronization:** When the energy density of the system reaches its critical value, the transition from the deconfined phase of quarks and gluons to the hadronic phase occurs. The exact mechanism of hadronization is not known and it represents an important open question. Several phenomenological models of hadronization are used, which successfully predict particle yields and explain some experimental observations (see Section 1.6).
- **Freeze-out:** After hadronization, the system is in a hot hadron gas phase and continues its expansion and cooling. This stage is usually described by phenomenological transport models using hadronic degrees of freedom. The particles interact through both elastic and inelastic collisions. The cross section, and hence the range, for inelastic collisions is smaller compared to that of elastic ones, since the former require some threshold energy. During the system expansion, the average distances between hadrons increase, until they become larger than the range for inelastic collisions. At this stage, inelastic collisions cease, thus "freezing" the chemical abundances of particles (*chemical freeze-out*), which from this moment can only change as a result of particle decays. After the chemical freeze-out, particles continue to interact through elastic collisions until their mean free path becomes larger than the system size. At this stage, the system is so dilute that the elastic collisions also cease (*kinetic freeze-out*), and the momentum distributions of particles are no longer modified. After the kinetic freeze-out, particles fly freely towards the detectors.

1.5.2 Thermal Models of Particle Production

The Statistical Hadronization Model (SHM) is a phenomenological model of hadronization, which is widely used to predict particle yields in high-energy heavy-ion collisions. This model predicts particle emission from a thermalized source, assuming instantaneous hadronization and fixing the particle abundances at the chemical freeze-out. The fit of

SHM to the measured particle multiplicities gives an estimate of the temperature at the chemical freeze-out. The observed multiplicities of many particle species measured by ALICE at $\sqrt{s_{NN}} = 2.76$ TeV are successfully described by the statistical hadronization model, including loosely bound states such as light nuclei and hypernuclei (Fig. 1.16) [32]. It is still not clear how particles with binding energies of the order of few hundreds of KeV can be formed in an environment with a temperature $T \sim 100$ MeV.

Coalescence models describe the formation of these object as a result of the binding of their constituents, which are close enough in the phase space, in later stages at lower temperatures. Although this interpretation conceptually provides a more plausible explanation for the production mechanism of loosely bound states, the quantitative predictions of coalescence models are not satisfactory.

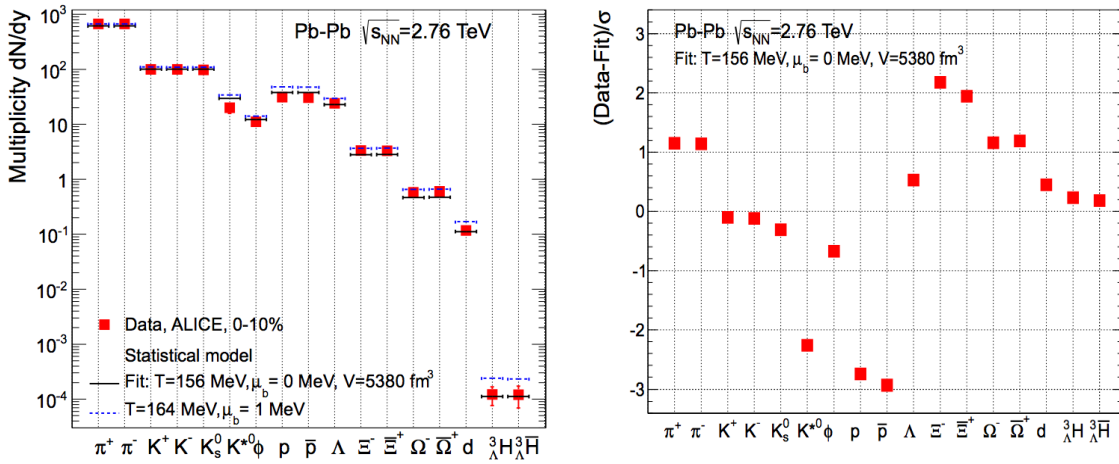


Fig. 1.16 : Hadron yields measured by ALICE at $\sqrt{s_{NN}} = 2.76$ TeV and fit with the statistical hadronization model (left). Deviations between thermal fit and data normalized to the error of the data points (right). The yield of protons and anti-protons appears to be overestimated by the model (this "proton anomaly" is discussed in Ref. [32]).

1.6 Experimental Signatures of the QGP

The typical lifetime of the quark-gluon plasma is ~ 10 fm/ c . During its evolution, the system passes through many thermodynamical stages which all contribute in a non-trivial way to the properties of the emitted particles. What is observed in the detectors are only the final products of the collisions, whose properties have been influenced by the whole space-time evolution of the system. This makes the study of the QGP an extremely difficult task. To this end, several experimental probes are used, which are sensitive to different properties of the QGP. Given the complexity of the system and its dynamical

evolution, in many cases, theoretical models have to be used for the interpretation of the results in order to disentangle the contributions originating from different phases. The results collected from different experiments and using different experimental probes need to be interpreted within the same theoretical scenario, which is constantly under development. In this paragraph, the main experimental signatures of the QGP are presented. This is not an exhaustive review, but rather a presentation of the main results of the research on the QGP and the illustration of the experimental techniques used in this field.

1.6.1 Collective Flow

Hadrons are produced at the hadronization hypersurface. Their thermal distributions are modified by the "blueshift" caused by the rapidly expanding source as well as by the intense rescattering in the late stages. The degree of anisotropy in the collective expansion of the system depends on the amount of overlay of the two colliding nuclei: the expansion is spherically symmetric (*radial flow*) in case of total overlay and asymmetric (*anisotropic flow*) for partial overlay (Fig. 1.17). The geometry of the overlap region depends on the impact parameter b , i.e. the distance between the centers of the colliding nuclei, in the plane transverse to the beam. Central collisions are defined by $b = 0$, while in semi-central collisions $b \neq 0$ (see Chapter 4).

The transverse momentum distributions of identified hadrons (π , K and p) have been measured by ALICE in central (head-on) Pb–Pb collisions at $\sqrt{s_{\text{NN}}} = 2.76$ TeV [33]. The measured p_{T} distributions appear harder, i.e. less steep and characterized by a larger $\langle p_{\text{T}} \rangle$, compared to those measured at RHIC at $\sqrt{s_{\text{NN}}} = 200$ GeV (Fig. 1.18 left). The expansion velocity of the medium, extracted from a Blast-wave fit to the hadron spectra, implies a $\sim 10\%$ higher radial flow at the LHC compared to its value measured at RHIC (Fig. 1.18 right).

In semi-central collisions, the initial geometrical anisotropy of the overlap region results in an azimuthal anisotropy in the particle emission. The azimuthal distribution of the emitted particles can be expressed by:

$$\frac{dN}{d\phi} = \frac{1}{2\pi} \left[1 + 2 \sum_{n \geq 1} v_n \cos(n(\phi - \Psi_{\text{RP}})) \right] \quad (1.18)$$

where Ψ_{RP} indicates the orientation of the reaction plane, defined by the impact parameter and the beam direction. The second harmonic, called *elliptic flow*, gives information on the internal viscosity of the quark-gluon plasma. The results obtained for the elliptic flow, both at RHIC and at the LHC, indicate that the hot and dense

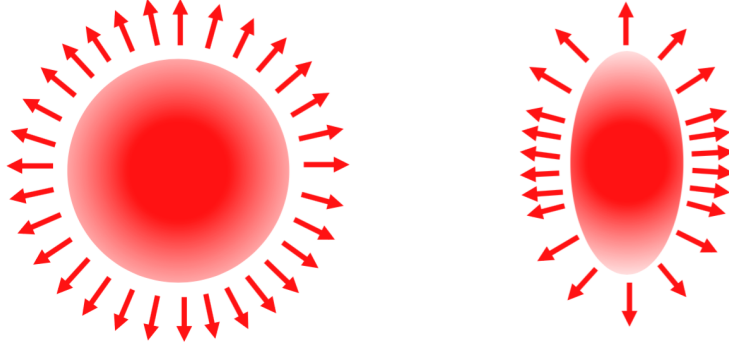


Fig. 1.17 : Collective flow in central collisions (left) and in semi-central collisions (right). The density of the arrows in this sketch is proportional to the expansion velocity of the matter.

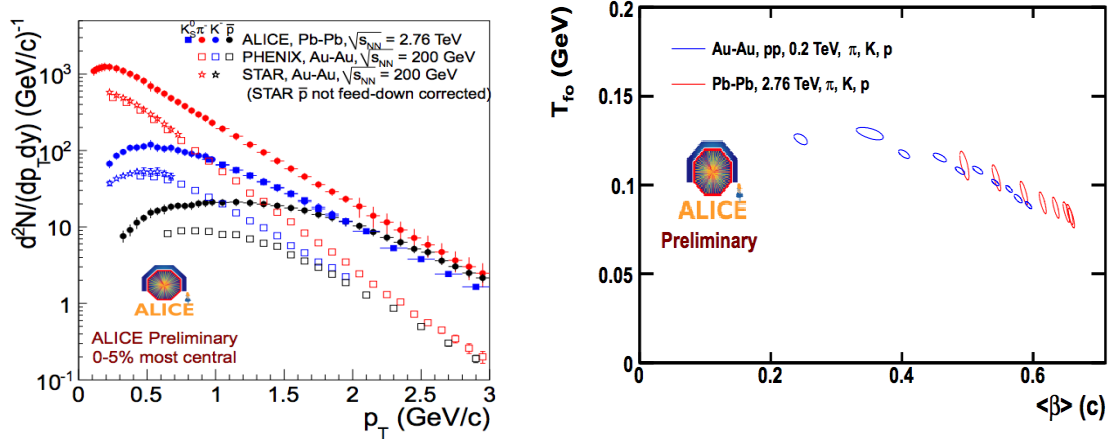


Fig. 1.18 : Transverse momentum distributions of identified hadrons measured by ALICE, compared to previous results from PHENIX and STAR at RHIC [33] (left). Freeze-out temperature and radial flow extracted from Blast-wave fits to hadron spectra (right).

matter created in heavy-ion collisions behaves like a strongly interacting fluid with an exceptionally low viscosity [30, 34]. The average v_2 shows an increasing trend with \sqrt{s} (Fig. 1.19 left). The p_T -integrated v_2 of charged particles is found to increase by about 30% from the highest RHIC energy ($\sqrt{s_{NN}} = 200$ GeV) to the LHC energy [35], but the p_T -differential v_2 measured at the LHC and RHIC are compatible (Fig. 1.19 right). The 30% increase follows from an increase in the average p_T due to a larger radial flow at higher energy.

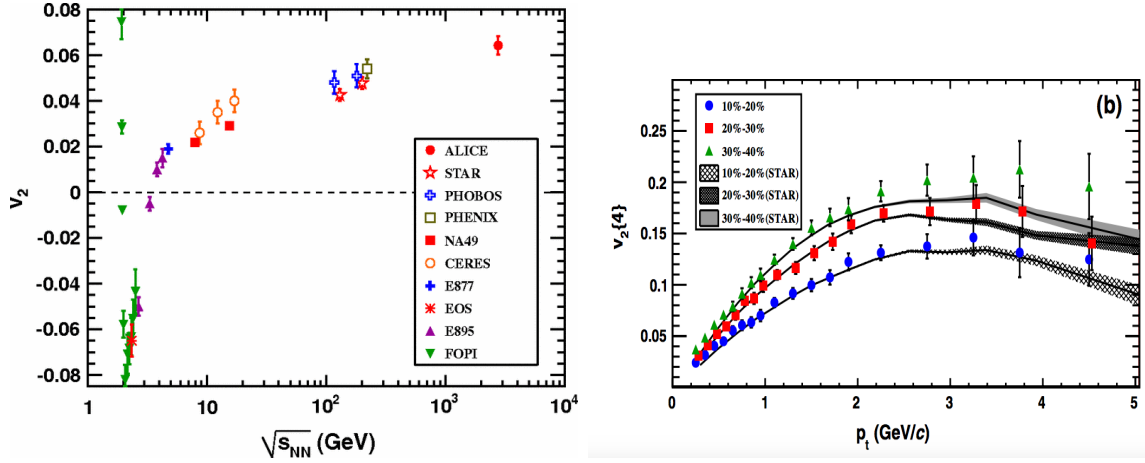


Fig. 1.19 : Energy dependence of p_T -integrated average v_2 (left). Comparison between the p_T -differential v_2 of charged particles measured by ALICE at the LHC and by STAR at RHIC (right) [35].

1.6.2 Strangeness Enhancement

An enhanced strangeness production in nucleus-nucleus collisions, relative to smaller collision systems at the same center-of-mass energy, was proposed in 1980 by Johann Rafelski and Rolf Hagedorn as one of the experimental signatures of the QGP formation [36]. Considering that the dominant production mechanism of $s\bar{s}$ pairs is gluon fusion ($gg \rightarrow g^* \rightarrow s\bar{s}$), strangeness enhancement can be explained by the larger gluon density in the deconfined phase, besides a lower energy threshold for strangeness production in the deconfined phase, due to the lower mass of the "bare" s quark compared to the "dressed" (constituent) s quark. The enhancement is expected to be smaller for collisions at larger \sqrt{s} and should be greater for particles containing more (anti-)strange quarks. A large enhancement of (anti-)baryons (Λ , Ξ and Ω) was observed in Pb–Pb collisions, compared to the measurement in p–Pb and p–Be collisions, at the SPS [37]. The STAR Collaboration at RHIC also reported an enhanced production of strangeness in Au–Au collisions at $\sqrt{s_{NN}} = 200$ GeV, compared to pp collisions [38]. It was also established that the magnitude of this enhancement increases with the number of participants. The production of (anti-)baryons was measured by ALICE in Pb–Pb collisions at $\sqrt{s_{NN}} = 2.76$ TeV. Fig. 1.20 shows the strangeness enhancement measured by ALICE, compared to previous measurements at the SPS and RHIC.

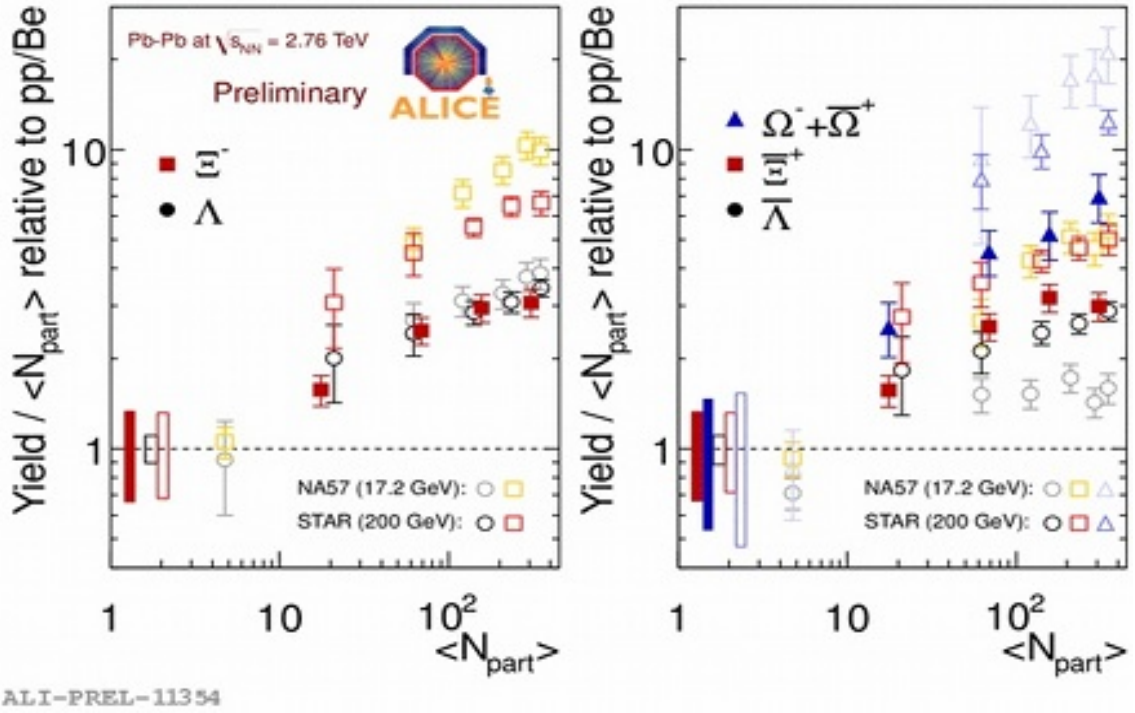


Fig. 1.20 : Strangeness enhancement for Λ , Ξ and $\Omega^+ + \Omega^-$ as a function of the mean number of participants $\langle N_{\text{part}} \rangle$ (left). Comparison with lower energy measurements at SPS and RHIC, indicated by the hollow symbols (right).

1.6.3 Quarkonium Suppression

A clear experimental evidence of the QGP formation is the suppression of bound states of heavy quarks, called *quarkonia*, due to the screening of their interaction potential produced by free color charges in the deconfined medium. In vacuum, the spectrum of quarkonia can be described by non-relativistic quantum mechanics, assuming an interaction potential given by Eq.(1.7):

$$V(r) = -\frac{\alpha_s}{r} + k \cdot r \quad (1.19)$$

where k is the $q\bar{q}$ color string tension, describing confinement, while α_s/r describes the attractive potential [39]. The presence of color charges roaming freely in the deconfined medium has the effect of screening the color charges of the two heavy quarks when the quarkonium is immersed in the QGP. This effect is analogous to the screening of the atomic nucleus electric charge by the innermost electrons, causing the outermost electrons to feel a smaller effective charge. The Coulomb-like potential of quarkonium is modified in the medium and can be expressed by:

$$V(r) = -\frac{\alpha_s}{r} \exp(-r/\lambda_D) \quad (1.20)$$

where λ_D is the Debye length, which describes the screening effect. For electromagnetic plasma, the Debye length depends on the temperature of the plasma and the charge density ρ [40]:

$$\lambda_D = \sqrt{\frac{T}{8\pi\alpha_{\text{em}}\rho}} \quad (1.21)$$

Assuming that the same expression holds also for the QGP⁵ and considering that $\rho \propto T^3$ for an ultra-relativistic gas, one obtains:

$$\lambda_D \sim \frac{1}{T} \sqrt{\frac{1}{8\pi\alpha_s}} \quad (1.22)$$

This expression indicates that for increasing temperature the Debye length gets smaller, thus reducing the interaction potential between heavy quarks in quarkonia, which essentially melt in the QGP. The dissociation temperature is expected to be smaller for excited states of quarkonia, as in fact it is observed experimentally.

The suppression in the production of quarkonia in high energy heavy-ion collisions can be quantified using the *nuclear modification factor* (R_{AA}). This is defined as the ratio between the quarkonia production in nucleus-nucleus and in pp collisions, where the latter is scaled by the average number of binary collisions $\langle N_{\text{coll}} \rangle$:

$$R_{AA} = \frac{[d^2 N_{AA}/dp_T d\eta]}{\langle N_{\text{coll}} \rangle [d^2 N_{pp}/dp_T d\eta]} \quad (1.23)$$

The nuclear modification factor for inclusive J/Ψ production has been measured by ALICE in Pb–Pb collisions at $\sqrt{s_{NN}} = 2.76$ TeV and at $\sqrt{s_{NN}} = 5.02$ TeV as a function of the collision centrality⁶ (Fig. 1.21 left). The suppression of J/Ψ production measured at the LHC energy is smaller compared to the suppression measured by PHENIX at the RHIC energy $\sqrt{s_{NN}} = 200$ GeV (Fig. 1.21 right). The smaller suppression observed at the LHC energies can be explained by a larger contribution from recombination of $c\bar{c}$ pairs at hadronization, which is a competing process leading to J/Ψ regeneration. This mechanism is more efficient at higher energies due to a more abundant production of heavy quarks [41].

⁵This assumption is not justified but the results are still valid.

⁶This is defined by the average number of participant nucleons (see Chapter 4).

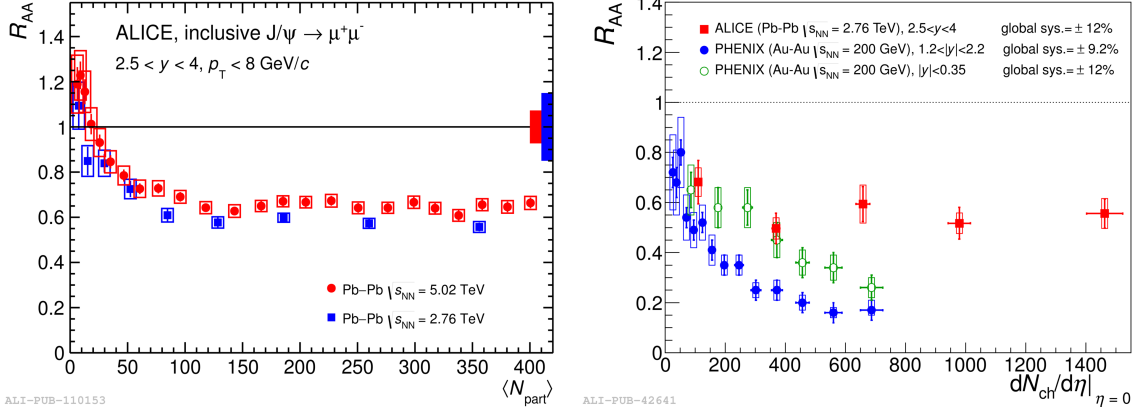


Fig. 1.21 : Nuclear modification factor measured by ALICE at $\sqrt{s_{\text{NN}}} = 2.76$ TeV and $\sqrt{s_{\text{NN}}} = 5.02$ TeV (left). Comparison between the R_{AA} measured by ALICE at $\sqrt{s_{\text{NN}}} = 2.76$ TeV and by PHENIX at $\sqrt{s_{\text{NN}}} = 200$ GeV (right).

1.6.4 In-medium Parton Energy Loss

Partons produced in high-energy heavy-ion collisions lose energy when traveling through the QGP. Their energy loss depends on the density of the matter, the path length in the medium and the nature of the parton: gluons lose more energy compared to quarks due to their larger color charge (gluons carry color and anti-color charges simultaneously, while quarks carry only one color charge). The dominant mechanism of energy loss is gluon radiation, sometimes called *gluonstrahlung*, while a minor contribution is given by parton-parton collisions. For quarks, an important phenomenon, predicted by QCD, is the *dead-cone effect*. This is the absence of emission of gluon radiation at forward angles, within a cone of amplitude $\theta = m/E$, where m is the mass of the quark, and E its energy. Based on this effect, the energy loss for heavy quarks is expected to be smaller compared to light quarks. The experimental observable that is used to study the parton energy loss in the medium is the nuclear modification factor (R_{AA}) as a function of p_{T} :

$$R_{\text{AA}}(p_{\text{T}}) = \frac{dN_{\text{AA}}/dp_{\text{T}}}{\langle N_{\text{coll}} \rangle dN_{\text{pp}}/dp_{\text{T}}} \quad (1.24)$$

High- p_{T} hadrons, which are produced by fragmentation of high-energy partons, are expected to be suppressed ($R_{\text{AA}} < 1$) due to parton energy loss in the medium. The R_{AA} of charged hadrons measured by ALICE at the LHC indicates a larger energy loss, due to the higher density of the medium, compared to RHIC energies (Fig. 1.22).

The smaller energy loss of heavy quarks compared to light quarks, due to the dead cone effect, results in a precise mass hierarchy in the R_{AA} of identified hadrons: $R_{\text{AA}}(\pi) < R_{\text{AA}}(D) < R_{\text{AA}}(B)$. This is illustrated in Fig. 1.23, which shows the nuclear

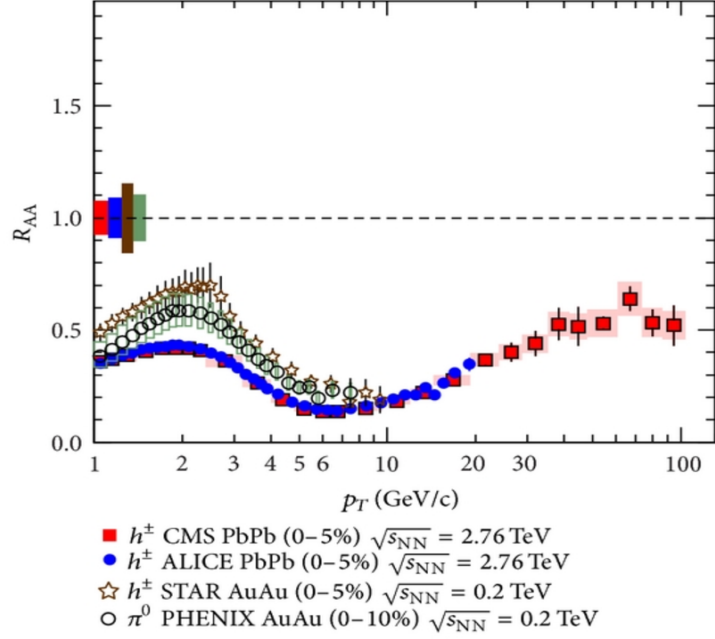


Fig. 1.22 : Nuclear modification factor R_{AA} of charged hadrons measured by ALICE [42] and CMS [43] experiments at midrapidity for (0-5)% most central Pb–Pb collisions at $\sqrt{s_{NN}} = 2.76$ TeV. For comparison, shown are the R_{AA} of charged hadrons at midrapidity for (0-5)% most central collisions measured by STAR [44] and R_{AA} of neutral pions at midrapidity for (0-10)% most central collisions measured by PHENIX [45] for Au–Au collisions at $\sqrt{s_{NN}} = 200$ GeV at RHIC.

modification factor for non-prompt J/Ψ from B decays measured by CMS [46], compared to the R_{AA} of prompt D-mesons and charged pions measured by ALICE [47, 48]. The mass hierarchy is evident between B and D-mesons, while it is less pronounced for charged pions.

In-medium energy loss of high-energy partons, produced back-to-back in the initial hard parton-parton scattering, create an imbalance between the energies of the two jets produced in the fragmentation of the outgoing partons (Fig. 1.24).

This phenomenon (called *jet quenching*) is due to the different path lengths traveled inside the medium by the two outgoing partons, which lose different amounts of energy. Jet quenching has been observed soon after the first Pb–Pb run at the LHC by the ATLAS Collaboration, who reported a large imbalance between the transverse energies of di-jets in opposite hemispheres [49]. The observable used to quantify the energy imbalance is defined by:

$$A_J = \frac{E_T^1 - E_T^2}{E_T^1 + E_T^2} \quad (1.25)$$

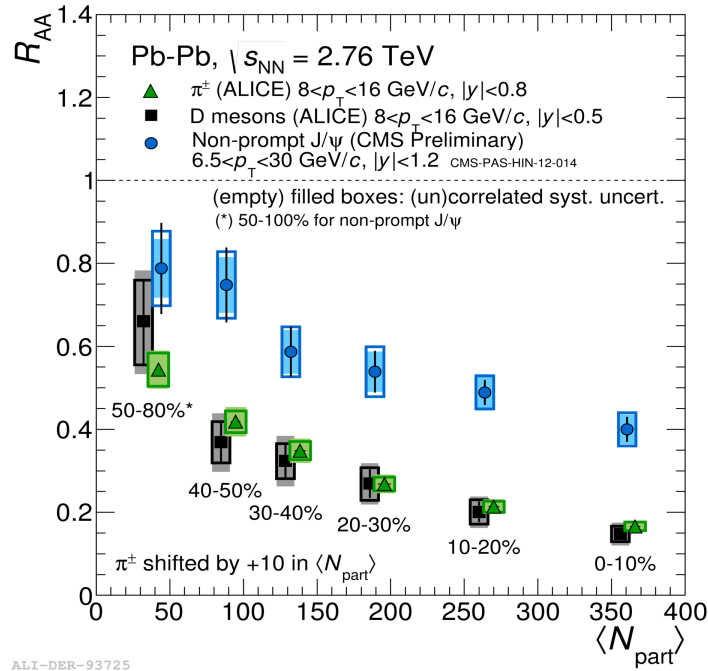


Fig. 1.23 : Nuclear modification factor of non-prompt J/Ψ (originating from B decays) measured by CMS [46] compared to R_{AA} measurements of charged pions [47] and prompt D-mesons from ALICE [48].

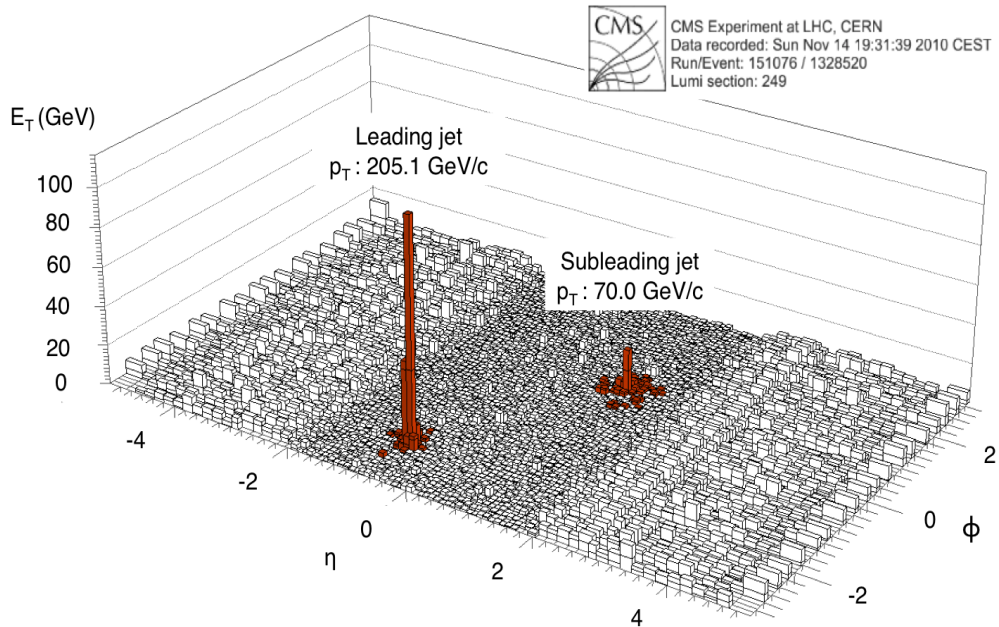


Fig. 1.24 : Imbalance between transverse energies of two back-to-back jets measured by CMS in Pb-Pb collisions at $\sqrt{s_{NN}} = 2.76$ TeV in (η, ϕ) cells with the calorimeters.

where E_T^1 is the transverse energy of the most energetic jet in the event (leading jet) and E_T^2 the one of the most energetic jet in the opposite hemisphere (sub-leading jet). The A_J distribution has been measured by ATLAS in Pb–Pb collisions at $\sqrt{s_{NN}} = 2.76$ TeV and in pp collisions at $\sqrt{s} = 7$ TeV for comparison (Fig. 1.25 top). The A_J distribution measured in peripheral Pb–Pb collisions has a peak at zero and it is consistent with the measurement in pp collisions, as well as with MC simulation not including jet quenching. The peak in the A_J distribution moves to higher values in more central collisions, reaching a value ≈ 0.5 in the centrality class (0-10%). The difference in azimuthal angle ($\Delta\phi_{\text{jet}}$) between the two jets has also been measured for different centrality classes, showing that the two jets are essentially back-to-back in all centrality ranges (Fig. 1.25 bottom). The measured distributions of $\Delta\phi_{\text{jet}}$ appear broader for more central collisions, as expected from the energy degradation of partons traversing the hot and dense medium.

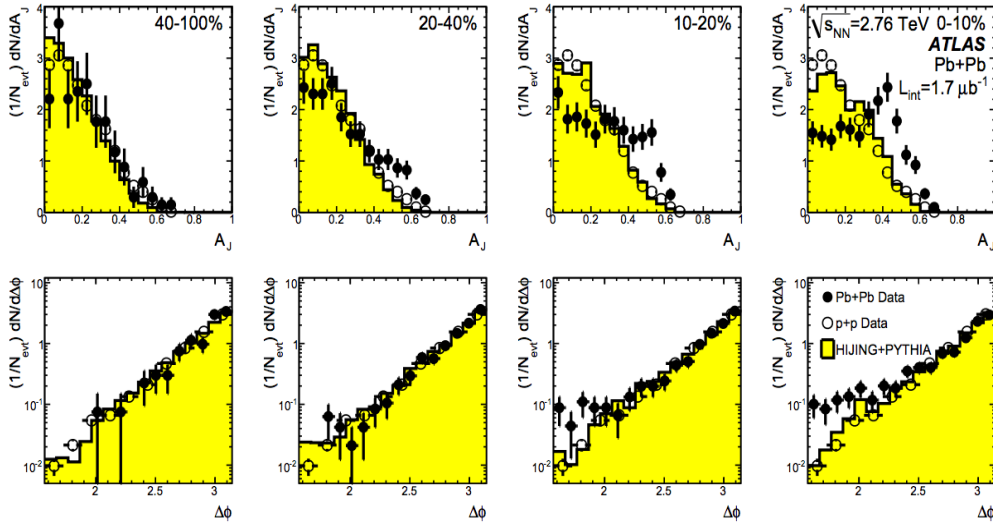


Fig. 1.25 : Transverse energy asymmetry A_J (top) and azimuthal angle difference $\Delta\phi_{\text{jet}}$ (bottom) between leading and subleading jets measured by ATLAS in Pb–Pb collisions at $\sqrt{s_{NN}} = 2.76$ TeV for different centrality classes compared to the measurements in pp collisions at $\sqrt{s} = 7$ TeV and the expected distributions without jet quenching obtained from MC simulations [49].

1.7 Summary of the main Global Properties of the QGP

The main global properties of the quark-gluon plasma created at the LHC are compared to those measured at lower energies in past experiments. The size of the fireball and the decoupling time have been measured using the intensity interferometry (HBT) [50]. An increasing trend with the center-of-mass energy is observed (Fig. 1.26).

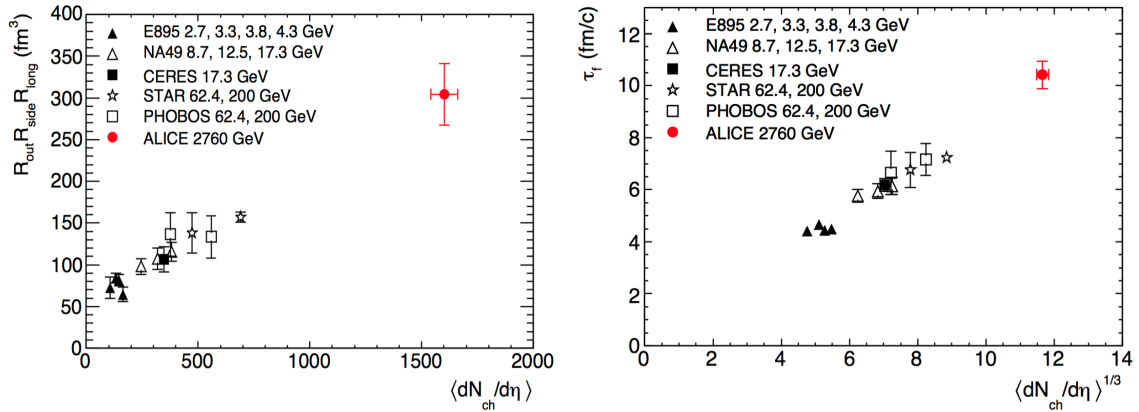


Fig. 1.26 : Product of the three pion HBT radii at $k_T = 300 \text{ MeV}/c$ (left) and decoupling time extracted from $R_{long}(k_T)$ (right). The ALICE results (red filled dots) are compared to those obtained for central Au–Au and Pb–Pb collisions at lower energies at the AGS [51], SPS [52–54], and RHIC [55–60].

Figure (Fig. 1.27) shows the charged particle multiplicity density per participant pair, measured at midrapidity, for various collision systems as a function of the center-of-mass energy [61, 62]. This is related to the energy density reached in the collision, based on Bjorken estimate (1.16). The higher energy density results in a higher initial temperature of the QGP, which is confirmed by the temperature measured from the direct photon spectrum (see next chapter), and also in a larger expansion velocity, as seen from the harder particle spectra measured by ALICE at $\sqrt{s_{NN}} = 2.76 \text{ TeV}$.

To conclude, the system created at the LHC is larger, longer-lived, hotter and denser compared to that created in previous experiments at lower energies.

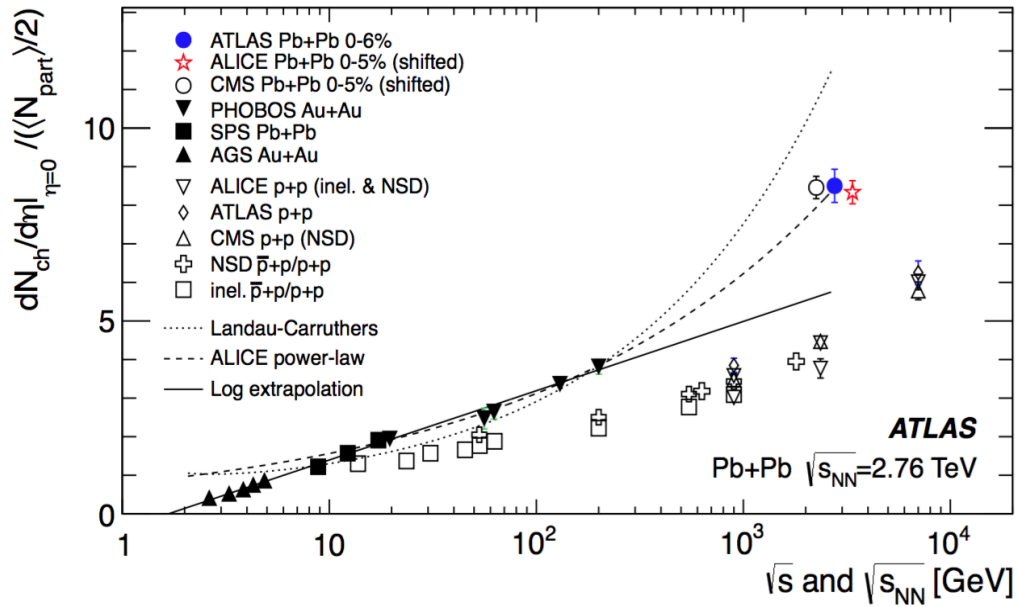


Fig. 1.27 : Charged particle multiplicity density at mid-rapidity per participant pair for various collision systems and energies [61, 62]. The lines represent various phenomenological extrapolations from the SPS and RHIC energies to the LHC

Chapter 2

Electromagnetic Probes

2.1 Introduction

Electromagnetic radiation is emitted continuously by the hot and dense matter created in ultrarelativistic heavy-ion collisions during its space-time evolution [63]. All stages contribute with different processes to the production of real photons and dileptons, i.e. lepton-antilepton pairs produced by internal conversion of virtual photons (Fig. 2.1).

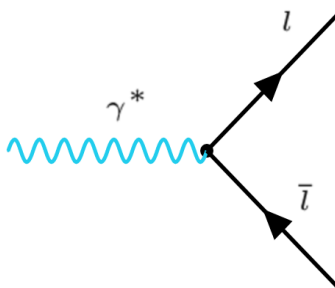


Fig. 2.1 : Feynman diagram representing the production of a dilepton pair from internal conversion of a virtual photons.

Photons and leptons, which are essentially affected only by electromagnetic interaction, are called *electromagnetic probes*¹.

¹Leptons are also affected by the weak force, hence a more proper name for both categories would be *electro-weak probes*. However, only the electromagnetic interaction is relevant for these particles due to its much larger strength compared to the weak interaction.

Their mean free path into the hot and dense matter is:

$$\lambda_{\text{em}} \sim \frac{1}{n\sigma_{\text{em}}} \quad (2.1)$$

where n is the number of particles per unit volume and σ_{em} is the cross section for electromagnetic interactions. This can be compared to the mean free path of hadronic probes, which is roughly of the same order of magnitude of the system size:

$$\frac{\lambda_{\text{em}}}{\lambda_{\text{strong}}} \sim \frac{\sigma_{\text{strong}}}{\sigma_{\text{em}}} \sim \frac{\alpha_s^2}{\alpha_{\text{em}}^2} \sim 10^4 \quad (2.2)$$

This equation shows that particles interacting only through the electromagnetic force travel undisturbed through the medium, which is essentially transparent, thus carrying direct and undistorted information on their production process. Strongly interacting probes instead suffer from intense re-scattering off the particles in the hot and dense matter. Their momentum distribution is inevitably modified thus losing memory about their original properties. The electromagnetic interaction, besides representing a great advantage for photons and dileptons, is also responsible for their low production rates compared to hadronic probes. The measurement of such rare particles and the enormous backgrounds typical of all photon measurements represent major experimental challenges for the measurements of electromagnetic probes in high energy nuclear physics.

2.2 Photon Sources

Real and virtual photons can be divided into two main categories, based on their production sources:

- **Direct Photons:** These originate directly from the interaction region and include the following sub-categories: *prompt photons*, produced in the initial hard parton-parton scattering or annihilation, photons generated during the pre-equilibrium stage (*pre-equilibrium photons*), those emitted in jet-medium electromagnetic interaction and *thermal photons*, emitted by the hot QGP and hadron gas. The latter are assumed to be in local thermal equilibrium.
- **Decay Photons:** These originate from electromagnetic hadron decays after freeze-out and represent the vast majority of all produced photons.

Among these two main classes, the main focus is on direct photons, particularly on its thermal component, which brings information on the temperature of the system. Great

interest also goes to the study of prompt photons, which provide an important test for perturbative QCD, used to calculate their production rates at high p_T .

The study of a particular component of direct photons requires the discrimination of decay photons, which represent the main source of background for all direct photon measurements, and the identification and separation of all other components. The decay photon spectrum can be constrained experimentally and is usually obtained from simulations of electromagnetic hadron decays, in which the measured momentum distributions of hadrons are used as input to the simulation (see Section 2.6). Although different components of direct photons mainly contribute to different regions of the direct photon spectrum, experimentally it is extremely difficult to disentangle them due to the non-negligible superpositions of their individual contributions. The separation of different components of direct photons is usually obtained from theoretical model calculations. The production mechanisms and the calculations of production rates for real and virtual photons are essentially the same, but the experimental techniques used to measure them, as well as the observables of interest, are very different. For this reason, the study of real photons and dileptons are treated separately in this chapter, after a general discussion on the calculation of their production rates.

2.3 Prompt Photon Production

Prompt photons are produced in the initial hard scattering between partons in the incoming nuclei. The leading order contributions to this process are given by quark-antiquark annihilation and gluon Compton scattering (Fig. 2.2).

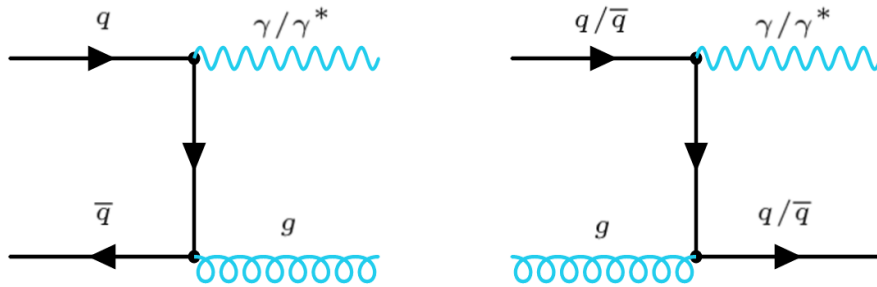


Fig. 2.2 : Feynman diagrams representing quark-antiquark annihilation (left) and gluon Compton scattering (right).

One of the most important higher-order contributions to prompt photons is the emission of *fragmentation photons* by an outgoing high-energy parton (Fig. 2.3).

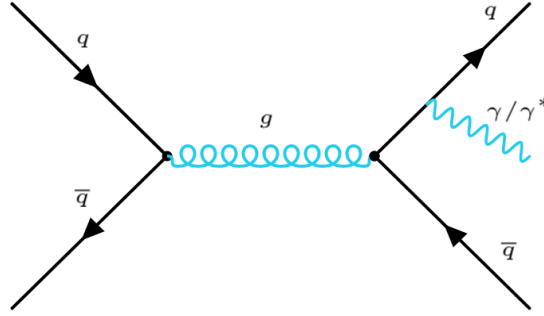


Fig. 2.3 : Feynman diagram representing the emission of a fragmentation photon.

The contribution of fragmentation photons in Pb–Pb collisions might be modified compared to pp collisions by in-medium energy loss of high-energy partons ("jet-medium interaction") and by cold nuclear matter effects. These photons most likely contribute to the low- p_T region of the direct photon spectrum. The calculation of this contribution requires a detailed knowledge of the energy loss mechanisms and cold nuclear matter modifications. Little effort has been dedicated to evaluating this contribution using the latest advances in parton energy loss and hydrodynamical modeling of heavy-ion collisions. The contribution from fragmentation photons is currently obtained neglecting the parton energy loss.

The production rate of prompt photons in Pb–Pb collisions can be calculated using perturbative QCD or by scaling the prompt photon spectrum measured in pp collisions at the same center-of-mass energy by the average number of binary collisions:

$$\left[E \frac{d^3 N_\gamma^{prompt}}{d^3 p} \right]_{AA} = \langle N_{coll} \rangle \left[E \frac{d^3 N_\gamma^{prompt}}{d^3 p} \right]_{pp} \quad (2.3)$$

In the latter approach, which neglects nuclear modifications of the parton distribution functions due to shadowing, isospin effects and in-medium parton energy loss, the collision between two nuclei is regarded as an incoherent superposition of elementary nucleon-nucleon collisions. Fig. 2.4 shows the direct photon spectrum measured by PHENIX in central (0-20%) Au–Au collisions at $\sqrt{s_{NN}} = 200$ GeV [64], in comparison to the expected contribution of prompt photons obtained from a fit to direct photon measurements in pp collisions [64] and from a perturbative QCD calculation [65].

The direct photon spectrum measured in nucleus-nucleus collisions is in agreement with the expected contribution of prompt photons in the high- p_T region ($p_T > 3$ GeV/ c), where the predictions from the fit and the pQCD-based approach give consistent results. The two methods, instead, give significantly different predictions for the prompt photon

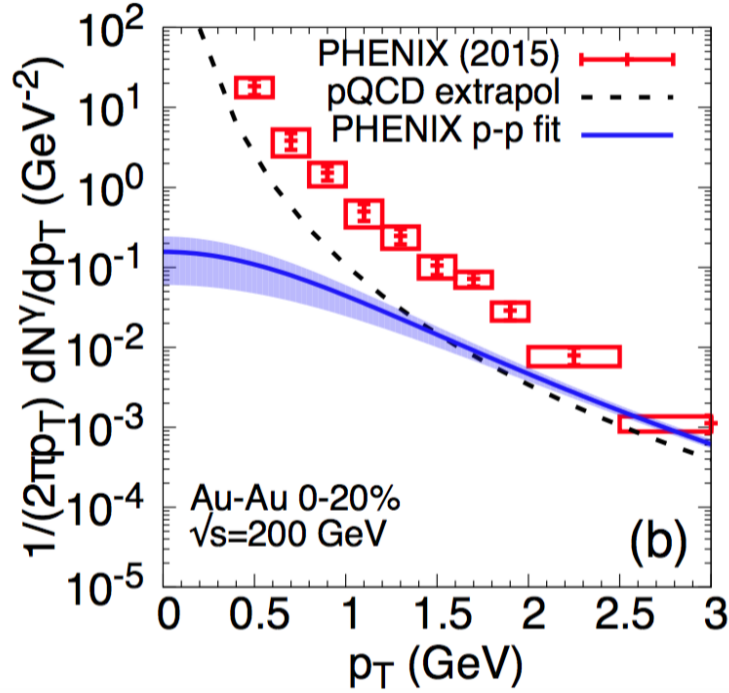


Fig. 2.4 : Direct photon spectrum measured by PHENIX in central (0-20%) Au–Au collisions at $\sqrt{s_{\text{NN}}} = 200$ GeV [64], in comparison to the prompt photon background as predicted by a fit to direct photon measurements in pp collisions [64] and to a perturbative QCD calculation [65].

spectrum at low- p_{T} ($p_{\text{T}} \lesssim 1.5$ GeV/ c). This can be explained by the different criteria used for the extrapolation of the spectrum in the low- p_{T} range. The fit is poorly constrained at low- p_{T} due to the large experimental uncertainties of direct photon measurements in pp collisions. Moreover, this procedure is based on the assumption that the prompt photon contribution saturates for $p_{\text{T}} < 1 - 2$ GeV/ c . Perturbative QCD, on the other hand, is based on the assumption that the power-law dependence observed at high- p_{T} continues also at low- p_{T} , perhaps overestimating the contribution from prompt photons². Nevertheless, the measured spectrum shows an excess in the low momentum range compared to the prompt photon contribution, which is attributed to thermal photons.

2.3.1 Drell–Yan Process

Dilepton production in the initial hard scattering includes contributions from the processes shown in Fig. 2.2 and from the Drell-Yan process. The latter takes place when a quark

²It is questionable how reliable are pQCD calculations in the low momentum range

in one hadron and an antiquark in another hadron annihilate, creating a virtual photon (or Z boson) which then decays into a pair of oppositely charged leptons (Fig. 2.5).

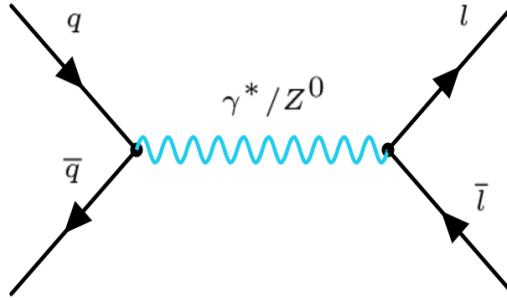


Fig. 2.5 : Feynman diagram representing the Drell-Yan process.

This process was first suggested by Sidney Drell and Tung-Mow Yan in 1970 [66] to describe the dilepton production in high-energy hadron collisions. Experimentally, this process was first observed by J.H. Christenson and his collaborators in proton–uranium collisions at the Alternating Gradient Synchrotron [67]. At the LHC energies, the contribution from the Drell-Yan process is expected to be significant only in the high-mass region of the dilepton spectrum ($m_{l+l-} \gtrsim 5 \text{ GeV}/c^2$).

2.4 Thermal Emission Rate

The standard picture of the space-time evolution of heavy-ion collisions, as already described in Section 1.5.1, starts with a fast approach to local thermal equilibrium ($\tau = 0.1 - 1 \text{ fm}/c$), followed by a rapid expansion of the deconfined matter ($\tau \approx 10 \text{ fm}/c$), typically described by relativistic hydrodynamics. After hadronization, the interactions of particles in the hot hadron gas phase are described using phenomenological transport models. In this paragraph, the calculation of the thermal emission rate in the partonic and hadronic phases are discussed.

The initial conditions for hydrodynamics, such as the initial temperature and energy density, are provided at a fixed time τ and depend on some parameters that are adjusted to measurements. The main ingredients for a hydrodynamical simulation are the equations of motion, an equation of state, transport coefficients such as shear and bulk viscosities, and a criterion to decide at which time the hydrodynamic simulation is stopped. Fig. 2.6 shows the temperature profile for a simulated central Pb–Pb collision at $\sqrt{s_{\text{NN}}} = 2.76 \text{ TeV}$ obtained from the hydrodynamical model calculation used in Ref. [65, 68]. In this event,

the hottest temperature reached by the plasma is ≈ 600 MeV at $\tau_0 = 0.4$ fm/ c , where the hydrodynamical simulation is started.

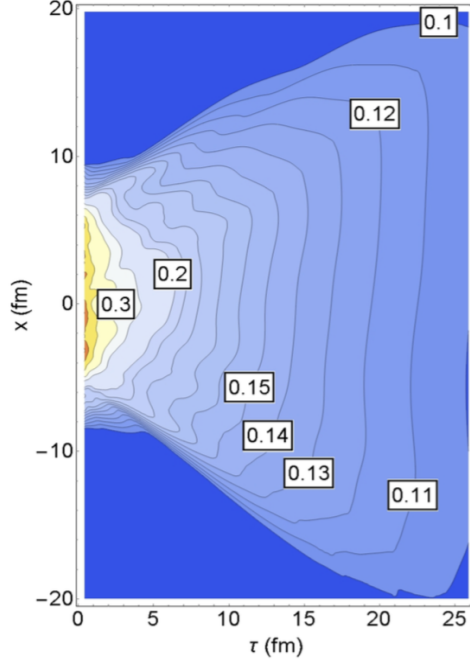


Fig. 2.6 : Temperature profile predicted by a hydrodynamical simulation of a central Pb–Pb collision at $\sqrt{s_{\text{NN}}} = 2.76$ TeV. The vertical axis indicates the transverse expansion of the system. Contours are shown every 10 MeV for temperatures below 200 MeV. Labels indicate the temperature of the corresponding contour, expressed in GeV.

The static production rate of photons and dileptons are obtained from the scattering amplitudes of the photon production processes, calculated using the QCD rules, which are then convoluted with the energy distributions of elementary partons:

$$\frac{dN}{d^4x d^3p} = \frac{1}{(2\pi)^3 2E} \int \frac{d^3p_1}{(2\pi)^3 2E_1} \frac{d^3p_2}{(2\pi)^3 2E_2} \frac{d^3p_3}{(2\pi)^3 2E_3} \times n_1(E_1) n_2(E_2) [1 \pm n_3(E_3)] \times \sum_i \langle |M|^2 \rangle (2\pi)^4 \delta(p_1 + p_2 - p_3 - p) \quad (2.4)$$

in this equation, p_1 and p_2 are the momenta of the incoming partons, p_3 the momentum of the outgoing parton and p is the momentum of the produced photon.

In the QGP phase, the calculation of the scattering amplitudes includes all processes of the order $\sim (\alpha_{\text{em}} \alpha_s)$, where the temperature dependence of the strong coupling constant [69] is taken into account. The energy distributions of partons are given by the Fermi-Dirac and Bose-Einstein thermal distributions, for quarks and gluons respectively:

$$n_i(E_i) = \frac{1}{\exp(E_i/T) \pm 1} \quad (2.5)$$

The thermal emission rate of photons and dileptons is obtained by integrating the static production rates over the space-time evolution of the system, whose description is provided by relativistic hydrodynamics:

$$\frac{d^4 N_{\gamma/l+l^-}}{d^4 k} = \int d^4 x \frac{d^4 \Gamma_{\gamma/l+l^-}}{d^4 k} (K^\mu, u^\mu(x), T(x), \pi^{\mu\nu}(x), \Pi(x)) \quad (2.6)$$

where $T(x)$ is the temperature profile, $u^\mu(x)$ is the flow velocity of the plasma, $\pi^{\mu\nu}(x)$ is the shear viscosity tensor and $\Pi(x)$ is the bulk pressure. The latter two give modest contributions to the thermal photon spectrum and are usually neglected, unlike for the v_n 's (see e.g. Ref. [65]). The integral runs over the space-time volume of the plasma. Fig. 2.7 shows the thermal photon spectra obtained for different ranges of the temperature with and without the flow effects, respectively.

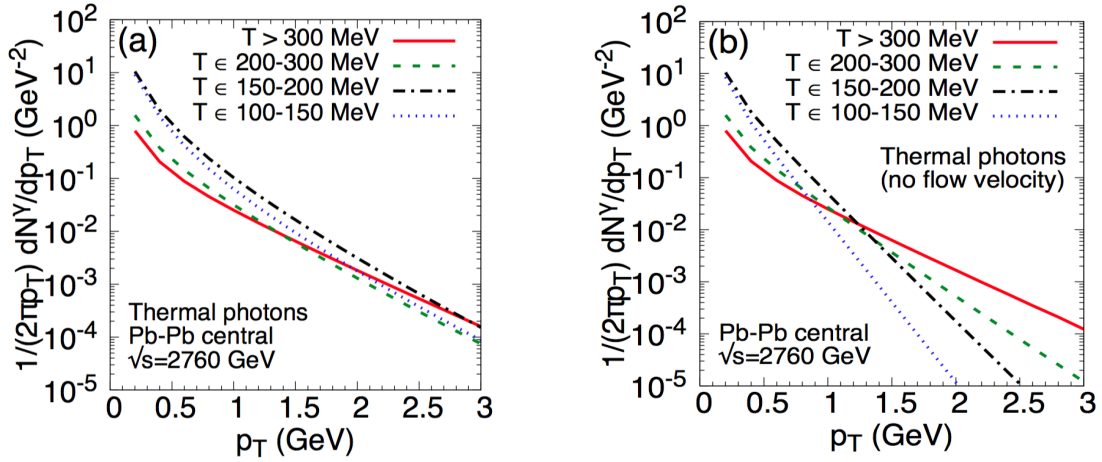


Fig. 2.7 : Thermal photon spectra obtained from hydrodynamical simulation of a central Pb–Pb collision at $\sqrt{s_{NN}} = 2.76$ TeV for different ranges of temperatures with (left) and without (right) the inclusion of flow effects in the calculation of the emission rates. The effect of flow is to shift the thermal photon spectrum to higher p_T (Doppler shift).

The emission rate of thermal photons is large at high temperature, despite the small space-time volume with $T > 300$ MeV. The contribution from the highest temperatures dominates the high- p_T region of the thermal photon spectrum. The emission rate decreases with temperature, while the space-time volume becomes larger at lower temperatures, so thermal production remains abundant. The effect of flow is to shift the thermal photon spectrum to higher p_T , thus modifying its slope (Fig. 2.7 right). The effect is stronger at lower temperatures when the flow velocity is higher. Flow has no effect on

the dilepton invariant mass distribution, which is Lorentz-invariant. Thermal dileptons from the partonic phase give a significant contribution to the invariant mass region $m_\phi < m_{l+l^-} < m_{J/\Psi}$, while thermal emission in the hadron gas phase contributes to lower masses ($m_{l+l^-} < 1$ GeV). The low-mass region is particularly interesting to study medium modifications of low-mass vector mesons, such as their mass and width, which are preserved by their decay products due to their weak interaction with the hot and dense medium (see Section 2.7).

2.5 Photon Production in the Early Stages

Thermal emission rate is calculated assuming local thermal equilibrium of the plasma. The hydrodynamical simulation is started at a fixed time $\tau_0 \approx 0.1 - 1$ fm/ c . Thermalization is assumed to be a fast process, which is however gradual. It is not clear the amount of near-equilibrium emission which is missing in the calculation. Assuming that near-equilibrium photon emission can also be computed within the hydrodynamical framework, the starting point of the simulation can be set to an earlier time than τ_0 . The exact time at which the system can be considered nearly equilibrated is not known, so usually the initialization time is varied within a range $\tau_0 \approx 0.1 - 1$ fm/ c , which reflects our limited knowledge of the early stages of the system evolution. However, photon emission out of equilibrium might be dominated by hard modes which contribute mainly to the high p_T region of the direct photon spectrum. This region is well described by the prompt photon component, which would imply that the non-thermal contribution from the early stages is negligible or anyhow below the sensitivity of experimental measurements.

2.6 Real Photon Measurements

In high energy physics, real photon measurements are usually performed using calorimetry or the photon conversion method (PCM), which is based on tracking and identification of electron-positron pairs produced by photon conversion in the detector material. The main target of the real photon measurements is the study of the p_T -distribution of direct photons, with particular interest in the region which is dominated by thermal radiation (the low-intermediate p_T region: $1 \lesssim p_T \lesssim 3$ GeV/ c), from which the temperature of the created matter can be extracted. The decay photon spectrum, which represents the background for direct photon analysis, is described by the so-called *hadronic cocktail*. This contains the p_T -distributions of decay photons from the relevant hadronic sources and it is generated using MC particle generators, including the simulation of detector

effects (radiative losses and resolution). Hadrons are generated according to measured relative abundances and their decays are simulated based on real branching ratios. Their momentum distributions are parametrized from the measured spectra, or obtained using m_T -scaling starting from some reference distribution (usually neutral pions). The direct photon spectrum is obtained by subtracting the hadronic cocktail from the inclusive photon spectrum. Fig. 2.8 shows the direct photon spectrum measured by ALICE in central (0 – 20%), semi-central (20 – 40%) and peripheral (40 – 80%) Pb–Pb collisions at $\sqrt{s_{NN}} = 2.76$ TeV [70].

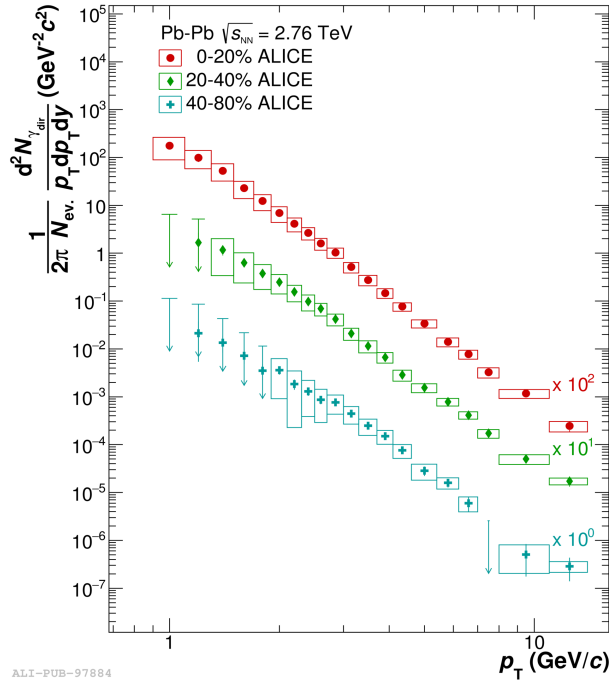


Fig. 2.8 : Direct photon spectrum measured by ALICE in Pb–Pb collisions at $\sqrt{s_{NN}} = 2.76$ TeV for three different centrality classes [70].

Direct photons originating from different sources give dominant contributions to different regions of the direct photon spectrum: the high- p_T region is dominated by prompt photons, while the low-intermediate p_T region contains a dominant contribution from thermal radiation. Therefore, the direct photon spectrum can be described by a two component function:

$$\frac{dN^{\text{dir}}}{dp_T} = A \exp(-p_T/\langle T_{\text{eff}} \rangle) + B \left(1 + p_T^2/c\right)^{-n} \quad (2.7)$$

The thermal component of the direct photon spectrum, which follows a Boltzmann-like exponential distribution, gives information on the temperature of the hot and dense

matter created in the collision. Photons are emitted by a rapidly expanding source, whose temperature diminishes during its evolution. The direct photon spectrum thus contains contributions from different phases, at different temperatures, and it is affected by a strong Doppler shift. The inverse slope parameter of the thermal component thus gives an *average effective temperature* $\langle T_{\text{eff}} \rangle$ of the created matter. Fig. 2.9 shows the direct photon spectra measured for central (0 – 20%) and semi-central (20 – 40%) collisions by ALICE in Pb–Pb collisions at $\sqrt{s_{\text{NN}}} = 2.76$ TeV and by PHENIX in Au–Au collisions at $\sqrt{s_{\text{NN}}} = 200$ GeV, for comparison. The values of $\langle T_{\text{eff}} \rangle$ extracted from an exponential fit to the low- p_T region of the direct photon spectra are also reported.

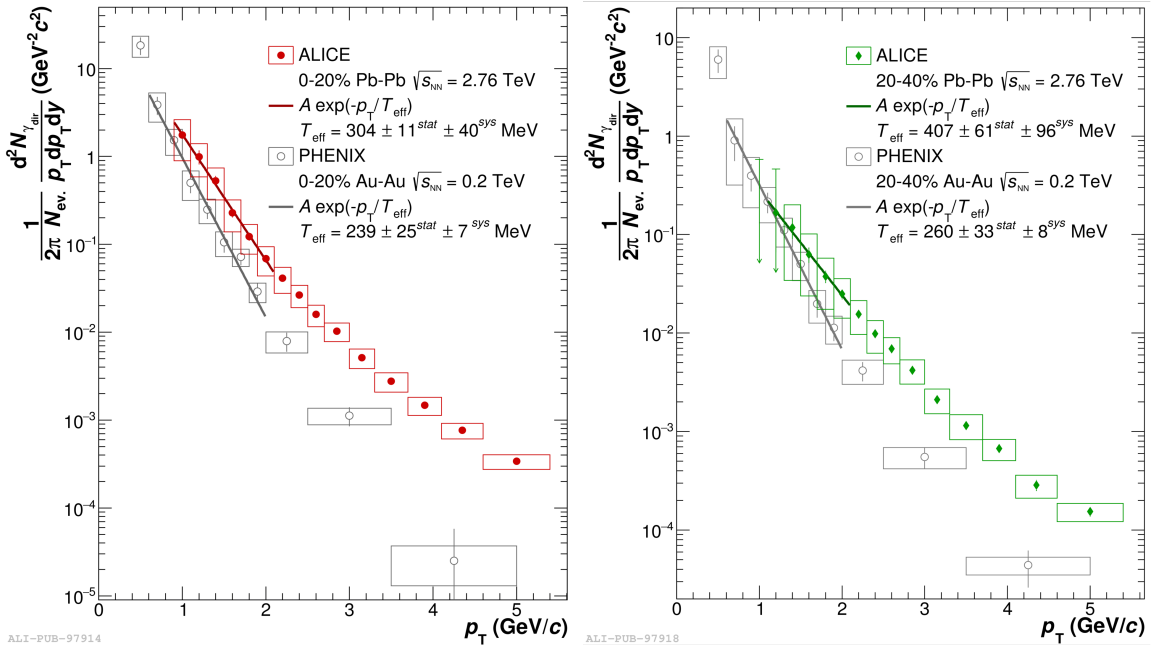


Fig. 2.9 : Direct photon spectra measured for central (0 – 20%) (left) and semi-central (20 – 40%) (right) collisions by ALICE in Pb–Pb collisions at $\sqrt{s_{\text{NN}}} = 2.76$ TeV and by PHENIX in Au–Au collisions at $\sqrt{s_{\text{NN}}} = 200$ GeV. The measured values of the average effective temperature, extracted from an exponential fit to the low- p_T region of the direct photon spectra, are reported in the upper right corner of each figure [70].

The larger value of the temperature measured at the LHC energies, compared to RHIC energies, is due to larger energy density in the collision region, which produces a hotter matter, and to the larger blue shift caused by stronger collective flow. The temperature measured in central (0–20%) and semi-central (20–40%) collisions are compatible within statistical and systematic uncertainties, although data might indicate a higher temperature in the centrality range 20–40%, contrary to expectations. More precise measurement is needed to clarify this aspect.

Prompt photons are described by a power-law distribution, according to NLO per-

turbative QCD calculations. It has been established that the contribution from prompt photons in high energy collisions between nuclei can be obtained from that measured in pp collisions at the same center-of-mass energy, scaled by the average number of binary nucleon-nucleon collisions $\langle N_{\text{coll}} \rangle$, which can be obtained from the Glauber model of nucleus-nucleus collisions (see Chapter 4):

$$\left[\frac{dN^{\text{prompt}}}{dp_T} \right]_{AA} = \langle N_{\text{coll}} \rangle \left[\frac{dN^{\text{dir}}}{dp_T} \right]_{pp} \quad (2.8)$$

Fig. 2.10 shows the direct photon spectra measured by ALICE for different centralities, compared to the predictions from NLO pQCD calculations [70].

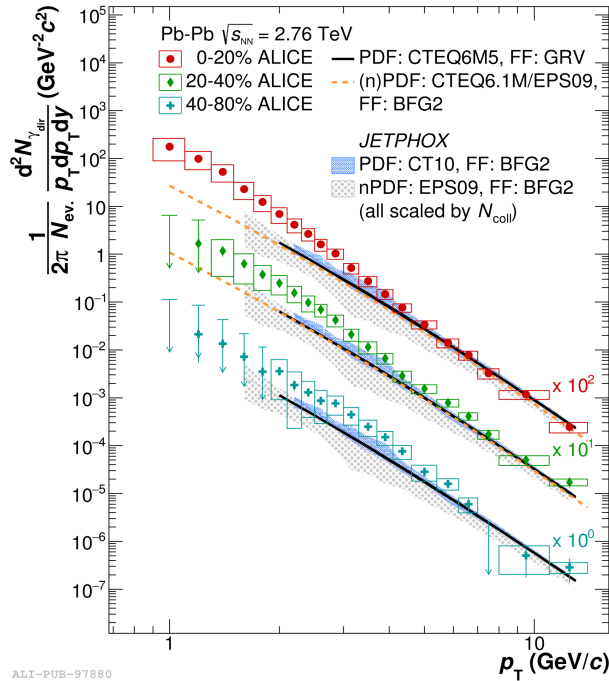


Fig. 2.10 : Direct photon spectra measured by ALICE for different centrality classes, compared to NLO pQCD calculations [70].

Thermal photons do not carry only information on the temperature of the hot and dense matter, but also on its formation time. The observable that is used to estimate the QGP formation time is the direct photon elliptic flow v_2 . In contrast to hadrons, which receive the full asymptotic flow at hadronization, photons are emitted continuously during the system expansion, from its early stages characterized by large temperatures and small flow (which has not been built up yet), till late stages characterized by large flow and smaller temperatures. Fig. 2.11 shows the predicted shapes of the thermal photon v_2 , as a function of p_T , for different values of the QGP formation time obtained from theoretical calculations for central Au–Au collisions at $\sqrt{s_{NN}} = 200$ GeV [71].

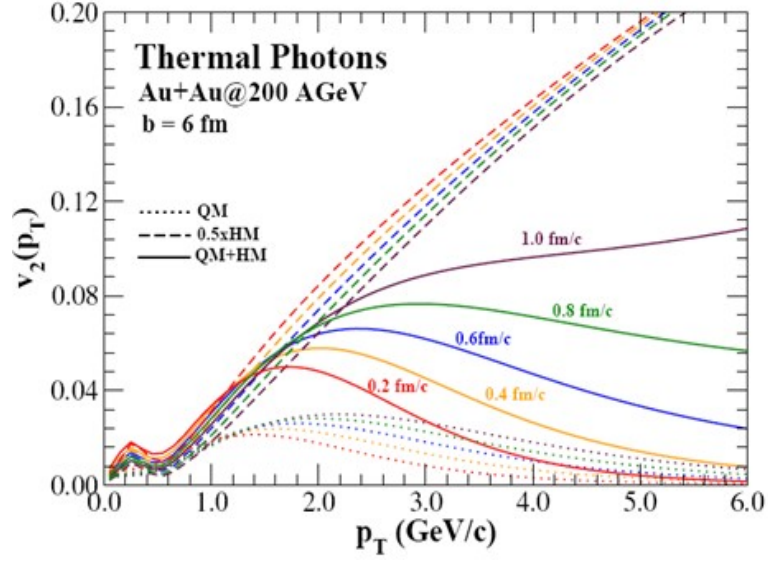


Fig. 2.11 : Elliptic flow v_2 , as a function of p_T , in central Au–Au collisions at $\sqrt{s_{NN}} = 200$ GeV, calculated for different values of the QGP formation time [71].

The large direct photon elliptic flow, measured by PHENIX at RHIC [73] and by ALICE at the LHC [72] (Fig. 2.12), whose magnitude is comparable to the elliptic flow of all charged hadrons, suggests a large contribution from late stages. This is in contradiction with the measured direct photon spectrum, which contains a large contribution from early stages at high temperatures. This *direct photon puzzle* is still unsolved at the present time.

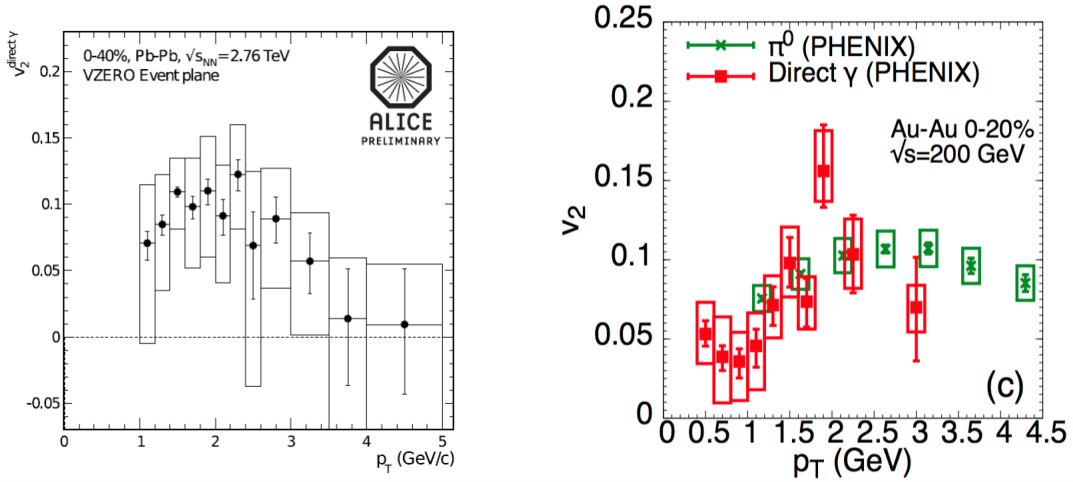


Fig. 2.12 : Direct photon elliptic flow v_2 , as a function of p_T , measured by ALICE in central Pb–Pb collisions at $\sqrt{s_{NN}} = 2.76$ TeV [72] (left) and by PHENIX in minimum bias Au–Au collisions at $\sqrt{s_{NN}} = 200$ GeV [73] (right).

2.7 Dilepton Measurements

Dileptons are characterized by their transverse momentum p_{T}^{ll} and by an additional kinematic variable compared to real photons, i.e. their invariant mass:

$$m_{\text{ll}} = \sqrt{(E_1 + E_2)^2 - |\vec{p}_1 + \vec{p}_2|^2} \quad (2.9)$$

This quantity is by definition Lorentz-invariant, hence independent of the reference frame in which dileptons are measured. In consequence, the temperature of the matter extracted from the dilepton invariant mass spectrum is not affected by the Doppler shift due to the expanding source. This represents one of the main advantages of dileptons compared to real photons.

Dilepton measurements are based on the analysis of their invariant mass distribution. Dilepton unlike-sign pairs, originating from the interaction region, are identified by using tracking and particle identification detectors. The background is made of two different components: the combinatorial and correlated background. The former, arising from the sequential pairings executed to obtain the unlike-sign spectrum, is usually described using the invariant mass distribution of same-sign pairs, corrected for possible acceptance effects, or that of unlike-sign pairs from different events (mixed events). The correlated background originates from kinematically correlated dilepton pairs, i.e. cross pairs or dileptons from hadrons flying inside the same jet. This component is conveniently included in the like-sign distribution since all processes contributing to the correlated background are charge symmetric. Alternatively this contribution can be estimated from simulations. The latter approach is used when the combinatorial background is estimated using the event-mixing technique.

The contribution to the dilepton spectrum from hadronic decays is described by the *hadronic cocktail*, which is obtained using MC simulations (see Chapter 7). Detector effects present in the real measurement, such as the limited geometrical acceptance of the experimental apparatus and its finite momentum resolution, as well as radiative energy losses due to the presence of the magnetic field (needed for tracking) are included in the full simulation for the cocktail generation. Bremsstrahlung and resolution effects are not applied only to the hadronic cocktail but also to theoretical curves used to describe the dilepton spectrum in order to disentangle its contributions, especially thermal dileptons from partonic and hadronic origin. An alternative and, from different points of view, a better approach would be to unfold the distribution of *measured mass* to get the distribution of *true mass* of dileptons, thus correcting for the detector effects. This method is however limited by technical difficulties in inverting the detector response

matrix, which relates the measured momentum with the true momentum of a particle. All unfolding methods fail close to the resonances peaks, giving unstable and hence unreliable results.

The experimental techniques used for measuring dielectrons and dimuons are very different. In the ALICE experiment, electrons are measured using the detectors in the central barrel, which cover the pseudorapidity region $|\eta| \lesssim 0.9$, while muons are measured using a dedicated spectrometer installed in the forward pseudorapidity region $2.5 < \eta < 4$ (see next chapter). The dominant background components of dielectron and dimuon invariant mass spectra, as well as their hadronic contributions, are also different. As an example, a substantial contribution to the dielectron invariant mass spectrum, and to its combinatorial background, originates from π^0 -Dalitz decay. This contribution is absent in the dimuon spectrum since the π^0 decay into muons is kinematically forbidden, the π^0 mass being smaller than twice the muon mass.

The next section is dedicated to the description of the dielectron spectrum, which regards the specific research topic of this thesis work, although most of the theoretical arguments are also valid for the dimuon spectrum. A review of the main experimental results, of both dielectron and dimuon measurements, is presented as a conclusion of this chapter.

2.7.1 Dielectron Spectrum

Different regions of the dielectron invariant mass spectrum are sensitive to different stages of the collision. More specifically, the dielectron spectrum can be divided into the following three mass regions (Fig. 2.13):

- **High-mass region** ($m_{ee} > m_{J/\Psi}$): This region is dominated by dielectrons produced in the primordial stages (Drell-Yan), correlated semi-leptonic open heavy-flavor decays (mostly beauty) and heavy quarkonia.
- **Intermediate-mass region** ($m_\phi < m_{ee} < m_{J/\Psi}$): This is sensitive to thermal radiation from the partonic phase (QGP). A large contribution also comes from semi-leptonic open charm decays.
- **Low-mass region** ($m_{ee} < m_\phi$): This region is sensitive to late stages of the collision. It contains contributions from thermal radiation emitted by the hadronic gas phase and decays of low-mass resonances close to the freeze-out, of which it is possible to study their in-medium modifications. In the low-mass region it is easier to reach the kinematic domain $m_{ee} \ll p_T^{ee}$, where quasi-real virtual photons can be

measured. These provide an independent and complementary measurement to that of real direct photons.

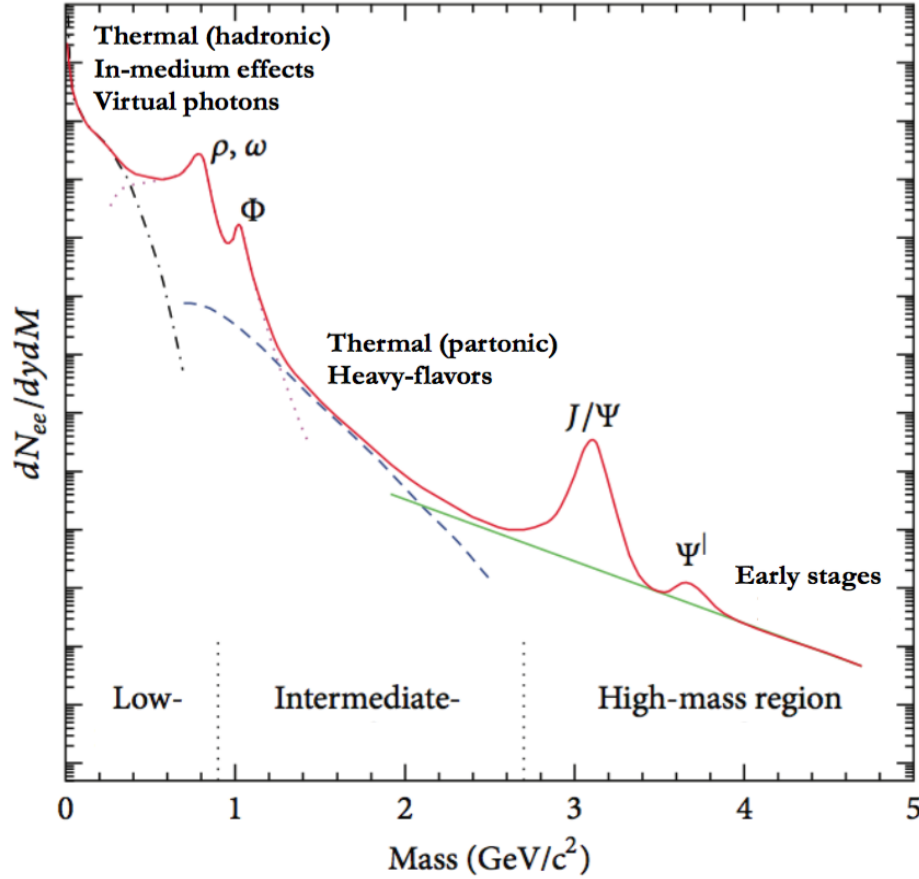


Fig. 2.13 : Schematic representation of the dielectron invariant mass spectrum with the three main regions and the observables that can be studied in each of them.

The dielectron spectrum can be used not only as a thermometer for the QGP, but also as a chronometer of the collision, with the time flowing from high-mass to low-mass.

2.7.2 Thermal Dileptons

The temperature of the QGP can be extracted from an exponential fit to the intermediate mass region of the p_T^{ee} -integrated dielectron spectrum, after subtracting the contribution from heavy-flavor decays:

$$\frac{dN}{dm_{ee}} \sim \exp(-m_{ee}/T) \quad (2.10)$$

Since m_{ee} is a Lorentz-invariant quantity, the inverse slope parameter T is not affected by the Doppler shift, and represents the average temperature of the QGP. The independence of the temperature measurement on the system expansion represents the main advantage of dielectrons, compared to real photon measurements. However, the analysis of the intermediate mass region of the dielectron spectrum requires a very good knowledge of the heavy-flavor contribution and also large statistics. The main uncertainties regarding heavy-flavors come from the measured charm and beauty cross sections and from the particle generators that are used to simulate the mass distribution of dileptons from heavy-flavour decays. From this point of view, dielectron measurements in pp collisions can be used to put more severe constraints on the heavy-flavor production in order to better tune the particle generators. Moreover, a better knowledge of the energy loss mechanisms of heavy quarks in the QGP is required in order to correctly scale the heavy-flavor contribution from pp to Pb–Pb collisions. Due to marginal statistics collected in Run 1 at the LHC, the dielectron analysis presented in this thesis work is mainly focused on the low-mass region ($m_{ee} < 900 \text{ MeV}/c^2$), with the target of studying the contribution of quasi-real virtual photons and in-medium modifications of low-mass vector mesons.

2.7.3 Quasi-real Virtual Photons

An independent and complementary method of measuring real direct photons is to measure virtual photons in the zero-mass limit. The fundamental assumption is that every source of real photons is also a source of virtual photons. Based on this assumption, the following limit holds:

$$\frac{(\gamma^*)^{\text{dir}}}{(\gamma^*)^{\text{incl}}} \xrightarrow{m_{ee} \rightarrow 0} \frac{\gamma^{\text{dir}}}{\gamma^{\text{incl}}} \quad (2.11)$$

The very low mass region of the dielectron spectrum is dominated by dielectrons from π^0 -Dalitz and η -Dalitz decays. These represent a huge background which makes the measurement of virtual direct photons almost impossible in the mass region $m_{ee} < m_\pi$. This represents a lower limit to the mass range that can be studied to access virtual direct photons. This limit can be overcome by considering dielectrons at high p_T^{ee} , in the kinematic range $p_T^{\text{ee}} \gg m_{ee}$, where the energy-momentum relation of the dilepton pair can be approximated by:

$$E_{ee} = \sqrt{m_{ee}^2 + |\vec{p}_{ee}|^2} \approx |\vec{p}_{ee}| \quad (2.12)$$

Virtual photons in this limit are called *quasi-real* virtual photons or virtual photons with *low-virtuality*. Their invariant mass distribution is described by the Kroll-Wada formula [74]:

$$\frac{d^2n_{ee}}{dm_{ee}} = \frac{2\alpha}{3\pi} \frac{1}{m_{ee}} \sqrt{1 - \frac{4m_e^2}{m_{ee}^2}} \left(1 + \frac{2m_e^2}{m_{ee}^2}\right) S dn_\gamma \quad (2.13)$$

here, m_e is the electron mass, while m_{ee} is the mass of the dielectron pair. The factor S is process dependent and for π^0 -Dalitz decay it is expressed as [75]:

$$S = |F(m_{ee}^2)|^2 \left(1 - \frac{m_{ee}^2}{m_h^2}\right)^3 \quad (2.14)$$

where m_h is the π^0 mass and $F(m_{ee})$ is the form factor. The factor S is 0 for $m_{ee} > m_h$ and goes to 1 as $m_{ee} \rightarrow 0$ or $m_{ee} \ll p_T^{ee}$.

The lower limit of the mass range used for quasi-real virtual photon measurement is imposed by the π^0 mass, while the upper limit is defined by the transverse momentum of the dielectron pair and by the lower edge of the mass region which is affected by dielectrons from in-medium ρ^0 -meson (see Section 2.7.4). The range used in this thesis for the extraction of virtual direct photons is $150 < m_{ee} < 300$ MeV/ c^2 (see chapter 9) in the p_T^{ee} ranges: $p_T^{ee} \in [1, 2]$ GeV/ c and $p_T^{ee} \in [2, 4]$ GeV/ c .

The p_T spectrum of direct photons is obtained from the inclusive (real) photon spectrum, given by calorimetric or external conversion measurements, scaled by the fraction of virtual direct photons:

$$\gamma^{dir}(p_T) = \frac{(\gamma^*)^{dir}}{(\gamma^*)^{incl}} \cdot \gamma^{incl}(p_T) \quad (2.15)$$

2.7.4 In-Medium Effects of Vector Mesons

Thermal dileptons produced in the hot hadronic gas phase give a large contribution to the low mass region of the dielectron spectrum ($m_{ee} < 1$ GeV). Their production is largely mediated by low-mass vector mesons (ρ^0 , ω and ϕ) (Fig. 2.14). Among these, the ρ^0 -meson gives the largest contribution, due to its strong coupling to the $\pi\pi$ channel.

The spectral functions of low-mass vector mesons in a hot and dense hadronic medium are expected to be modified compared to the vacuum. This effect has since long been proposed as a signature of chiral symmetry restoration [76]. To this end, the ρ^0 meson represents an ideal probe considering its short lifetime ($\tau_\rho = 1.3$ fm/ c) compared to that of the hot fireball, and its dilepton decay channel. This particle lives its entire life

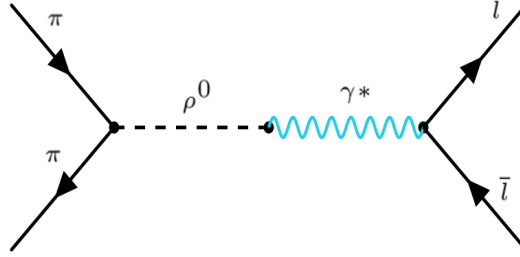


Fig. 2.14 : Feynman diagram representing dilepton production mediated by the ρ^0 resonance.

in a hot and dense medium and its spectral properties are carried undisturbed by its decay products. Regarding the in-medium modifications of the ρ^0 properties, two main scenarios were proposed:

- **Dropping-mass:** elaborated by C. M. Rho and G. E. Brown and collaborators [77], it is based on a direct connection to chiral symmetry restoration and it predicted a shift of the ρ^0 pole mass.
- **Broadening:** developed by R. Rapp and J. Wambach and collaborators [78], it is based on hadronic many-body theory and it predicted a broadening of the ρ^0 mass distribution (melting).

The characterization of the in-medium properties of the ρ^0 meson and the understanding of the underlying mechanism responsible for them aroused a lot of interest in the study of the dilepton continuum in the low-mass region in high energy nucleus-nucleus collisions (see Section 2.8.1).

2.8 Review of Experimental Results on Dileptons

This section provides a run-through of the main experimental findings of dilepton measurements and the major milestones of theoretical developments in this field. The review of experimental results starts from the earlier generations of experiments at the SPS. The review continues with the results at higher energies from PHENIX and STAR at RHIC, and culminates with the illustration of the current status of dilepton measurements in ALICE at the LHC.

2.8.1 The First Dilepton Measurements: the SPS Era

The interest in studying the dilepton continuum dates back to the 1970s, triggered by the experimental detection of the Drell-Yan process ($q\bar{q} \rightarrow \gamma^* \rightarrow l^+l^-$) [66] and the J/Ψ . The first experimental findings of enhanced dilepton productions, called "anomalous pairs", both in the low-mass region ($m_{ll} < 1 \text{ GeV}/c^2$) and in the intermediate mass region ($1 < m_{ll} < 2.5 \text{ GeV}/c^2$) in pp collisions, have been disproved by Helios-1 [79] and, with higher precision by CERES [80]. The excess found at low mass was due to a severe underestimation of the contribution from η -Dalitz decay, while the enhanced dilepton production in the intermediate mass region was instead due to imprecise estimation of the open charm contribution.

These fake alarms however had already inspired Bjorken and Weisberg, which proposed for the first time the idea of dilepton radiation produced by partons as an additional contribution to the dilepton continuum. They estimated the contribution from this additional source to be a factor 10-100 higher than Drell-Yan in the low-mass region [81].

The heavy-ion experimental program at the Super-Proton Synchrotron (SPS) at CERN started in 1986 using fixed target experiments. The first generation of experiments sensitive to dilepton continuum, Helios-2 and NA38, found an indication for an anomalous dilepton excess [82], which however was not significant. The confirmation for the excess arrived with the second generation of experiments at the SPS: Helios-3, CERES and NA58. CERES measured the dielectron spectra for different collision systems and center-of-mass energies. While the dielectron spectra measured in proton-nucleus collisions at $\sqrt{s_{NN}} = 450 \text{ GeV}$ were compatible with the known hadronic sources (Fig. 2.15 left and middle), the spectrum measured in nucleus-nucleus collisions at $\sqrt{s_{NN}} = 200 \text{ GeV}$ showed a clear excess in the dielectron production compared to the expected contributions from hadronic sources, especially in the low-mass region, below the ρ^0 mass [83] (Fig. 2.15 right).

This observation gave a great boost to theoretical works, with hundreds of publications. The role of the ρ^0 as mediator in the processes which produce thermal dileptons in the hot hadronic gas had already been highlighted a few years before [84] and most of the theoretical models predicted an enhancement of the ρ^0 , due to regeneration via $\pi^+\pi^- \rightarrow \rho^0$, but no in-medium effects. Fig. 2.16 left shows the CERES measurement in comparison to some of these theoretical models. Although part of the enhancement, in correspondence to the vacuum ρ^0 pole is covered, the bulk of the excess located at lower masses is not described at all. Only models which predicted significant modifications of the ρ^0 meson line shape in the medium could reproduce the observed excess. Theoretical models used to describe CERES data indicated two possible scenarios: a dropping of

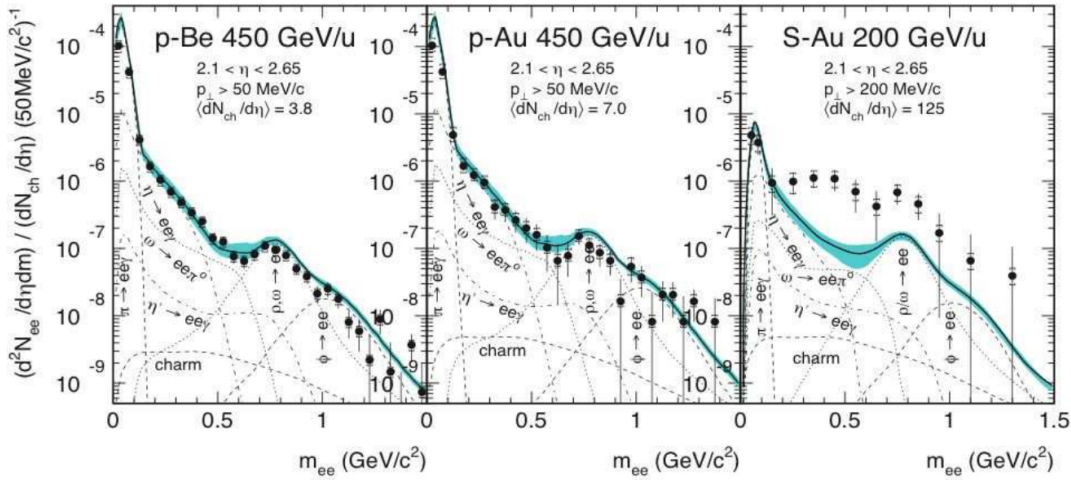


Fig. 2.15 : Dielectron invariant mass spectra measured by the CERES Collaboration in p–Be (left) and p–Au (middle) collisions at $\sqrt{s_{NN}} = 450$ GeV and in S–Au at $\sqrt{s_{NN}} = 200$ GeV (right) [83]. While no excess compared to the hadronic cocktail is seen in the measured spectra in proton-nucleus collisions, a large enhancement is visible in nucleus-nucleus collisions, representing the first clear evidence of new physics in the dilepton sector.

its mass or a broadening of its width [77, 78] (see Section 2.7.4). Unfortunately, the mass resolution of the CERES experiment did not enable a clear discrimination between these two possible scenarios, which both fitted the data very well. The ambiguity was not solved with the new data in Pb–Au collisions at $\sqrt{s_{NN}} = 158$ GeV (Fig. 2.16 right).

An enhanced dilepton production was also observed in the intermediate mass region by Helios-3 for S–W with respect to p–W collisions at $\sqrt{s_{NN}} = 200$ GeV [86, 87] (Fig. 2.17). Theoretical arguments based on enhanced open charm production and thermal radiation from partonic phase were used to explain the excess, while experimentally this remained an open question.

The answers to the aforementioned ambiguities and unsolved questions came with NA60, an experiment of the third generation, specifically designed and built for dilepton measurements. A silicon inner tracker with very high readout speed complemented the existing muon spectrometer. Track matching between the muon spectrometer and the inner tracker improved the mass resolution by a factor ~ 5 , allowing to a better separation between prompt and decay muons. The faster readout allowed to operate the experiment at higher interaction rate, resulting in a factor > 1000 in statistics. The enormous technological progress of the experimental apparatus resulted in a big jump in data quality. Fig. 2.18 left shows the dimuon invariant mass spectrum measured in In–In

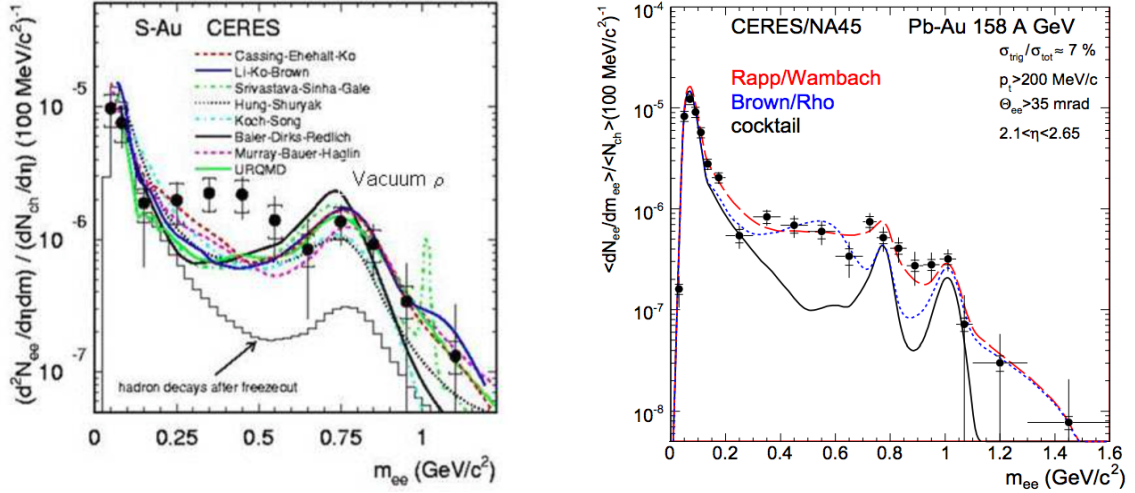


Fig. 2.16 : Dielectron spectrum measured by CERES in S–Au collisions at $\sqrt{s_{NN}} = 200 \text{ GeV}$ [83], in comparison to the theoretical models which predicted the ρ^0 regeneration without any in-medium effect (left). Dielectron spectrum measured by CERES in Pb–Au collisions at $\sqrt{s_{NN}} = 158 \text{ GeV}$ [85], compared to the two main models predicting in-medium modifications of the ρ^0 meson and the contribution from vacuum ρ^0 , shown as reference.

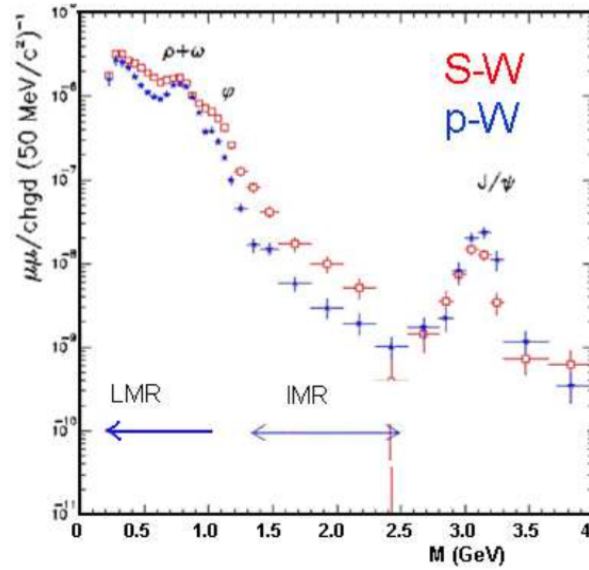


Fig. 2.17 : Dimuon invariant mass spectra measured by Helios-3 in S–W and p–W collisions at $\sqrt{s_{NN}} = 200 \text{ GeV}$ [86, 87].

collisions at $\sqrt{s_{NN}} = 158 \text{ GeV}$ [88, 89], obtained after removing fake matches between the spectrometer and the inner tracker and after subtracting the combinatorial background, estimated using the event-mixing technique. The ρ^0 and ω mesons are completely resolved.

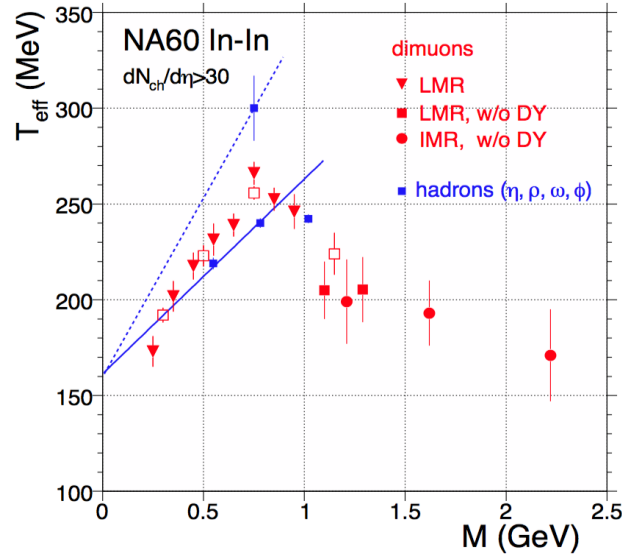


Fig. 2.19 : Inverse slope parameter T_{eff} measured by NA60 as a function of mass in In–In collisions at $\sqrt{s_{\text{NN}}} = 158$ GeV [90, 91]. The linear trend in the low mass region indicates a dominant hadronic source, affected by the radial flow, while the rather constant trend in the intermediate mass region indicates a partonic source of radiation, where flow has not built up yet.

2.8.2 Dilepton Measurements at RHIC: PHENIX and STAR

The dilepton experimental program has been continued at higher energies at the Relativistic Heavy-Ion Collider (RHIC) by PHENIX and STAR. The dielectron invariant mass spectra measured by PHENIX in pp collisions [94] and in d–Au collisions [95] at $\sqrt{s_{\text{NN}}} = 200$ GeV are shown in Fig. 2.20, in comparison with the expectations from hadronic sources (hadronic cocktail).

Data are in agreement with the expected contributions from hadron decays in both collision systems, showing no strong cold nuclear matter effects in d–Au collisions. The intermediate mass region of the dielectron spectrum measured in pp and in d–Au collisions is sensitive to heavy-flavour production. The charm and beauty cross sections can be extracted by fitting the intermediate mass region, after subtracting the contributions from light-flavoured hadron decays, with the two-component function:

$$\frac{dN}{dm_{ee}} = A \left[\frac{dN}{dm_{ee}} \right]_{\text{charm}} + B \left[\frac{dN}{dm_{ee}} \right]_{\text{beauty}} \quad (2.16)$$

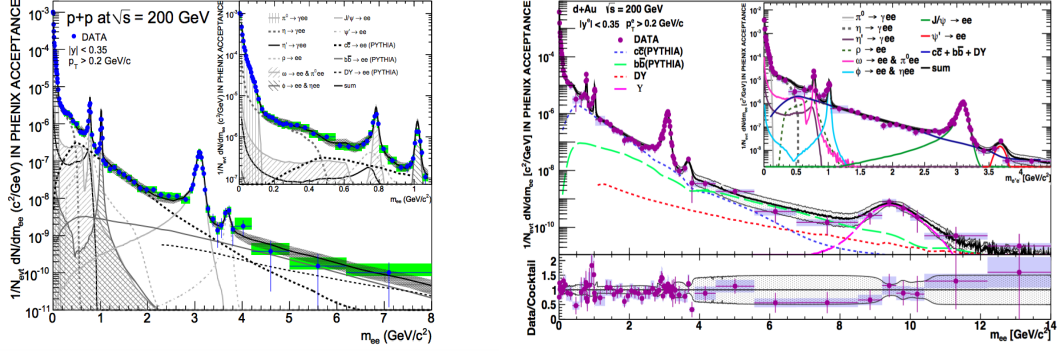


Fig. 2.20 : Dielectron invariant mass spectra measured by PHENIX in pp collisions (top) [94] and in d–Au collisions (bottom) [95] at $\sqrt{s_{NN}} = 200$ GeV, compared to the expected contributions from hadron decays. The measured spectra are in agreement with the hadronic cocktail for both collision systems, showing evident no cold nuclear effects in d–Au collisions.

the mass distributions for $c\bar{c}$ and $b\bar{b}$ decays are obtained from simulations, while A and B are the fit parameters, proportional to the charm and beauty cross sections. The measured $\sigma_{c\bar{c}}$ and $\sigma_{b\bar{b}}$ are in agreement with other heavy-flavour measurements [96].

The first dielectron measurement in Au–Au collisions at $\sqrt{s_{NN}} = 200$ GeV reported by PHENIX [97] (Fig. 2.21 left) showed a very large excess, reaching a factor ~ 10 , in the low-mass region compared to the hadronic cocktail, and the measured enhancement in the dielectron yield showed an increasing trend with centrality (Fig. 2.21 right).

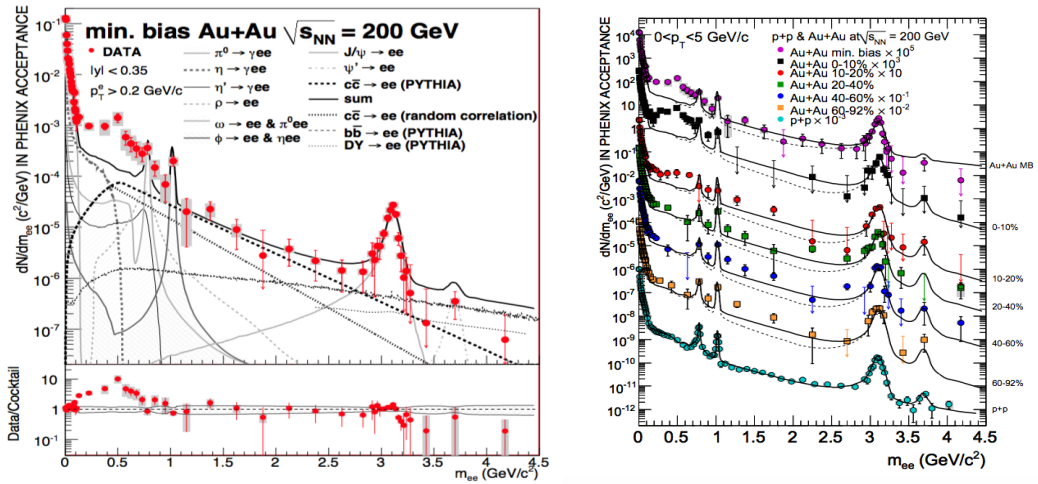


Fig. 2.21 : Dielectron invariant mass spectrum measured by PHENIX in Au–Au collisions at $\sqrt{s_{NN}} = 200$ GeV, compared to the hadronic cocktail [97] (left) and measured spectra in pp and in Au–Au collisions for different centralities.

The fraction of virtual direct photons has been extracted in the kinematic domain $p_T^{ee} \gg m_{ee}$ from the two-component fit:

$$f(m_{ee}) = r \cdot f_{\text{dir}}(m_{ee}) + (1 - r) \cdot f_c(m_{ee}) \quad (2.17)$$

where f_{dir} is the mass distribution of virtual photons, given by the Kroll-Wada formula, and f_c is the cocktail shape. Fig. 2.22 shows the fit results for the transverse momentum range $1 < p_T^{ee} < 1.5 \text{ GeV}/c$ and the fraction of virtual direct photons measured in pp and in Au–Au collisions, compared to the expectations from NLO pQCD calculations.

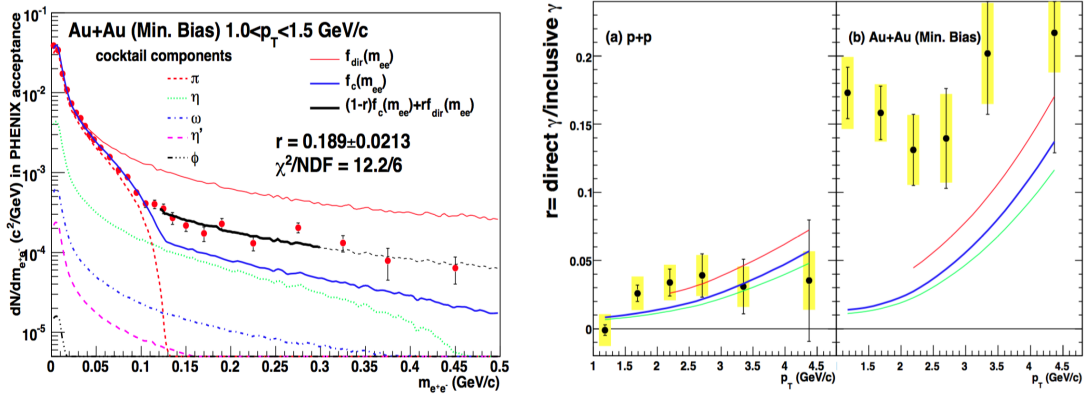


Fig. 2.22 : Fit to the low-mass region to extract the fraction r of virtual direct photons, using the two component function: $f(m_{ee}) = r \cdot f_{\text{dir}}(m_{ee}) + (1 - r) \cdot f_c(m_{ee})$ (left). Fraction of virtual direct photons as a function of p_T measured in pp and Au–Au collisions, in comparison with the expectations from NLO pQCD calculations.

The invariant cross section of virtual direct photons has been measured by scaling the measured inclusive photon spectrum by the fraction r of virtual direct photons (Fig. 2.23):

$$\left[E \frac{d^3\sigma}{d^3p} \right]_{\text{dir}} = r \cdot \left[E \frac{d^3\sigma}{d^3p} \right]_{\text{incl}} \quad (2.18)$$

The temperature extracted from the exponential fit to the low- p_T region is $T_{\text{eff}} = 221 \pm 19 \text{ (stat)} \pm 19 \text{ (syst)} \text{ MeV}$, consistent with hydrodynamical models based on an initial temperature $300 < T_{\text{init}} < 600 \text{ MeV}$ and a formation time $0.6 < \tau_0 < 0.15 \text{ fm}/c$ [103].

More recently, the STAR measurement of the dielectron invariant mass spectrum in Au–Au collisions at $\sqrt{s_{\text{NN}}} = 200 \text{ GeV}$ has been published [100]. The enhancement observed by STAR in the low-mass region is smaller compared to PHENIX, and it is compatible with models that involve the broadening of the ρ^0 meson.

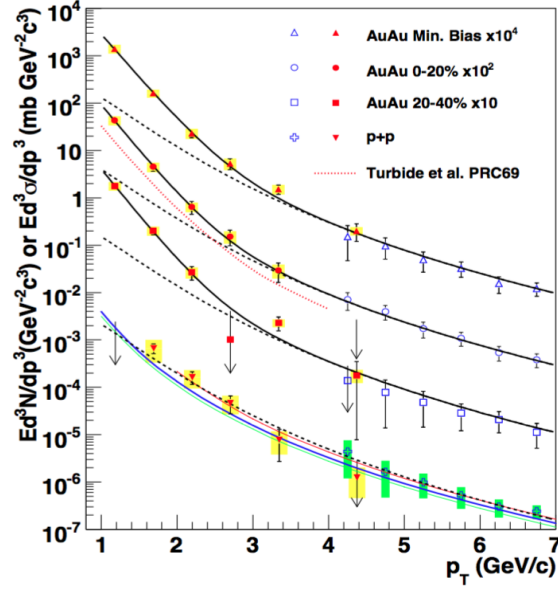


Fig. 2.23 : Invariant cross section of direct photons as a function of p_T measured in pp and in Au–Au collisions at $\sqrt{s_{NN}} = 200$ GeV. The filled points are from [97] and open points are from [98, 99]. The three curves on the pp data represent NLO pQCD calculations, and the dashed curves show a modified power-law fit to the pp data, scaled by T_{AA} . The dashed (black) curves are exponential plus the T_{AA} scaled pp fit.

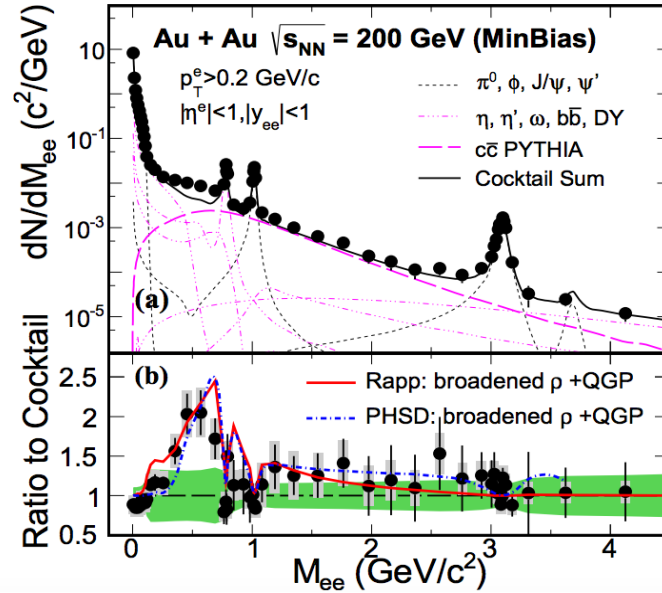


Fig. 2.24 : Dielectron invariant mass spectrum measured by STAR in Au–Au collisions at $\sqrt{s_{NN}} = 200$ GeV, in comparison to the hadronic cocktail [100]. The excess measured in the low-mass region is smaller compared to PHENIX, and it is consistent with models predicting radiation from the QGP and a broadened ρ^0 as sources of the excess.

The inconsistency in the excess measurements between PHENIX and STAR has been solved with the new data from PHENIX, collected in 2010 after the installation of the Hadron Blind Detector (HBD). This is a Cherenkov detector using GEMs, which provides improved hadron rejection capabilities. In addition, the track reconstruction algorithm has been significantly improved in order to reduce the ring sharing problem in the RICH detector: the new algorithm forbids a ring to be associated with multiple tracks, and it associates a track only with signal electron candidates tagged by the HBD. The new detector and the improved tracking algorithm have contributed to reducing the hadron contamination from 30% to less than 5% in all centrality ranges. Finally, new methods for photon conversion rejection have been implemented, which have contributed to reducing the combinatorial background. Fig. 2.25 shows the new PHENIX measurement in minimum bias Au–Au collisions at $\sqrt{s_{NN}} = 200$ GeV [101].

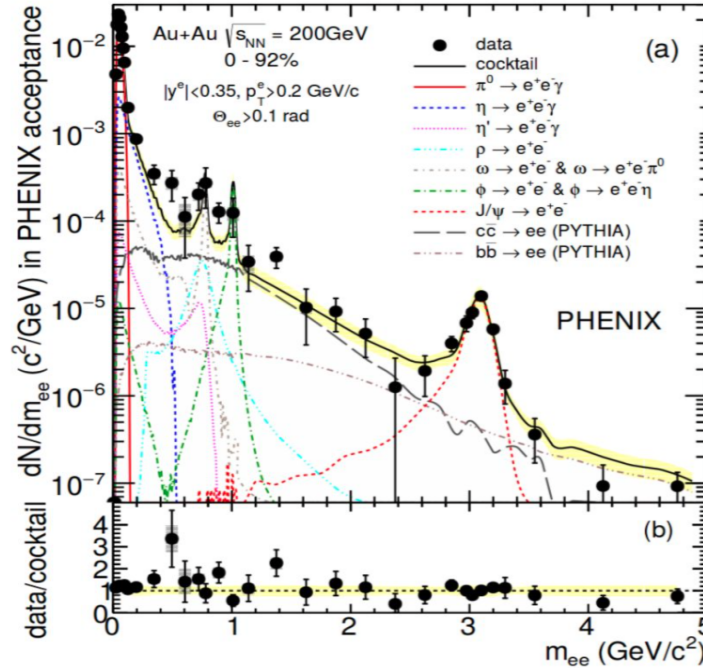


Fig. 2.25 : Dielectron invariant mass spectrum measured by PHENIX in minimum bias Au–Au collisions at $\sqrt{s_{NN}} = 200$ GeV after the installation of the HBD [101]. The measured enhancement in the low mass region is reduced compared to the previous measurement, and it is now consistent with the excess measured by STAR.

The huge excess seen in 2004 data is not confirmed, and the measured enhancement in the low-mass region is now consistent with the STAR measurement, and with models predicting the ρ^0 broadening (Fig. 2.26).

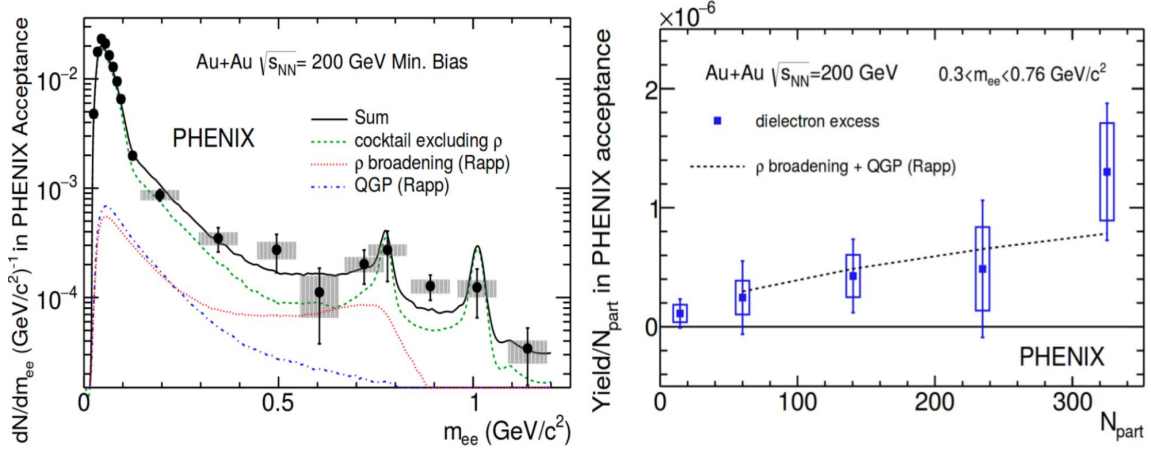


Fig. 2.26 : Dielectron enhancement measured by PHENIX using the 2010 data in comparison to the hadronic cocktail including a broadened ρ^0 (left) and dielectron excess as a function of centrality (right). [101].

2.8.3 Dilepton Measurements at the LHC

The dielectron invariant mass spectra have been measured in pp collisions at $\sqrt{s} = 7$ TeV and in p–Pb collisions at $\sqrt{s_{NN}} = 5.02$ TeV with the ALICE experiment at the LHC (Fig. 2.27). The measured spectra in pp and p–Pb collisions are both in agreement with the expected contributions from hadronic sources, within the statistical and systematic uncertainties. In p–Pb collisions data might favor a lower charm production.

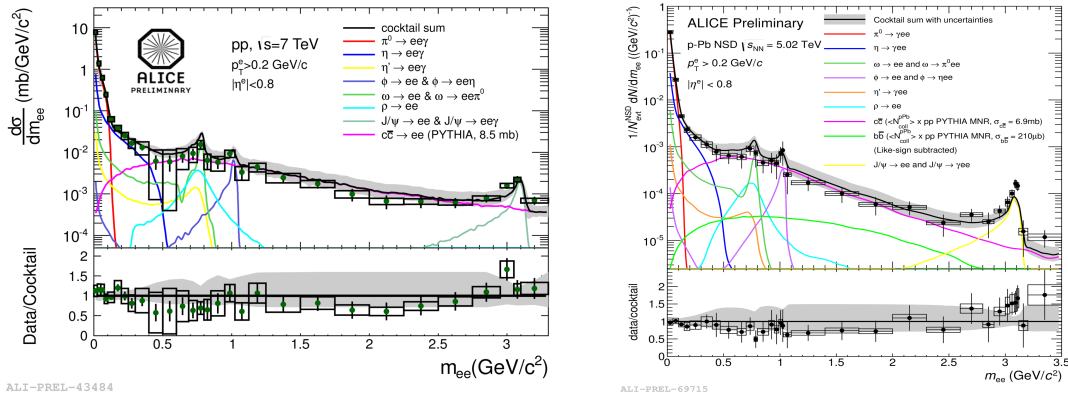


Fig. 2.27 : Dielectron invariant mass spectra measured in pp collisions at $\sqrt{s} = 7$ TeV (left) and in p–Pb collisions at $\sqrt{s_{NN}} = 5.02$ TeV (right) compared to the expected contributions from hadronic sources.

In pp collisions, the contribution from virtual photons has been extracted from the two-component fit (2.17) in the kinematic range $p_T^{ee} \gg m_{ee}$ (Fig. 2.28 left). The fraction

r of virtual direct photons extracted from the fit is consistent with the measurement of real direct photons using the photon conversion method (PCM) [70] (Fig. 2.28 right).

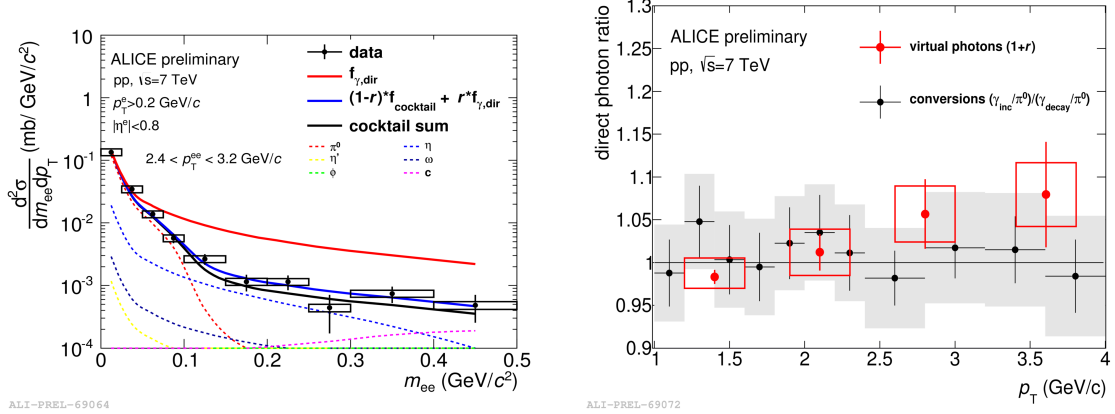


Fig. 2.28 : Example of the two-component fit to the dielectron spectrum in the low-mass region (left) and virtual direct photon ratio $(1+r)$ measured in pp collisions at $\sqrt{s} = 7$ TeV in comparison with the real photon measurement [70] (right).

The invariant cross-section of virtual direct photons has been extracted in pp collisions using the inclusive photon spectrum, measured using the photon conversion method, and the fraction r of direct photons, measured from low-mass dielectrons. This measurement it is consistent with the expectations from NLO pQCD calculations [102] (Fig. 2.29).

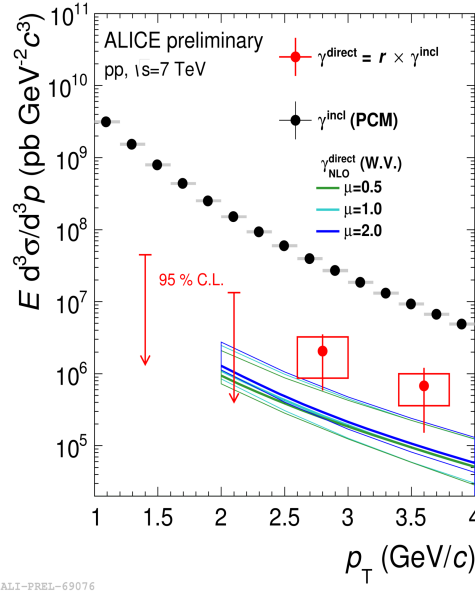


Fig. 2.29 : Direct photon spectrum measured in pp collisions at $\sqrt{s} = 7$ TeV in comparison to expectations from NLO pQCD calculations [102].

Dimuon invariant mass spectra have been measured by ALICE, for three collisions systems at different center-of-mass energies, using the forward muon spectrometer ($2.5 < \eta < 4$). The measured spectra are well described by the contributions from the known hadronic sources (Figs. 2.30 and 2.31). No precision study of the dimuon continuum can be done due to the large statistical uncertainties and the relatively large threshold on the dimuon transverse momentum ($p_T^{\mu\mu} > \text{GeV}/c$).

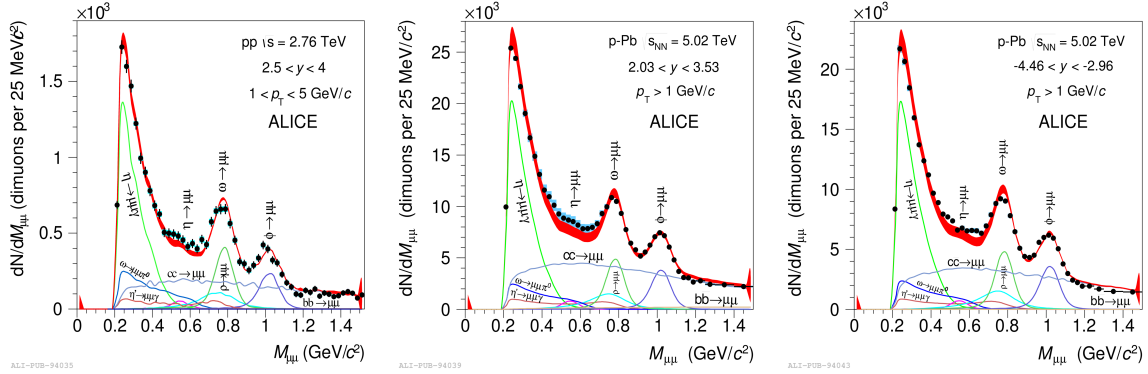


Fig. 2.30 : Dimuon invariant mass spectra measured in pp collisions at $\sqrt{s} = 2.76$ TeV (left), in p–Pb collisions at $\sqrt{s_{NN}} = 5.02$ TeV for the p-going (middle) and Pb-going directions (right) [104]. The measured spectra are in agreement with the expected contributions from hadronic sources.

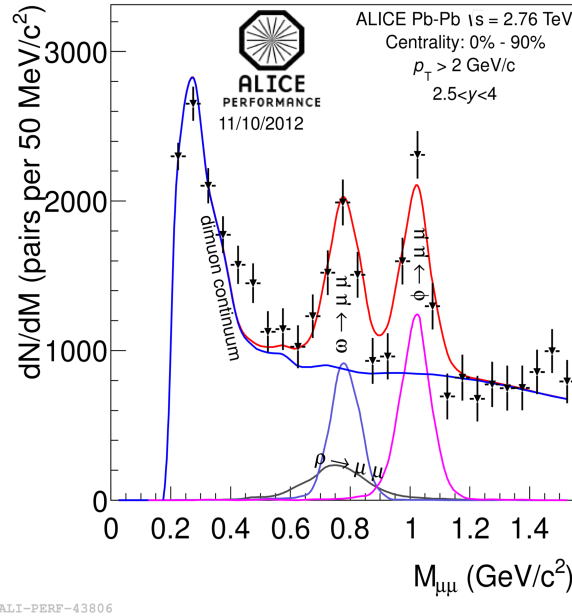


Fig. 2.31 : Dimuon invariant mass spectrum measured in Pb–Pb collisions at $\sqrt{s_{NN}} = 2.76$ TeV for integrated centrality range.

Chapter 3

The Experimental Setup and the Analysis Framework

3.1 Introduction

This chapter contains a description of the particle accelerator, the ALICE experimental setup and the analysis framework. The detectors used in the analysis for this thesis work are treated in more details, while the rest of the detectors are only briefly mentioned.

3.2 The Large Hadron Collider (LHC)

The Large Hadron Collider (LHC) is the largest and most powerful particle accelerator in the world. It is located as deep as 175 meters beneath the French-Swiss border near Geneva, Switzerland. It accelerates protons as well as Pb ions to unprecedented energies. The LHC is a circular collider with a circumference of 27 km, in which high energy particle beams travel in opposite directions inside two parallel beam pipes kept at ultrahigh vacuum (the pressure inside the beam pipe is about 10^{-7} Pa). Particles are injected into the LHC at 450 GeV from the SPS, and then boosted to energies at the TeV scale by accelerating radio-frequency cavities, tuned to oscillate at 400 MHz, which sort the particle beams into discrete packets called "bunches". Particles travel inside the LHC main ring curved by a strong magnetic field created by powerful superconducting magnets. In order to maintain the superconducting state, necessary to conduct electricity without resistance or energy loss, the electromagnets are operated at a temperature of 1.9 Kelvin. The cooling system uses 120 tons of liquid helium, circulating into 40,000 leak-tight pipes, making it the largest and most complex cryogenic system in the world.

Thousands of magnets of different types and sizes are used to guide the beams around the accelerator. These include 1232 dipole magnets, each 15 meters long which are used to bend the beams, and 392 quadrupole magnets, each 5–7 meters long, which focus the beams. Close to the 4 interactions points, on both sides, another type of magnet is used to "squeeze" the beams closer together in order to increase the luminosity and hence the chances of collisions. One point of the LHC (Point 6) hosts the Beam Dumping System, where horizontally deflecting extraction kickers (MKD) switch on to divert the beam towards a proper absorber. This operation is performed when the intensity of the circulating beams has dropped below a minimum threshold which does not guarantee a high frequency of collisions, and a new filling is required. All operations and different working phases of the LHC are steered by the CERN Control Center. The beams collide in 4 intersection points, where the LHC experiments are located: ALICE, ATLAS, CMS and LHCb.

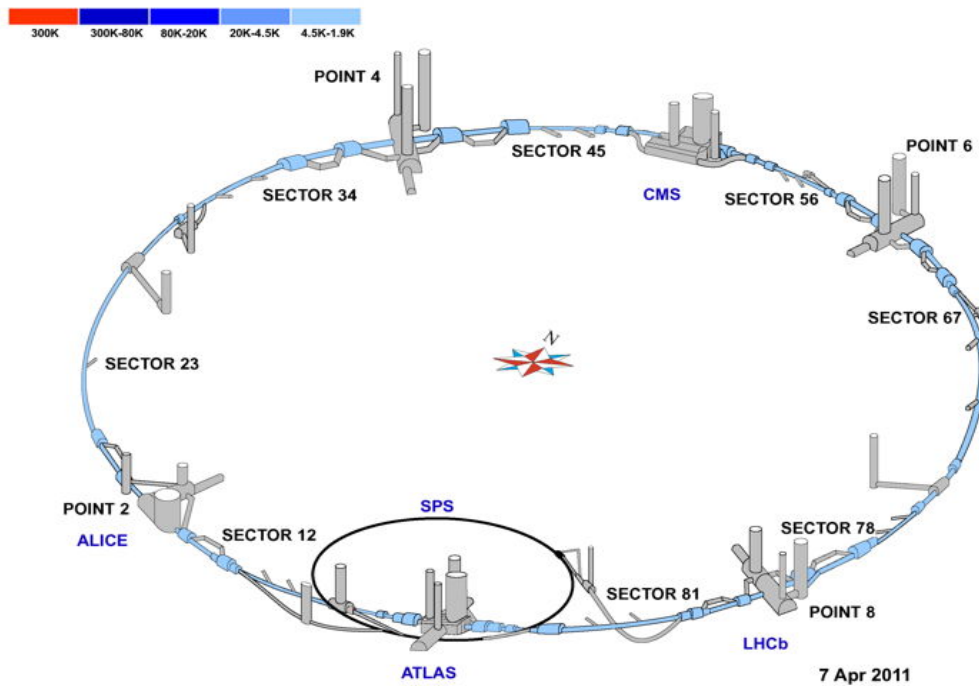


Fig. 3.1 : LHC diagram, showing the four main experiments: ALICE, ATLAS, CMS and LHCb.

3.3 The ALICE Detector

ALICE (A Large Ion Collider Experiment) is dedicated to the study of ultrarelativistic heavy-ion collisions at the CERN Large Hadron Collider (LHC) [105]. The primary goal of its scientific research program is to investigate the properties of the strong interaction under extreme conditions of energy density and temperature. This is achieved by creating microscopic and ephemeral drops of quark-gluon plasma in collisions between heavy nuclei and by measuring the properties of the particles produced in the collisions. Several experimental probes are used to investigate and characterize the properties of this novel state of matter. Although the main interest of this experiment is the study of collisions between ions, the experimental program of ALICE also includes the studies of proton-proton and proton-nucleus collisions, used as fundamental references for vacuum and cold nuclear matter effects in Pb–Pb measurements, respectively. The study of pp and p–Pb collisions is also interesting to investigate some QCD-related topics, such as multi-partonic interactions or collectivity effects in high-multiplicity pp and p–Pb collision events (for which ALICE is in competition with other LHC experiments). The detector has been specifically designed to cope with enormous particle multiplicities that were expected in Pb–Pb collisions at the LHC energies. The ALICE excellent tracking and particle identification capabilities, over a broad range in momentum, allow for a comprehensive study of charged hadrons, electrons, muons and photons produced in heavy-ion collisions. The ALICE detector has been built by a collaboration including over 1000 physicists and engineers from 105 universities and research institutes in 30 countries. Its overall dimensions are $16 \times 16 \times 26 \text{ m}^3$ with a total weight of approximately 10 000 t. The ALICE experimental setup is divided into three main parts (Fig. 3.2):

- **Central barrel:** it contains several sub-detectors, covering the pseudorapidity range $|\eta| \lesssim 0.9$. These are used for tracking, determination of the collision vertex and particle identification. The detectors in the ALICE central barrel are embedded in a large solenoid magnet, previously used in the L3 experiment at LEP, which creates the magnetic field used for tracking. The detectors in the ALICE central barrel are used in measurements of charged hadrons, electrons, and photons.
- **Forward muon spectrometer:** this is a detector specifically dedicated for tracking and identification of muons. It is located on one side of the ALICE experimental hall, in the forward pseudorapidity region ($2.5 < \eta < 4$). It is used for measurements of heavy quarkonia and dimuons.

- **Forward detectors:** These include hadronic calorimeters and scintillators, used for timing, determination of the collision centrality and event plane.

An array of scintillators (ACORDE) on top of the L3 magnet is used for cosmic ray measurements [106]. It is operated when the beams are not circulating in the collider, e.g. during maintenance operations or regular shut-down periods.

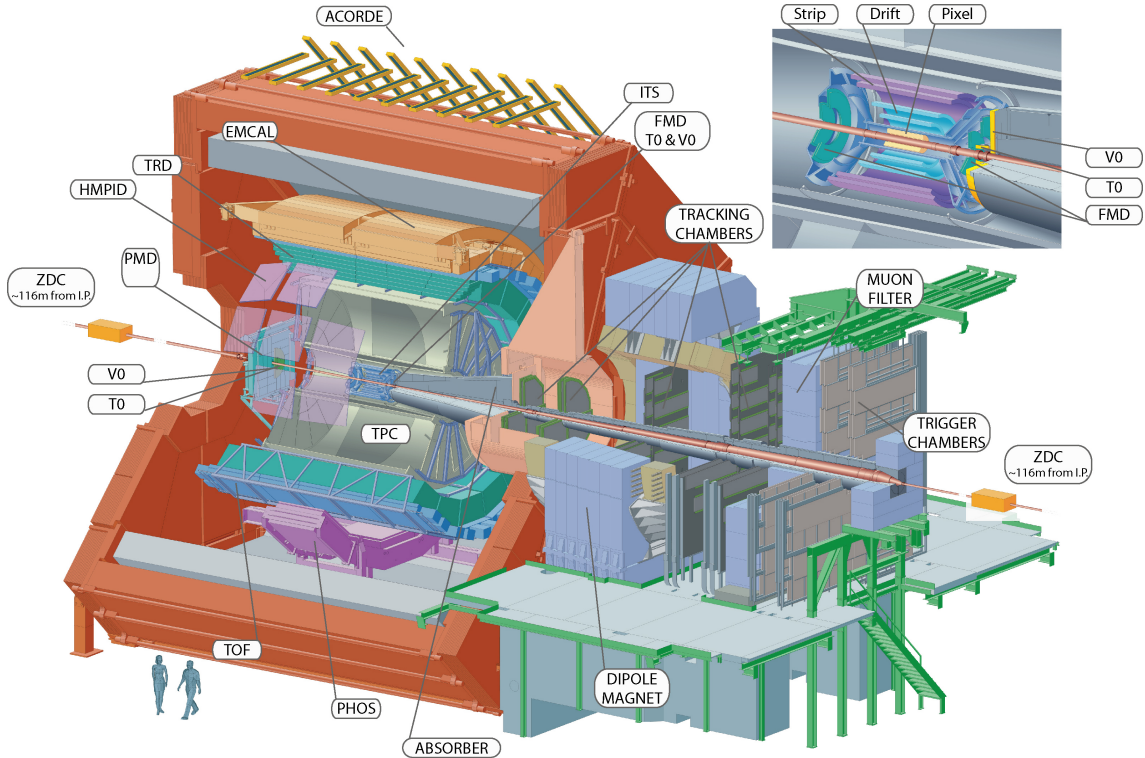


Fig. 3.2 : ALICE schematic layout.

3.3.1 Inner Tracking System (ITS)

The Inner Tracking System (ITS) [107] is the first detector encountered by particles produced in the collision events, that travel through the experimental apparatus. It consists of 6 cylindric layers of silicon detectors, concentric and coaxial to the beam pipe, with a total pseudorapidity coverage $|\eta| \leq 0.9$. Three different technologies have been used for this detector: the two innermost layers are made of Silicon Pixel Detectors (SPD), the two central layers of Silicon Drift Detectors (SDD) and the two outermost layers of double sided Silicon Strip Detectors (SSD) (Fig. 3.3). The detector radius ranges from 3.9 cm for the innermost layer up to 43 cm for the outermost layer. The main parameters of the various layers of the ITS are summarized in Table 3.1. The

Layer	Type	r (cm)	$\pm z$ (cm)	Area (m ²)	Ladders	Ladders/stave	Det./ladder	Total channels
1	pixel	3.9	16.5	0.09	80	4	1	5 242 880
2	pixel	7	16.5	0.18	160	4	1	10 485 760
3	drift	14.9	22.2	0.42	14	–	6	43 008
4	drift	23.8	29.7	0.89	22	–	8	90 112
5	strip	39.1	45.1	2.28	34	–	23	1 201 152
6	strip	43.6	50.8	2.88	38	–	26	1 517 568

Table 3.1 : Main parameters of the ITS detectors [107].

ITS is used in the determination of the primary and secondary vertices, and in the track reconstruction in the vicinity of the collision point. It is also used as a standalone tracker to reconstruct low momentum tracks which do not reach the Time Projection Chamber, the main tracking detector of the ALICE experiment (see next section). The ITS has particle identification capabilities via the measurement of particle energy loss in the silicon detectors, which are complementary to the PID signals from other detectors. A more detailed description of the ITS can be found in [107].

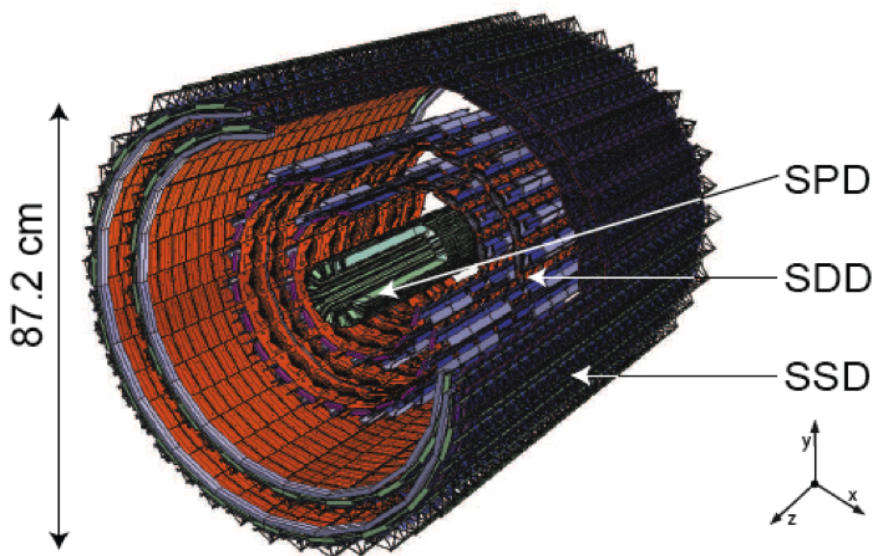


Fig. 3.3 : Schematic view of the inner tracking system (ITS) and its supporting structures.

3.3.2 Time Projection Chamber (TPC)

The Time Projection Chamber (TPC) is the largest detector and the main tracking device in the ALICE central barrel [108]. It is used for track finding and reconstruction, charged particle momentum measurement, via their curvature radius in the magnetic

field, and for particle identification, via the measurement of the particle's specific energy loss in the TPC gas. The TPC is cylindrical in shape, coaxial with the beam pipe, with an active gas volume ranging from about 85 cm to 250 cm, in the radial direction, and a length of 510 cm, in the beam direction. The TPC volume is divided into two symmetric parts by a disc-shaped high voltage membrane, parallel to and equidistant from the two endcaps, which is used to create a highly uniform electrostatic field in the two drift regions of ~ 250 cm length. The TPC end-plates are each segmented into 18 trapezoidal sectors and equipped with multi-wire proportional chambers, containing 560,000 electronics channels, with cathode pad readout covering an overall active area of 32.5 m^2 . The sectors are segmented radially in two chambers with varying pad sizes, optimized for the radial dependence of the track density. The TPC active volume is filled with a gas mixture that is ionized by the passage of charged particles. The gas mixture, containing 90% Ne and 10% CO_2 , is characterized by low diffusion, low-Z and large ion mobility. These requirements are needed for a good momentum and PID resolution, and to guarantee the highest possible acquisition rate. More recently it has been proposed to add 5% N_2 to the mixture, which turned out to provide higher gas gain stability and a better control of the drift velocity. Both gas mixtures require a high drift field (400 V/cm) to secure an acceptable drift time (88ms and 92ms respectively). The field cage of the TPC is surrounded by double-shelled containment vessels with CO_2 as an insulator. Composite materials based on carbon fiber were chosen for high mechanical stability and low material budget (only 3.5% of a radiation length for tracks with normal incidence). Charged particles traversing the TPC create ionization traces in the gas mixture. Depending on the electrical charge and momentum of the particle the track curvature will be larger or smaller in either direction. Electrons produced in the ionization drift at a constant velocity towards the TPC endcaps, pushed by the uniform electrostatic field existing between the endplates and the HV membrane. As the electrons approach the reading pads, they feel a stronger electric field created by the multiwire proportional chambers, and further ionization is created (charge amplification). Ions produced in this multiplication process drift back towards the TPC volume and are collected by a metallic Gating Grid (GG), located close to the, used to avoid the ion back-flow into the drift region. Since ions move much slower than electrons, they would accumulate into the TPC, thus creating space-charge effects which would distort the electric field. The operation of the Gating Grid requires some time to collect all ions ($\sim 200 \mu\text{s}$), which results in a dead-time which intrinsically limits the TPC readout rate. The space coordinates of the reading pad and the time information of the collected signal allow for a 3-dimensional reconstruction of the particle's trajectory, based on the

knowledge of the electric field and hence of the drift time of ionization electrons. The collected charge depends on the amount of ionization created, which is a measure of the energy loss of the particle. This depends on the momentum and identity of the particle and the energy loss measurement is used for particle identification (see Section 5.2).

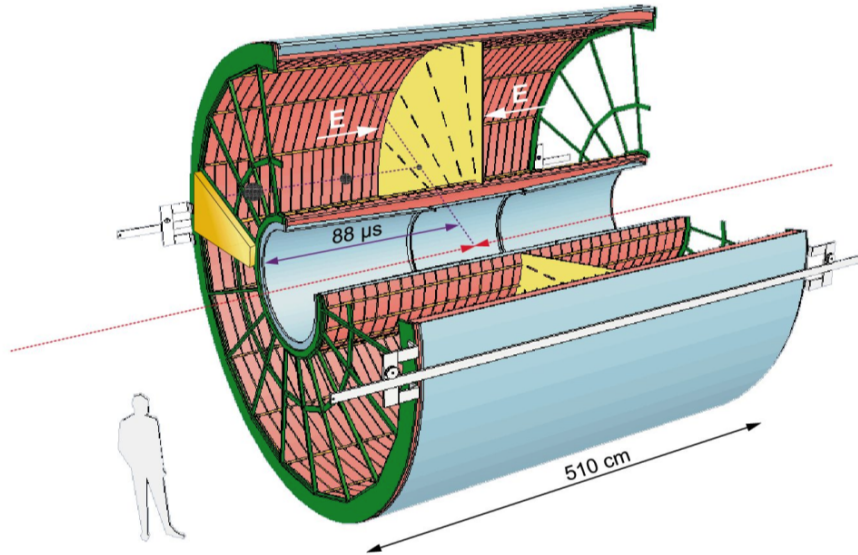


Fig. 3.4 : Schematic view of the Time Projection Chamber (TPC).

3.3.3 Time-Of-Flight (TOF)

The Time-Of-Flight detector (TOF) measures the time spent by particles to travel from the collision point to the TOF radius [109]. The starting time is provided by the T0 detector, a fast scintillator placed at forward rapidity (see next section). The TOF detector has a cylindrical shape, covering polar angles between 45 degrees and 135 degrees over the full azimuth. It has a modular structure with 18 sectors in ϕ , matching the TPC sectors in order to avoid dead zones. Each of these sectors is divided into 5 modules along the beam direction. The modules contain a total of 1638 detector elements (MRPC strips), covering an area of 160 m² with 157248 readout channels (pads). The detector chosen for the ALICE TOF is the Multigap Resistive Plate Chamber (MRPC). This is a stack of resistive glass plates. A high voltage is applied to the external surfaces of the stack. Further out there are pickup electrodes. A charged particle ionizes the gas and the high electric field amplifies this ionization by an electron avalanche. The resistive plates stop the avalanche development in each gap. They are however transparent to the fast signal induced on the pickup electrodes by the movement of the electrons. The total

signal is the sum of the signals from all gaps (the reason for many gaps is to achieve high efficiency), whereas the time jitter of the signal depends on the individual gap width (the reason for narrow gaps is to achieve good time resolution). The detector element is a long strip with an active area of $7.4 \times 120 \text{ cm}^2$. It has 96 readout pads of $2.5 \times 3.5 \text{ cm}^2$ arranged in two rows. It consists of 2 stacks of glass, each with 5 gas gaps of $250 \mu\text{m}$. Spacers made of nylon fishing line keep the distance between the glass plates fixed. The time resolution of the TOF MRPC is in the 50 ps range and the efficiency reaches 99.9 %.

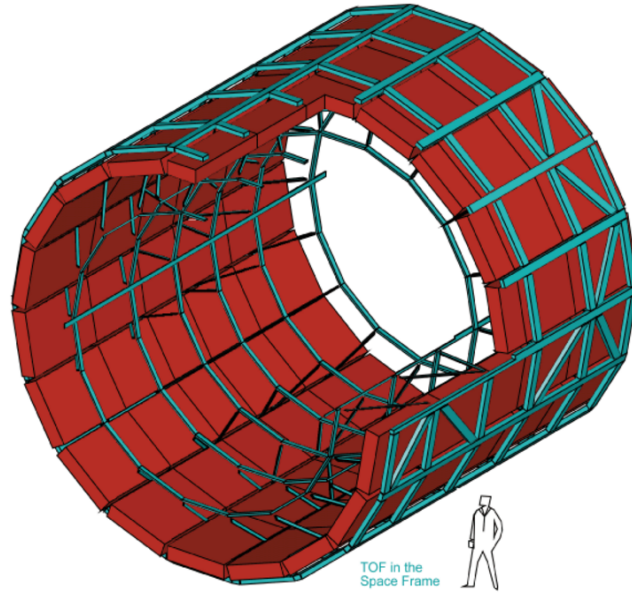


Fig. 3.5 : Schematic view of the Time-Of-Flight detector (TOF).

3.3.4 Forward Detectors (FWD)

A set of small forward detectors, installed at small angles to the beam, are used for timing information, trigger and centrality estimation. These include fast scintillators, calorimeters, Cherenkov and silicon detectors.

- **T0 Detector:** It consists of 2 arrays of PMTs equipped with Cherenkov radiators [110]. The arrays are installed on the opposite sides of the Interaction Point (IP), covering the pseudorapidity ranges: $-3.3 < \eta < -2.9$ and $4.5 < \eta < 5$. The main task of T0 is to supply fast timing signals which will be used in the L0 trigger for ALICE, to send a signal to activate the TRD and to deliver collision time reference for the Time-of-Flight (TOF) detector. The time resolution of T0 is better than

50 ps (σ). The triggering efficiency varies from about 50% for pp collisions up to 100% for A–A collisions. T0 is also used to give a fast evaluation of the multiplicity using a pre-programmed 3-grade scale (minimum bias, central and semi-central).

- **FMD:** It consists of 51,200 silicon strip channels distributed over 5 ring counters of two types which have 20 and 40 sectors each in azimuthal angle, respectively [110]. The main function of the FMD system is to provide (offline) precise charged particle multiplicity information in the pseudorapidity range $-3.4 < \eta < -1.7$ and $1.7 < \eta < 5.0$. The FMD will also allow the study of multiplicity fluctuations on an event by event basis.
- **V0 Detector:** The V0 detector consists of two arrays of scintillator counters (named V0A and V0C), installed on both sides of the ALICE collision vertex at small angles [110]. The V0A device is installed on the positive z-direction at a distance of about 340 cm from the interaction point (IP), while the V0C is installed on the negative z-direction along the absorber nose at a distance of 900 mm from the IP. The counters cover the pseudorapidity ranges $2.8 < \eta < 5.1$ (V0A) and $-3.7 < \eta < -1.7$ (V0C). Each array consists of 32 counters distributed in 4 rings. Each of these rings covers 0.5 - 0.6 unit of pseudorapidity and is divided into 8 sectors (45 degrees) in azimuth. This detector system has several functions. It provides minimum-bias (MB) triggers for the central barrel detectors in pp and Pb–Pb collisions, it serves as centrality estimator via the measurement of charged particle multiplicity and is used to reduce the background of beam-gas interactions.
- **ZDC:** The Zero Degree Calorimeters (ZDCs) are hadronic calorimeters, made by a stack of heavy metal plates grooved to allocate a matrix of quartz fibers (called “spaghetti calorimeters”), which detect the energy of the spectator nucleons [111]. This is used to determine the overlap region of the two colliding nuclei, i.e. the centrality. It is composed of four calorimeters, two to detect protons (ZP) and two to detect neutrons (ZN). These are located 115 meters away from the interaction point on both sides, exactly along the beam line.

3.3.5 Other Detectors

The ALICE experiment, besides the main tracking and PID detectors already described in the previous sections, is composed of many other detectors which give complementary information or have been specifically dedicated to some particular analyses. The Transition Radiation Detector (TRD) [112] contributes to the tracking, particle identification,

and triggering capabilities of the experiment. It has been specifically designed to identify electrons and to trigger on high-momentum electrons. The detector is segmented into 18 sectors (corresponding to the TPC and TOF segmentation), of which only 13 were installed in Run 1, creating small charge asymmetries (see Section 6.2.1). Every super-module contains 6 layers of multi-wire proportional chambers, each of which is preceded by a radiator and a Xe/CO₂-filled drift volume. The particle identification is based on the specific energy loss of charged particles and additional transition radiation photons, the latter being a signature for electrons. During the Long Shutdown 1, the detector was completed and now covers the full azimuthal acceptance. The readout and trigger components have been upgraded.

The High Momentum Particle IDentification (HMPID) [113] system enhances the particle identification capabilities of ALICE beyond the momentum range allowed by the energy loss measurements (ITS and TPC) and by the TOF. The HMPID detector has been designed to extend the useful range for the identification of p and K up to 3 GeV/*c* and of p up to 5 GeV/*c*, on a track-by-track basis. It provides inclusive particle ratios and transverse momentum spectra in the region relevant in the study of phenomena connected with the pre-equilibrium stage of the nucleus-nucleus collisions.

Two electromagnetic calorimeters, EMCal and PHOS, are used to measure π^0 , η and to improve jet reconstruction by measuring their neutral components. The calorimeter produces also a fast, high- p_T trigger and improves existing ALICE capabilities to measure high-momentum electrons [114, 115].

A Forward Muon Spectrometer (FMT), made of a carbon and concrete absorber, tracking and trigger chambers, is dedicated to muon measurements [116]. The spectrometer acceptance allows the measurement of resonances down to zero transverse momentum. The invariant mass resolution is of the order of 70 MeV in the J/Ψ region and about 100 MeV close to the Υ .

3.4 Particle Identification (PID)

Particle identification (PID) consists of the methods and techniques used to select the particle species of interest (electrons in this analysis). These are based on the different signals produced by different types of particles in the detectors dedicated for this purpose. The electron identification in the ALICE central barrel used for this thesis work is based on the average energy loss measured by the ITS and TPC, and the time-of-flight measured by the TOF system.

3.4.1 PID Based on Energy Loss Measurements

The average energy loss per unit of path length of a particle traversing a medium depends on the properties of the medium and on the mass and momentum of the particle. For moderately relativistic charged particles ($0.1 < \beta\gamma < 1000$) heavier than electrons, which lose energy primarily by ionization and atomic excitation, the mean rate of energy loss can be parametrized by the Bethe-Bloch equation:

$$\left\langle \frac{dE}{dx} \right\rangle = K z^2 \frac{Z}{A} \frac{1}{\beta^2} \left[\frac{1}{2} \ln \left(\frac{2m_e c^2 \beta^2 \gamma^2 T_{\max}}{I^2} \right) - \beta^2 - \frac{\delta}{2} \right] \quad (3.1)$$

The variables used in this equation are defined in Table 3.2. The dependence on the particle species is contained in the term T_{\max} , which is given by:

$$T_{\max} = \frac{2m_e c^2 \beta^2 \gamma^2}{1 + 2m_e \gamma / M + (m_e / M)^2} \quad (3.2)$$

For electrons a different version of the Bethe-Bloch equation is used, which is valid in the highly relativistic regime:

$$\left\langle \frac{dE}{dx} \right\rangle = \frac{2Z\pi e^4}{m_e v^2} \left[\ln \left(\frac{m_e v^2 E}{2I^2 (1 - \beta^2)} \right) - (\ln 2) \left(2\sqrt{1 - \beta^2} - 1 + \beta^2 \right) + 1 - \beta^2 + \frac{1}{8} \left(1 - \sqrt{1 - \beta^2} \right)^2 \right] \quad (3.3)$$

Fig. 3.6 shows the average energy loss per unit path length measured in the ITS (left) and in the TPC (right) for particles produced in Pb–Pb collisions at $\sqrt{s_{\text{NN}}} = 2.76$ TeV as a function of the particle momentum. Different bands can be clearly seen, corresponding to the patterns defined by the Bethe-Bloch equation for different particle species, which are shown by the black lines.

The detector PID response is expressed in terms of deviations between the measured signal and the expectation for a given mass hypothesis, in units of the detector PID resolution (σ). For example, the PID response of the TPC, for the electron's mass hypothesis, is given by:

$$n\sigma_{\text{TPC}} = \frac{\langle dE/dx \rangle_{\text{meas}} - \langle dE/dx \rangle_{\text{exp}}(\text{elec})}{\sigma_{\text{elec}}^{\text{TPC}}} \quad (3.4)$$

Variable	Definition
m_e	electron's mass
c	speed of light
β	v/c
γ	Lorentz factor: $\frac{1}{\sqrt{1-\beta^2}}$
I	Mean excitation energy
N_A	Avogadro's number
r_e	Classical electron radius
K	$4\pi N_A r_e^2 m_e c^2$
z	Atomic number of the particle
Z	Atomic number of the absorber
A	Mass number of the absorber
δ	Density effect correction to ionization energy loss
T_{\max}	Maximum kinetic energy which can be imparted to a free electron in a single collision

Table 3.2 : Definitions of the variables used in the Bethe-Bloch equation (3.1).

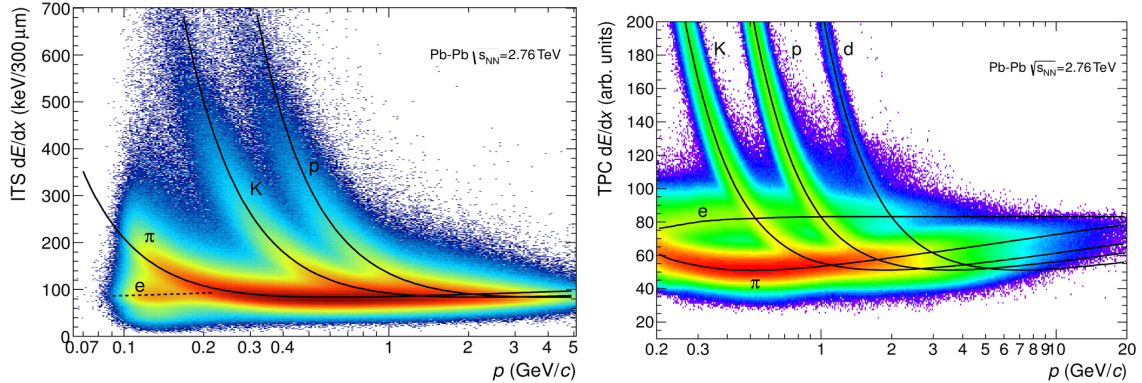


Fig. 3.6 : Mean rate of energy loss measured in the ITS (left) and in the TPC (right) for particles produced in Pb–Pb collisions at $\sqrt{s_{\text{NN}}} = 2.76$ TeV as a function of the particle momentum. The parametrizations given by the Bethe-Bloch equation for different particle species are represented by the black lines.

3.4.2 PID Based on Time-Of-Flight Measurements

The time-of-flight (t_{TOF}) measured by the TOF system, complemented with the measurement of the track length L and momentum p , provided by the tracking detectors, is used to calculate the particle mass:

$$m = p \cdot \frac{t_{\text{TOF}}}{L} \sqrt{1 - \frac{L^2}{c^2 t_{\text{TOF}}^2}} \quad (3.5)$$

The procedure which is actually used in ALICE is to compare the time-of-flight measured by the TOF for a given track with the expected values obtained using different mass hypotheses for the particle. The difference between the measured and the expected time-of-flight for a given mass hypothesis is expressed, as usual, in units of σ . For example, assuming the electron mass:

$$n\sigma_{\text{TOF}} = \frac{t_{\text{meas}} - t_{\text{exp}}(\text{elec})}{\sigma_{\text{elec}}^{\text{TOF}}} \quad (3.6)$$

Fig. 3.7 shows the velocity of particles, normalized to the speed of light (β), as a function of the particle momentum measured in Pb–Pb collisions at $\sqrt{s_{\text{NN}}} = 2.76$ TeV. Different bands correspond to different particle species, as indicated in the figure.

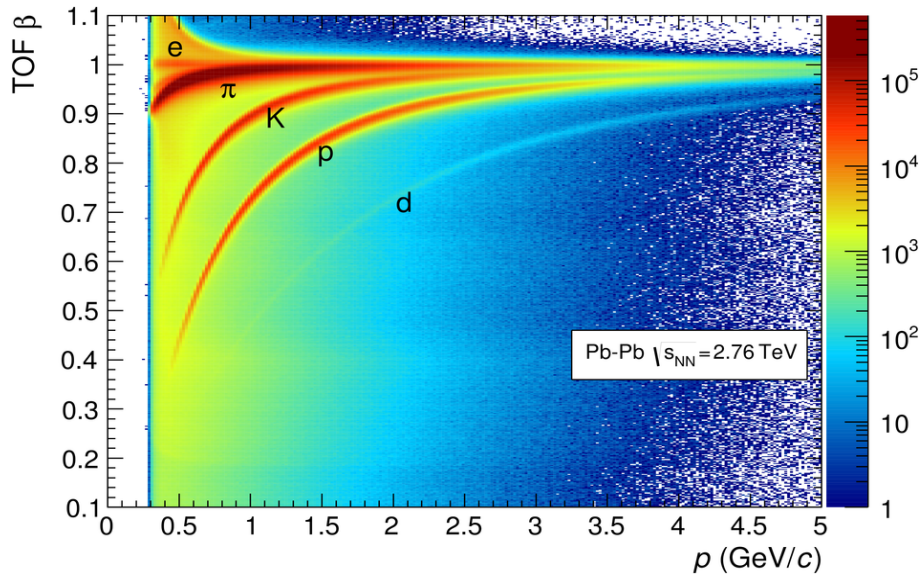


Fig. 3.7 : Particle velocity (β) as a function of momentum measured in Pb–Pb collisions at $\sqrt{s_{\text{NN}}} = 2.76$ TeV.

3.5 Analysis Framework

The software used for data reconstruction, simulation and off-line analysis is an Object-Oriented ROOT-based framework, written in the C++ programming language. The software is divided into two main substructures:

- **AliROOT:** This is the core of the software which contains the ROOT fundamental libraries and the ALICE specific libraries and tools used for data reconstruction, simulation and analysis.

- **AliPhysics:** This is the analysis-oriented part of the framework, which contains specific user analysis tasks and more complex and structured packages used by the analysis groups.

ALICE data and the output of simulation are published and made available for the analyzers by ALIEN (ALICE ENvironment) via the GRID infrastructure. This is a network of thousands of computers and computer clusters, connected via the internet, holding a limited amount of data and used to run the analysis tasks producing small output files, which are eventually merged together by the virtual analysis manager. This infrastructure has been created in order to efficiently handle huge amounts of data which would be impossible to store and analyze using one single computer. The data analysis proceeds in parallel on the computers connected to the GRID. These are placed at different locations in research institutes and universities, making the process much faster and less demanding in terms of computer resources and memory consumption since each computer handles only a fraction of the total amount of data.

3.6 Monte Carlo Simulations

Simulations are done using particle generators, which produce particles by simulating elementary processes or based of phenomenological hadronization models according to parametrized input distributions and particle ratios. Particle generators simulate also particle decays based on real measurements of their branching ratios. The particle generator widely used to simulate nucleus-nucleus collisions is HIJING (Heavy Ion Jet INteraction Generator) [117]. This combines a QCD-based model of jet production with the Lund string fragmentation model. A nucleus-nucleus collision is regarded as a superposition of multiple nucleon-nucleon collisions, with no collective effects, in which parton shadowing effects are also taken into account. Stable particles or long-lived decay products of the generated particles are "transported" through the detector, simulating all processes which characterize the interaction between particles and the detector material, including ionization, excitation, bremsstrahlung or other physical processes such as photon conversion in the material or absorption. The propagation of particles through the detector, in the ALICE magnetic field, is simulated by GEANT 3. The energy deposited by the simulated particles in the active elements of the detector is converted into digits, which are ADC counts, produced considering the real energy thresholds measured in the calibration and testing phase of the detectors during their construction and assembling. The signals produced by simulated particles traversing the experimental apparatus are treated on the same footing as real raw data, which are then reconstructed

by the offline framework. Dead or noisy channels and blind areas of the detectors are also taken into account during the reconstruction phase, in order to reproduce the detector status in the simulation on a run-by-run basis. The output of the simulation contains reconstructed tracks and their measured properties, such as momentum and PID signals, together with the information on the real kinematics of the particles that have produced them.

Chapter 4

Data Acquisition and Event Reconstruction

4.1 ALICE Data Acquisition (DAQ)

Collisions between oppositely circulating particles at the LHC occur at higher energies and rates than ever before. The amount of charged particles produced in high-energy collisions increases as a function of the center-of-mass energy of colliding particles (Fig. 1.27), thus a larger number of particles is created at the LHC energies. These particles travel through the detectors and produce several signals which are then used in the reconstruction of their trajectories and in the particle identification. Due to a larger geometrical coverage, more complex and sophisticated composition and finer granularities of modern particle detectors, larger numbers of signals are produced for each particle, thus the LHC experiments at CERN generate colossal amounts of data, corresponding to roughly 30 petabytes every year [118]. In order to efficiently cope with such a huge wealth of information, the LHC experiments have developed highly advanced data handling technologies, which includes high efficiency trigger, data acquisition systems and data archive.

The ALICE experiment, when running in heavy-ion mode, needs a storage capacity of up to 1.25 GByte/s [119], which by far exceeds that of the current generation of experiments (Fig. 4.1). ALICE needs a flexible data acquisition system capable of handling high rates of low multiplicity pp collisions, ranging from $\mathcal{L} = 10^{29} \text{ cm}^{-2} \cdot \text{s}^{-1}$ (during minimum bias data taking) to $\mathcal{L} = 10^{31} \text{ cm}^{-2} \cdot \text{s}^{-1}$ (when accumulating rare triggers) and lower rates of more "crowded" Pb–Pb events ($\mathcal{L} = 10^{27} \text{ cm}^{-2} \cdot \text{s}^{-1}$), which produce tens of thousands of charged particles.

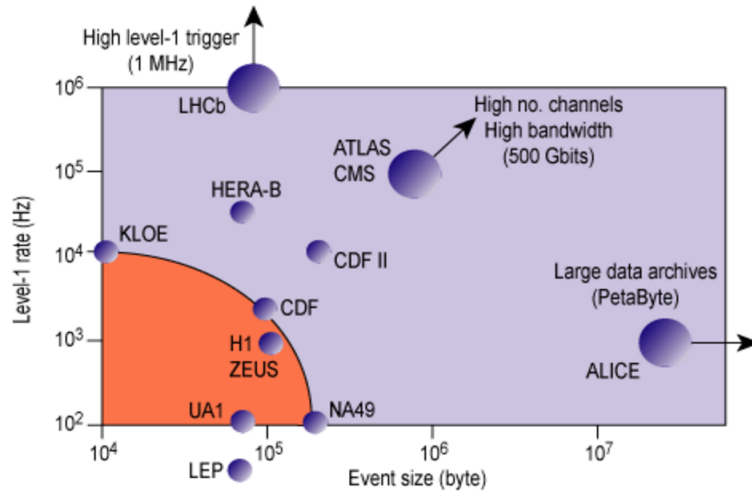


Fig. 4.1 : Data storage capacity of the ALICE experiment compared to that of other high energy experiments.

The ALICE data acquisition is schematically sketched in Fig. 4.2. At every bunch crossing the *Central Trigger Processor* (CTP) receives the signal from the triggering detectors and decides, within less than $1 \mu\text{s}$ from the collision, whether to collect the data from the collision event and sends its decision to each detector's *Front End Electronics* (FEE) via the *Detector Data Links* (DDL). In the case of a positive decision, the data collected by each subdetector are sent to a cluster of 300 computers, called *Local Data Collectors* (LDC). After a check of their integrity, data are processed and assembled into subevents and sent over the second layer of computers, the *Global Data Collectors* (GDC). This is a cluster of 40 computers which are responsible for the "event construction", i.e. each of these computers receives the event fragments by the LDC and builds a full event, which is sent to a temporary storage site in the experimental pit called *Local Data Storage* (LDC). Data are afterward moved to the *Permanent Data Storage* (PDS) at the CERN computing center, and eventually published via the GRID infrastructure for the offline physics analysis.

4.1.1 The ALICE Trigger System

Virtually, all collision events contain physics information that can be extracted by the offline analysis. In reality, a fraction of events that would be registered by the data acquisition system cannot be used because, for several reasons, they do not fulfill some quality requirements or do not have specific features for the offline analysis. The trigger is a system which decides whether to collect data from a given collision event according to some specific criteria. The role of the trigger is to reduce the amount of data to be

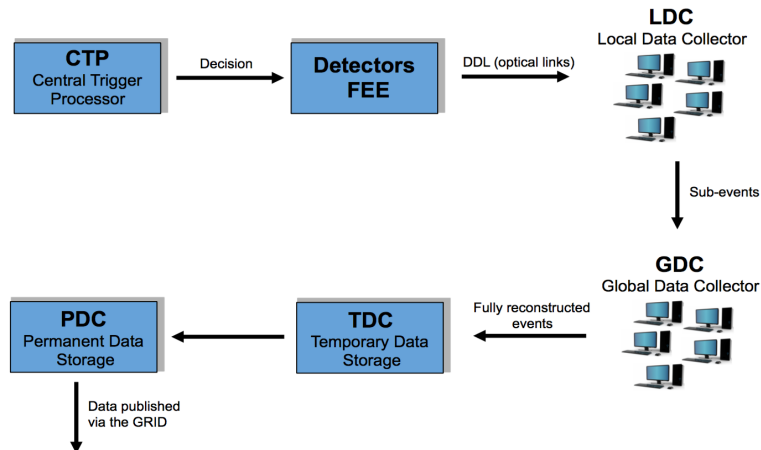


Fig. 4.2 : Schematic sketch of the ALICE data acquisition system (DAQ).

handled by the DAQ system by applying on-line filters which reject not interesting events before they are registered on tape. This is needed not only for a more efficient data recording but also to fit the available storage bandwidth, defined as the amount of data that can be transmitted in a given amount of time.

The *Central Trigger Processor* (CTP) represents the brain of the trigger system, i.e. the one who takes the decisions. It receives the trigger input from the triggering detectors and sends the trigger signal (accept or reject) to the readout system of the detectors via the *Local Trigger Unit* (LTU), which is the interface between the CTP and the readout system. The ALICE trigger system is a three-level system: the CTP can receive up to three consecutive trigger inputs (called L0, L1 and L2) and to each of them it can respond by sending trigger signals to the readout system. The second and the third trigger inputs are sent by the triggering detectors after further checks have been executed on-line and accepted by the CTP. The first decision is made at $1.2 \mu\text{s}$ after the event (L0), L1 decision comes after $6.5 \mu\text{s}$ and L2 trigger is issued after $88 \mu\text{s}$.

4.1.2 The High Level Trigger

The data flow that passes the L2 trigger can easily reach up to 25 GByte/s. This can be further reduced by the *High Level Trigger* (HLT) [120] to about 1.25 GByte/s, i.e. by well over one order of magnitude. The HLT receives a copy of the data that are sent to the DAQ by the CTP (after passing the L2 trigger) and does a full on-line event reconstruction using a large farm of computers made up of 1000 multi-processor nodes. The data are sent to several processing layers and analyzed on-line using automatic algorithms for specific pattern recognition (track finding, jet reconstruction, etc.). The results are eventually forwarded to the final stage for the trigger decision. The size

of selected events is reduced by using advanced data compression techniques, based on Huffman encoding [121], without losing the physics information contained in the event. It's worth to clarify that the main role of the HLT is the reconstruction of high momentum tracks (using fast but less precise tracking algorithms), mainly used in jet analyses. Events which are not pre-processed by the HLT are anyhow registered on tape. During the Pb–Pb data taking in 2011 the HLT was used to reduce the event size by storing the cluster information from the TPC instead of raw data in order to fit the available bandwidth of the connection to mass storage. In fact, the TPC is the main contributor to the ALICE data volume.

4.2 Offline Event Selection

The role of the offline event selection is to select the hadronic component of nucleus-nucleus interactions, excluding diffraction, by rejecting the machine-induced and physical background. The main components of the machine-induced background are represented by beam-gas inelastic interactions, where ions in the beam collide with residual molecules of gas inside the beam pipe, and interactions between the beam halo¹ with mechanical structures in the machine. This background component represents almost 25% of all selected events. The physical background is essentially represented by electromagnetic processes, where the electromagnetic field of one nucleus interacts with charged particles inside the other nucleus.

4.2.1 Machine Induced Background (MIB)

Beam-gas collisions can be rejected using the timing information from the VZERO detectors. These are two arrays of scintillators placed at different distances on either side of the interaction point along the beam axis (see Section 3.3.4). The bunch spacing (25 ns) is tuned such that two ion bunches cross at the geometric center of the ALICE experiment. During the crossing of two bunches, the following bunches are approaching the collision point from either side of the beam. Inelastic collisions can occur between these bunches and residual molecules of gas inside the beam pipe away from the nominal position of the interaction point. Such a collision produces a signal in the same side VZERO that is "too early" in time with respect to the signal coming from a beam-beam collision happening at $z = 0$ (Fig. 4.3). The timing information from VZERO is used to set its time gate to trigger on beam-beam collisions.

¹peripheral low-density region of the bunch of particles in the beam.

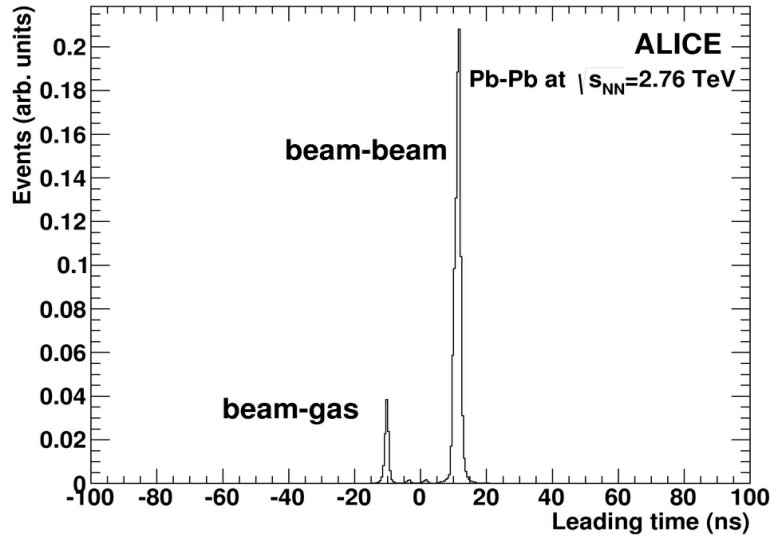


Fig. 4.3 : Time distribution of the signals in the VZERO detector on side A [122]. The peaks corresponding to beam-beam and beam-gas collisions are clearly visible.

Another source of machine-induced background are *parasitic collisions* involving debunched ions. The frequency of the RF accelerating cavities has to be an integer multiple of the revolution frequency for the particle to always see an accelerating electric field:

$$\nu_{\text{RF}} = N \cdot \nu_{\text{rev}}$$

The number N defines the number of RF buckets which can contain clumps of particles. Not all RF buckets are filled with ions, but usually several buckets are never loaded with particles to form a gap in the circumference. The purpose of this gap is that in the dump process it takes a short, but significant time to switch on the magnets which divert the beam from the LHC into the beam dump. During the circulation of the beams inside the LHC ions can "jump" from a full bucket to a supposedly empty bucket. In the bunch crossing region collisions can happen between ions in the "full" bucket and ions in an "empty" bucket, that is displaced by one or more RF cycles. These collisions are displaced along the z -axis and only part of the event would be visible to the detector. These parasitic collisions can be rejected exploiting the correlation between the sum and the difference between the times measured in the neutron ZDCs (Fig. 4.4).

These satellite collisions can also be rejected by a cut on the reconstructed vertex z -coordinate since they happen well outside the fiducial region $|z_{\text{vtx}}| < 10$ cm. This cut is normally used in most of the analyses in order to guarantee uniformity in the detector response and avoid edge effects.

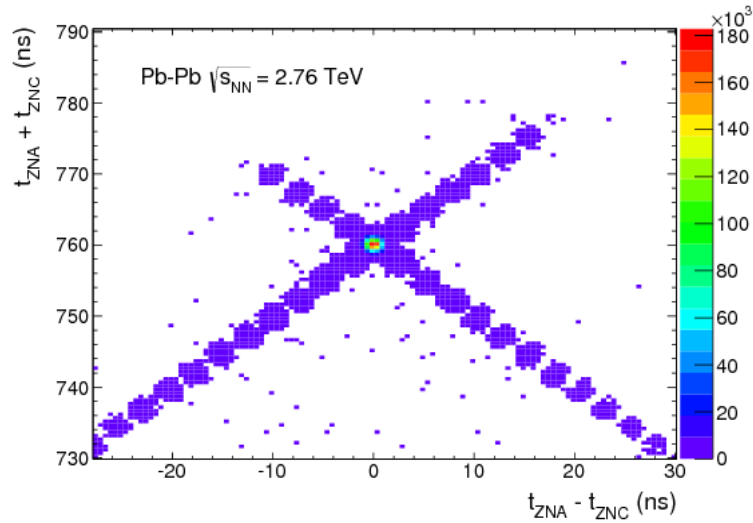


Fig. 4.4 : Correlation between the sum and the difference of times recorded by the neutron ZDCs on either side of the interaction region [122]. The large cluster in the middle corresponds to collisions between ions in the nominal RF buckets of each beam, while the small clusters along the diagonals (spaced by 25 ns in the time difference) correspond to collisions in which one of the ions is displaced by one or more RF buckets.

4.2.2 Physical Background

The cross section for electromagnetic (EM) processes at the LHC is very large (of the order of kbarn [122]), since it scales as the atomic number squared (Z^2). EM processes consist of photon-photon interactions, relevant only in ultra-peripheral collisions (see Section 4.4 for the definition of collision centrality) and photon-nucleus interactions, which produce low multiplicity events of soft particles. This second class of processes is also relevant only in peripheral collisions.

4.3 Reconstruction And Data Format

The data collected by the experiment contain all the necessary information for the reconstruction of the collision events in the format of *digits* (ADC counts) structured in ROOT trees. Such a data format, called *raw data*, cannot be directly used in the analysis and needs to be processed in a first reconstruction pass. As a preliminary step, a local reconstruction takes place in each subdetector independently, i.e. without exchanging information with other subdetectors. During this stage, called *clusterization*, the digits are converted into *clusters*, which are sets of adjacent digits coming from the same active element of a detector presumably produced by the same particle. Clusters are then used for the track and vertex reconstructions (see Section 4.6). The output

of the reconstruction framework is the *Event Summary Data* (ESD) which contains all information for the physics analysis. This is also structured in ROOT trees. ESDs contain all reconstructed tracks including their kinematic variables, secondary vertices, calibrated particle identification signals and global event properties. ESDs usually contain a lot more information than really needed, and running on these files makes the analysis more time consuming and more demanding in terms of computing resources. To make the data analysis faster and more efficient the information contained in the ESDs is filtered, retaining only the necessary variables and rejecting the redundant information. The files resulting from re-filtering of the ESDs are called *Analysis Object Data* (AOD) and approximately five times smaller in size than the original ESDs (see Table 4.1). Most of the analyses use AODs as input files, which is the recommended data format for any official analysis within the ALICE Collaboration. Nevertheless, some analyses, including the work for this thesis, use ESDs as input files since they are based on some particular variables which have not been transferred to AODs during the re-filtering. The usefulness and importance of some of these variables, missing in the AOD files, has been demonstrated in the present work and these variables will be included in the AODs productions in the next data taking.

The detector responses, and particularly the signals used for particle identification, usually need to be recalibrated after the first reconstruction pass. This is due to non-uniformity of the experimental apparatus, space charge effects in the TPC, distortions, etc.

Parametrized corrections of detector response are obtained, run by run, by a careful and detailed offline analysis. The reconstruction of raw data is repeated by implementing these corrections to get a new version of ESDs (and AODs by re-filtering), which will contain correctly recalibrated detector responses. This second reconstruction of raw data is called *reconstruction pass 2*. Sometimes additional recalibration or correction of detector responses are needed after the reconstruction *pass 2*, which lead to *pass 3*, *pass 4*, etc. The results of this thesis are based on reconstruction *pass 2* of the Pb–Pb data of the period LHC11h.

	Raw Data	ESD	AOD
Size (TB)	767.41	367.86	83.55

Table 4.1 : Data formats and their total size in Pb–Pb collisions at $\sqrt{s_{\text{NN}}} = 2.76$ TeV (period LHC11h).

4.4 Collision Centrality

Atomic nuclei are extended objects whose typical size is of the order of few fm. A collision between two nuclei, moving towards each other in opposite directions, can have different geometrical configurations based on the impact parameter b , defined as the distance between the directions of motion of the two approaching nuclei (Fig. 4.5). Nucleons involved in the collision are called *participants* or *wounded* nucleons, while the others are called *spectators*.

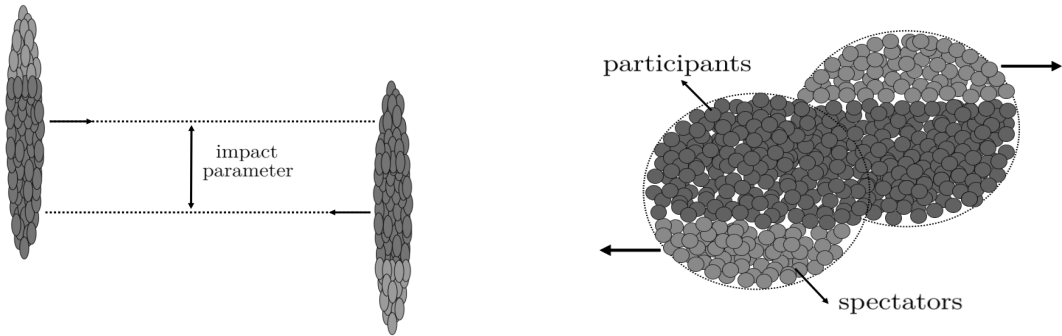


Fig. 4.5 : Schematic sketch of two nuclei moving in opposite directions towards each other. The distance between the directions of motion of the nuclei defines the impact parameter. Nuclei appear stretched because of the strong Lorentz contraction.

Collisions with small impact parameter ($b \approx 0$ fm) are referred to as *central collisions*, while those with large impact parameter are called *semi-central* or *peripheral collisions*. The centrality of the collision, which is directly related to the impact parameter, is expressed in terms of percentage of the total nuclear interaction cross section:

$$c = \frac{1}{\sigma_{\text{tot}}} \int_0^b \frac{d\sigma}{db'} db' \quad (4.1)$$

Experimentally, it is impossible to directly measure the impact parameter, the number of binary collisions or the number of participant nucleons. Nevertheless, these quantities can be inferred using a geometrical model of nucleus-nucleus collisions based on the *Glauber model* [123]. Roy Glauber in the 1950's used the quantum mechanical scattering theory to describe multiple scattering in composite systems [124–126]. His work was found extremely useful in the calculation of total cross sections in p–A and A–A collisions and it's nowadays used to connect some microscopic geometrical quantities, like the impact parameter, to macroscopic experimental observables, thus representing the "theoretical magnifying glass" of heavy-ion and proton-ion collisions. Two observables directly related to the centrality are the average charged-particle multiplicity and the energy deposited in the forward calorimeters by the spectators, called *zero degree energy* (E_{ZDC}). While the

charged-particle multiplicity decreases monotonously with increasing impact parameter, the zero-degree energy does not always show a monotonous behavior with the impact parameter: nuclear fragments with the same magnetic rigidity as the beam particles could be formed in the collision. These particles move inside the beam pipe curved by the magnetic field together with the beam particles and therefore are not detected by the forward calorimeters. The monotonic relationship between b and E_{ZDC} holds only for the most central collisions. For this reason, the zero-degree energy is used as a reliable centrality estimator only when combined with another observable that is monotonically correlated with the impact parameter. Nuclear collisions in the Glauber model are treated as superpositions of independent nucleon-nucleon interactions, where the participating nucleons of the projectile move along straight lines while interacting with the nucleons of the target. The nucleon-nucleon interaction cross section is assumed to be constant and independent on the number of binary collisions. The nucleon position is described by the nuclear density function, expressed by the Woods-Saxon functional form:

$$\rho(r) = \rho_0 \frac{1 + w(r/R)^2}{1 + \exp(\frac{r-R}{a})} \quad (4.2)$$

In this expression, R is the nucleus radius parameter, a is the nuclear skin thickness² and w describes nuclei where the maximum density is reached for $r > 0$ fm. Based on what we know from low energy electron-nucleus scattering experiments, ^{208}Pb nuclei have a spherical shape, $R = (6.62 \pm 0.06)$ fm, $a = (0.546 \pm 0.010)$ fm and $w = 0$ [128]. The Glauber model is combined with a model that describes the particle production in nuclear collisions to simulate the charged particle multiplicity distribution in a given detector. The purpose is to create a connection between the simulation, where one has direct access to the geometrical quantities, and the experiment. From the comparison between the simulated and the measured distribution, after tuning the proper parameters, the geometrical quantities of the collision can be inferred.

Particle production in nuclear collisions is described by a two-component model [129, 130], where nuclear collisions are treated as superpositions of processes produced by soft and hard interactions. While particle multiplicity scales with the number of participants (N_{part}) in soft processes, it is proportional to the number of binary nucleon-nucleon collisions (N_{coll}) in the case of hard processes. The relative contribution of soft and hard processes is a free parameter of the model. Based on this model, particle

²length scale over which nuclear density drops from 90% to 10% of its maximum value. It indicates how quickly the nuclear density falls off near the edge of the nucleus.

production can be described in terms of *ancestors*, i.e. independently emitting sources of particles, whose number is given by:

$$N_{ancestors} = f \cdot N_{part} + (1 - f) \cdot N_{coll} \quad (4.3)$$

The particle multiplicity is parametrized by a *negative binomial distribution* (NBD):

$$P_{\mu,k}(n) = \frac{\Gamma(n+k)}{\Gamma(n+1)\Gamma(k)} \cdot \frac{(\mu/k)^n}{(\mu/k+1)^{n+k}} \quad (4.4)$$

which gives the probability of measuring n particles per ancestor, where μ is the mean multiplicity per ancestor and k controls its width. The particle multiplicity distribution is simulated using a large number of nuclear collisions for different values of the parameters of the particle production model. The experimental distribution is fitted with the NBD-Glauber using a minimization procedure to find the parameters that result in the smallest χ^2 . Fig. 4.6 shows the multiplicity distribution, expressed in terms of signal amplitudes, measured by the VZERO detectors fitted with the NBD-Glauber.

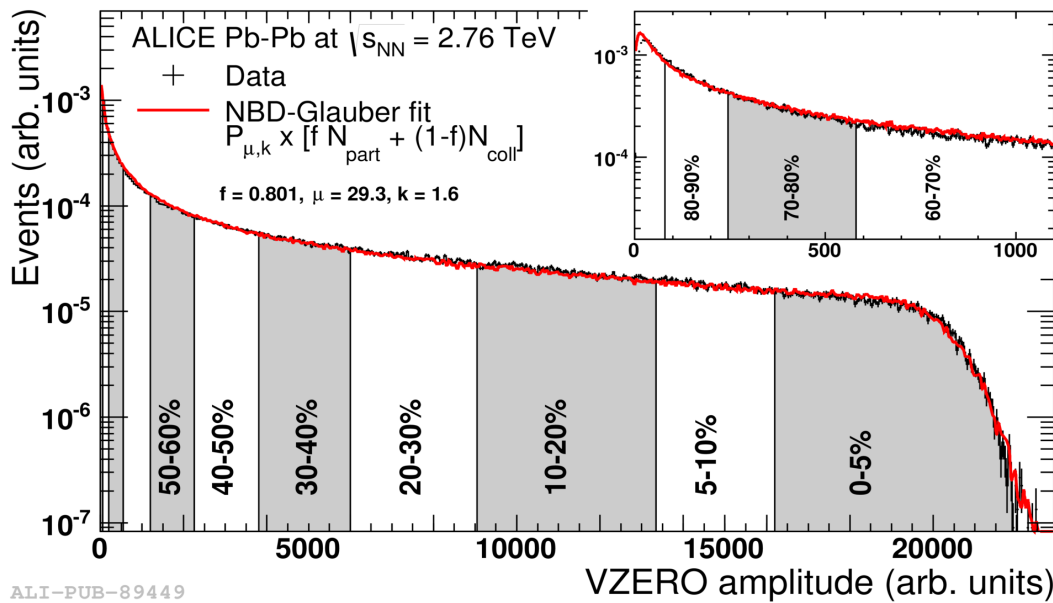


Fig. 4.6 : Distribution of amplitudes measured by the VZERO scintillators fitted by NBD-Glauber [122]. The centrality classes are indicated in the figure. The inset shows a zoom of the most peripheral region.

The centrality of the collision can be determined for any value of amplitude V_0 measured by the VZERO scintillators by integrating the amplitude distribution:

$$c = \frac{1}{\sigma_{tot}} \int_{V_0}^{\infty} \frac{d\sigma}{dV} dV \quad (4.5)$$

The centrality estimator used in this thesis is the average charged particle multiplicity measured in the VZERO detectors (VZEROA + VZEROC). This method results in the best resolution of the centrality measurement (Fig. 4.7).

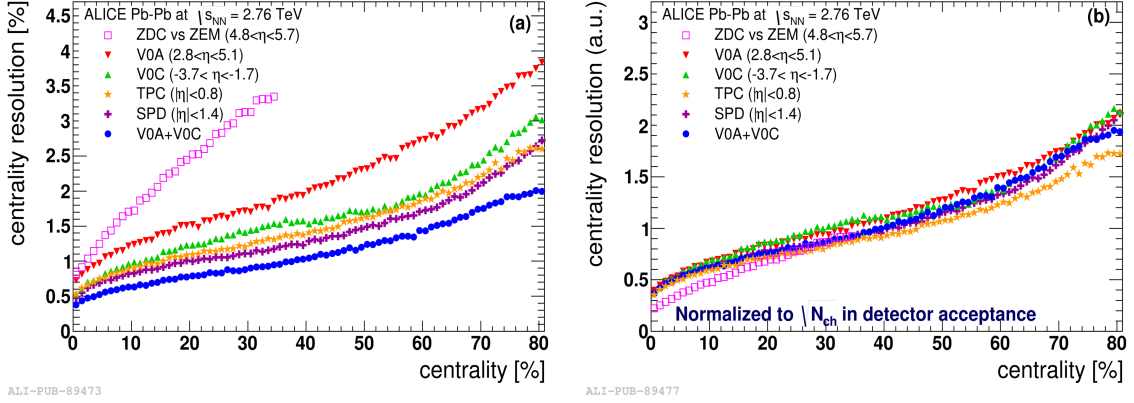


Fig. 4.7: Resolution in the centrality measurement for different centrality estimation methods (left). Resolution, in arbitrary units, scaled by $\sqrt{N_{ch}}$ measured in each detector (right) [122].

4.5 Reaction Plane

In semi-central collisions, the initial overlap region of the two nuclei has an elliptic shape. The impact parameter b and the direction of motion of the incoming nuclei (the z direction) define a plane, which is called *reaction plane* (Fig. 4.8).

The asymmetric spatial distribution of the hot and dense matter created in semi-central collisions is reflected in the angular distribution of the particles produced: more particles are emitted "in-plane" than "out-of-plane". This is due to the different pressure gradients, which drive the expansion of the system, in different directions of the ellipsoid: matter flows more along directions lying on the reaction plane due to a stronger push (Fig. 4.9).

The orientation of the reaction plane, called event plane angle Ψ_{RP} (Fig. 4.10), is expressed by the angle between the direction perpendicular to the reaction plane and the x -axis of the ALICE *global reference system* (going upward from the geometric center of the ALICE experiment).

The event mixing technique has been used in the present analysis to correct for the charge asymmetry in the combinatorial background estimation (see Section 6.2.2). In order to have similar momentum distributions only events with similar global features are mixed. Events are classified according to the z -coordinate of the vertex, the centrality of

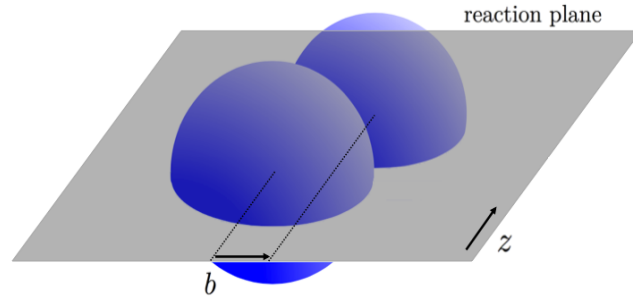


Fig. 4.8 : Schematic sketch of a semi-central collision in the center of mass system. The reaction plane is defined by the impact parameter b and the direction of motion of the two nuclei (z direction)

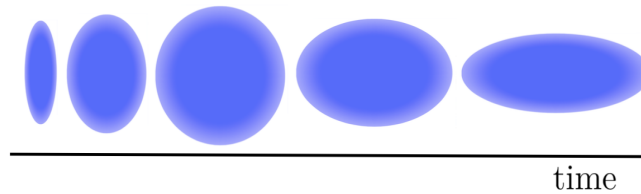


Fig. 4.9 : Schematic representation of the fire-ball evolution in semi-central collisions. The stronger push along the semi-major axis produces the asymmetric expansion of the system. The scale on this sketch is arbitrary

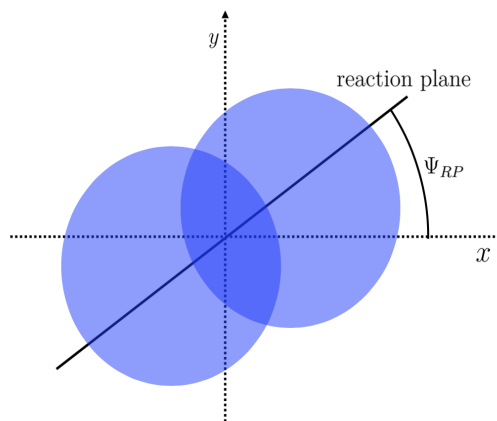


Fig. 4.10 : Orientation of the reaction plane.

the collision and the event plane orientation. Indeed, events with the same centrality and z -vertex position but with different event plane orientations result in different azimuthal

distributions of the particles produced and, due to geometrical asymmetries in the detector acceptance, cannot be regarded as "similar".

In semi-central collisions, the two colliding nuclei come into contact only partially. The regions of the nuclei which do not interact, containing the spectator nucleons, continue to move along their original direction (along the z axis) after the collision (Fig. 4.11)

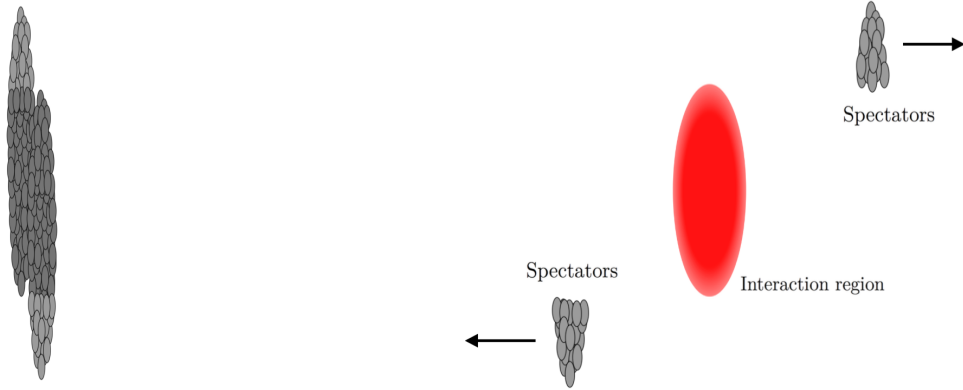


Fig. 4.11 : Schematic representation of a semi-central collision: the spectator nucleons, which do not participate into the collision, continue to move along the z axis.

The spectator nucleons can be measured using the neutron zero degree calorimeters (ZDC). These detectors are segmented into 2×2 towers and are located on either sides of the interaction point at a distance of about hundred meters (see Section 3.3.4). The orientation of the reaction plane can be measured by the \vec{Q} vector:

$$\vec{Q} = \frac{\sum_{i=1}^4 \vec{r}_i \cdot E_i}{\sum_{i=1}^4 E_i} \quad (4.6)$$

where \vec{r}_i is the position of the center of the i^{th} cell with respect to the geometrical center of the calorimeter, and E_i the energy measured in that cell. A recentering is necessary to account for beam displacements:

$$\vec{Q}' = \vec{Q} + \langle \vec{Q} \rangle \quad (4.7)$$

The direction of the impact parameter is given by the difference of the two \vec{Q} vectors measured on the A-side and C-side of the ZDCs.

4.6 Central Barrel Tracking

Track finding in a very high track density environment is one of the most challenging tasks of the ALICE experiment [131]. Tracking in the ALICE central barrel is based

on an inward-outward-inward propagation scheme which starts with the preliminary determination of the collision vertex using the inner tracker (ITS). Tracks are first reconstructed in the outer regions of the TPC, which is the main tracking detector, and are propagated inward to the ITS. Then tracks are propagated back from the ITS to the outer layers of the TPC and extended further to match the outer detectors. Eventually, tracks are refitted inward down to the point of closest approach to the interaction vertex. Once tracks are reconstructed, the position of the primary vertex is determined with higher precision using fully reconstructed tracks. The determination of secondary tracks (originating from displaced vertices) and cascades concludes the tracking procedure in the central barrel. The steps of track reconstruction are described in further details in this section.

4.6.1 Preliminary Vertex Determination

The primary vertex is the point³ where the collision occurs and from which the particles produced in the collision emerge. A preliminary determination of the primary vertex position can be done, already with quite high precision, using the SPD *tracklets*. These are defined as straight lines connecting pairs of clusters in the SPD layers, one cluster in each layer. The primary vertex is the space point where the maximum number of tracklets converge. This measurement is based on the straight line approximation of the particles trajectories. This is justified by the proximity of the two innermost layers of the ITS which makes the deviation between a curved and a straight trajectory negligible also for low momentum particles.

Particles produced in the collision, together with their decay products due to strong and electromagnetic interactions, are referred to as "*primary particles*", while those produced by weak decays of primary particles or created in the interaction between particles and the detector material are called "*secondary particles*". These definitions strictly depend on the tracking capabilities of the ALICE detector, including the resolution in the measurement of the primary vertex.

4.6.2 TPC Seed Finding

Track reconstruction begins in the outer regions of the TPC where the track density is the lowest. The first step in the tracking procedure and the most time-consuming is the

³It's not a point in its strictly geometrical sense. A collision between two Pb nuclei happens in an extended region of space with a radius of few fm. The interaction region is anyhow smaller than the typical distances traveled by particles so that it can safely be referred to as a point.

seed finding. Track seeds are sets of a few neighbor clusters, located in the outer layers of the TPC, roughly compatible with a track, i.e. lying on a helix pointing roughly to the primary vertex. One of the most common algorithms used for seed finding is the combinatorial seeding [132]. This method searches for all pairs of clusters in the outer regions of the TPC, separated by few pad rows (usually no more than 20), compatible with a helix which can be projected down to the primary vertex. The main steps of the algorithm are as follows:

- Loop over all clusters in the i^{th} pad row of the TPC.
- Loop over all clusters in the j^{th} pad row, $n \leq 20$ rows closer to the inner wall of the TPC, within a given window defined by the curvature of a track with minimum momentum above a certain threshold pointing down to the main vertex. Track parameters and their corresponding covariance are calculated using the errors on the points and the uncertainty on the position of the primary vertex. This is the only step where a vertex constraint (not too strong) is applied. In the following tracking procedure, tracks are allowed to have any impact parameter at the primary vertex, both along the z direction and in the transverse plane.
- Using the calculated helix parameters and their covariance matrix the Kalman filter is applied starting from the outer cluster in the TPC to the inner one to find the clusters to be associated with the track. The Kalman filter is a simultaneous track recognition and reconstruction algorithm, which offers a natural way to take into account multiple scattering, the magnetic field inhomogeneities and energy loss. It allows the reconstruction of complicated decay topologies (such as cascades) and it provides an efficient way to match tracks between different detectors.
- If at least 50% of the potential clusters are correctly associated with a track candidate, the track is saved as seed.

The procedure is schematically sketched in the following figure (Fig. 4.12)

4.6.3 Track Reconstruction

Track seeds are propagated inward following the helical trajectory defined by the initial track parameters. Whenever a cluster, which satisfies a proximity cut, is associated with the existing track, the track parameters and their corresponding covariance matrix are updated. The cluster association criterion takes into account the energy loss and the Coulomb multiple scattering suffered by the particle for every track segment. These

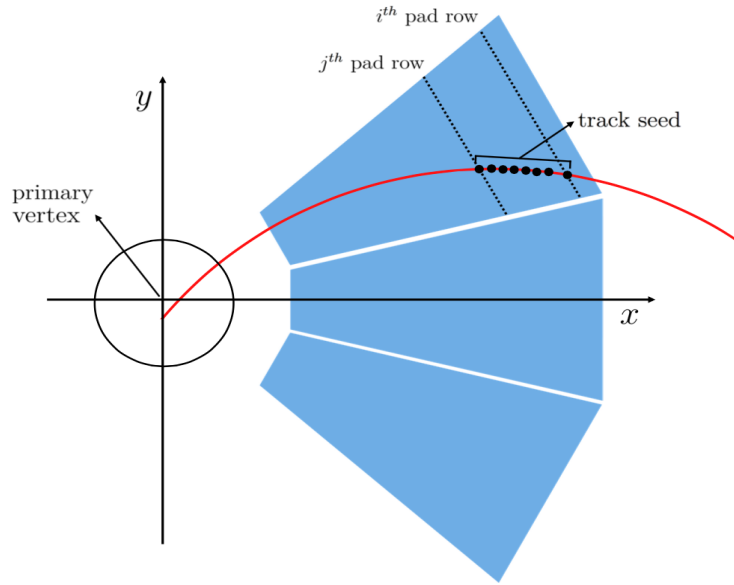


Fig. 4.12 : Schematic view of the combinatorial seeding algorithm.

effects produce small variations in the track curvature. The particle mass, needed to calculate these corrections, is assigned based on the specific energy loss measured by the TPC and the track momentum. In case the information is not conclusive (especially at high momentum) the pion mass is assigned. Once the tracking in the TPC is complete the algorithm does a preselection of the tracks checking some quality criteria. Tracks with less than 20 clusters and those missing more than 50% of the clusters expected for that track are rejected. If two tracks share a significant amount of clusters in the TPC (between 25% and 50%, depending on their momentum) the worse track, in terms of some quality parameters, is discarded. Tracks fulfilling these criteria are propagated further down for matching with the ITS. Track extrapolation to the ITS is a delicate task because the distance between the inner wall of the TPC and the outer layer of the ITS is rather large (~ 0.5 m) and the track density in the ITS is usually so high that there are always several clusters within the prolongation window defined by the multiple scattering. This is also the case between two ITS layers. This leads to a non-negligible probability of wrong cluster-track matching if just the criterion of minimal χ^2 is applied. For this reason, several prolongation hypotheses are built starting from clusters lying on the outermost layer of the ITS which give a χ^2 below a given threshold, and not just the one with minimal χ^2 .

Tracking in the ITS is performed in two passes, with and without the vertex constraint. Each track candidate is propagated down and, at each ITS layer, several further prolongation hypotheses are built considering all clusters within the window defined by

multiple scattering. In summary, for each track entering the ITS from the TPC there is a "tree" of possible extensions, and the most probable candidate is eventually selected based on the quality of the whole track (Fig. 4.13).

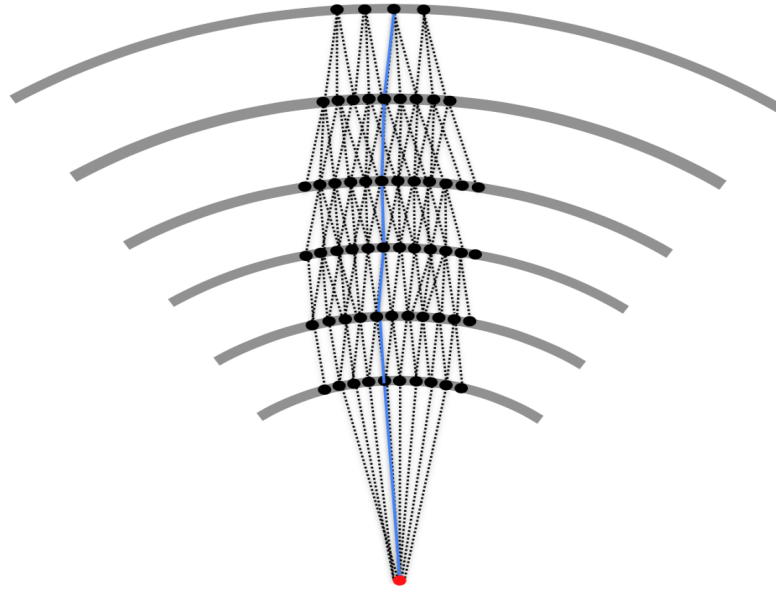


Fig. 4.13 : Schematic representation of the ITS tracking. Several prolongation hypotheses are made at each layer considering all hits within the window defined by multiple scattering. The best track candidate (shown in blue) is chosen among the possible branches based on the quality of the whole track.

When the ITS tracking is complete, all tracks are extrapolated to their point of closest approach to the primary vertex, and the back-propagation starts. Tracks are refitted by the Kalman filter in the outward direction using the points already associated at the previous stage. During the outward propagation, the track length integral and the time-of-flight for 5 particle hypotheses (electrons, muons, pions, kaons and protons) are updated at each step. When the back-propagation in the TPC is complete, the track is extended outward to match a tracklet in the TRD and a cluster in the TOF. At this stage, the track length integration and the computation of the time-of-flight stops. The track is then propagated further out to match (possible) clusters in the EMCAL, HMPID and PHOS. The detectors located at radii larger than the TPC are not used to update the track parameters but only for particle identification purposes. The final stage of track reconstruction is the inward propagation and refit of the data points already found, starting from the outer layers of the TPC to the point of closest approach to the primary vertex. At this stage the track parameters, their covariance matrix and the curvature are determined.

4.6.4 Final Vertex Determination

Global tracks, reconstructed in ITS and TPC, are used to find the position of the interaction vertex with higher precision compared to the procedure based on the SPD tracklets. Tracks are extrapolated to the point of closest approach to the nominal position of the beam line and the far outliers are removed. The distributions of the coordinates of the points of closest approach are then fitted using proper weights for the tracks to further reduce the contribution from tracks with large DCA. In low multiplicity events, to improve the precision in the determination of the transverse vertex position, the nominal beam position is also added as an independent fit parameter with errors corresponding to the transverse spread of the beam.

4.6.5 ITS Standalone Tracking

The tracking efficiency drops sharply at low momentum due to multiple scattering and energy loss (see Fig. 10.2). In order to improve the tracking capability at low momentum, an ITS standalone tracking procedure is performed using those ITS clusters not associated with any global track. The helical seeds for this algorithm are built using two clusters from the three innermost layers of the ITS and the primary vertex. Tracks are propagated to the other layers associating hits found within a proximity cut. As a final step, all clusters found are refitted using the Kalman filter from the outermost layer of the ITS down to the primary vertex. The clusters associated with a reconstructed track are removed from further searches. The ITS standalone tracking enables the reconstruction of tracks down to $p_T \sim 80 \text{ MeV}/c$ [122]. This kind of "ITS tracklets" can be used for the photon conversion rejection using the pre-filter approach (see Chapter 5).

4.6.6 Tracking Performances

The tracking efficiency as a function of transverse momentum is shown in Fig. 10.2. This is defined as the ratio between the reconstructed tracks and the generated primary particles in the simulation. The sharp drop at low p_T is due to the energy loss in the detector material which causes the particles to spiral down because of their small curvature radius in the magnetic field. These low momentum particles do not leave enough clusters in the TPC for the reconstruction. The behavior at higher p_T is determined by the cluster loss in the dead zones between active sectors in the TPC. The tracking efficiency is almost independent on the occupancy, showing no substantial difference between different colliding systems and centralities. Fig. 4.15 shows the ITS-TPC matching efficiency as a function of p_T in Pb–Pb collisions at $\sqrt{s_{NN}} = 2.76 \text{ TeV}$ for different requirements in the

ITS. The fraction of tracks with at least one fake cluster in the ITS in the most central collisions (0-5%) is about $\sim 7\%$ at $1 \text{ GeV}/c$ and drops below 2% at $10 \text{ GeV}/c$. This is mostly due to the very high track density in the ITS.

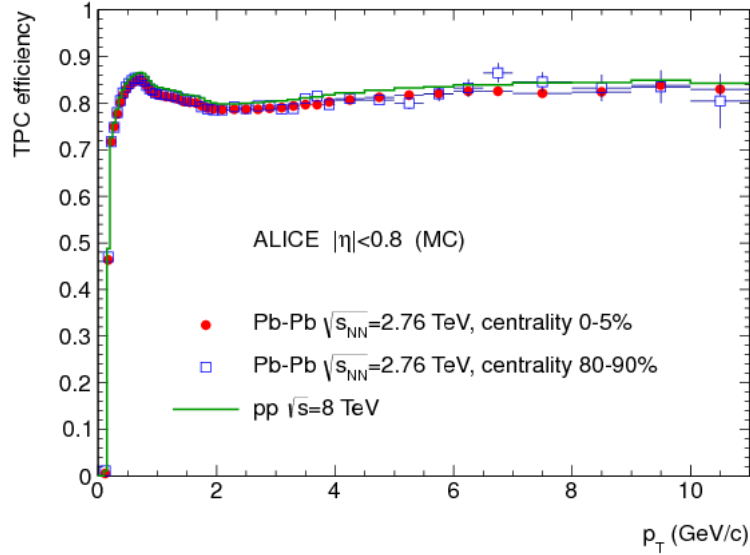


Fig. 4.14 : Tracking efficiency as a function of p_T for pp and Pb–Pb collisions (simulation). The tracking efficiency does not depend on the detector occupancy.

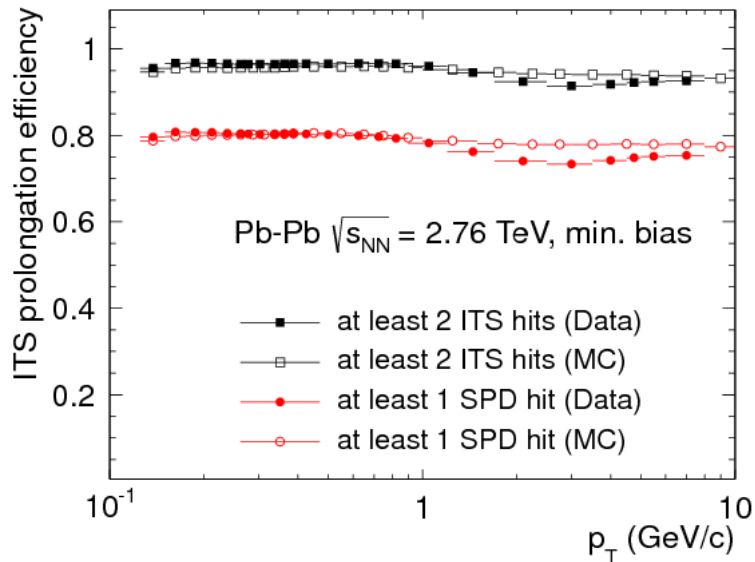


Fig. 4.15 : ITS-TPC matching efficiency as a function of p_T in Pb–Pb collisions at $\sqrt{s_{NN}} = 2.76 \text{ TeV}$. The data and Monte Carlo (MC) efficiencies are shown by solid and open symbols respectively.

Fig. 4.16 (left) shows the impact parameter resolution in the transverse plane for three colliding systems as a function of p_T . A clear improvement of the resolution is

visible for heavier colliding systems due to the better determination of the primary vertex in high multiplicity environments. Transverse momentum resolution for global tracks is around $\sim 1\%$ at $1 \text{ GeV}/c$ and it increases reaching $\sim 10\%$ at $50 \text{ GeV}/c$ in Pb–Pb collisions as shown in Fig. 4.16 (right).

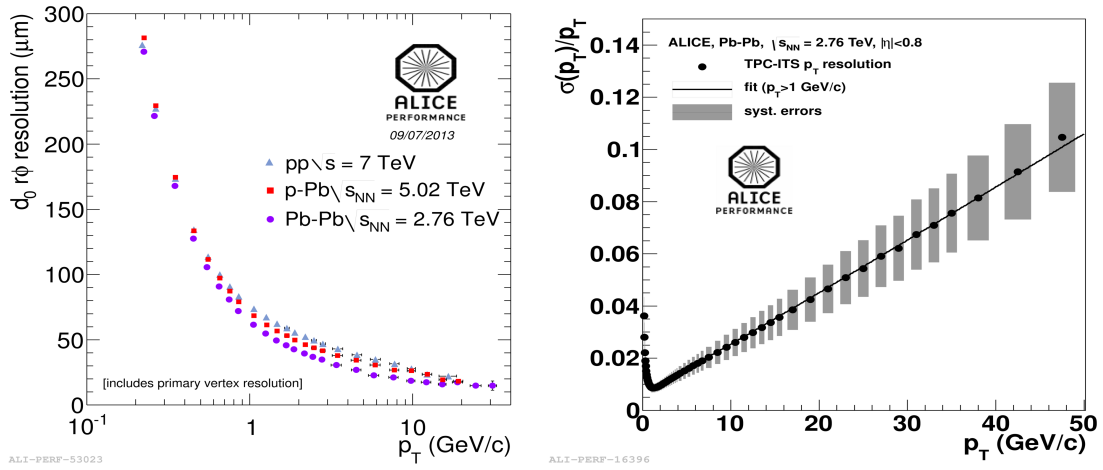


Fig. 4.16 : Impact parameter resolution in the transverse plane for three colliding systems as a function of p_T (left). Transverse momentum resolution as a function of p_T for global tracks in Pb–Pb collisions at $\sqrt{s_{NN}} = 2.76 \text{ TeV}$ (right) [122].

4.6.7 Secondary Tracks

The search for secondary tracks, i.e. those originating from particle weak decays or photon conversion in the material, is done among those tracks with a distance of closest approach to the primary vertex exceeding a given limit (0.5 mm in pp and 1 mm in Pb–Pb collisions). Pairs of unlike-sign secondary tracks are then combined to search for V0 topologies. The position of the secondary vertex is determined by the *point of closest approach* (PCA) of the two unlike-sign tracks. The criteria used by the *V0 finder algorithm* to select the V0 candidates are:

- The distance of closest approach between two tracks is requested to be less than 1.5 cm
- The PCA is requested to be closer to the interaction vertex than the innermost hit in the ITS of both tracks.
- The cosine of the *pointing angle*, defined as the angle between the total V0 momentum and the vector connecting the primary to the secondary vertex, is requested to be larger than 0.9 (this cut is relaxed for V0 candidates with p_T below $1.5 \text{ GeV}/c$).

Two main algorithms for V0 finding are used by the ALICE reconstruction framework: the "*offline*" and the "*on-the-fly*" V0 finders. In the offline algorithm, secondary tracks are searched among global ITS–TPC tracks, propagated down to the primary vertex, and the track momentum is estimated at the PCA to the vertex. The energy loss corrections are therefore overestimated for these tracks since they are applied also for layers of the detector which was actually never crossed. Moreover, the track momentum is not estimated at the secondary vertex, which is the true production point. This causes a small bias in the measurement of the particle direction (Fig. 4.17). The effects of the propagation of secondary tracks to the primary vertex are discussed in Appendix A.

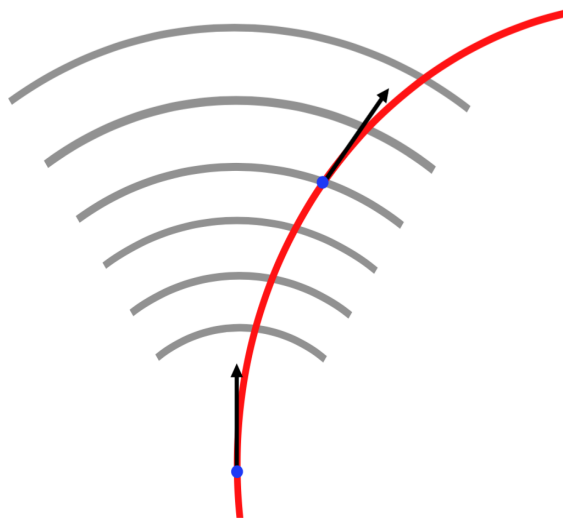


Fig. 4.17 : This sketch illustrates the working principle of the offline V0 finder. If momentum is estimated at the point of closest approach to the primary vertex its direction is different from the one estimated at the true production point (in the 4th ITS layer in this picture).

The "*on-the-fly*" algorithm works as part of the ITS tracker, having access to the track parameters at each tracking step in the ITS. In this algorithm, the pairings between unlike-sign particles to search for V0 topologies is done "*on-the-fly*" during the inward propagation. For each of these pairs, the track momenta are estimated at the point of closest approach between the two tracks, which is the closest point to the true secondary vertex.

Fig. 4.18 shows the transverse distribution of secondary vertices of electrons produced by photon conversion in the material. The detector geometry and the material distribution in the simulation is verified by comparing the distributions of secondary vertices in data and Monte Carlo.

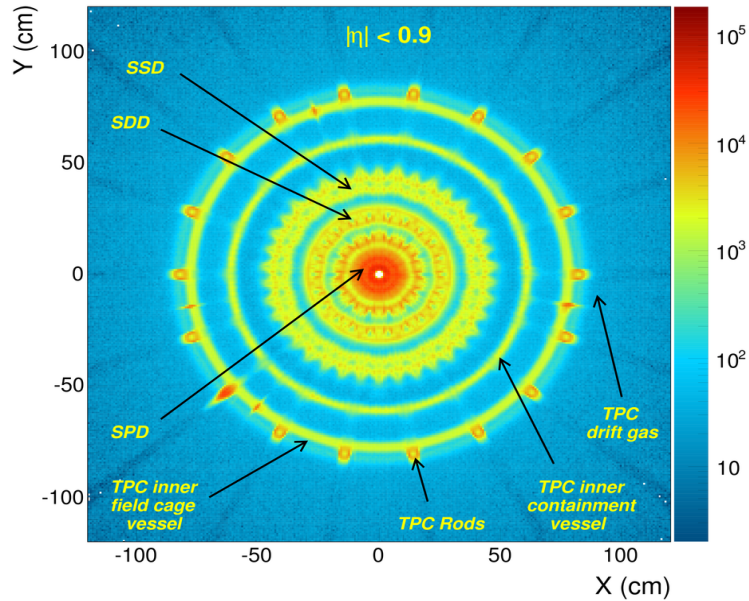


Fig. 4.18 : Transverse distribution of the reconstructed photon conversion points for $|\eta| < 0.9$. The ITS layers and the TPC, including the mechanical structures, are clearly visible.

4.7 Monte Carlo Sample

Monte Carlo (MC) simulations are essential to understanding the detector effects and to investigating some physical processes since one has direct access to the identity of the particles produced in the simulation and their kinematic variables. This is particularly important for the cut tuning in real data analysis. Monte Carlo simulations are also used for the efficiency calculation, needed to correct the final spectrum before the comparison with theoretical expectations. The Monte Carlo productions mainly used in this analysis were the LHC13c7a/b/c, corresponding to the following centrality classes: (0-10 %), (10-50 %) and (50-90 %). These productions were *anchored* to the LHC11h data taking period. The same detector configuration and status have been reproduced in the simulation, including detector defects, dead ITS pixels, noisy channels, low voltage, etc.

These MC productions were specifically dedicated to dielectron studies and contained events generated by HIJING, which is widely used to generate heavy-ion collision events, and an enriched sample of particles forced to decay into dielectrons. This enrichment of particles of interest was needed to have higher statistics in the simulation. Table 4.2 shows the list of additional dielectron sources included in the simulation and their forced decay channels. For comparison, the real branching ratios for the same decay channels are also shown.

Particle	Decay channel	BR (real)	BR (sim)
π^0	e^+e^-	$(6.46 \pm 0.33) \times 10^{-8}$	1
η	e^+e^-	$< 5.6 \times 10^{-6}$ (C.L.=90%)	1
η'	e^+e^-	$< 2.1 \times 10^{-7}$ (C.L.=90%)	1
ρ^0	e^+e^-	$(4.72 \pm 0.05) \times 10^{-5}$	1
ω	$\pi^0 e^+e^- + e^+e^-$	$(7.7 \pm 0.6) \times 10^{-4} + (7.28 \pm 0.14) \times 10^{-5}$	1
ϕ	e^+e^-	$(2.954 \pm 0.030) \times 10^{-4}$	1
J / ψ	e^+e^-	$(5.94 \pm 0.06)\%$	1

Table 4.2 : Enriched dielectron sources and their branching ratios for the dielectron decay channel, both in reality and in the simulations used in the present analysis. Real branching ratios are taken from [133].

4.8 Event And Run Selection

Data analyzed for this thesis work have been collected in 2011, during the second Run of Pb–Pb collisions at $\sqrt{s_{\text{NN}}} = 2.76$ TeV. The run list used for the analysis contained only the runs classified as "good runs" by the *Quality assurance* group, based on some quality parameters concerning the detectors alignment, track matching, calibration, etc.

Data have been collected for two opposite magnetic field orientations along the beam axis, indicated as "*positive polarity*" and "*negative polarity*". Particle spectra from runs with different field orientations have been analyzed separately because of detector geometrical asymmetries, mainly due to hardware problems in the ITS and the partial azimuthal coverage of the installed TRD modules (see Chapter 6). These geometrical asymmetries and the particle spectra for opposite magnetic field configurations were well reproduced in the MC simulations.

In this analysis, only single Pb–Pb collision candidates have been considered applying the *physics selection*. This rejected most of the pileup, beam-gas interactions, collisions with de-bunched ions or with mechanical structures of the machine and physical background.

The analysis presented in this thesis has been performed for two wide centrality classes: (0-10%) and (10-50%). These have been selected using the centrality triggers *kCentral* and *kSemiCentral* respectively, which imposed a minimum multiplicity threshold in the

V0 detectors. Fig. 4.19 shows the centrality distributions of events selected using the just mentioned ALICE centrality triggers. While for semi-central collisions the centrality distribution was to good approximation uniform, for central collisions a decreasing trend was observed in the range 8-10% caused by non-uniformity of the trigger efficiency. The impact of non-uniform centrality distribution on the dielectron spectrum measured in the centrality range 0-10% is discussed in Section 6.5.

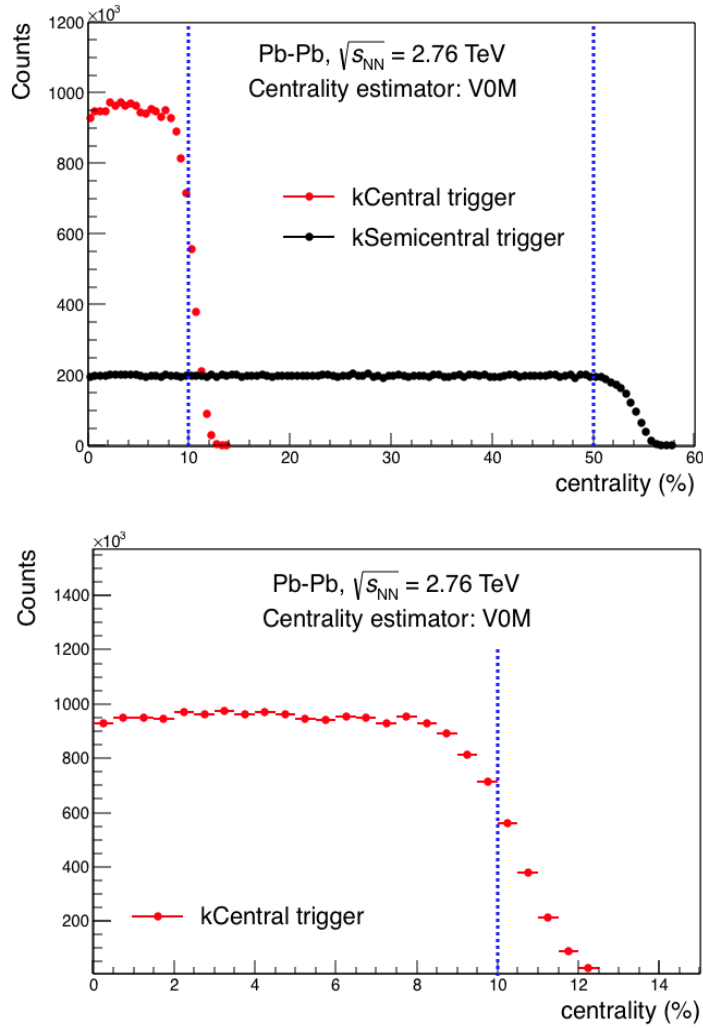


Fig. 4.19 : Centrality distributions of events selected using the $kCentral$ and $kSemicentral$ triggers (top). The former showed some deviations from flatness in the range 8-10% caused by non-uniformity of the trigger efficiency (bottom). The blue dashed lines indicate the offline event selection.

In order to keep the conditions of the detectors as uniform as possible, avoid edge effects and reject residual parasitic collisions the analysis has been restricted to the region around the geometrical center of the ALICE experiment defined by $|z_{vtx}| < 10$ cm.

Fig. 4.20 shows the vertex z -coordinate distribution, both in MC simulations and data, and the selected fiducial region.

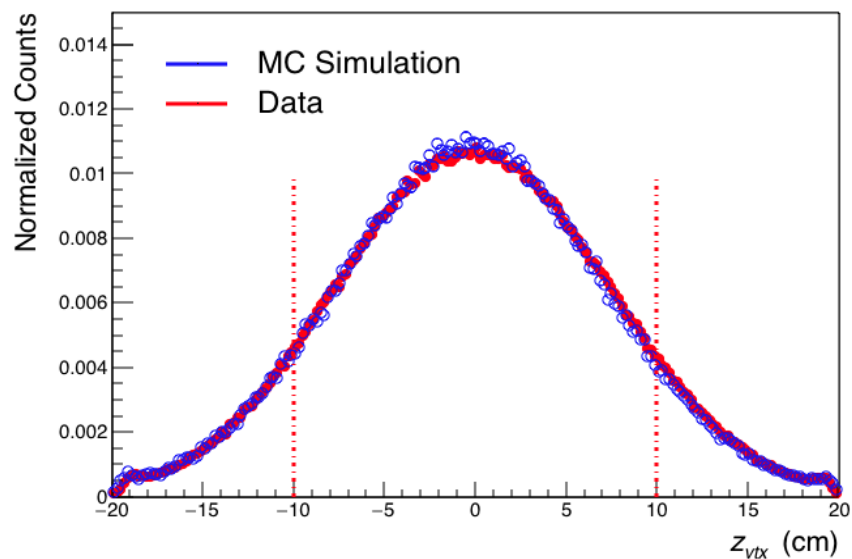


Fig. 4.20 : Vertex z -coordinate distribution measured in data (red) and the selected fiducial region $|z_{vtx}| < 10$ cm. The z_{vtx} distribution in MC simulations (blue) is also shown for comparison.

Chapter 5

Track Selection and Photon Conversion Rejection

5.1 Track Quality Cuts

High energy nuclear collisions produce a large multitude of tracks and a careful selection of the tracks of interest is the basic starting point of any analysis. Tracks produced by particles originating from the primary vertex are called primary tracks, while those produced by weak decay products or from photon conversion in the detector material, originating from displaced vertices, are called secondary tracks. Dielectrons generated by internal conversion of virtual direct photons originate from the interaction region and therefore produce primary tracks. The track selection criteria applied in this analysis have been optimized to ensure a good overall quality of the reconstructed tracks and to reject secondary tracks, which only contribute to combinatorial background. In this section, the main variables used in the track selection are listed, including their brief description and the corresponding cuts applied. The full list of track cuts includes some additional requirements applied to reject electrons from photon conversion in the material. These complementary track cuts are presented in Section 5.3 which is specifically dedicated to the illustration of the conversion rejection methods.

Particular emphasis has been put in the correspondence between data and MC simulation for all variables used in the track selection. Strict cuts on variables whose distributions in data are very different from those in MC simulation would result in an overestimation or underestimation of the pair reconstruction efficiency, thus causing a bias in the final measurement. For this reason, less rigid cuts have been applied in the case of poor matching, ensuring the best compromise between the reliability of the detector description in the simulation and the track quality requirements.

- **Distance of Closest Approach (DCA) to the primary vertex:**

The selection of primary tracks and the first level of secondary track rejection has been done by cutting on the distance of closest approach (DCA) between the track and the primary vertex. Fig. 5.1 show the p_T -integrated distributions of transverse and longitudinal DCA to the primary vertex for primary and secondary track candidates. The separation between these two categories has been done, in the study of cut optimization, by exploiting the V0-finder algorithm: secondary track candidates are those tagged by the V0-finder¹, while primary track candidates have been selected among those belonging to the complementary track sample, i.e. rejecting tracks tagged by V0, and having no common ITS cluster with other tracks (the reason for this last requirement will be explained in Section 5.3.1).

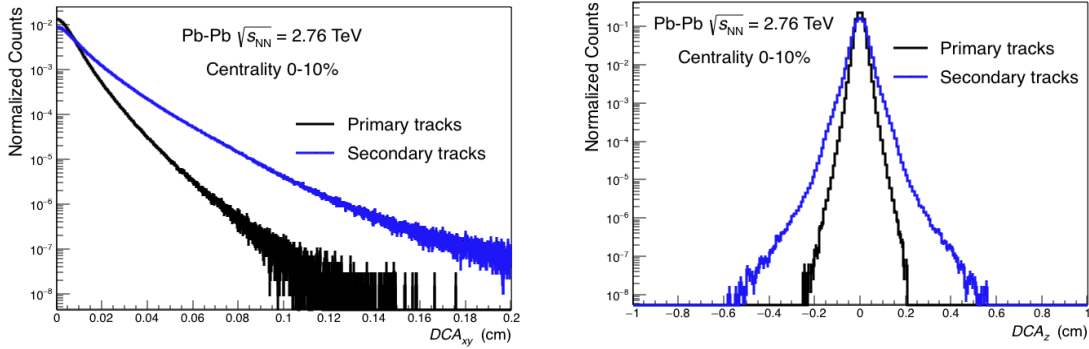


Fig. 5.1 : DCA distributions, in the transverse plane (left) and along the z-axis (right), for primary and secondary track candidates, selected using the V0-finder algorithm.

The separation between primary and secondary tracks is more clear at low p_T , while at higher momenta both categories tend to have similar DCA distributions because of their smaller curvature in the magnetic field. High momentum particles, in fact, travel along almost straight lines so that their tracks point down to the primary vertex also in the case of displaced production vertices.

In the selection of primary tracks a maximum $|DCA_z| = 0.1$ cm has been required, while a p_T -dependent cut has been applied to the DCA_{xy} , parametrized as follows:

$$DCA_{xy}^{\max}(p_T) = 0.00515869 + \frac{0.0101668}{p_T^{1.34489}} \text{ cm} \quad (5.1)$$

This cut corresponds to 3 RMS of the DCA_{xy} distribution for primary track candidates in each p_T range. In the choice of the DCA cuts, the worse resolution

¹This sample inevitably contains some "contamination" from primary tracks. This contamination is smaller than 5% and the tagging efficiency of secondary track of the V0-finder is larger than 90%.

in the measurement of DCA_z with respect to DCA_{xy} was taken into account ($\sim 170 \mu\text{m}$ for DCA_z and $\sim 65 \mu\text{m}$ for DCA_{xy} at $1 \text{ GeV}/c$ [105]). Fig. 5.2 shows the distributions of DCA_{xy} and DCA_z as functions of p_T for all reconstructed tracks, together with the selected regions indicated by the black dashed lines.

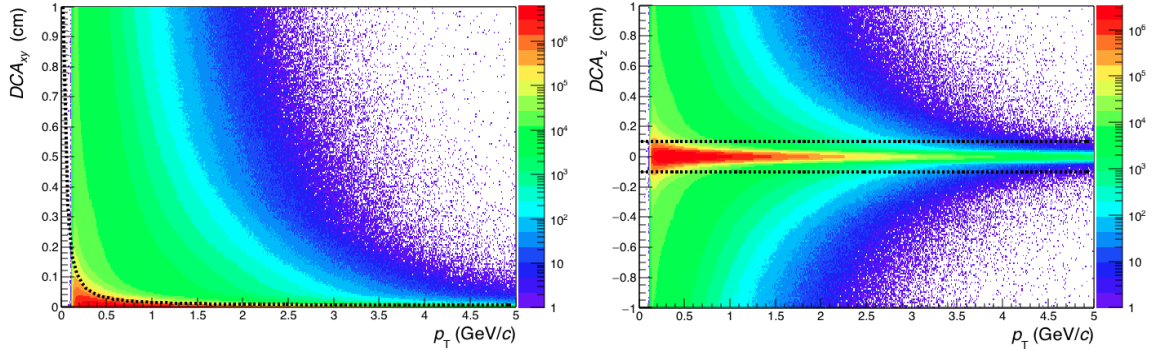


Fig. 5.2 : DCA distributions as functions of p_T in the transverse plane (left) and along the z-axis (right). Black dashed lines represent the borders of the selected regions.

A good matching was found between the DCA distributions in data and MC simulation (Fig. 5.3).

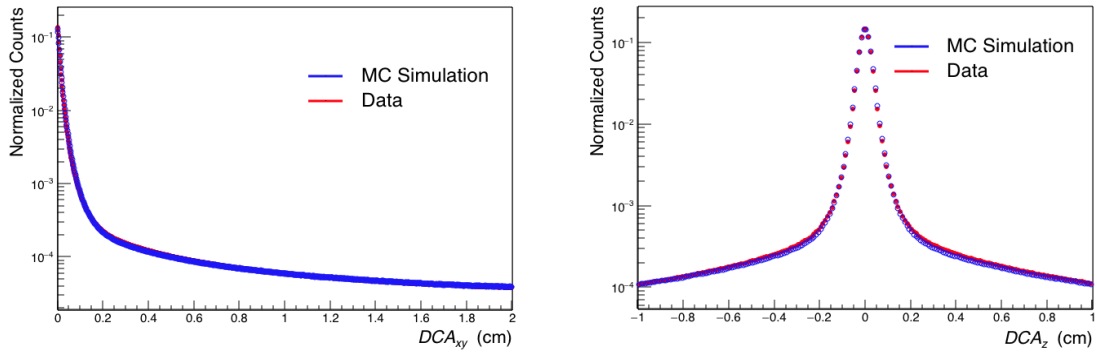


Fig. 5.3 : DCA distributions in the transverse plane (left) and along the z-axis (right) in data and MC simulation.

- **Kink daughters:**

Weakly decaying charged particles that produce one or more neutral particles in their decays (such as $K^\pm \rightarrow \mu^\pm + \nu$) leave tracks which show an abrupt change in their curvature (Fig. 5.4). Neutral particles are in fact invisible to tracking detectors since they do not produce ionization. The charged decay products are referred to by using the technical jargon "*kink daughters*", due to the "kink" visible

in their reconstructed tracks. These tracks, identified and flagged by the kink-finder algorithm, have been rejected in the present analysis, being secondary tracks.

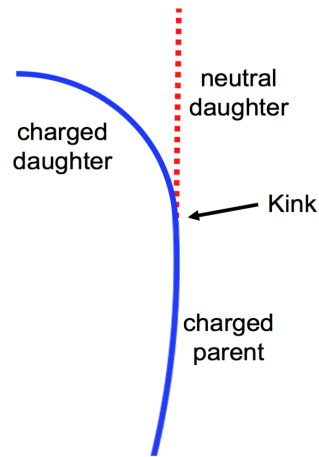


Fig. 5.4 : Kink topology.

- **ITS and TPC refit:**

A successful refit by the Kalman filter, both in ITS and TPC, has been required for all reconstructed tracks.

- **ITS tracking:**

All tracks have been required to have a minimum number of ITS clusters equal to 4, with at least one of those located in the first ITS layer (SPD). The requirement of having a hit in the first layer of the detector which is encountered by particles is imposed to suppress electrons produced by photon conversion in the detector material and secondary tracks from late weak decays: particles produced at radii larger than the first ITS layer are expected to be rejected since they will potentially produce hits only starting from the ITS layer following their production vertex. This cut does not affect conversions happening in the beam pipe. Although this requirement was quite effective in reducing conversion electrons, its rejection power was limited by the wrong cluster associations in the ITS (see Section 5.3.1).

- **TPC tracking:**

Charged particles traversing the TPC volume produce ionization and the induced signals are readout by dedicated electronics. If the charge in a search window of 5 pads in wire direction and 5 bins in time direction exceeds a certain threshold and fulfills all necessary quality criteria, it is called a *cluster*. The maximum number of clusters (n_{cl}) is 159, which corresponds to the total number of pad rows in the

TPC². All reconstructed tracks have been requested to have a minimum number of clusters in the TPC equal to 70.

The relevant quantity for the p_T -resolution of a track is the effectively sampled track length of a particle in the TPC. The effective number of TPC clusters is called number of *crossed rows* (n_{cr}), since this corresponds to the number of pad rows traversed by the particle. This includes the number of found clusters and a number of missing clusters which are assigned if a cluster is found on one of the neighboring pad rows (Fig. 5.5). The minimum number of crossed rows equal to 100 has been required for the selected tracks.

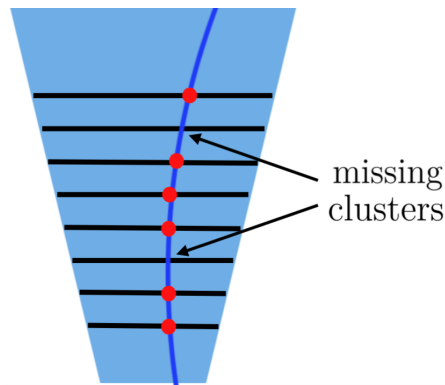


Fig. 5.5 : Schematic illustration of a track with missing clusters which are assigned to contribute to the effective number of clusters (crossed pad-rows). This track has $n_{cl} = 6$ and $n_{cr} = 8$.

Another variable used in the track selection is the number of *findable clusters*, defined as the number of geometrically possible clusters which can be assigned to a track. It takes into account dead zones due to chamber boundaries or the limited η -acceptance of the TPC. Clusters on dead front-end cards are counted as findable. A minimum ratio of crossed rows over findable clusters of 60% has been required in this analysis.

Not all TPC clusters assigned to a track are used in the dE/dx calculation. Clusters which are located very close to the chamber boundaries or from overlapping tracks are not used for energy loss calculation. The minimum number of clusters used for the dE/dx calculation in the TPC has been set to 50. This quantity is very important for the dE/dx -resolution.

The quality of the fit for reconstructed TPC tracks is expressed in terms of χ^2 per

²Curling tracks might actually have a number of clusters larger than 159. These tracks, which are reconstructed separately by the tracking algorithm, do not belong to the category of global tracks considered in the present analysis.

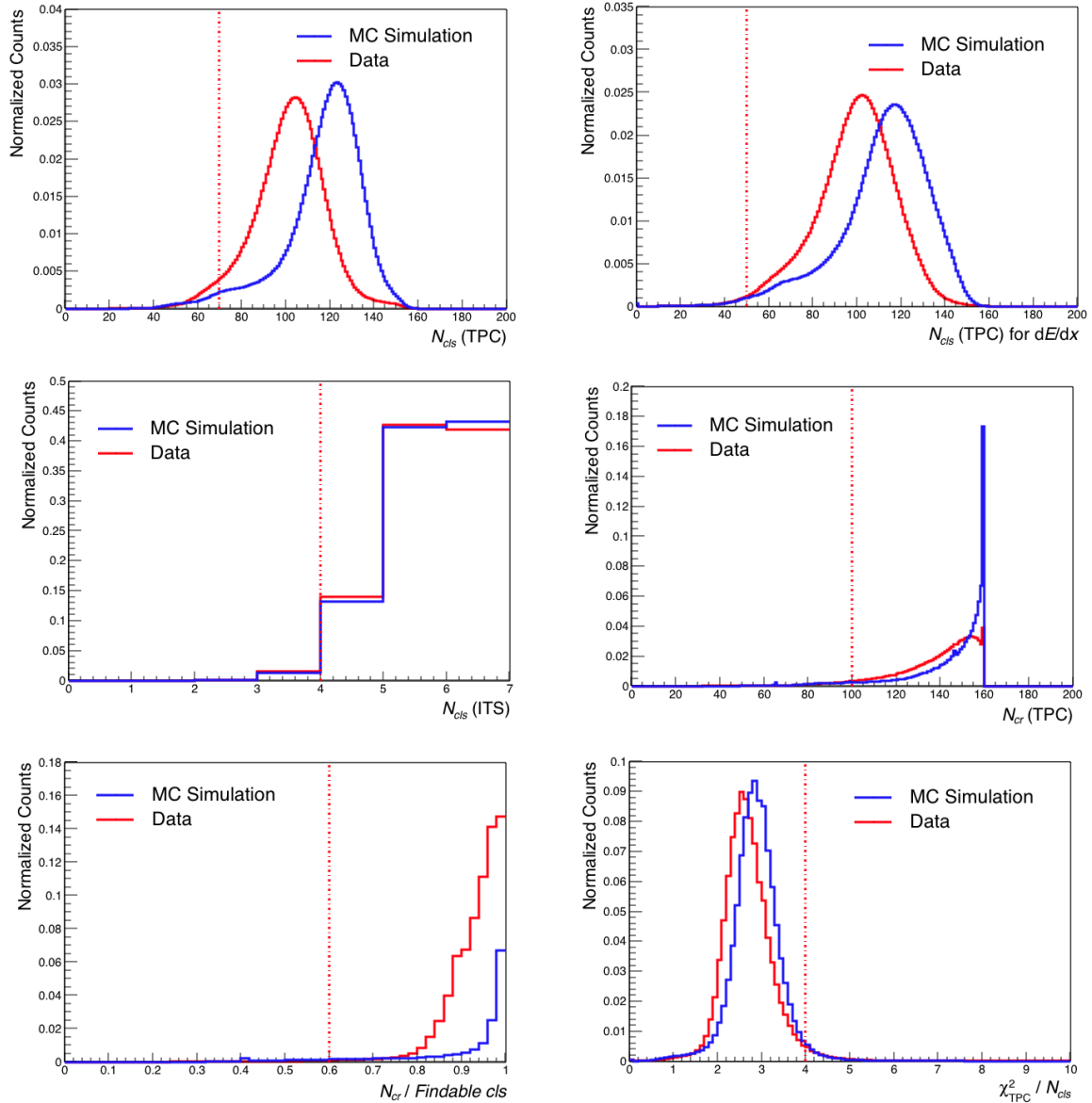


Fig. 5.6 : Distributions of some of the variables used for track selection in real data. The corresponding distributions obtained from MC simulations are also shown for comparison. Red dashed lines indicate the cuts that have been applied.

cluster. Tracks have been required to have a maximum χ^2/n_{cl} of 4.

The distributions of some of the variables used for track selection, both in data and in MC simulations, are shown in Fig. 5.6. Red dashed lines indicate the cuts applied.

The cuts that have been applied are not too strict due to a non-perfect matching between MC simulation and data. A good level of quality of the tracks has been ensured, being these cuts within the recommended limits.

- **p_T -threshold and geometrical acceptance:**

Tracks with transverse momenta lower than 400 MeV/ c have been rejected. This threshold has essentially been imposed by the requirement of having the time-of-flight measurement available, needed to reduce hadronic contamination in the selected electron sample (see paragraph 5.2). Most of the particles with transverse momenta below this threshold did not reach the TOF radius due to their curvature in the magnetic field or got absorbed in the TRD material. This cut rejected mainly background electrons, mostly coming from photon conversion in the material or low-momentum π^0 and η Dalitz-decays. Low- p_T electrons mainly contribute to the very low-mass region of the dielectron spectrum at low p_T^{ee} , outside of the region of interest for virtual photon measurement, thus only a little signal is affected by the low- p_T threshold.

An upper threshold on particles transverse momenta has also been applied due to the overlapping dE/dx signals of electrons and pions at high p_T , which contributed to enhancing the hadronic contamination. The upper limit on p_T is set at 5 GeV/ c . Above this threshold electrons and pions are almost indistinguishable. A negligible percentage of the inclusive electron sample has been rejected by this upper threshold.

Due to the limited geometrical coverage of the detectors in the ALICE central barrel, and in order to avoid edge effects, only tracks within the pseudorapidity window $|\eta| < 0.8$ have been accepted. The tracking and PID efficiency is the highest for these tracks since they traverse the full readout size of the TPC.

Table 5.1 summarizes the track selection criteria that have been applied in the present analysis.

5.2 Particle Identification

In the present analysis, particle identification (PID) has been performed using the average energy loss per unit path length (dE/dx) measured by the TPC and ITS, where the latter is used to exploit its hadron rejection capability at low momentum, complemented with the time-of-flight measurement by TOF. The strategy for electron selection has been optimized in order to have a high purity electron sample, so to reduce to a minimum the

variable	requirement
DCA_{xy}	$0.00515869 + 0.0101668/p_T^{1.34489}$ cm
$ DCA_z $	≤ 0.1 cm
Kink daughters	rejected
TPC refit	successfully executed
ITS refit	successfully executed
ITS N_{cls}	≥ 4
SPD requirement	hit in the first layer
TPC N_{cr}	≥ 100
TPC N_{cls}	≥ 70
TPC N_{cls} for dE/dx	≥ 50
TPC N_{cr} / findable clusters	≥ 0.6
χ_{TPC}^2/N_{cls}	≤ 4
p_T	$\in [0.4, 5]$ GeV/ c
η	$\in [-0.8, 0.8]$

Table 5.1 : List of the track selection cuts used in this analysis.

impact of hadronic contamination on the dielectron invariant mass spectrum. A good calibration of the detectors PID response is of crucial importance for the particle selection, also to guarantee a good matching between the PID signals in data and MC simulation. A parametrized calibration of the detector response, in the form of *splines*, was performed on a run-by-run basis during the reconstruction pass. The parametrizations have been made available to the analyzers and the splines can be automatically loaded when running the analysis tasks. Higher order corrections sometimes might be needed, depending on the analysis, due to small residual distortions in the detector response. A recalibration of the TPC response was necessary due to an off-centered and non-constant trend of its signal as a function of charged particle multiplicity and pseudo-rapidity, most probably due to the TPC occupancy, space charge effects and the non-uniformity of the TPC

active volume. The following paragraphs describe in details the procedure used for the TPC post-calibration and the particle identification strategy.

5.2.1 TPC post-calibration

The distribution of $n\sigma_{\text{TPC}}$ for electrons has been studied using a track sample containing conversion electron candidates. These have been selected using the V0-finder algorithm and imposing some additional requirements and pair cuts to specifically select conversion electrons. The additional cuts used here for selecting conversion electrons are the same that have been used for their rejection (see Section 5.3).

The $n\sigma_{\text{TPC}}$ distribution for electrons appears not to be centered at zero and its width is different from unity, showing a dependency on the charged track multiplicity and pseudorapidity (Fig. 5.7).

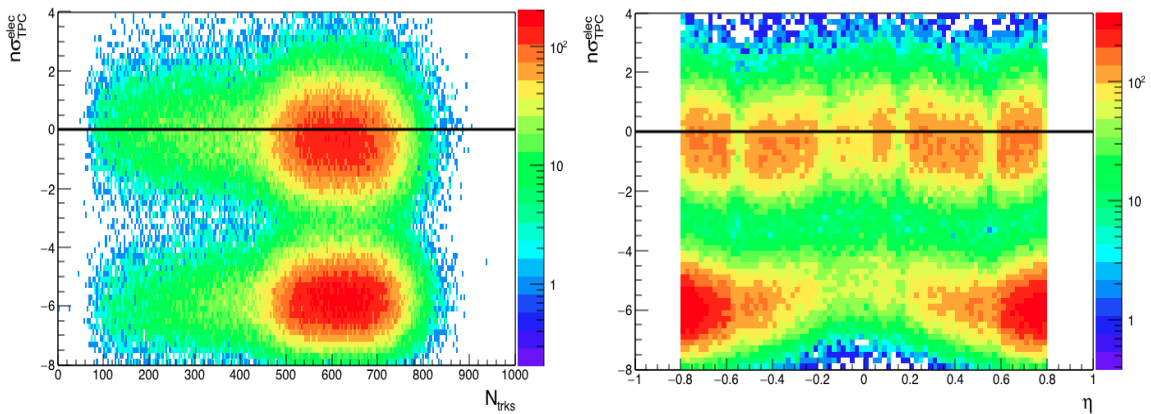


Fig. 5.7 : Multiplicity dependence (left) and η dependence (right) of $n\sigma_{\text{TPC}}$ distribution for electrons. The lower band corresponds to the residual pion contamination in the track sample selected for this study.

The observed trend as a function of charged particle multiplicity might indicate that this effect is related to the TPC occupancy and space charge effects, which are stronger in a high multiplicity environment. The distortions in pseudorapidity instead suggest some inhomogeneities in the TPC active volume, most probably related to a non-uniform gas pressure and electric and/or magnetic field.

In order to correct for these distortions, the $n\sigma_{\text{TPC}}$ distribution has been projected into different η and multiplicity intervals, and in each of them the electron mean and width have been extracted by fitting the distribution using a two Gaussian fit, to describe both the electron and pion curves (Fig. 5.8). A good overall quality of the fit, expressed in terms of χ^2 per degree of freedom, was found for each η and multiplicity range.

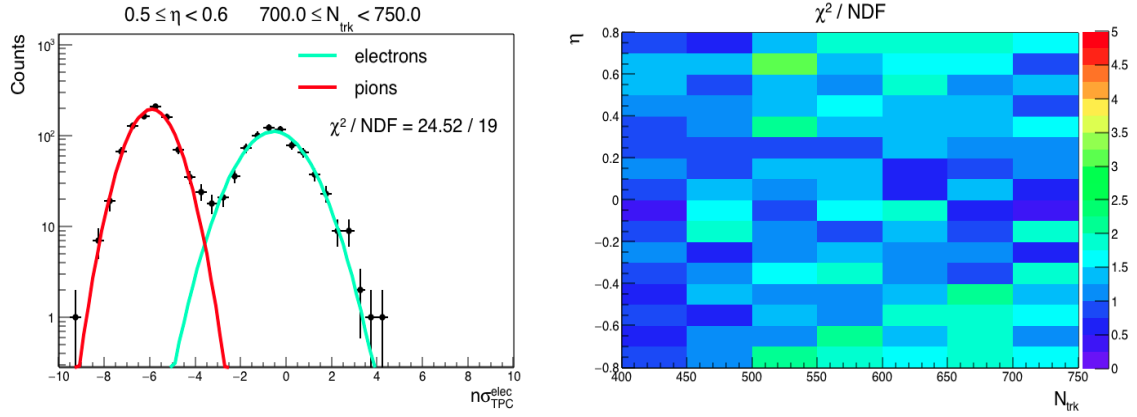


Fig. 5.8 : Example of the two gaussian fit of the $n\sigma_{\text{TPC}}^{\text{elec}}$ distribution to extract mean and width of the electron curve (left). χ^2 of the two Gaussian fit per degree of freedom in different η and multiplicity ranges (right).

The mean and width of the electron $n\sigma_{\text{TPC}}$ follow linear trends as functions of multiplicity in each η range (Figs. 5.9 and 5.10). These have been parametrized using linear fits in order to get continuous functions in each η range to be used in the correction of the TPC response.

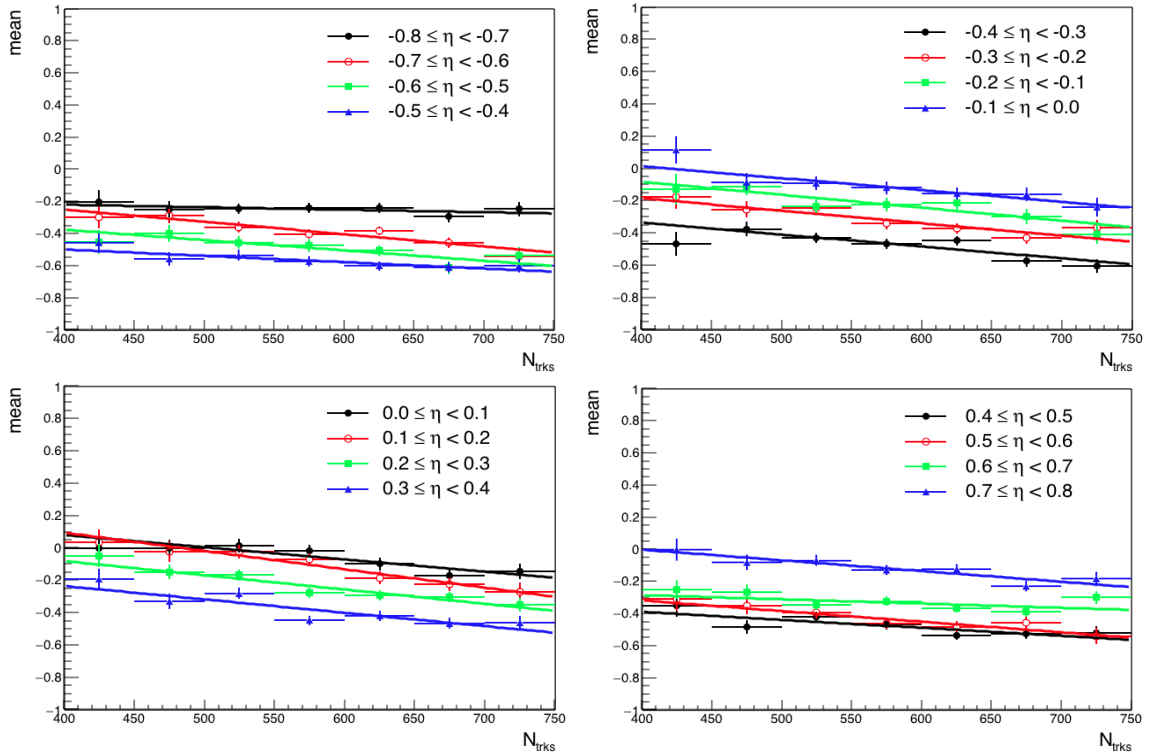


Fig. 5.9 : Mean of the electron $n\sigma_{\text{TPC}}$ distribution as a function of multiplicity for different η ranges.

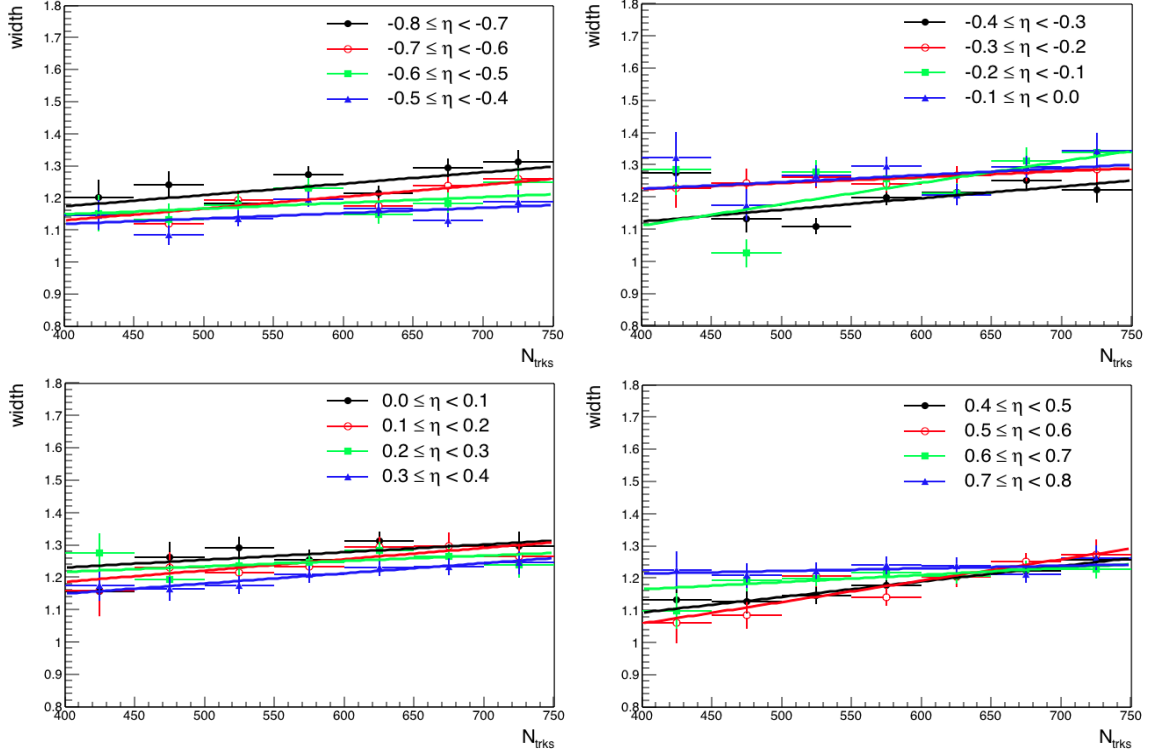


Fig. 5.10 : Width of the electron $n\sigma_{\text{TPC}}$ distribution as a function of multiplicity for different η ranges.

The TPC signal has been modified based on the measured charged particle multiplicity and pseudorapidity of the track by applying the following transformation:

$$n\sigma_{\text{TPC}}^{\text{elec}} \rightarrow \frac{n\sigma_{\text{TPC}}^{\text{elec}} - \langle n\sigma_{\text{TPC}}^{\text{elec}} \rangle}{w} \quad (5.2)$$

where $\langle n\sigma_{\text{TPC}}^{\text{elec}} \rangle$ is the mean and w is the width of the $n\sigma_{\text{TPC}}^{\text{elec}}$ distribution extracted from the Gaussian fit in the corresponding η range.

Fig. 5.11 shows the effects of the TPC post-calibration on the electron $n\sigma_{\text{TPC}}$ distributions. The distortions have been strongly reduced and the distributions appeared more stable and well centered at zero.

Further dependencies of the TPC signal on other variables have been found to be negligible after the TPC recalibration and have been ignored.

5.2.2 Electron Identification Strategy

The electron identification strategy used in the present analysis was based on the PID signals from the main tracking detectors (ITS and TPC) and from the TOF system.

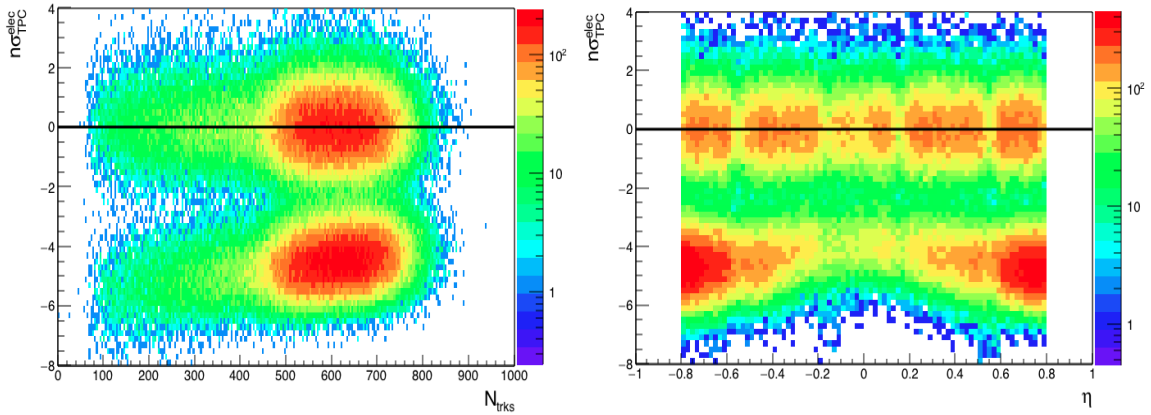


Fig. 5.11 : Multiplicity dependence (left) and η dependence (right) of $n\sigma_{\text{TPC}}^{\text{elec}}$ distribution for electrons, after the TPC post-calibration. The distortions have been strongly reduced and the distributions appeared to be well centered at zero.

Only tracks having a TOF signal available, i.e. having an associated hit in the TOF, are accepted in order to exploit its high hadron rejection capabilities. The TOF was mainly inefficient for particle momenta below ~ 300 MeV/ c mainly for geometrical reasons since the curvature of low-momentum particles prevents them from reaching the TOF radius. The first level of electron selection was represented by a cut on the time-of-flight: only tracks whose time-of-flight was within 3σ from the expected value for electrons have been accepted. Although the TOF cut efficiently rejected a significant fraction of hadrons, some of them survived this first selection due to incorrect TOF–TPC track matching: a track produced by a hadron, which at low momentum should have a larger time-of-flight compared to an electron, matched a TOF hit produced by a particle with smaller time-of-flight, compatible with that of an electron.

The ITS PID information was then used to improve the hadron rejection, especially at low momentum, requesting the tracks to have $n\sigma_{\text{ITS}}^{\text{elec}} < 1$.

The final electron identification was done using the average dE/dx measured by the TPC, by selecting particles within a range of $n\sigma_{\text{TPC}}^{\text{elec}}$ which is asymmetric with respect to the expected value for electrons: the upper limit has been fixed at 3, while a momentum dependent lower limit has been applied. The latter was chosen due to the increasing overlap between the pion and electron bands at higher momenta. This momentum dependent cut has been parametrized as:

$$n\sigma_{\text{TPC}}^{\text{min}} = -3 \cdot \exp(-p) \quad (5.3)$$

The electron identification strategy used in this analysis is summarized in Table 5.2.

variable	requirement
$n\sigma_{TOF}^{elec}$	$\in [-3, +3]$
$n\sigma_{ITS}^{elec}$	≤ 1
$n\sigma_{TPC}^{elec}$	$\in [-3 \cdot \exp(-p), +3]$

Table 5.2 : Electron identification strategy.

The effect on the electron identification of the different selection levels in the three sub-detectors is shown in Fig. 5.12.

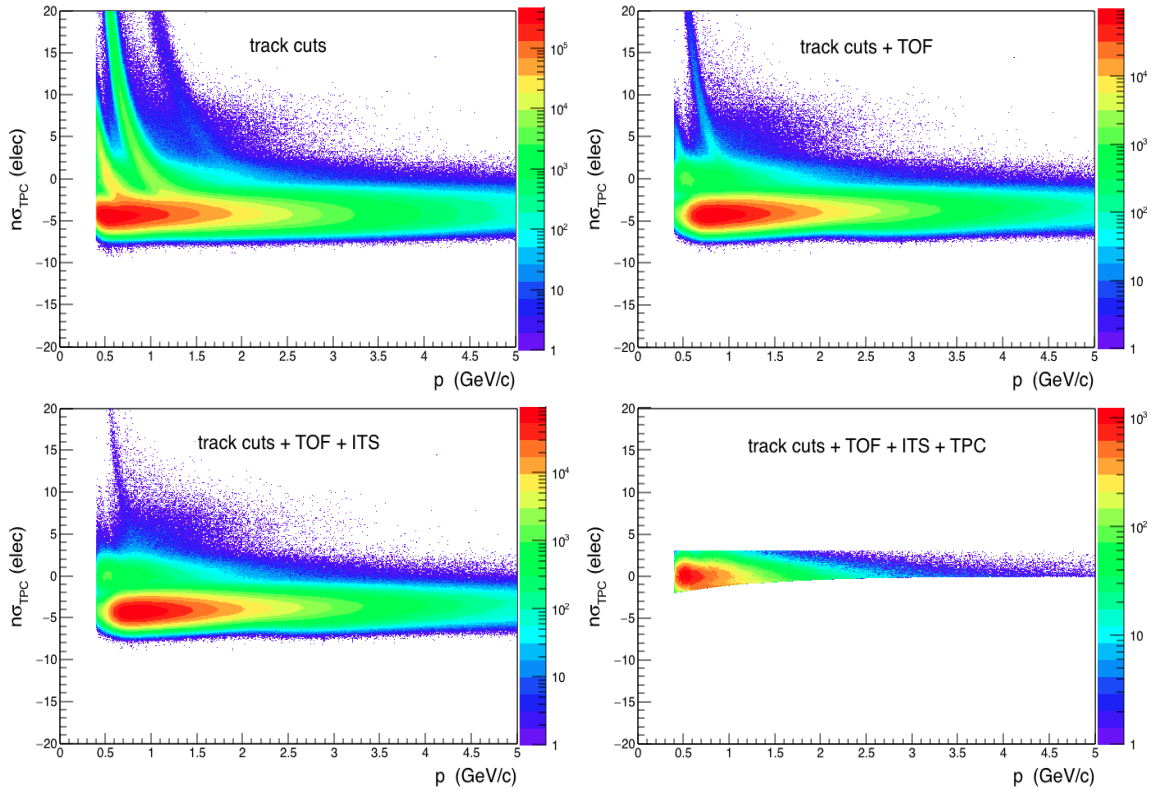


Fig. 5.12 : Effect of the different cuts on the electron selection.

The hadron contamination has been estimated, for each momentum range, after the TOF and ITS selections, by fitting the $n\sigma_{TPC}^{elec}$ distribution with multiple Gaussians and integrating the contribution of particles different from electrons within the selected range (Fig. 5.13).

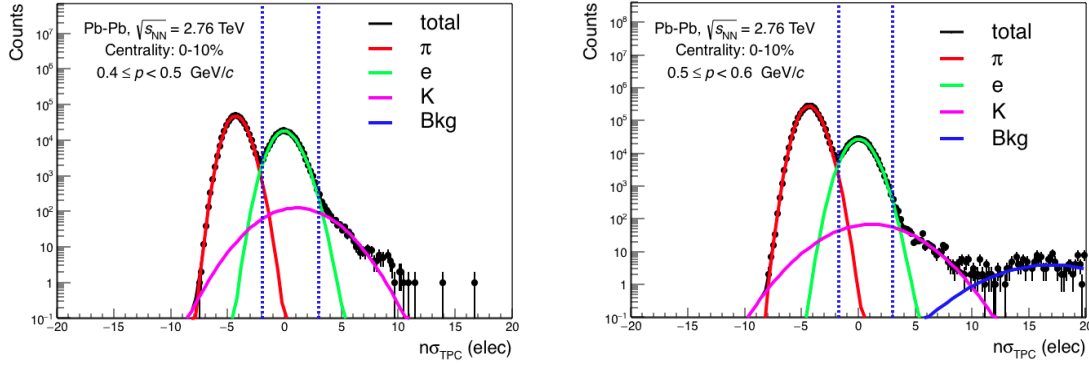


Fig. 5.13 : Distributions of $n\sigma_{\text{TPC}}^{\text{elec}}$ after TOF and ITS cuts for two momentum ranges to illustrate the method for the electron purity estimation.

Fig. 5.14 shows the electron purity, defined as the estimated fraction of electrons within the selected region, as a function of the particle momentum in central (0–10%) and semi-central collisions (10–50%).

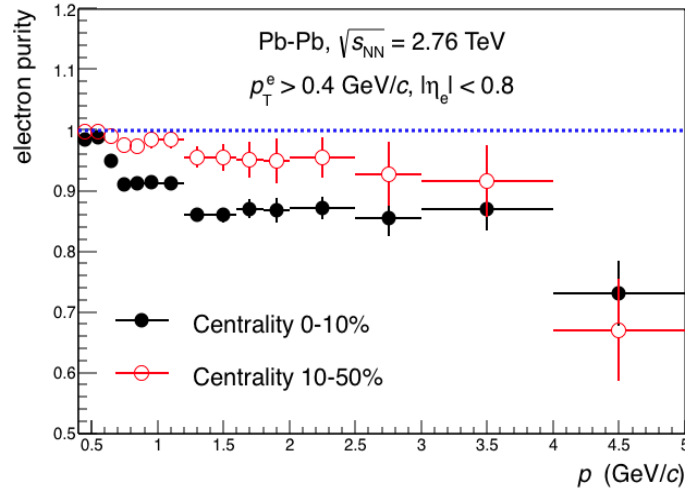


Fig. 5.14 : Electron purity in central (black) and semi-central (blue) collisions.

In semi-central collisions the electron purity was higher compared to central collisions due to a better PID resolution and to the reduced contribution from the background caused by the TOF-TPC mismatch. The impact of the hadron contamination on the dielectron invariant mass spectrum has been studied using the MC simulation. This is described in details in Section 6.3. The contribution from the hadronic background to the dielectron invariant mass spectrum was found to be of the order of $\sim 2\%$.

5.3 Photon Conversion Rejection

Electrons produced by photon conversion in the detector material amounted to over $\sim 70\%$ of all particles in the selected track sample, thus representing the dominant component of the combinatorial background (Fig. 5.15). The signal-to-background ratio in the mass region of interest for the analysis of virtual photons ($150 < m_{ee} < 300 \text{ MeV}/c^2$) was $\sim 10^{-3} \div 10^{-2}$ (see Section 6.4), therefore the background suppression was of crucial importance for the low-mass dielectron measurement.

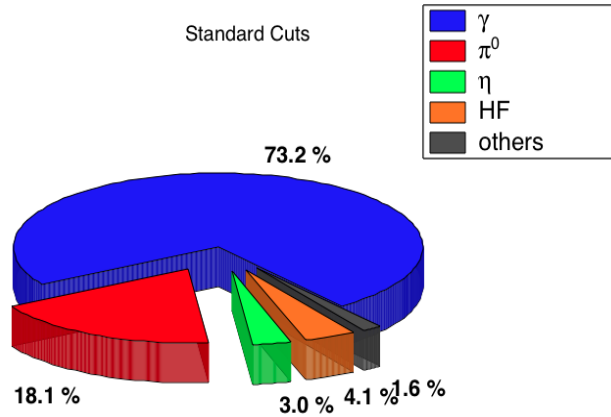


Fig. 5.15 : Illustration of the relative contributions to the selected track sample obtained from MC simulations. This is only an approximate representation since the relative particle abundancies measured in real data are not well reproduced in MC simulations. Moreover, some electron sources, such as η' and ω , are missing in the simulation. The small decay branching ratios of these particles into dielectrons, which are of the order of $\sim 10^{-5}$, have been ignored by HIJING.

Electron-positron pairs produced by photon conversion in the material have distinctive features, which are strictly connected to the physical process in which they are produced and depend on the way these particles interact with the detector: these are low-mass and small opening angle e^+e^- pairs which display a preferred orientation with respect to the magnetic field. These correlations can be used to tag and remove conversion candidates from the selected track sample (see Section 5.3.2). The rejection efficiency of methods based on pair correlations was however limited due to the small fraction of (conversion) pairs where both components were found in the reconstructed track sample (Fig. 5.16).

One of the two partners was not reconstructed due to detector inefficiency at low momentum, the track selection cuts, the low p_T -threshold applied and the limited acceptance of the detectors in the ALICE central barrel. Since pair cuts failed when only

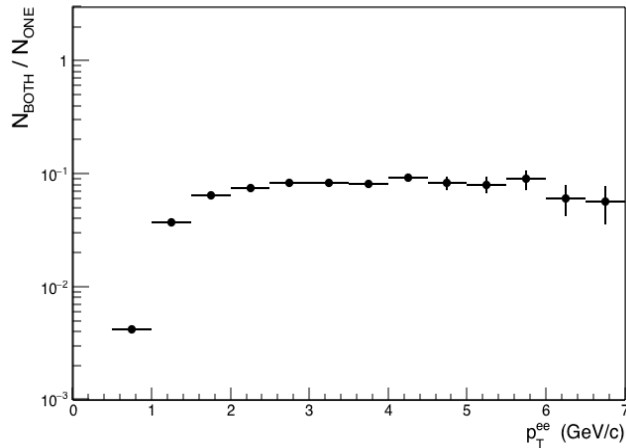


Fig. 5.16 : Fraction of dielectron pairs from photon conversion in the material where both conversion products are reconstructed.

one component of the pair was detected, a consistent effort has been put in developing a complementary method for rejecting conversion electrons on a single-track basis, which exploited some particular features of the tracking algorithm. This method is extensively discussed in the following paragraph, while the next one is dedicated to the description of pair rejection methods.

5.3.1 Conversion Rejection on a Single Track Basis

Electrons produced by photon conversion in the material, except those originating from the beam pipe, should be removed by the requirement of having a hit in the first SPD layer. However, this requirement was not so effective since the distribution of production vertices of particles that have passed the track selection cuts, including the first hit requirement, revealed the presence of many conversion electrons, some of them produced at very large distance from the first SPD layer (Fig. 5.17). This study was based on MC simulation, where the position of the production vertex of particles has been retrieved from the MC stack.

The reason for this paradox and for the low conversion rejection efficiency of the first layer requirement is related to the features of the track reconstruction algorithm and to the high track density in the inner tracker. During the inward track propagation, the tracking algorithm searched for compatible points to be assigned to the reconstructed track seed. Considering the high density of fired hits in the ITS, a wrong cluster assignment could occur, picking a cluster produced by another track or a *isolated cluster*, i.e. not assigned to any track. The latter are produced by noisy pixels which turned on even when not

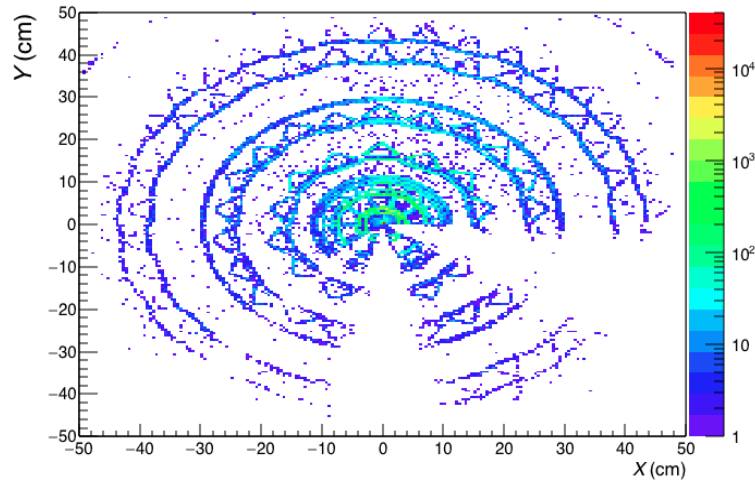


Fig. 5.17 : Distribution of production vertices of electrons whose tracks have passed all track selection cuts, including the requirement of having a hit in the first SPD layer.

fired by any particle (in Pb–Pb collisions almost $\sim 60\%$ of all ITS clusters were isolated). This mechanism of wrong cluster assignment is schematically illustrated in Fig. 5.18.

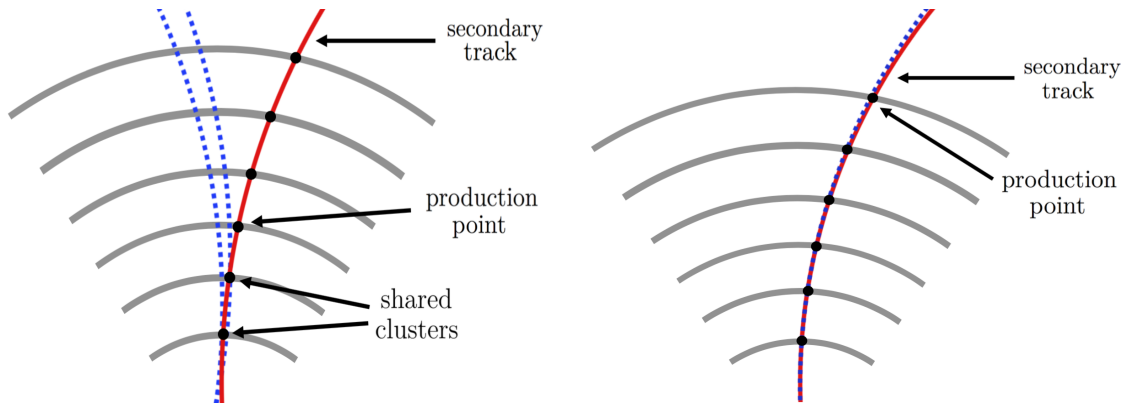


Fig. 5.18 : Schematic illustrations of wrong cluster assignment. In the left figure, a secondary track, produced by a conversion electron originating from the third ITS layer, has shared clusters in the two innermost layers with two different primary tracks. On the right, a secondary track produced in the outermost ITS layer shares an entire track segment with another primary track.

The probability for incorrect cluster association in a given layer is proportional to the detector occupancy, which was relatively high in the innermost ITS layer. The cluster in the first SPD layer was therefore wrongly assigned to conversion electron tracks, which thus managed to pass the first hit requirement. This tracking feature holds more generically for all secondary tracks.

The mechanism of wrong cluster association produced even more drastic effects for

late conversions. Besides the first layer requirement, all tracks were requested to have at least 4 clusters in the ITS. This means that tracks produced by photon conversion in the outermost layers of the ITS had several wrongly assigned clusters. The probability that several random clusters were aligned such that they were compatible with a track was too low to explain the high abundance of late conversions observed. In fact, it has been established that these tracks shared an entire segment of a close primary track.

This mechanism of wrong cluster association resulted in a poor quality of ITS tracking, which could be quantified by the χ_{ITS}^2 per cluster. Conversion electrons have, on average, a larger $\chi_{\text{ITS}}^2/N_{\text{cls}}$ compared to electrons from other sources (Fig. 5.19). The quality of ITS tracking became worse with increasing distance of the particle production point from the primary vertex. This was due to the longer segment of another primary track to be matched with the track seed.

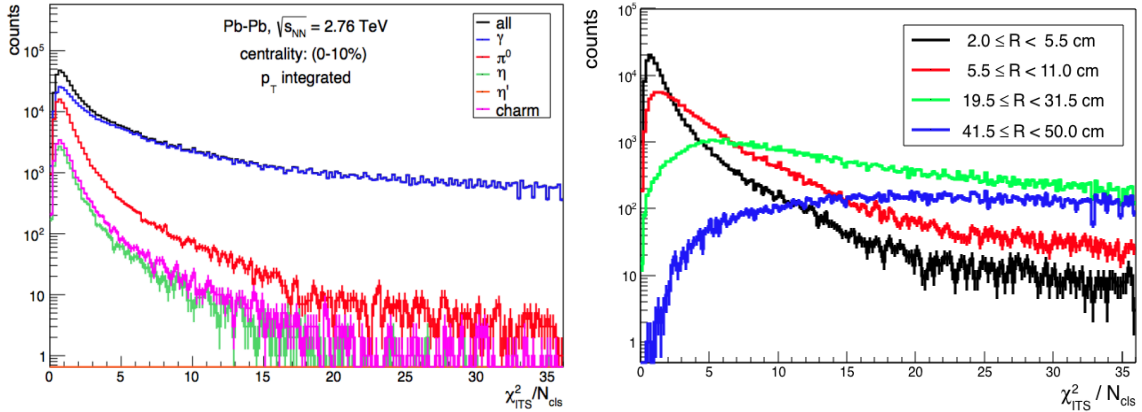


Fig. 5.19 : Distribution of $\chi_{\text{ITS}}^2/N_{\text{cls}}$ for electrons produced by different sources (left) and for secondary particles produced at different radial distance from the primary vertex (right).

The $\chi_{\text{ITS}}^2/N_{\text{cls}}$ is a variable which offered the possibility to reject a fraction of tracks originating from displaced vertices, especially those produced at large distances from the primary vertex. The additional requirement for tracks to have $\chi_{\text{ITS}}^2/N_{\text{cls}} < 5$ has been included to the track selection cuts.

The number of ITS clusters used in the track reconstruction as well as their positions were recorded by the tracking algorithm, which also kept track of those clusters assigned to multiple tracks, which were tagged as *shared clusters*. The fraction of shared clusters in the ITS, defined as the number of shared clusters divided by the total number of ITS clusters for that track, was a useful variable which allows a straightforward and clear separation between primary and secondary tracks. The latter tend to have on average a larger fraction of shared clusters than primary tracks. This can be seen in Fig. 5.20 which

shows the fraction of shared clusters as a function of particle momentum for electrons originating from different sources. While electrons from conversion show a rather uniform distribution, electrons from η (which can be regarded as primary electrons) show a peak at zero.

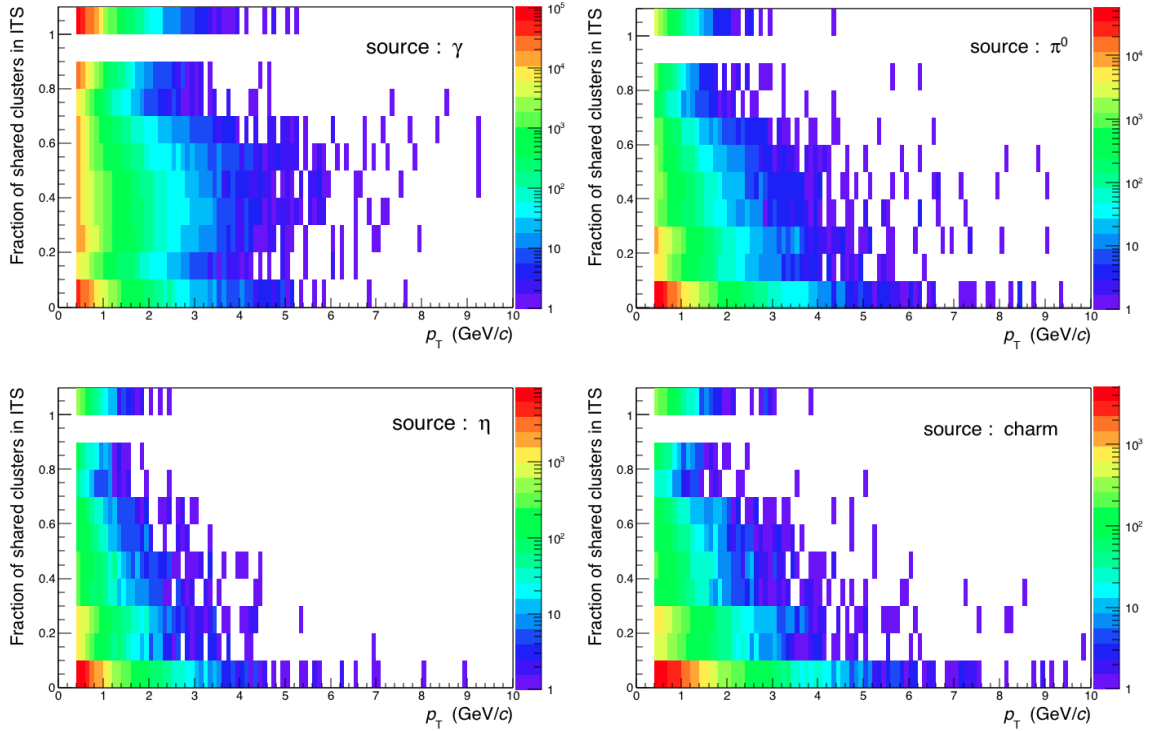


Fig. 5.20 : Fraction of shared clusters in ITS for electrons originating from different sources. The fraction of shared clusters is a discrete variable, here wider bins are chosen for better illustration.

The average fraction of shared clusters increases as the radial distance between the production point and the primary vertex becomes larger (Fig. 5.21). Cutting on this variable resulted in an efficient rejection of late conversions and, more generically, secondary tracks produced at large radial distances from the primary vertex. The maximum fraction of shared clusters has been set to 40%, representing the best compromise between the rejection efficiency of secondary tracks and the signal loss, i.e. the rejection of good tracks.

The secondary track rejection can be also done by exploiting a different parametrization of primary tracks: the TPC tracks constrained to the vertex. While global tracks are TPC-ITS tracks propagated to the primary vertex with the parameters updates at each cluster association, the TPC tracks constrained to the vertex did not have any parameter update in the ITS, so that they suffered from a minor bias due to wrong matching with

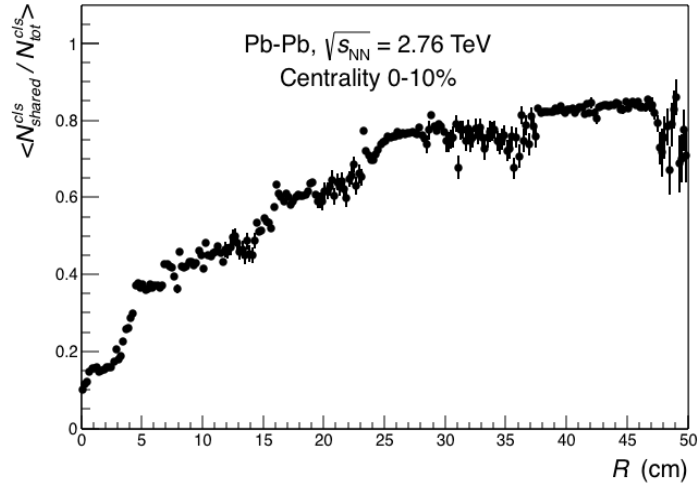


Fig. 5.21 : Average fraction of shared clusters in ITS of electrons as a function of the radial distance from the primary vertex.

another primary track. The difference between these two parametrizations was expressed in terms of the so-called *golden- χ^2* , defined as:

$$\chi_G^2 = (G - U)^T \cdot (\text{cov}_G - \text{cov}_U)^{-1} \cdot (G - U) \quad (5.4)$$

where G and T are 5 components vectors containing the parameters of the global track and TPC track respectively, while cov_G and cov_U are the covariant matrices of these two parametrizations. The golden- χ^2 distribution for electrons originating from different sources is shown in Fig. 5.22.

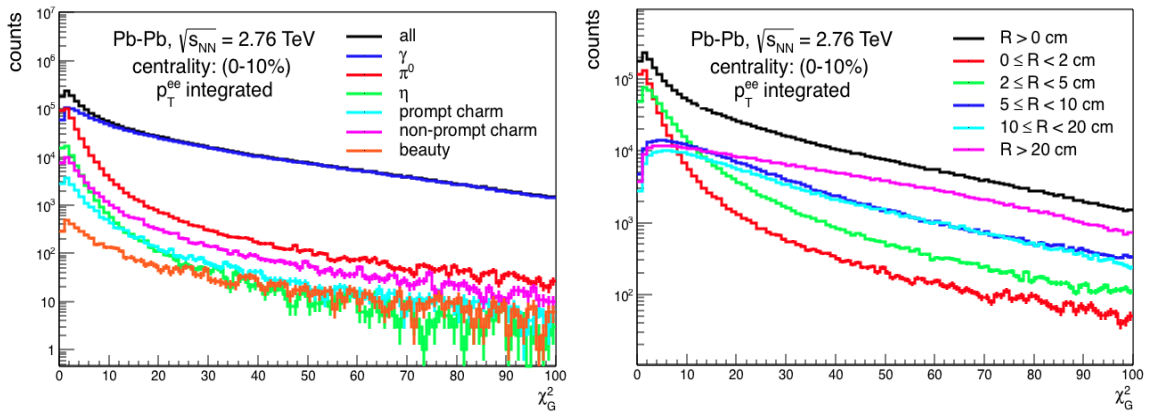


Fig. 5.22 : Golden- χ^2 distribution for electrons originating from different sources (left) and for different radial distances from the primary vertex (right).

Conversion electrons tend to have a broader χ_G^2 distribution and the average χ_G^2 increases with the radial distance from the primary vertex. Tracks having a χ_G^2 larger than 10 have been rejected in this analysis. The additional track cuts introduced for the secondary track rejection are summarized in the Table 5.3, while Fig. 5.23 shows the matching between data and MC simulation regarding the distributions of these variables.

variable	maximum value
$\chi_{ITS}^2/N_{cls}^{ITS}$	5
$N_{shared}^{ITS}/N_{cls}^{ITS}$	40%
χ_G^2	10

Table 5.3 : Additional cuts for secondary track rejection.

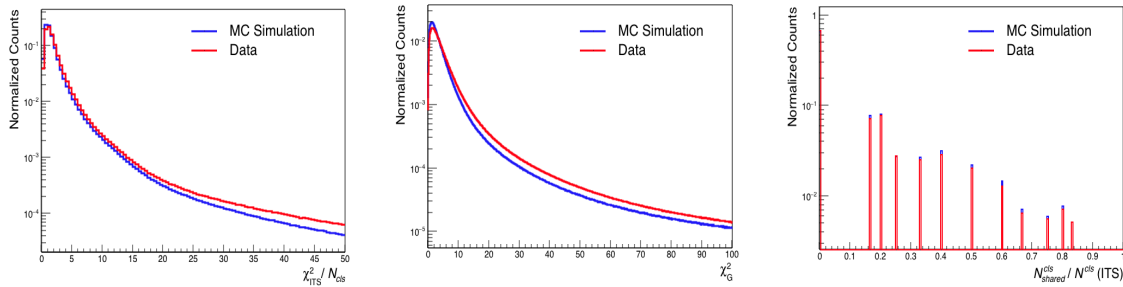


Fig. 5.23 : Comparison between data and MC simulation regarding the distributions of χ_{ITS}^2/N_{cls} , golden- χ^2 and fraction of shared clusters in ITS.

These additional track cuts reduced the absolute number of conversion electrons as well as their relative contribution to the selected track sample (Fig. 5.24).

5.3.2 Conversion Rejection Using Pair Cuts

Conversion rejection methods using pair cuts exploit the pair correlations between the conversion products and their relative orientation with respect to the magnetic field. Electrons and positrons produced by photon conversion in the material have zero mass (neglecting the recoil momentum of the nucleus involved in the process) and, as a consequence, no intrinsic opening angle. These particles are bent only in the azimuthal direction by the magnetic field. The tracks produced by conversion electrons have been extended inward to the primary vertex by the tracking algorithm and their

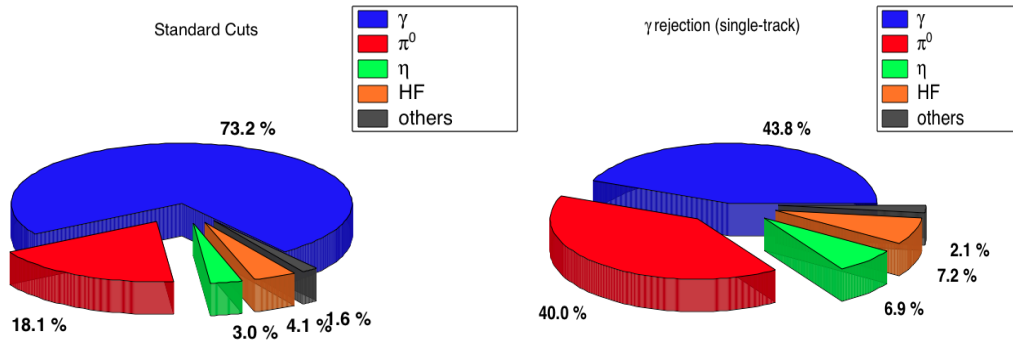


Fig. 5.24 : Composition of the track sample before the additional track cuts (left) and after the conversion rejection cuts on single-track basis (right).

momenta have been estimated at the point of closest approach to the primary vertex. This procedure created an artificial opening angle (and mass), which become larger for increasing distances of the conversion point from the primary vertex (Fig. 5.25).

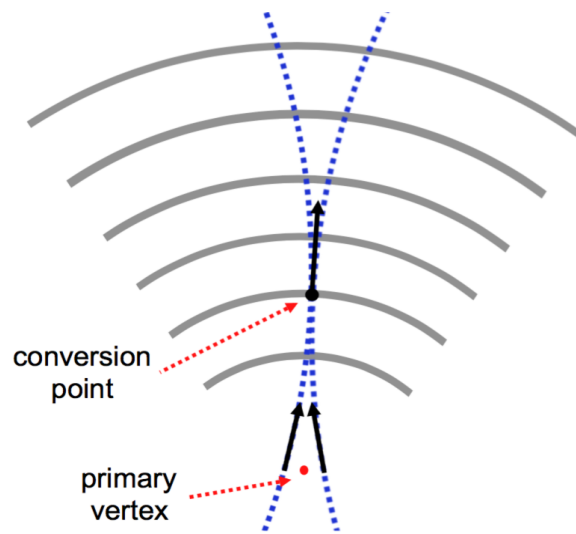


Fig. 5.25 : Schematic illustration of the artificial "creation" of the opening angle (and mass) of conversion pairs by the tracking algorithm.

Given a pair of particles, the vector connecting the ends of the momentum vectors of the two particles defines the orientation of their opening angle. The expected orientation of the opening angle of a conversion pair is given by:

$$\vec{w}_{\text{exp}} = \vec{p} \times \vec{z} \quad (5.5)$$

where $\vec{p} = \vec{p}_1 + \vec{p}_2$ is the total momentum of the photon, and \vec{z} is the orientation of the magnetic field (the z-axis). The measured orientation of the opening angle is given by:

$$\vec{w}_{\text{meas}} = \vec{p} \times \vec{u} \quad (5.6)$$

here \vec{u} is a unit vector perpendicular to the plane defined by the electron-positron pair ($\vec{u} = (\vec{p}_1 \times \vec{p}_2) / |\vec{p}_1 \times \vec{p}_2|$). A discriminating variable to identify conversion electrons is the angle, called ϕ_V , between the expected and measured orientation of their opening angle:

$$\cos(\phi_V) = \vec{w}_{\text{exp}} \cdot \vec{w}_{\text{meas}} \quad (5.7)$$

Conversion pairs should have $\phi_V = 0$ or $\phi_V = \pi$, depending on the charge ordering of the two particles, while no preferred value exists for electrons originating from other sources (Fig. 5.26).

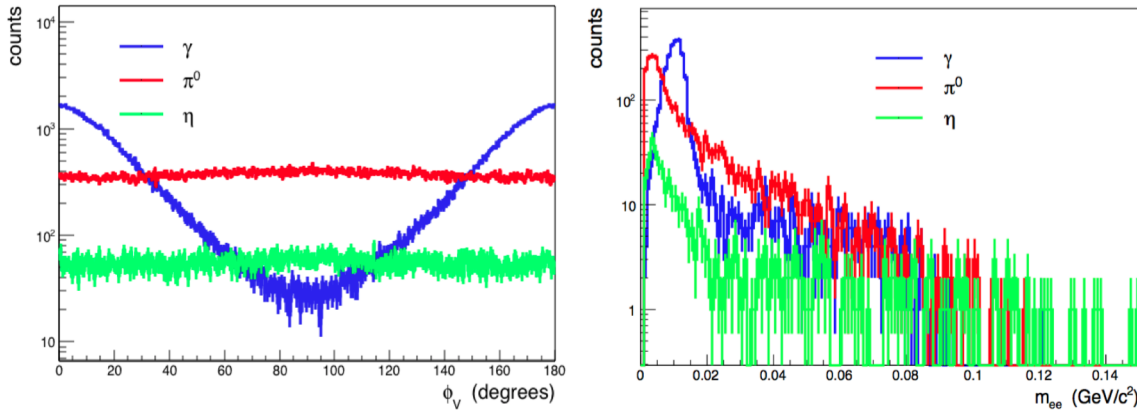


Fig. 5.26 : ϕ_V distribution (left) and mass distribution (right) for correlated e^+e^- pairs originating from different dielectron sources.

The ϕ_V distribution for conversion electrons is characterized by two broad peaks at 0 and π , whose widths are an artifact of the tracking feature. For zero opening angle, in fact, ϕ_V is not defined and the resulting distribution is uniform. For close conversions, the artificial opening angle created by the inward track propagation is small and the resulting ϕ_V distribution shows less deviation from flatness. This contributes to the broadening of the two symmetric peaks.

The ϕ_V angle can be exploited, together with the mass, to identify conversion electron candidates. Considering that in most of the cases only one component of a pair was reconstructed, a track sample with looser cuts has been used for tagging particles in

the selected set of tracks in order to enhance the probability to retrieve its missing partner (Fig. 5.27). In particular, no p_T threshold has been applied, a wider acceptance has been considered, looser cuts have been applied on the DCA to the primary vertex ($DCA_{xy} < 1$ cm, $DCA_z < 3$ cm) and less strict requirements have been requested regarding the general TPC cuts and the hit on the first ITS layer.

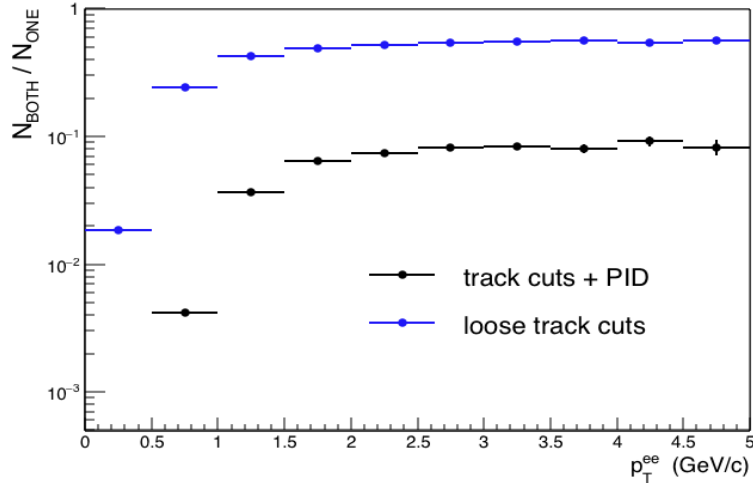


Fig. 5.27 : Fraction of pairs with both components detected, as a function of p_T^{ee} , for different cuts applied on the set of tracks used for tagging. The probability to retrieve the missing partner is larger when looser cuts are applied.

Pairs between particles, one taken from the set of tracks selected for the analysis and the other one taken from the sample with looser cuts, have been considered. Particles in the selected track sample have been tagged as conversion candidates if the mass and ϕ_V of the pairs they form with the other particles satisfied the following requirements:

$$5 < m_{ee} < 15 \text{ MeV}/c^2$$

$$0^\circ < \phi_V < 40^\circ$$

$$140^\circ < \phi_V < 180^\circ$$

Fig. 5.28 shows the $\phi_V - m_{ee}$ distribution of correlated electron-positron pairs produced by photon conversion, after they have passed the single track rejection. The regions used for tagging the conversion candidates are also indicated.

The tagging criterion holds for both opposite-sign and same-sign pairs. The latter have been considered in order to enhance the rejection efficiency of this method by exploiting the pair correlations between "cross pairs", i.e. same-sign pairs originating from the conversions of two photons produced by the same source (like $\pi^0 \rightarrow \gamma\gamma$). Fig. 5.29

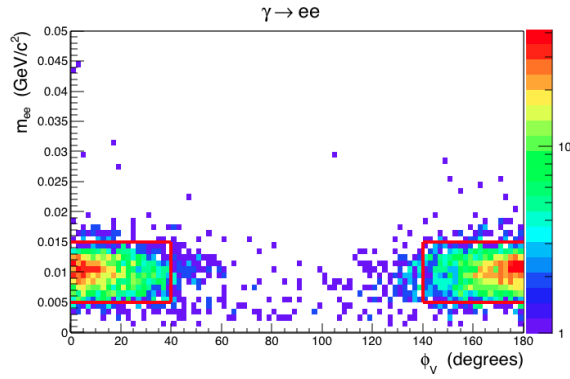


Fig. 5.28 : $\phi_V - m_{ee}$ distribution of correlated electron-positron pairs produced by photon conversion. Their tracks have passed the single-track conversion rejection. The regions used to define the conversion pair candidates are also indicated.

shows the $\phi_V - m_{ee}$ distributions for positive and negative same-sign pairs. Two clear peaks are visible at very low mass for $\phi_V \approx 0$ and $\phi_V \approx \pi$.

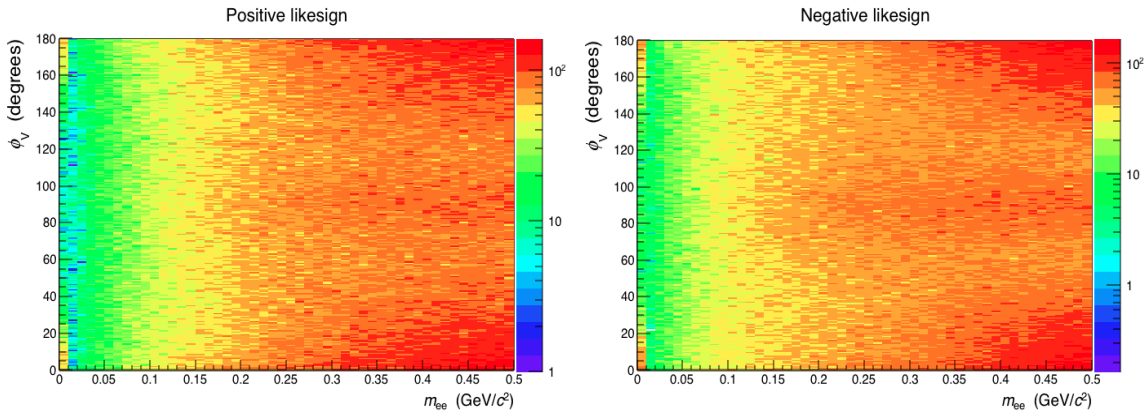


Fig. 5.29 : $\phi_V - m_{ee}$ distributions of positive (left) and negative (right) same-sign pairs. Two clear peaks are visible at low mass for $\phi_V \approx 0$ and $\phi_V \approx \pi$, coming from the correlations of "cross pairs".

Tracks that were tagged as conversion candidates have been rejected from the track sample before the pairings with all other tracks were done to obtain the opposite-sign invariant mass distribution. This procedure of active background rejection reduced the contribution of conversion candidates to the combinatorial background. This resulted in an overall improvement of the signal-to-background ratio by a factor ≈ 1.5 , approximately constant in the low-mass region ($m_{ee} < 700 \text{ MeV}/c^2$) (Fig. 5.30). No significant improvement was observed in the statistical significance, defined as $s = S/\sqrt{S + 2B}$, S being the signal (background subtracted yield) and B the background (see Chapter 6).

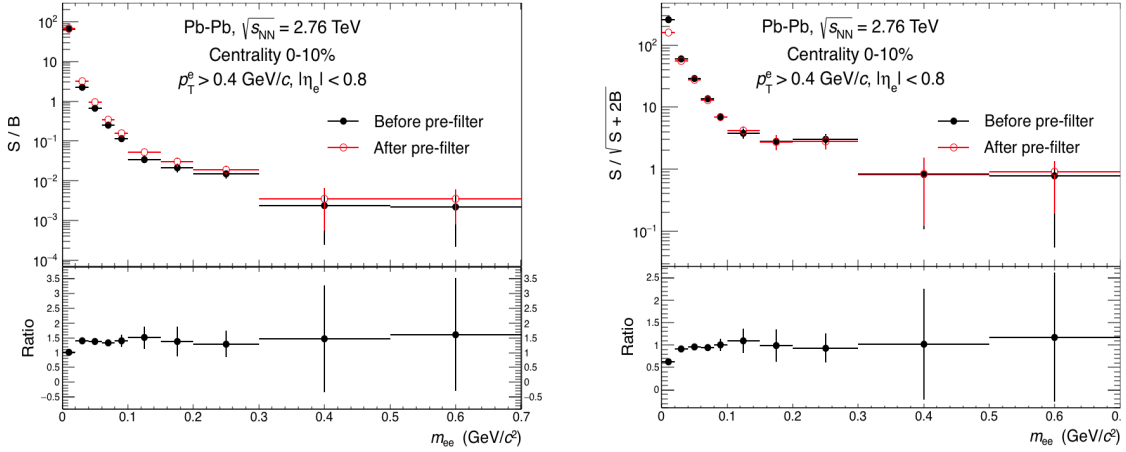


Fig. 5.30 : Effect of pair pre-filter on the S/B ratio(left) and on the statistical significance (right). The improvement of the S/B ratio in the low mass region is ≈ 1.5 , while no effect has been observed in the significance.

The rejection criterion of a conversion electron can be fulfilled not only when a pair was formed with its partner, but also with an uncorrelated electron or with a hadron (random rejection). Fig. 5.31 shows the rejection probability of conversion electrons due to the pairings with different particles (the real partner, an uncorrelated electron and a hadron).

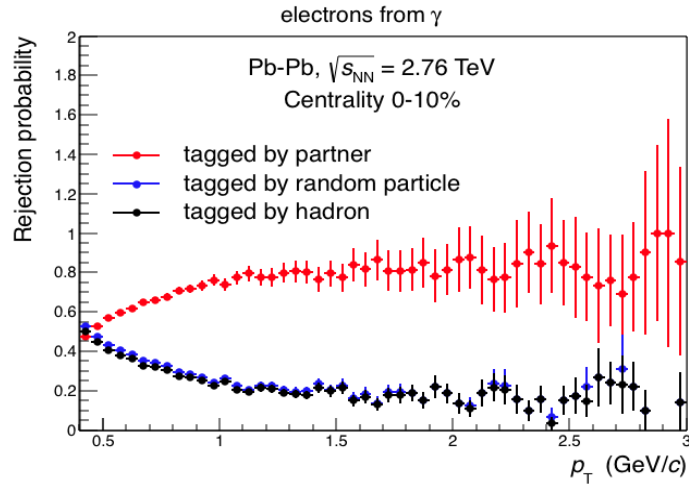


Fig. 5.31 : Rejection probability of conversion tracks due to different mechanisms: pairing with its partner (red), with an uncorrelated electron (blue) and with a hadron (black).

The increasing trend of the random rejection at low- p_T is due to the decreasing probability to detect the second component of the pair at low momenta.

The hadron contamination was expected to increase after the application of the

pre-filter due to its preferred rejection of (conversion) electrons. The purity of the electron sample obtained after the pre-filter has been estimated and a negligible decrease was found both in central and semi-central collisions (Fig. 5.32). No further optimization of the PID scheme has been done after the pre-filter.

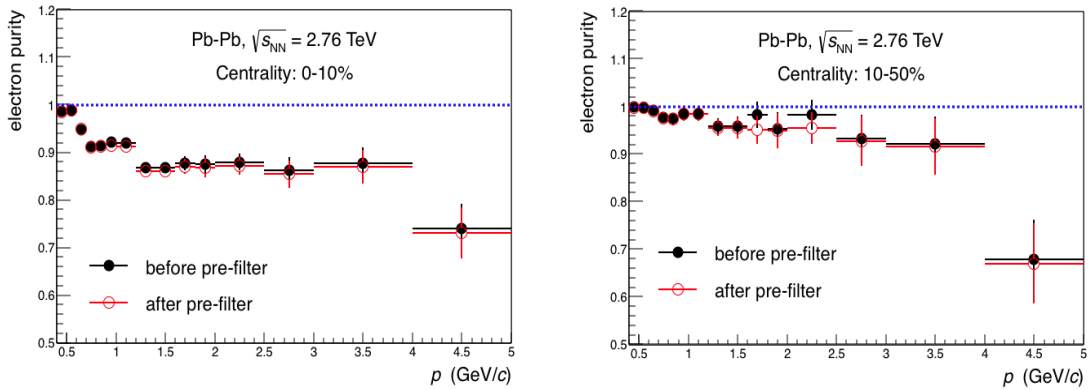


Fig. 5.32 : Effect of pair pre-filter on electron purity in central (left) and semi-central collisions (right).

The random rejection of signal, which occurs when "good" tracks fulfilled the rejection criteria, affected the pair reconstruction efficiency. The additional correction needed to take into account the signal loss due to the pre-filter has been calculated using the MC simulations and incorporated into the pair efficiency calculation (see Chapter 7).

The pair pre-filter gave a further contribution to reducing the relative abundance of conversion electrons to the selected track sample. Fig. 5.33 shows the relative abundances of electrons from different sources in the selected set of tracks, obtained from MC simulations, before and after conversion rejection methods for comparison. The relative contribution of conversion electrons has been reduced from $\approx 73\%$ to $\approx 37\%$, while the contribution of primary electrons, like those from η -Dalitz decay, has been increased by a factor > 2 .

5.3.3 Comparison Between Single-track and Pair Rejection Methods

Fig. 5.34 shows the rejection probability, of both conversion and primary electrons, obtained for three different cases: when single-track rejection or pair pre-filter only have been applied, and when both methods have been combined.

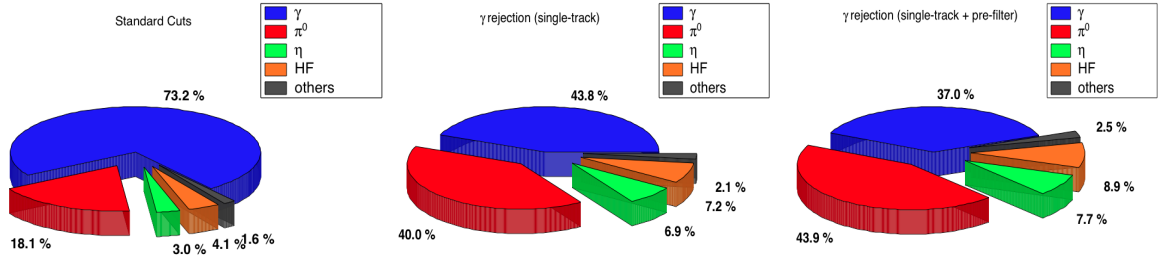


Fig. 5.33 : Relative abundances of electrons from different sources in the selected track sample before conversion rejection (left), after single-track conversion rejection (middle) and after the application of both conversion rejection methods (single-track and pair pre-filter) (right). The relative contribution of conversion electrons is significantly reduced (from $\approx 73\%$ to $\approx 37\%$), while that of primary electrons is increased by a factor >2 .

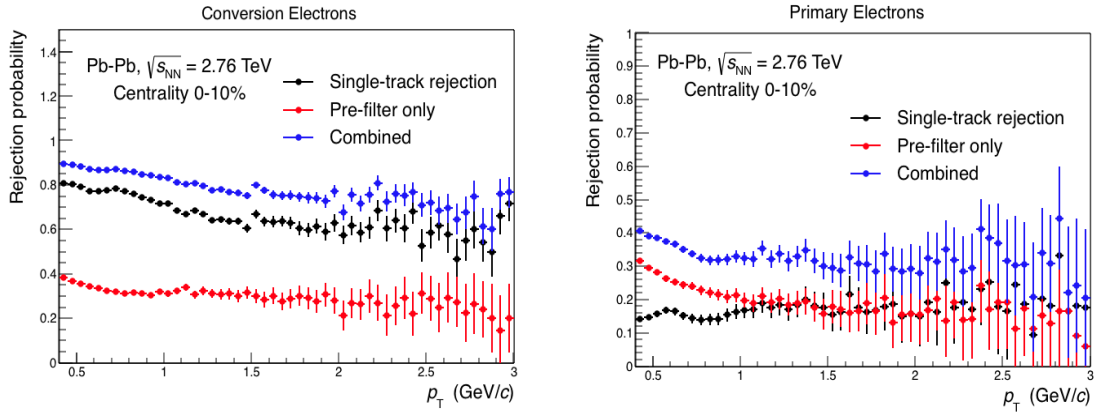


Fig. 5.34 : Rejection probability of conversion electrons (left) and primary electrons (right) due to different conversion rejection methods.

The conversion rejection on a single-track basis is twice more efficient compared to pair rejection due to the low fraction of pairs with both components reconstructed. This limited the rejection power of the methods based on pair correlations. The rejection probability of primary electrons was higher in the pre-filter case, due to the relatively large number of random pairings with uncorrelated partners which fulfilled the rejection requirements. This was due to the large phase space population obtained when using loose cuts on the partner. The combined effect of the two complementary rejection methods gave a rejection probability of conversion electrons around $\approx 90\%$ and a loss of primary electrons $\sim 40\%$. As already mentioned, the correction for signal loss due to the latter has been included in the pair reconstruction efficiency (see Chapter 7).

Chapter 6

Background Estimation and Signal Extraction

6.1 Introduction

This chapter contains the description of the different components of the combinatorial background and the illustration of the methods used for its estimation. Detector inhomogeneities created a small charge asymmetry which affected the invariant mass distribution used for the background description. The procedure used to calculate the correction factor for this geometrical effect is explained. The contribution from the hadronic background, i.e. the effect of hadron contamination on the dielectron spectrum, is shown and the correction factor is illustrated. In the second part of this chapter, which is dedicated to the signal extraction, the dielectron raw yield, the signal-to-background ratio and the statistical significance of this measurement are presented. Finally, the effect of non-uniform efficiency of the *kCentral* trigger on the dielectron spectrum is discussed.

6.2 Background Components

The combinatorial background in the dielectron spectrum originates from the sequential pairings between oppositely charged dielectron pairs. This contains two components: the *uncorrelated background*, due to random pairings, and the *correlated background*. The latter contains contributions from "cross pairs" and from dielectron pairs produced in the decays of different hadrons flying into the same jet or in back-to-back jets. In the cross pairs, there is a direct correlation between the first electron (positron) and the parent of

the second electron (positron) or between the parents of the two particles. The main processes which produce cross pairs are the following:

- **Double conversion:** These are pairs in which the two components are produced in the conversions of two different photons which originate from the same hadron decay, e.g. $\pi^0 \rightarrow \gamma\gamma \rightarrow e^+e^-e^+e^-$.
- **Dalitz & conversion:** In these pairs, one electron (positron) comes from Dalitz decay of a neutral meson and the other electron (positron) comes from the conversion of the photon produced in the same neutral meson decay.
- **Double Dalitz:** These are dielectron pairs produced by neutral meson 4-body decays.

These are schematically illustrated in Fig. 6.1.

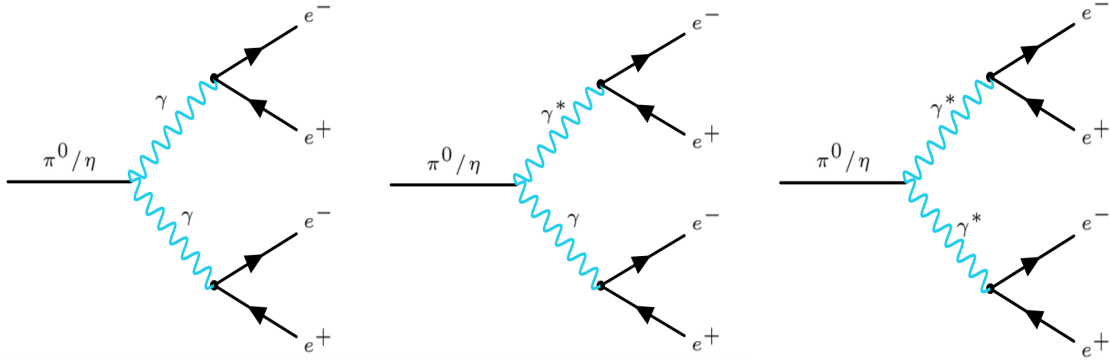


Fig. 6.1 : Processes that generate cross pairs: Double photon conversion (left), Dalitz decay & photon conversion (middle) and Double Dalitz decay (right).

The invariant mass of cross pairs is constrained by the kinematics of the process, since these pairs ultimately originate from the same hadron source. Cross pairs mainly contribute to the low-mass region of the dielectron spectrum.

The combinatorial background can be described by the invariant mass distribution of same-sign pairs, defined by the geometric mean:

$$\left[\frac{dn}{dm_{ee}} \right]_{\text{bkg}} = 2 \cdot \sqrt{\left[\frac{dn}{dm_{ee}} \right]_{++} \cdot \left[\frac{dn}{dm_{ee}} \right]_{--}} \quad (6.1)$$

where $\left[\frac{dn}{dm_{ee}} \right]_{++}$ and $\left[\frac{dn}{dm_{ee}} \right]_{--}$ are the invariant mass distributions of positive and negative same-sign pairs, respectively. All processes contributing to correlated background

are charge symmetric, i.e. give identical contributions to the unlike-sign and like-sign mass distributions. In consequence the like-sign spectrum described by Eq.(6.1) conveniently incorporates the simultaneous description of both background components.

6.2.1 Charge Asymmetry

The like-sign invariant mass distribution, as defined in Eq.(6.1), did not reproduce the background shape due to some distortions caused by *charge asymmetry* (Fig. 6.2).

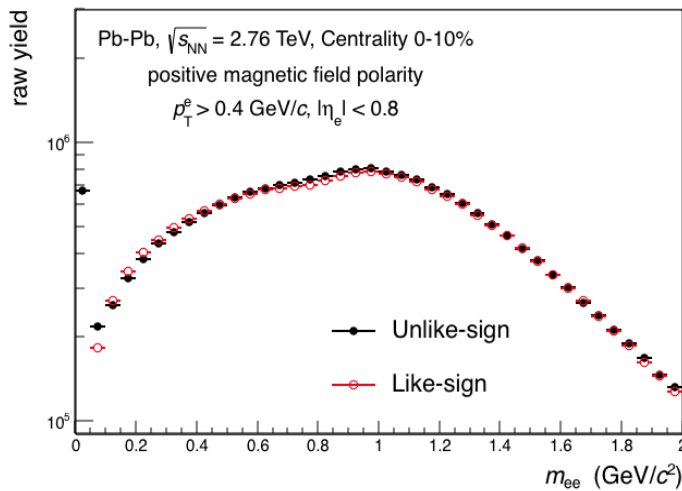


Fig. 6.2 : Distortions in the like-sign distribution caused by charge asymmetry.

Charge asymmetry was created by the different geometric acceptance of unlike-sign and like-sign dielectron pairs due to the detector inhomogeneity. Fig. 6.3 shows a sketch of the configuration of the ALICE experimental apparatus during Run 1 data taking period. The main geometrical asymmetries of the detector were due to the incomplete TRD installation, with five missing modules, in addition to some hardware problems in the Silicon Pixel Detectors, which created some gaps in its azimuthal coverage.

Particles hitting the TRD had a larger probability to be absorbed before reaching the TOF compared to those that passed through the gaps. This resulted in the modulation effect visible in the ratio between the azimuthal distributions of electrons and positrons (Fig. 6.4 right): electrons emitted at angles $0 < \phi < 1.5$ rad were bent in a region where no TRD module was installed, while positrons emitted at azimuthal angles within the same range were bent in the opposite direction, hitting the TRD. The effect was opposite when the magnetic field was reversed. The TRD modulation and the effect of the gaps in the ITS created an excess of particles with a given charge. These effects of charge asymmetry were stronger at low p_T , since the curvature of the particles was

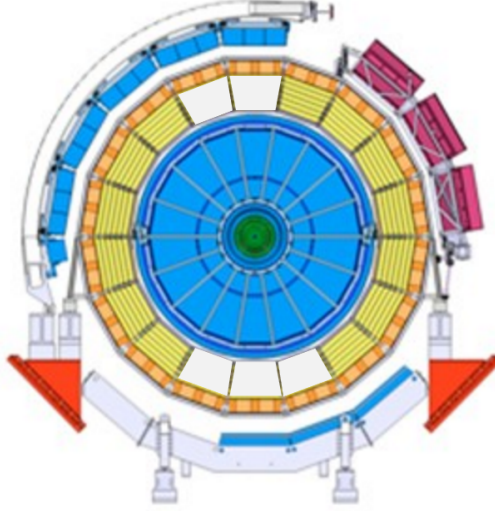


Fig. 6.3 : Sketch of the ALICE experimental apparatus during Run 1 data taking period. The TRD modules are indicated in the figure by the yellow blocks surrounding the TPC, indicated in blue. The white blocks represent the missing TRD modules.

such that they interacted with different regions of the detector which have different features and different acceptance, while at higher p_T particles were bent much less by the magnetic field, thus they had a larger probability to interact with the same region of the detector. The excess of particles with a given charge was therefore not uniform in p_T and this created significant differences between the transverse momentum distributions of electrons and positrons (Fig. 6.4 left). In summary, the shapes of unlike-sign background and the like-sign invariant mass distribution are the same, but they appear different because of the different acceptance. The effects created by this charge asymmetry have been corrected before using the like-sign distribution as background estimator.

6.2.2 Acceptance Correction: the R-factor

The correction factor for the different acceptance of same-sign and opposite-sign pairs, the so-called R -factor, has been defined as the ratio between the invariant mass distributions of unlike-sign and like-sign pairs, in which the two particles were taken from different events:

$$R = \frac{\left[\frac{dn}{dm_{ee}} \right]_{+-}^{\text{mix}}}{2 \cdot \sqrt{\left[\frac{dn}{dm_{ee}} \right]_{++}^{\text{mix}} \cdot \left[\frac{dn}{dm_{ee}} \right]_{--}^{\text{mix}}}} \quad (6.2)$$

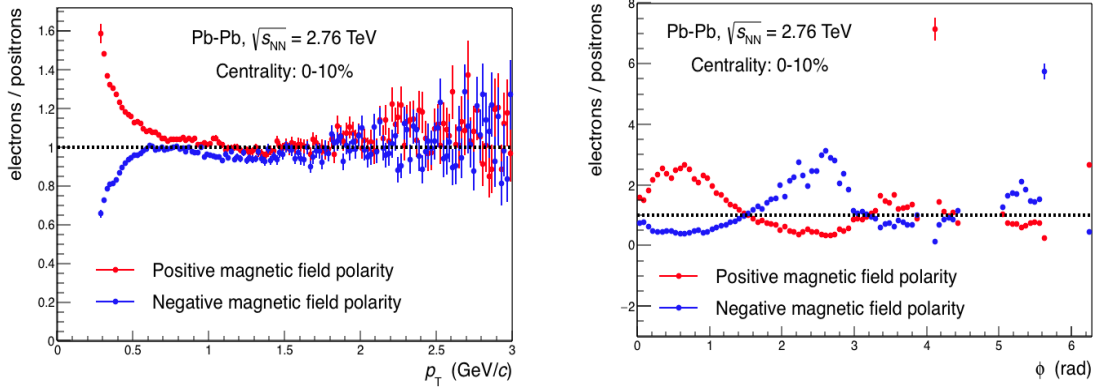


Fig. 6.4 : Ratio between electrons and positrons as a function of p_T (left) and ϕ (right). The modulation in ϕ was due to the geometrical inhomogeneity of the experimental apparatus created by a non-uniform installation of the TRD, while the gaps were due to some hardware problems in the SPD.

Different events have, by definition, no correlation with each other and hence the R -factor, which is expected to be one in case of zero charge asymmetry, can only depend on the different geometrical acceptance of same-sign and opposite-sign pairs. The charge asymmetry correction has been obtained by multiplying the like-sign distribution by the R -factor:

$$B_{\text{corr}} = 2 \cdot R \cdot \sqrt{\left[\frac{dn}{dm_{ee}} \right]_{++} \cdot \left[\frac{dn}{dm_{ee}} \right]_{--}} \quad (6.3)$$

The events from which the two particles were taken have been required to have similar global features. In fact, as an example, in events with large multiplicity, particles have on average smaller momenta compared to events with lower multiplicity. Different momentum distributions produced also different mass distributions and mixing events with very different characteristics might result in unwanted distortions in the correction factor. During the on-line event-mixing procedure, events were sorted into different categories, defined by the centrality, z -coordinate of the primary vertex and orientation of the event plane. The ranges that defined these categories are indicated in Table 6.1.

In the calculation of the R -factor, only pairs of particles taken from different events belonging to the same category have been considered. Charge asymmetry had opposite effects for different magnetic field orientations and in consequence the shape of the R -factor also depended on the magnetic field orientation. Fig. 6.5 shows the R -factor shapes in central collisions (0-10%), for opposite magnetic field orientations and in different transverse momentum ranges.

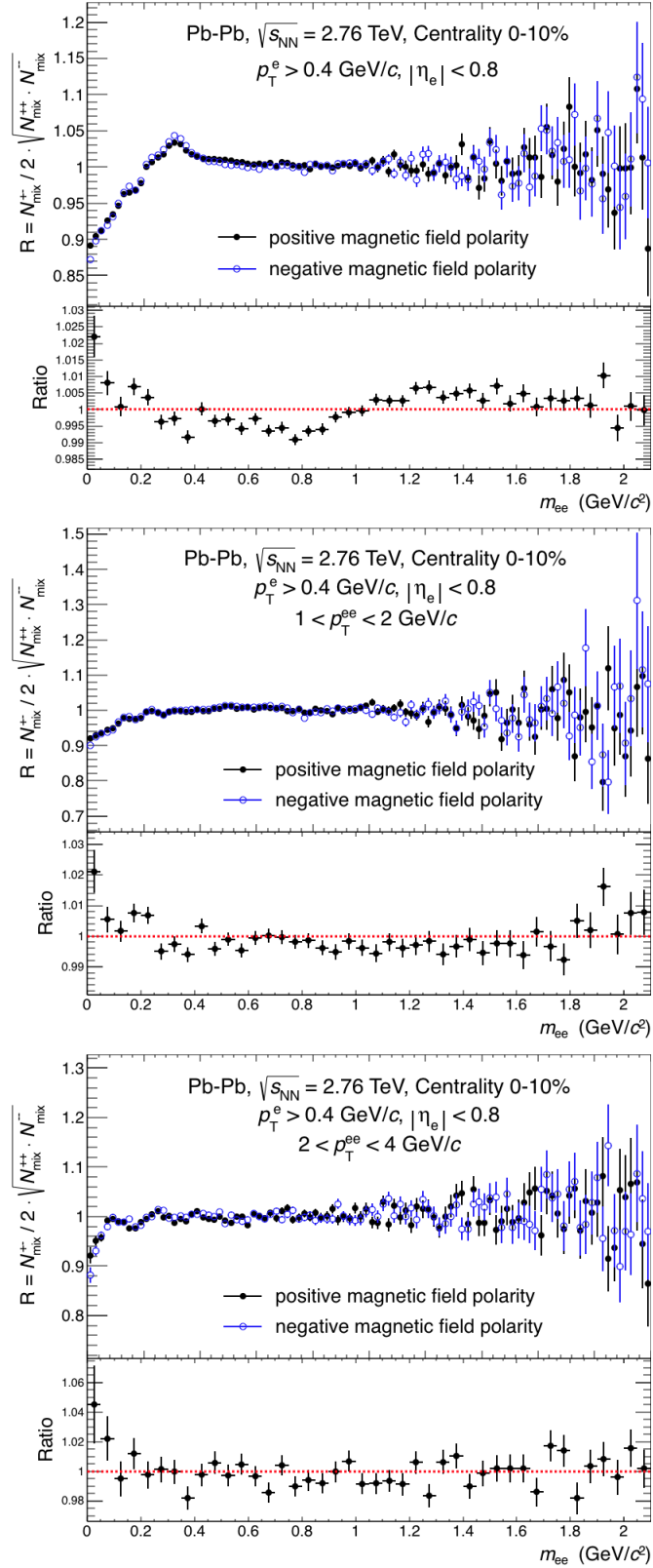


Fig. 6.5 : R -factor shapes in central collisions (0-10%) for opposite magnetic field polarities for p_T^{ee} -integrated (top) and in the p_T^{ee} ranges: $1 < p_T^{ee} < 2$ GeV/c (middle) and $2 < p_T^{ee} < 4$ GeV/c (bottom).

centrality (%)	z -coordinate of the vertex (cm)	event plane angle (rad)
[0, 2.5, 5, 7.5, 10]	[-10, -6, -2, 2, 6, 10]	$[-\pi/2, \pi/2]$
[10, 20, 30, 40, 50]	[-10, -5, 0, 5, 10]	$[-\pi/2, -\pi/4, 0, \pi/4, \pi/2]$

Table 6.1 : Ranges used to define the three dimensional cells used to sort events during the on-line event-mixing procedure.

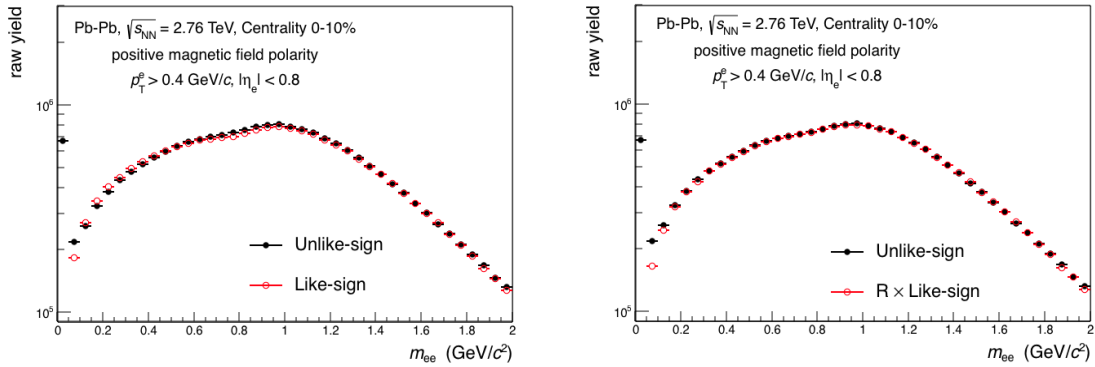


Fig. 6.6 : Dielectron invariant mass distributions of unlike-sign and like-sign pairs when no acceptance correction has been applied (left) and after the acceptance correction obtained from the event-mixing (right).

A deviation from flatness of the order of $\approx 2\%$ has been observed in the ratio between the R -factors obtained for opposite magnetic field orientations. High precision has been required in the background estimation due to the extremely small S/B ratio in the low-mass region. For this reason, the analyses of the two lists of runs, corresponding to different magnetic field orientations, have been performed separately. The final spectra have been merged together after the efficiency correction.

Fig. 6.6 shows the effect of the R -factor correction on the like-sign invariant mass distribution compared to the case when no correction has been applied.

6.3 Hadronic Background

The sample of selected tracks contained a small fraction of hadrons that were wrongly identified as electrons by the particle identification procedure. The hadron contamination was of the order of $\sim 10\%$ for central and $\sim 5\%$ for semi-central collisions (see Section 5.2.2). These hadrons entered the sequential pairings thus generating an additional

contribution to the dielectron invariant mass spectrum, given by the invariant mass spectrum of electron-hadron and hadron-hadron pairs. In the case of uncorrelated pairs, cross-pairs or particles inside the same jets or in back-to-back jets, their contribution has been removed by the combinatorial background subtraction since this was charge symmetric. Correlated pairs, instead, generated a fake signal, shifted to lower masses due to the electron mass assignment also to hadron tracks in the calculation of the invariant mass. The hadronic background, defined by the invariant mass distribution of correlated electron-hadron and hadron-hadron opposite-sign pairs, has been estimated using the MC simulations. A correction factor has been calculated in order to remove the hadronic background from the total invariant mass distribution.

The same level of hadron contamination estimated in real data has been reproduced in the simulations. To this end, the π/e , K/e and p/e ratios have been estimated from real data in each momentum range by fitting the $n\sigma_{TPC}$ using multiple skewed Gaussians. In the simulation, samples of pure electrons, pions, kaons and protons from HIJING sources have been selected.

The electron sample has been artificially "contaminated" by randomly selecting hadrons based on the estimated hadron-to-electron ratios. The inclusion probability has been defined by:

$$P_{incl}^h(p) = \frac{N_e(p)}{N_h(p)} \cdot \left(\frac{h}{e}\right)_{fit} \quad (h = \pi, K, p) \quad (6.4)$$

where $N_e(p)$ and $N_h(p)$ were the number of electrons and the number of hadrons of the type h in selected arrays for a given momentum range. Fig. 6.7 shows the hadron contamination as a function of the particle momentum, for central (0-10%) and semi-central (10-50%) collisions, estimated in real data and, for comparison, that obtained in the simulation with the method described above.

Fig. 6.8 shows the invariant mass distribution of correlated electron-hadron and hadron-hadron pairs in comparison to the invariant mass distribution of all pairs.

Correlated pairs contained particles produced in the decay of the same resonance, and higher order correlations¹. Bremsstrahlung and momentum resolution effects have been applied to the tracks produced by electrons², while they have been ignored for tracks produced by hadrons. In the latter case, the mass shift produced by resolution was negligible and radiative energy losses were much smaller compared to electrons. Proper weights have been used to adjust the input p_T spectra of HIJING sources (see Section

¹Particles which belong to the final products of a decay cascade started by the same unstable hadron.

²The procedure to simulate radiative energy loss and resolution is discussed in Section 7.4.1

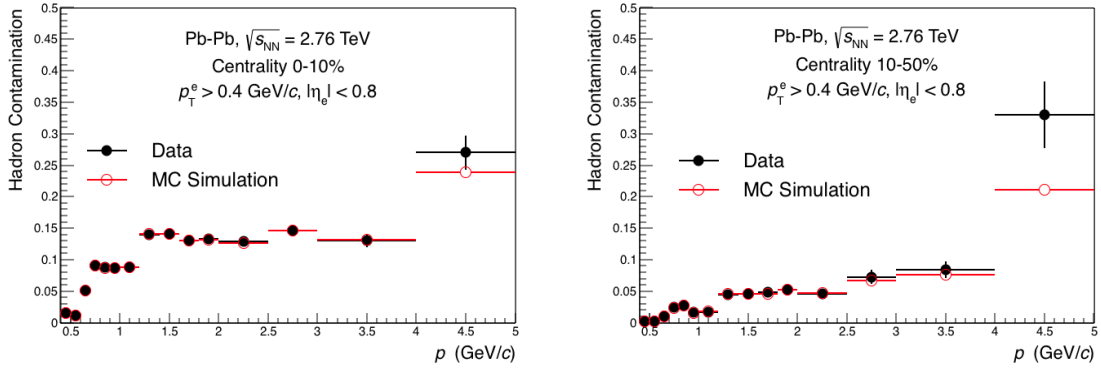


Fig. 6.7 : Comparison between the hadron contamination as a function of particle momentum estimated in real data and that obtained in the simulation, for central (left) and semi-central (right) collisions.

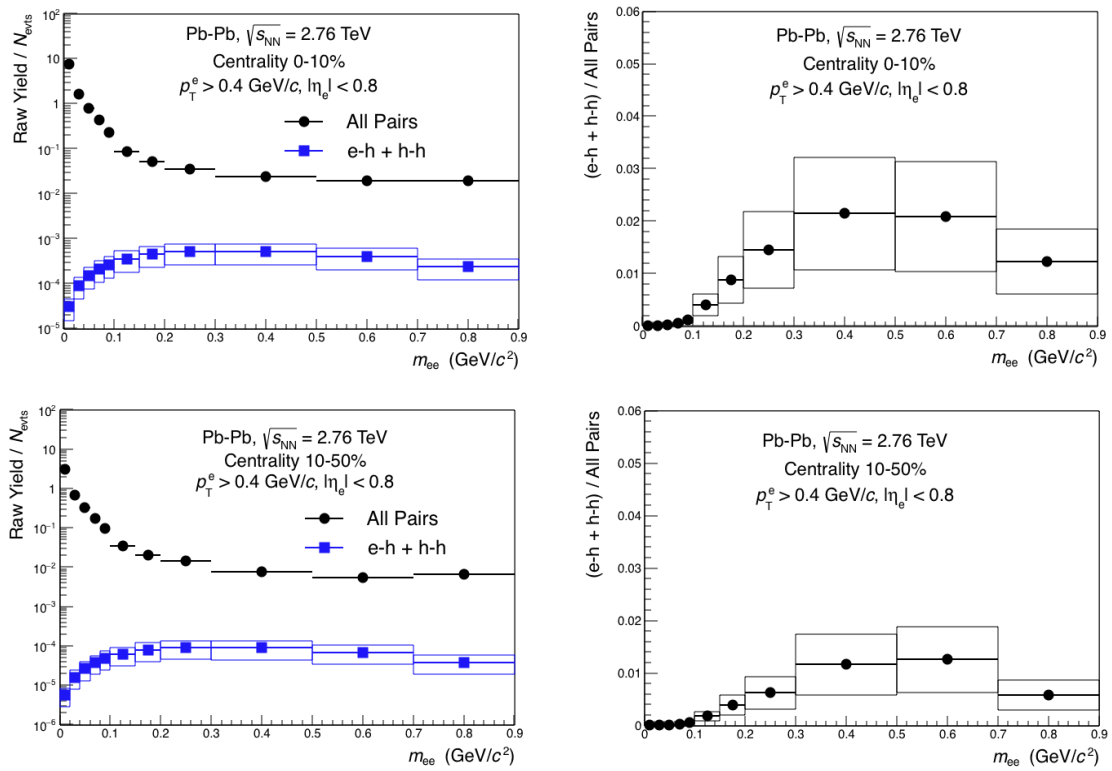


Fig. 6.8 : Invariant mass distribution of correlated electron-hadron and hadron-hadron pairs (hadronic background) in comparison to the total invariant mass distribution (left) and its relative contribution (right) for central (top row) and semi-central (bottom row) collisions.

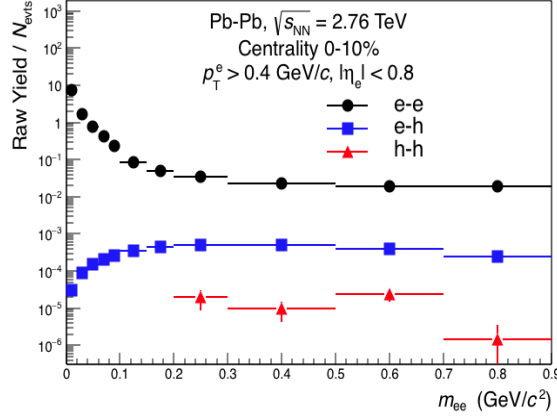


Fig. 6.9 : Individual components of the hadronic background (electron-hadron and hadron-hadron invariant mass spectra) in comparison to the invariant mass distribution of dielectron pairs.

7.3), including a normalization factor to scale the contribution from heavy-flavor decays. Dielectrons from η' , ρ^0 , ω and ϕ were missing in the simulation since the branching ratios of these particles into dielectrons were set to zero in HIJING. The correction factor is hence overestimated around the mass regions of these resonances ($0.75 \lesssim m_{ee} \lesssim 1.1 \text{ GeV}/c^2$). A systematic uncertainty of 50% has been applied to the contribution from the hadronic background in order to account for possible missing contributions in the simulation and for the uncertainties in the estimate of the single-track hadron contamination. This has been added in quadrature to all other systematic uncertainties (see Section 8.2). The impact of the hadron contamination on the dielectron invariant mass spectrum was negligible at low mass ($m_{ee} < 100 \text{ MeV}/c^2$) and it reached a maximum value of $\sim 2\%$ in central collisions and $\sim 1\%$ in semi-central collisions. Fig. 6.9 shows the electron-hadron and hadron-hadron components of the hadronic background separately in comparison to the invariant mass spectrum of electron-positron pairs for central collisions.

The contribution of the hadron-hadron component to the total hadronic background was negligible ($\sim 10^{-5}$). Among all electron-hadron pairs, the largest contribution ($\approx 94\%$) came from correlated heavy-flavor decays. In order to remove the contribution from the hadronic background from the total mass spectrum, the latter has been multiplied by the following correction factor:

$$F = 1 - \frac{e - h + h - h}{\text{All pairs}} \quad (6.5)$$

Fig. 6.10 shows these correction factors for central and semi-central collisions in different transverse momentum ranges.

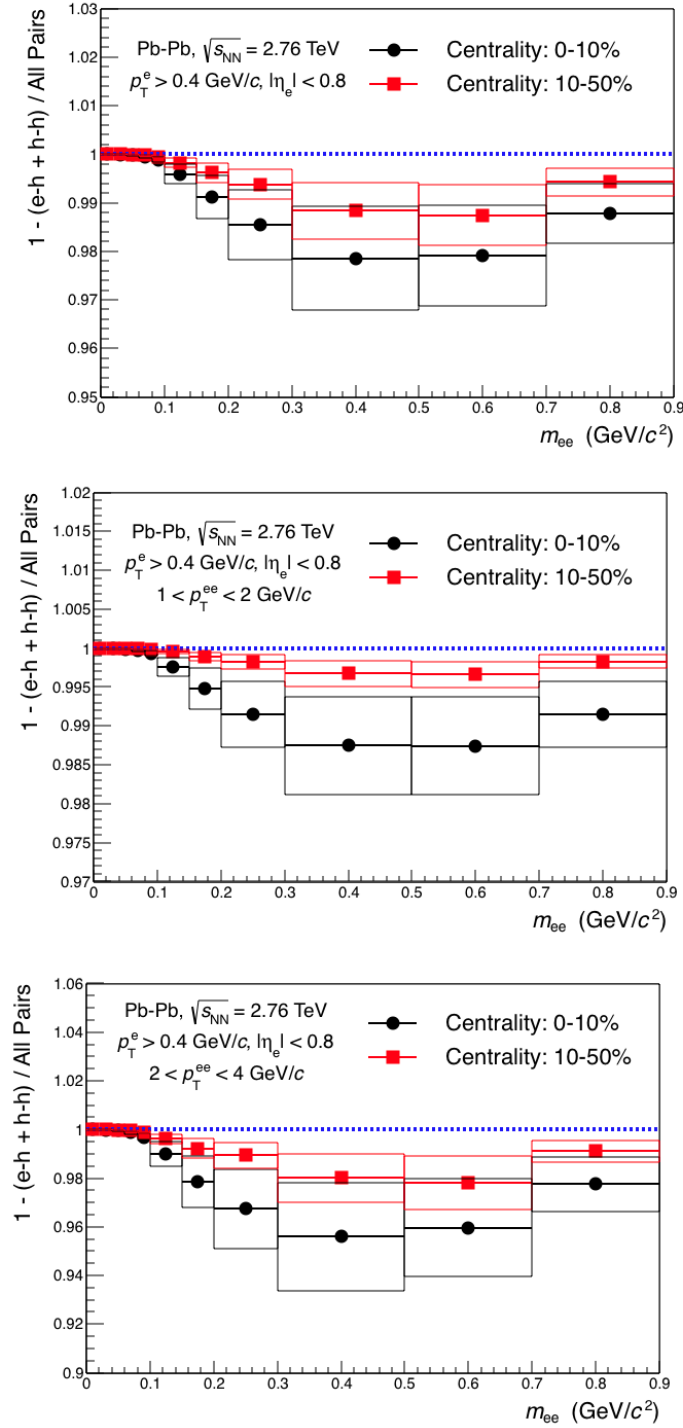


Fig. 6.10 : Correction factors, for central and semi-central collisions and in different transverse momentum ranges, used to remove the contribution of the hadronic background from the dielectron raw yield.

6.4 Signal Extraction

The dielectron raw yield as a function of the invariant mass ($S(m_{ee})$) has been extracted by subtracting the R -factor corrected like-sign invariant mass distribution from the unlike-sign foreground:

$$S = \left[\frac{dn}{dm_{ee}} \right]_{+-} - 2 \cdot R \cdot \sqrt{\left[\frac{dn}{dm_{ee}} \right]_{++} \cdot \left[\frac{dn}{dm_{ee}} \right]_{--}} \quad (6.6)$$

This was then corrected to remove the contribution of hadronic background. Fig. 6.11 shows the dielectron raw yield per event, for the negative magnetic field polarity, in central (0-10%) and semi-central (10-50%) collisions and in different transverse momentum ranges.

The statistical significance is defined by the ratio between the raw yield S and its statistical uncertainty:

$$s = \frac{S}{\Delta S} \quad (6.7)$$

The statistical uncertainty on the raw yield, assuming Poissonian distributions for the observed number of counts in all invariant mass bins for the unlike-sign U and background B distributions³, was given by:

$$\Delta S = \sqrt{(\Delta U)^2 + (\Delta B)^2} \quad (6.8)$$

The unlike-sign mass spectrum U was given by the sum of the signal S and the "true" background B_0 , $U = S + B_0$, hence:

$$\Delta S = \sqrt{(\Delta S)^2 + (\Delta B_0)^2 + (\Delta B)^2} \quad (6.9)$$

It was reasonable to assume that the statistical fluctuations of the "true" background B_0 and the estimated background B were of the same magnitude ($(\Delta B_0)^2 = (\Delta B)^2 = B$). Assuming Poissonian statistics also for the dielectron signal, one gets:

$$s = \frac{S}{\sqrt{S + 2B}} \quad (6.10)$$

Fig. 6.12 shows the S/B ratio and statistical significance for central (0-10%) and semi-central (10-50%) collisions with negative magnetic field polarity for different transverse momentum ranges.

³The statistical uncertainty of the R -factor can be neglected due to the larger statistics in event-mixing compared to real events.

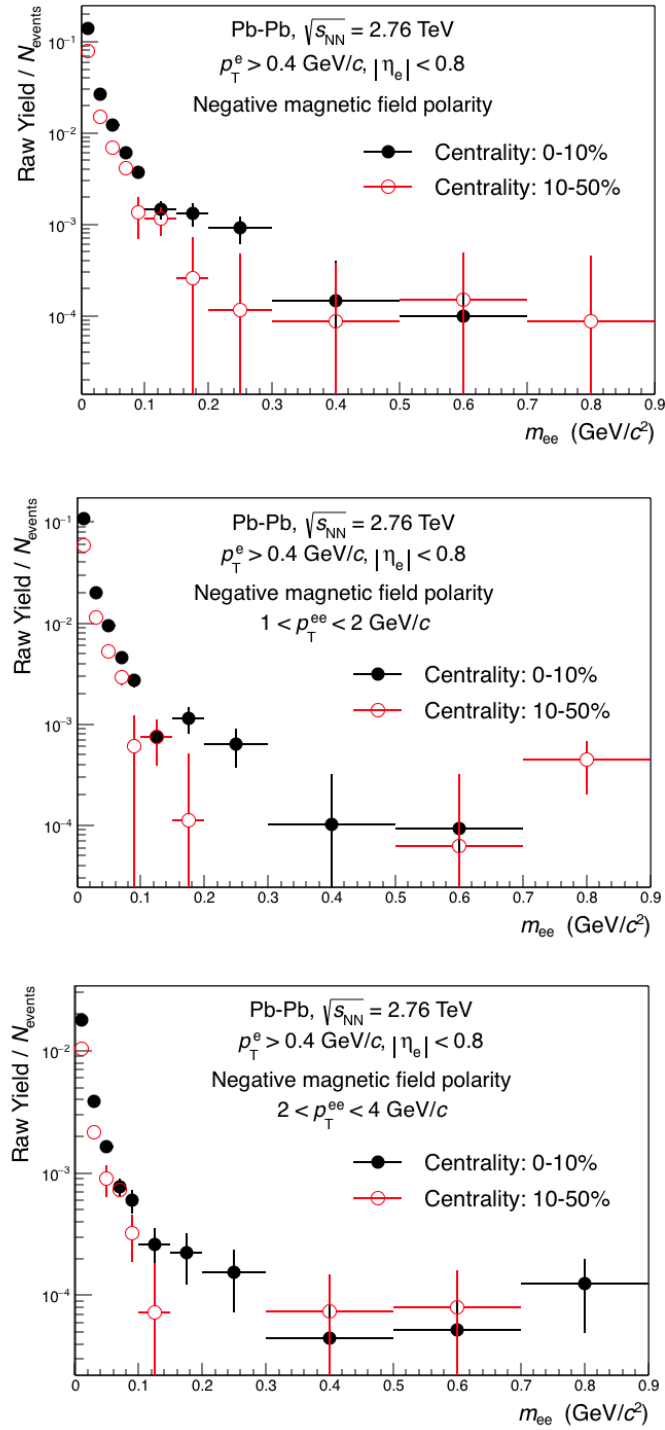


Fig. 6.11 : Dielectron raw yield, normalized to the number of events with negative magnetic field polarity, in central (0-10%) and semi-central (10-50%) collisions in different transverse momentum ranges.

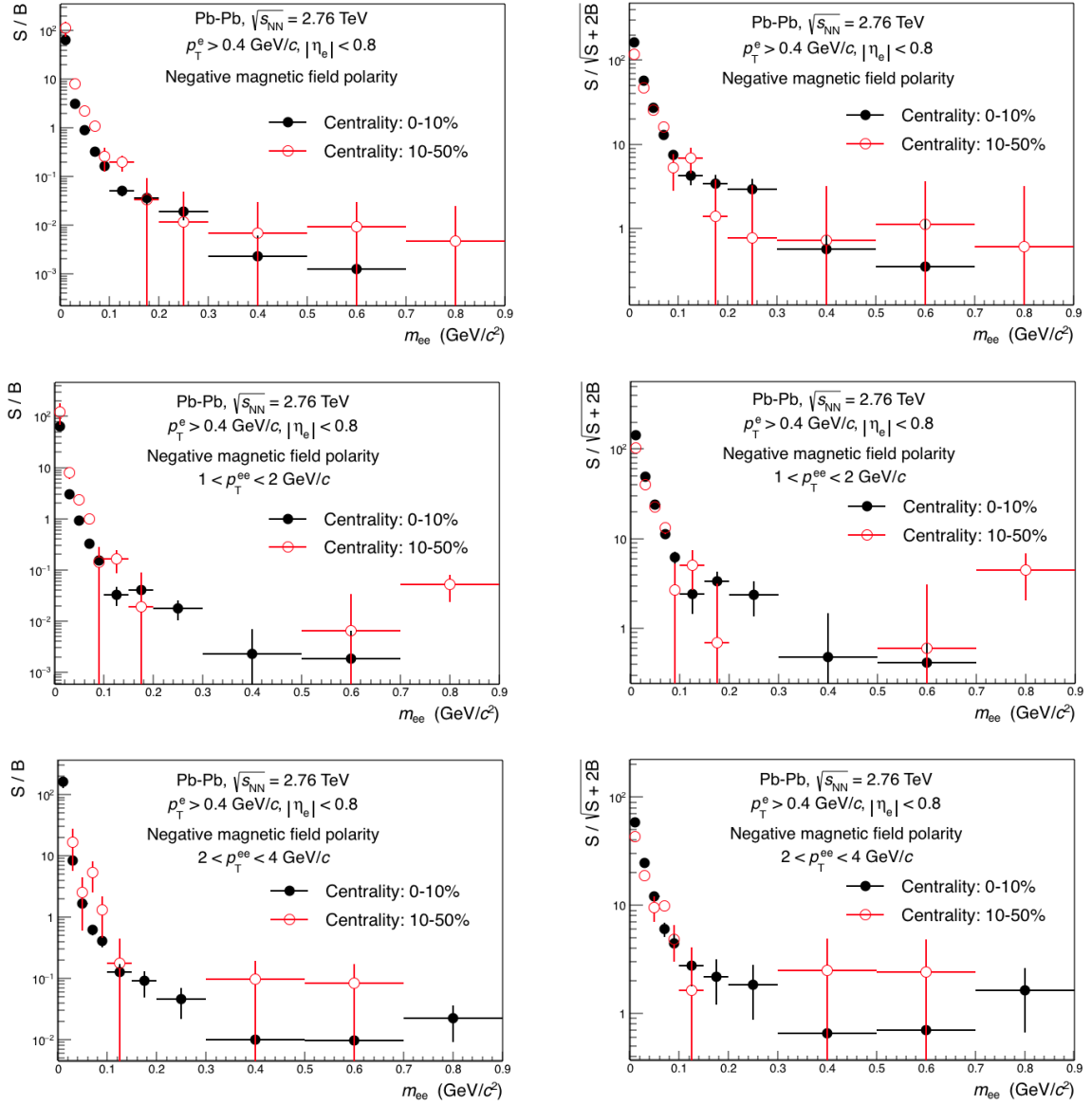


Fig. 6.12 : S/B ratio (left) and statistical significance (right) for central (0-10%) and semi-central (10-50%) collisions with magnetic field polarity for different transverse momentum ranges.

6.5 Impact of the Non-Uniformity in the *kCentral* Trigger Efficiency

The centrality distribution in Pb–Pb collisions is uniform since the collision probability between two nuclei is identical for different impact parameters. As shown in Section 4.8, however, the centrality distribution for events selected using the *kCentral* centrality trigger was not uniform in the full range 0-10%. A decreasing trend has been observed in the centrality range 8-10% caused by non-uniformity in trigger efficiency. For convenience and for a better illustration, the graph of the centrality distribution is reported in Fig. 6.13.

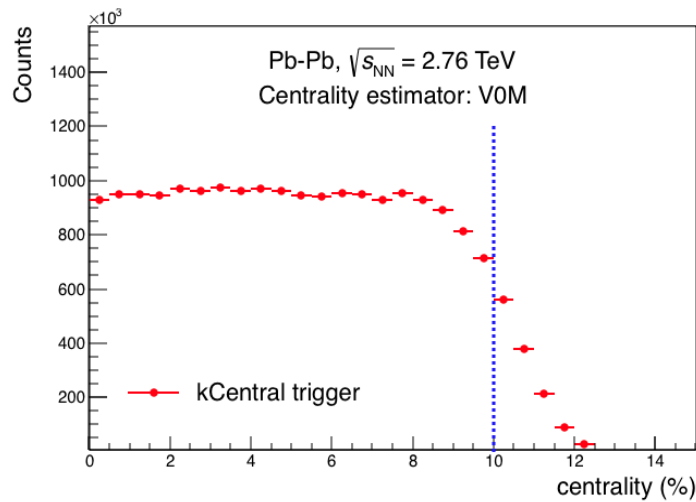


Fig. 6.13 : Centrality distribution of events selected using the *kCentral* centrality trigger. The distribution is not uniform over the whole range 0-10%, but it shows a decreasing trend in the range 8-10% due to non-uniformity of the trigger efficiency.

The dielectron invariant mass spectrum could be affected by a non-uniform centrality distribution due to differences in the momentum distributions of electrons for different centralities. In more central collisions, for example, characterized by higher multiplicities, the momentum distribution of electrons are steeper (their average momentum is smaller) compared to more peripheral collisions, due to the different number of particles which share the initial energy. In the case presented here, events with centrality in the range 0-8%, where the distribution showed smaller deviations from flatness, contributed in the right proportion to the dielectron spectrum while a smaller contribution came from events with centrality in the range 8-10%. The effect on the dielectron invariant mass spectrum of the non-uniform efficiency of the *kCentral* trigger has been studied by applying a "centrality flattening" procedure, which gave a uniform centrality distribution over the full

range 0-10%. The spectrum obtained for a flat centrality distribution has been compared to that obtained using the *kCentral* trigger. The centrality flattening procedure consisted in a random rejection of events according to a centrality-dependent probability. The rejection probability has been defined by:

$$P = \frac{y - y_0}{y} \quad (6.11)$$

where y is the number of counts in a given centrality bin and y_0 is the number of counts corresponding to the centrality range around 10%. This is illustrated in Fig. 6.14 left, while Fig. 6.14 right shows the random rejection probability in the centrality range 0-10%.

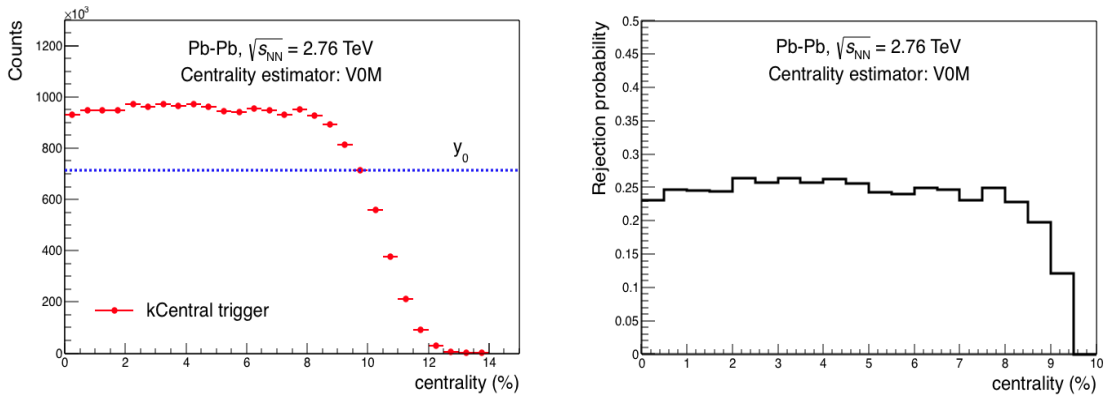


Fig. 6.14 : Illustration of the procedure to obtain the random rejection probability used in the "centrality flattening" procedure (left). Rejection probability of events as a function of centrality in the range 0-10% (right).

Fig. 6.15 shows the dielectron invariant mass spectra, for different transverse momentum ranges, obtained using the *kCentral* trigger in comparison to those obtained after the centrality flattening. These spectra were consistent within their statistical uncertainties in all p_T ranges, so it was concluded that the non-uniformity of the *kCentral* trigger efficiency did not produce a significant effect on the dielectron invariant mass spectrum measured in central (0-10%) Pb–Pb collisions.

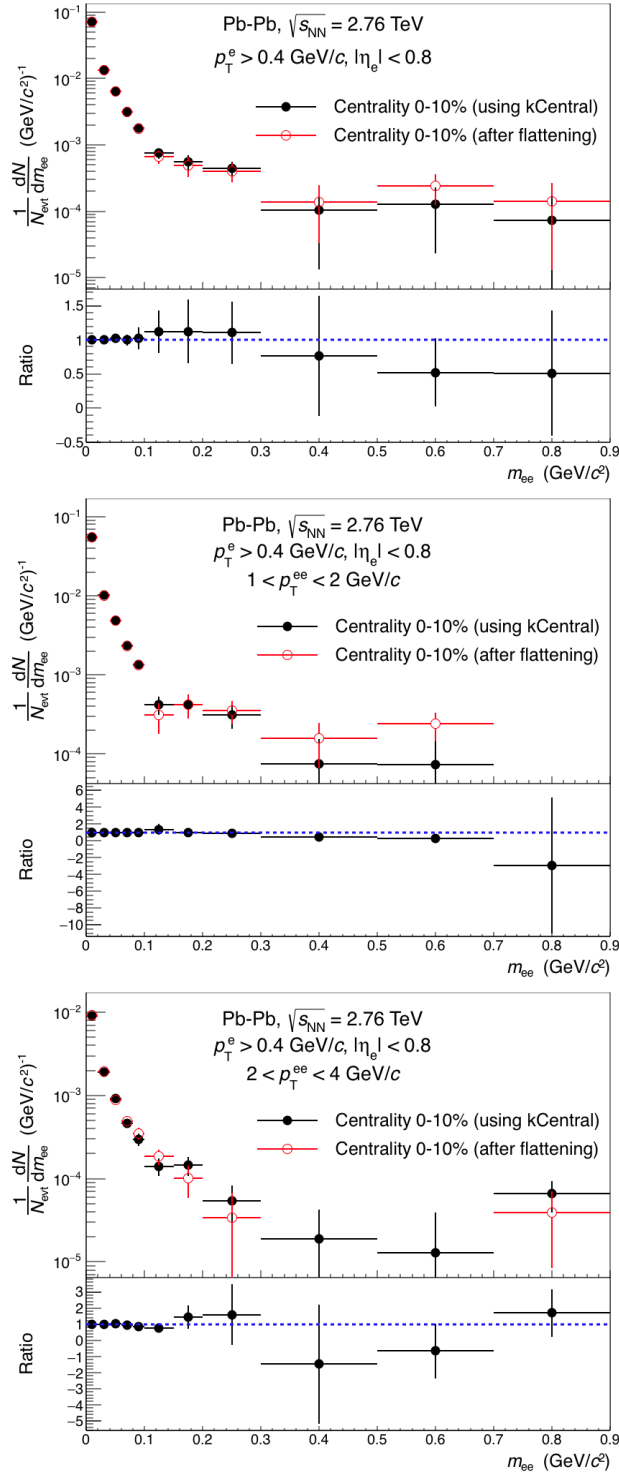


Fig. 6.15 : Comparison between the dielectron invariant mass spectra, for different transverse momentum ranges, measured in Pb–Pb collisions at $\sqrt{s_{NN}} = 2.76$ TeV in the centrality range 0-10% for events selected using the *kCentral* trigger and after the "centrality flattening" procedure.

Chapter 7

Efficiency Calculation and Hadronic Cocktail Simulation

7.1 Introduction

The dielectron raw yield as a function of the invariant mass needs to be corrected for the pair reconstruction efficiency. This is defined as the reconstruction probability of dielectron pairs produced in the collisions. The corrected spectrum represents the dielectron production as a function of the invariant mass in Pb–Pb collisions at $\sqrt{s_{\text{NN}}} = 2.76$ TeV in the selected kinematic region ($p_{\text{T}}^e > 400$ MeV/ c and $|\eta_e| < 0.8$). The corrected spectrum is represented in comparison with the expected contributions from hadron decays (hadronic cocktail) and from thermal dileptons. The former is obtained from simulations of hadron decays, constrained by the experimental measurements of the p_{T} -differential cross-section of the hadronic sources, while the latter is obtained from theoretical model calculations based on hydrodynamics and hadronic many-body theory (see Chapter 9). This chapter contains the description of the strategy used to estimate of the single-electron and pair reconstruction efficiencies and the illustration of how the hadronic cocktail is generated. The detector effects and their impact on the efficiency estimation, as well as in the cocktail simulation, are also discussed.

7.2 MC Simulations

The single-electron and pair reconstruction efficiencies have been estimated using "full MC simulations", namely including the propagation of the particles produced by the event generator through the ALICE experimental apparatus using GEANT 3, which

simulates their interaction with the detectors. The effects of tracking on single particle distributions (such as the momentum shift of secondary tracks) have also been included in the full simulation. The efficiency has been calculated by selecting electrons produced in the decays of HIJING sources and electrons from injected ω mesons. Electrons from other dielectron sources of the enriched sample have not been included in the efficiency calculation since only their two-body decays have been implemented in the simulation (see Table 4.2). These dielectron pairs would have given a partial coverage of the phase space ($m_{ee} - p_T^{ee}$) since only the mass regions around the resonances would have been populated. Electrons from the all dielectron sources have been selected to build the detector response matrices used to describe the detector effects.

7.3 Correction of the Input Spectra

7.3.1 Electrons from HIJING Sources

The p_T spectra of dielectron sources generated by Hijing are different from reality, and their shapes need to be corrected in order to avoid a wrong estimation of the pair reconstruction efficiency due to the non-uniformity of the single-electron reconstruction efficiency as a function of p_T^e , η_e and ϕ_e (Fig. 7.7). In fact, since the single-track efficiency has a decreasing trend moving to low- p_T^e , a steeper p_T distribution of an electron source, compared to the real distribution, would result in a larger yield of electrons at low p_T where the efficiency is smaller, thus causing an overall underestimation of the pair reconstruction efficiency.

The p_T distributions of dielectron sources produced by HIJING have been corrected by applying p_T -dependent weights. These are defined, for each dielectron source X and for each centrality range, as the ratio between the p_T spectrum obtained (or retrieved) from ALICE measurements and the p_T spectrum from Hijing:

$$w(p_T) = \frac{\left[\frac{dN^X}{dp_T} \right]_{\text{ALICE}}}{\left[\frac{dN^X}{dp_T} \right]_{\text{HIJING}}} \quad (7.1)$$

The parametrizations of the p_T spectra of neutral pions measured by ALICE in Pb–Pb collisions at $\sqrt{s_{\text{NN}}} = 2.76$ TeV [134] have been used for the centrality ranges: (0-5 %), (5-10 %), (10-20 %), (20-40 %), while the parametrization of the measured p_T spectrum of charged pions has been used for the centrality range (40-50 %) [47] due to the unavailability of π^0 measurement in this centrality range. Fig. 7.1 shows the pion spectra measured by ALICE in Pb–Pb collisions at $\sqrt{s_{\text{NN}}} = 2.76$ TeV in different centrality classes

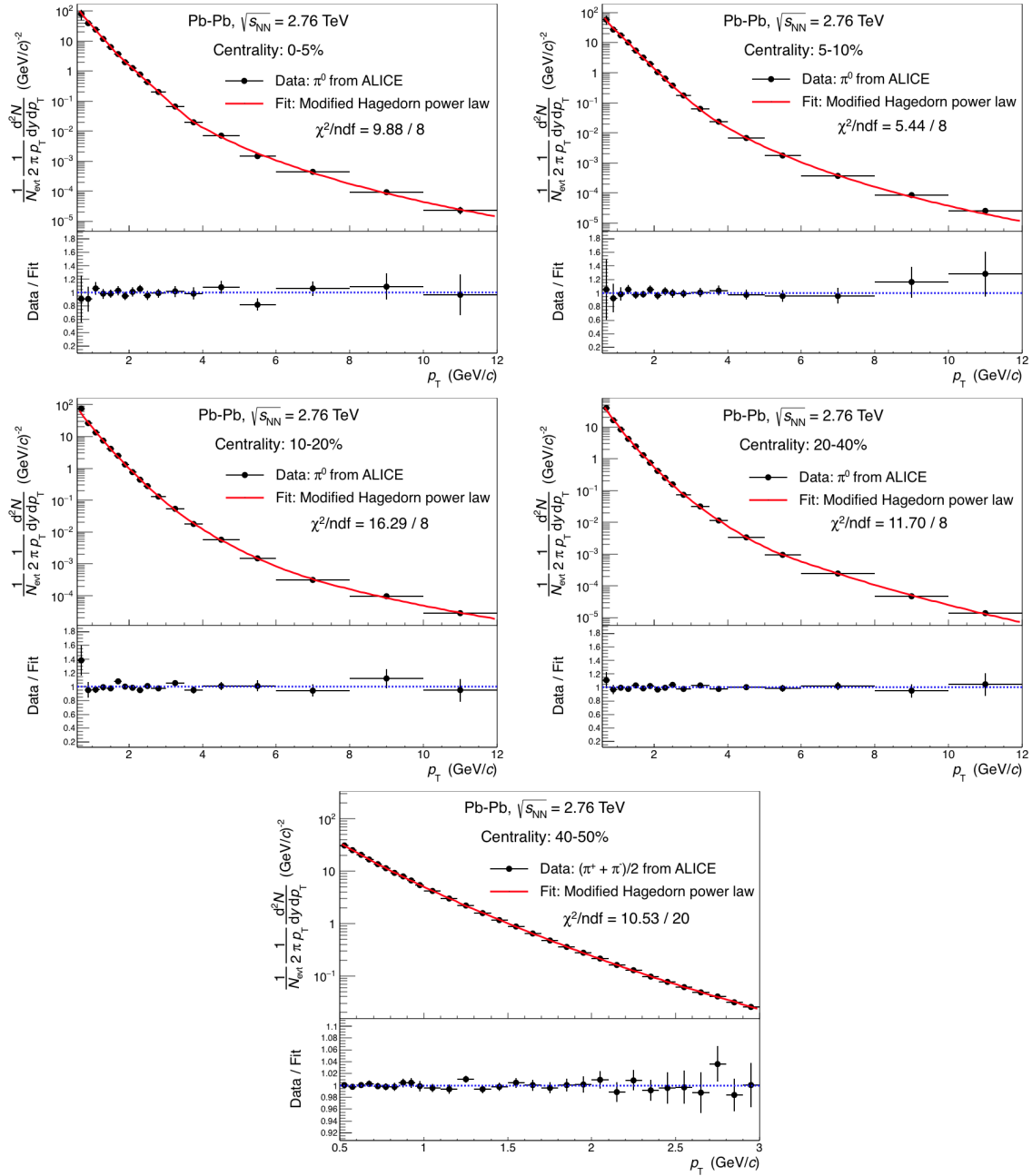


Fig. 7.1 : Neutral pion p_T spectra measured by ALICE in Pb–Pb collisions at $\sqrt{s_{NN}} = 2.76$ TeV in the centrality ranges: (0-5 %), (5-10 %), (10-20 %), (20-40 %) [134] (upper and middle row) and charged pion p_T spectrum measured in the centrality range (40-50%) [47] (bottom). The parametrizations have been obtained from a fit with the Modified Hagedorn power-law function [135].

and their parametrizations obtained from a fit with the modified Hagedorn power-law function [135].

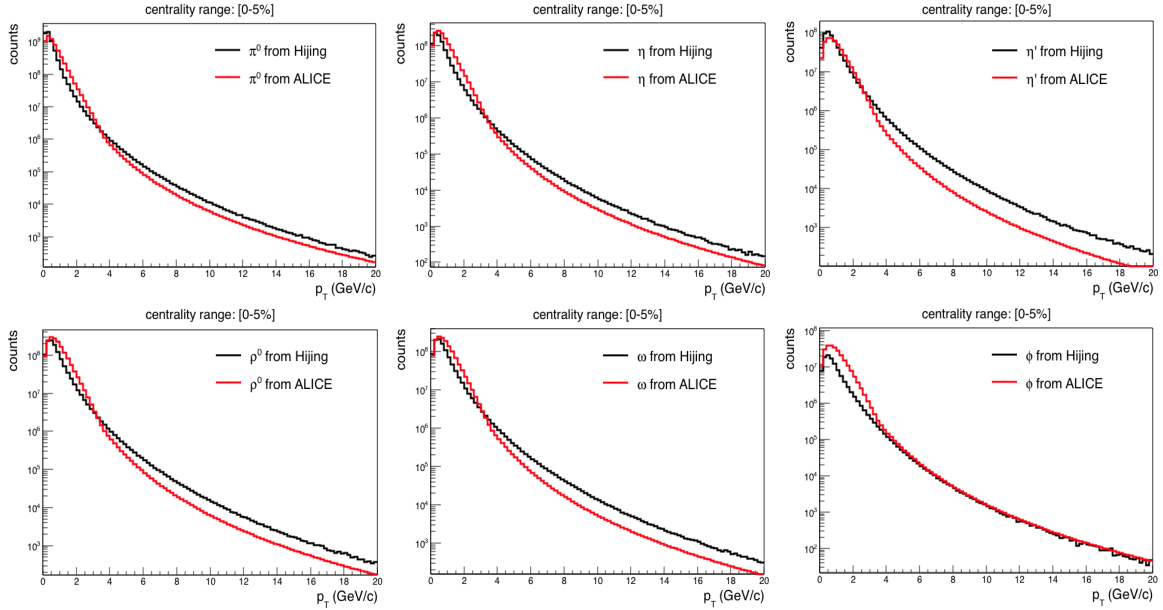


Fig. 7.2 : Comparison between the p_T spectra of the main dielectron sources from ALICE measurement in Pb–Pb collisions at $\sqrt{s_{NN}} = 2.76$ TeV (or from π^0 m_T -scaled spectra) and the corresponding distributions from Hijing in the centrality range (0-5 %).

The p_T distributions of the other light flavor mesons in the same centrality ranges have been obtained from the measured pion spectra based on m_T -scaling. According to this property of the hadron spectra, which has been found by the WA80 Collaboration for π^0 and η [136], the spectral shapes of hadrons are almost identical when plotted as a function of their transverse mass. The latter is defined as:

$$m_T = \sqrt{m^2 + p_T^2} \quad (7.2)$$

The m_T -scaling is an extremely useful property which allows to obtain the unknown meson spectra starting from a reference measured distribution. This procedure however has some limits, especially at low momenta, which are discussed in Section 7.7. This regards the calculation of the η contribution to the hadronic cocktail. Fig. 7.2 shows the comparison between the shapes of the p_T distributions of the main dielectron sources from ALICE measurement, or from m_T -scaling starting from the measured pion spectra, and the corresponding distributions from Hijing in the centrality range (0-5 %).

The shape of the p_T spectra of heavy-flavor mesons generated by HIJING, using the default $c\bar{c}$ and $b\bar{b}$ cross sections, have not been corrected. This is justified by the fact that the dielectron invariant mass spectrum obtained using HIJING sources and the heavy-flavor contributions of the hadronic cocktail in Pb–Pb collisions at $\sqrt{s_{NN}} = 2.76$ TeV have identical shapes in the intermediate mass region $1 < m_{ee} < 3$ GeV/ c^2 , which contains

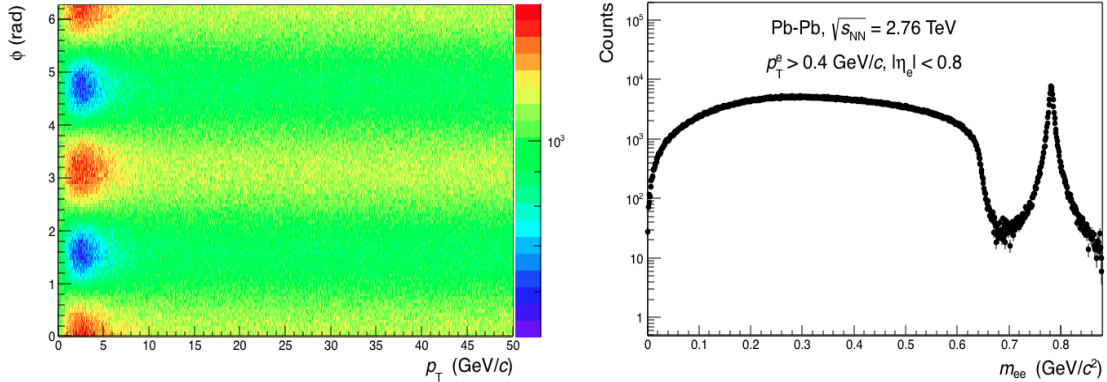


Fig. 7.3 : p_T - ϕ distribution of the ω meson from the enriched sample of dielectron sources (left) and invariant mass distribution of dielectrons from this source (right).

a dominant contribution from heavy-flavor decays (see Section 7.6.1). The input p_T spectrum of the J/Ψ from HIJING has not been corrected. This dielectron source can be ignored due to its negligible contribution to the low-mass region of the dielectron spectrum.

7.3.2 Electrons from the Enriched Sample

The additional dielectron sources embedded into the simulation have been produced with uniform p_T and η distributions and with sinusoidal azimuthal angle distributions (Fig. 7.3). Only dielectrons from the ω meson have been included in the efficiency calculation in order to benefit from the large statistics of this source and to exploit its coverage of the low-mass region due to its forced three-body decay ($\omega \rightarrow \pi^0 e^+ e^-$).

The p_T and ϕ distributions of electrons from the injected ω meson have been corrected using proper weights. The azimuthal angle distribution has been made uniform, while the p_T spectrum of the ω meson has been corrected using as reference the π^0 - m_T scaled spectrum.

7.4 Efficiency Calculation and Detector Effects

Charged particles radiate energy when they are accelerated by the electromagnetic fields of nuclei or by an external magnetic field. The total power radiated is proportional to m^{-4} when the acceleration is perpendicular to the particle velocity, and to m^{-6} when the particle's acceleration and its velocity are parallel. Electrons, due to their small mass, suffer from significant radiative energy loss (bremsstrahlung) when propagating through

the ALICE detector. The momentum of electrons is also affected by the finite momentum resolution of the detector and by the angular smearing due to the tracking procedure. Fig. 7.4 shows the distribution of $\Delta p = p^{\text{gen}} - p^{\text{rec}}$ for electrons with generated momenta in the range: $0.50 < p^{\text{gen}} < 0.51 \text{ GeV}/c$.

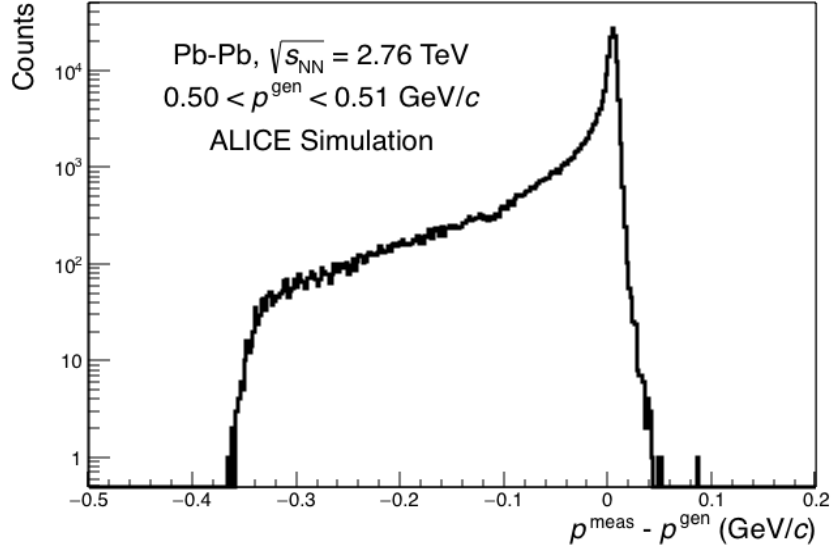


Fig. 7.4 : Distribution of $\Delta p = p^{\text{gen}} - p^{\text{rec}}$ for electrons with generated momenta in the range: $0.50 < p^{\text{gen}} < 0.51 \text{ GeV}/c$. The left tail is produced by radiative energy loss in the ALICE magnetic field.

The Δp distribution has a finite width, due to the momentum resolution of the detector, and a left tail due to the radiative energy loss. In consequence, the reconstructed momentum of electrons can be significantly different from the "true" momentum at their production. The dielectron invariant mass spectrum is also affected by radiative energy loss and momentum resolution. These produce a mass shift of the spectrum to lower values due to the dominant effect of bremsstrahlung: $m_{ee}^{\text{rec}} \neq m_{ee}^{\text{true}}$.

The correction for these detector effects could be done, in principle, using the unfolding methods. These rely on the detector response matrices, obtained from full MC simulations, which contain the connection between generated and reconstructed momenta (see next section). All unfolding methods however fail in the vicinity of resonance peaks, giving unstable and therefore unreliable results. For technical difficulties and for historical reasons the corrected dielectron spectrum, the hadronic cocktail and all theoretical curves describing the contribution from thermal dileptons are represented as a function of the measured mass, not the "true" mass. The inverse procedure is then applied to the generated particles in the efficiency calculation using the aforementioned detector

response matrices to transform the "true" momentum of electrons, with which they have been generated, into its corresponding "measurable" value: $\vec{p}_{gen} \rightarrow \vec{p}_{meas}$.

The reconstruction efficiency of single electrons is defined by the ratio between the reconstructed and generated electrons within the selected acceptance ($0.4 < p_T^e < 5 \text{ GeV}/c$ and $|\eta_e| < 0.8$):

$$\epsilon(x) = \frac{\left[\frac{dN^e}{dx} \right]_{\text{rec}}}{\left[\frac{dN^e}{dx} \right]_{\text{gen}}} \quad \text{with } x = p_T^e, \theta_e, \phi_e \quad (7.3)$$

The transformation of the generated into measurable momentum has been done before the low- p_T threshold and acceptance cut have been applied.

The pair reconstruction efficiency is defined, for each p_T^{ee} range, as the ratio between reconstructed and generated dielectron pairs, as a function of their (measured) invariant mass:

$$\epsilon(m_{ee}, p_T^{ee}) = \frac{\left[\frac{dN^{ee}}{dm_{ee}^{\text{rec}}} (p_T^{ee, \text{rec}}) \right]_{\text{rec}}}{\left[\frac{dN^{ee}}{dm_{ee}^{\text{meas}}} (p_T^{ee, \text{meas}}) \right]_{\text{gen}}} \quad (7.4)$$

In the following paragraph, the procedure used to obtain the detector response matrices and the method to simulate the detector effects are illustrated.

7.4.1 Detector Response Matrices

The detector response matrices are two dimensional histograms containing $\Delta p = p^{\text{meas}} - p^{\text{gen}}$, $\Delta \theta = \theta^{\text{meas}} - \theta^{\text{gen}}$ and $\Delta \phi = \phi^{\text{meas}} - \phi^{\text{gen}}$ of electrons and positrons as a function of the particle "true" momentum (Fig. 7.5). Electrons from HIJING and from the enriched dielectron sources have been used to obtain the response matrices.

In the efficiency calculation, the analysis of events from the run lists corresponding to opposite magnetic field orientations has been performed using the corresponding response matrices. This was necessary due to a slight shift in the reconstructed azimuthal angle of electrons and positrons due to their opposite bending in the ALICE magnetic field. This effect was the opposite when the magnetic field was reversed. The usage of the proper response matrix to describe the angular smearing was done to keep track of this effect (Fig. 7.6).

The generated momentum vector of an electron (positron) has transformed into its corresponding measurable value based on the following procedure:

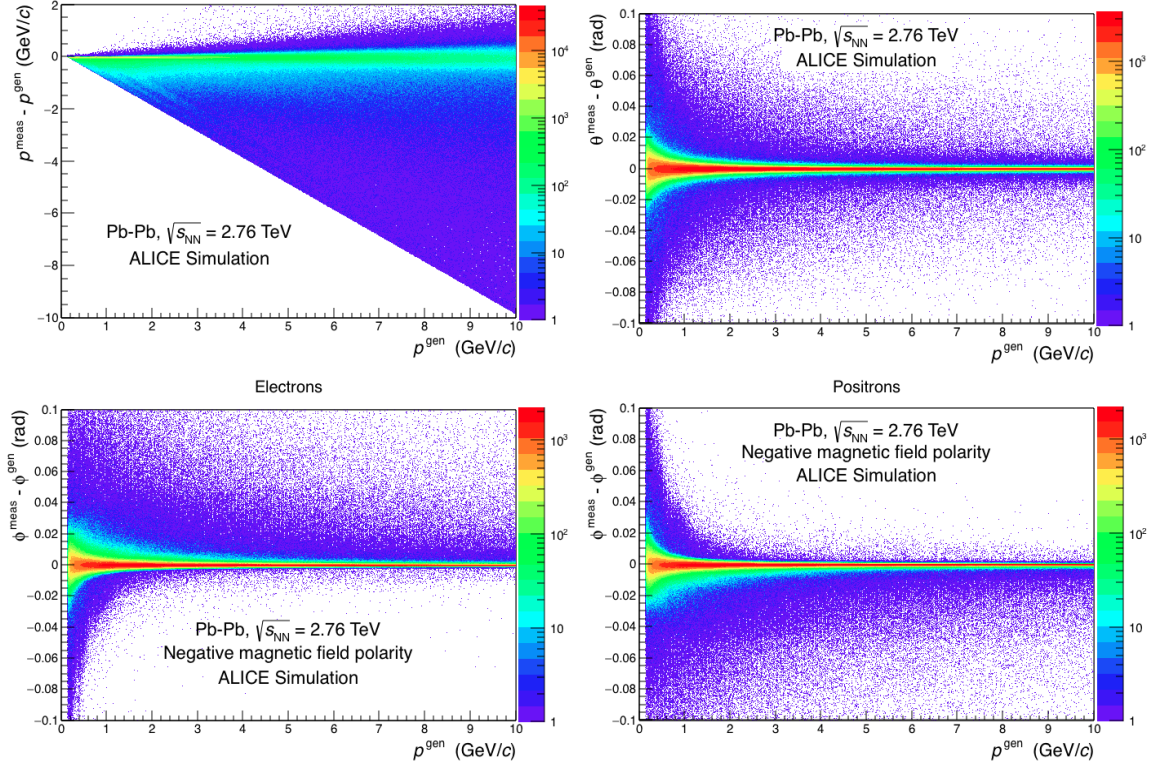


Fig. 7.5 : Detector response matrices used to transform the generated momentum of electrons into its corresponding "measurable" value. These response matrices refer to negative magnetic field orientations.

- **Projections:** The Δp , $\Delta\theta$ and $\Delta\phi$ distributions corresponding to the same generated momentum have been obtained by projecting the corresponding slices of the detector response matrices.
- **Random numbers:** Three random numbers have been extracted based on the projected distributions, one for Δp , one for $\Delta\theta$ and one for $\Delta\phi$, respectively.
- **Transformation:** The measurable values of p , θ and ϕ have been obtained by adding the extracted random numbers to the generated values of p , θ and ϕ : $p^{\text{meas}} = p^{\text{gen}} + \Delta p$, $\theta^{\text{meas}} = \theta^{\text{gen}} + \Delta\theta$ and $\phi^{\text{meas}} = \phi^{\text{gen}} + \Delta\phi$.

Finally, the three components of the measurable momentum vector have been obtained from:

$$\begin{cases} p_x^{\text{meas}} = p^{\text{meas}} \sin(\theta^{\text{meas}}) \cos(\phi^{\text{meas}}) \\ p_y^{\text{meas}} = p^{\text{meas}} \sin(\theta^{\text{meas}}) \sin(\phi^{\text{meas}}) \\ p_z^{\text{meas}} = p^{\text{meas}} \cos(\theta^{\text{meas}}) \end{cases} \quad (7.5)$$

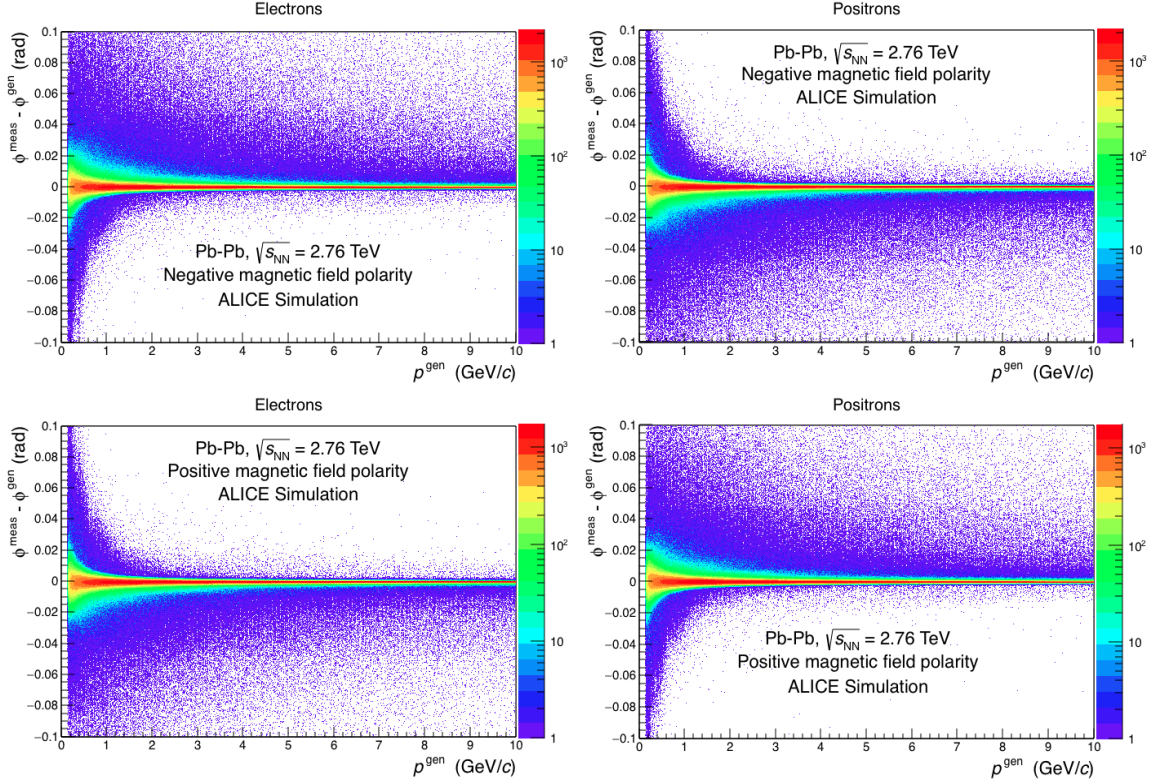


Fig. 7.6 : Detector response matrices for azimuthal angle transformation of electrons (left) and positrons (right) for opposite magnetic field orientations.

After the above transformation, the low p_T threshold and η range selection have been applied to the generated particles.

7.5 Reconstruction Efficiency of Single Electrons

The reconstruction efficiencies of single electrons, as a function of p_T^e , η^e and ϕ^e , in central (0-10%) Pb–Pb collisions at $\sqrt{s_{NN}} = 2.76$ TeV, corresponding to different track selection cuts, are shown in Fig. 7.7.

Particle identification caused a significant track loss due to the stringent cuts used to reduce to a minimum the hadron contamination in the selected track sample. The shape of the efficiency as a function of η^e reflects the geometry of the TOF detector, whose surface was not fully instrumented. The dead areas of the ITS, caused by some hardware problems during the data taking, are visible in the graph of the efficiency as a function of the azimuthal angle. The pair pre-filter also caused some track loss, especially at low momentum, due to the random rejection of signal tracks. This was due to the large phase space density at low momentum which gave a relatively large probability for signal tracks

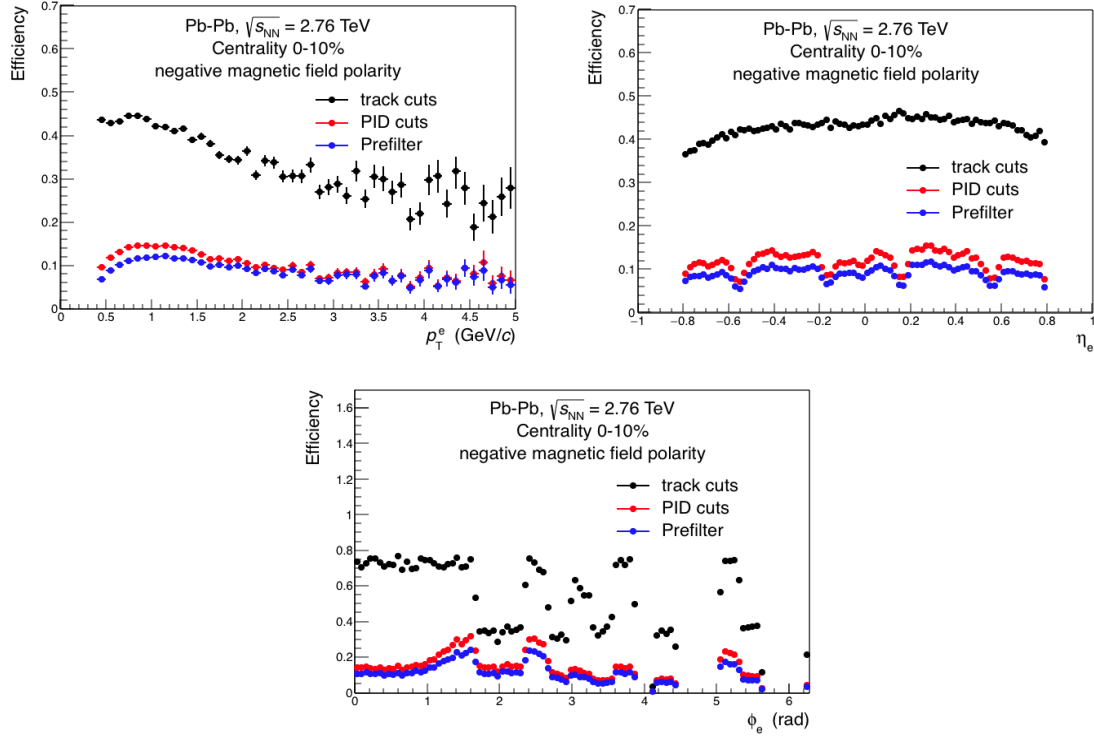


Fig. 7.7 : Single track reconstruction efficiency of electrons in central (0-10 %) Pb-Pb collisions at $\sqrt{s_{NN}} = 2.76$ TeV as a function of p_T^e (top left), η^e (top right) and ϕ^e (bottom) for different track selection cuts. Only the case corresponding to negative magnetic field configuration is shown.

to form low-mass pairs with random partners, thus enhancing the probability of fulfilling the rejection criterion of conversion pairs. At higher p_T^e , the reconstruction efficiency of electrons after the pre-filter was more similar to that before the pre-filter.

The track reconstruction efficiency of electrons and positrons were different, especially at low momentum (Fig. 7.8).

This was due to the geometric asymmetries of the experimental apparatus connected to the opposite curvature of electrons and positrons in the magnetic field: these particles interacted with different regions of the detector. At higher p_T^e , the relative difference between the reconstruction efficiency of electrons and positrons was smaller since high momentum tracks moved along almost straight trajectories, thus interacting with the same active element of the detector. The trend of the efficiency for electrons and positrons was opposite when the magnetic field was reversed.

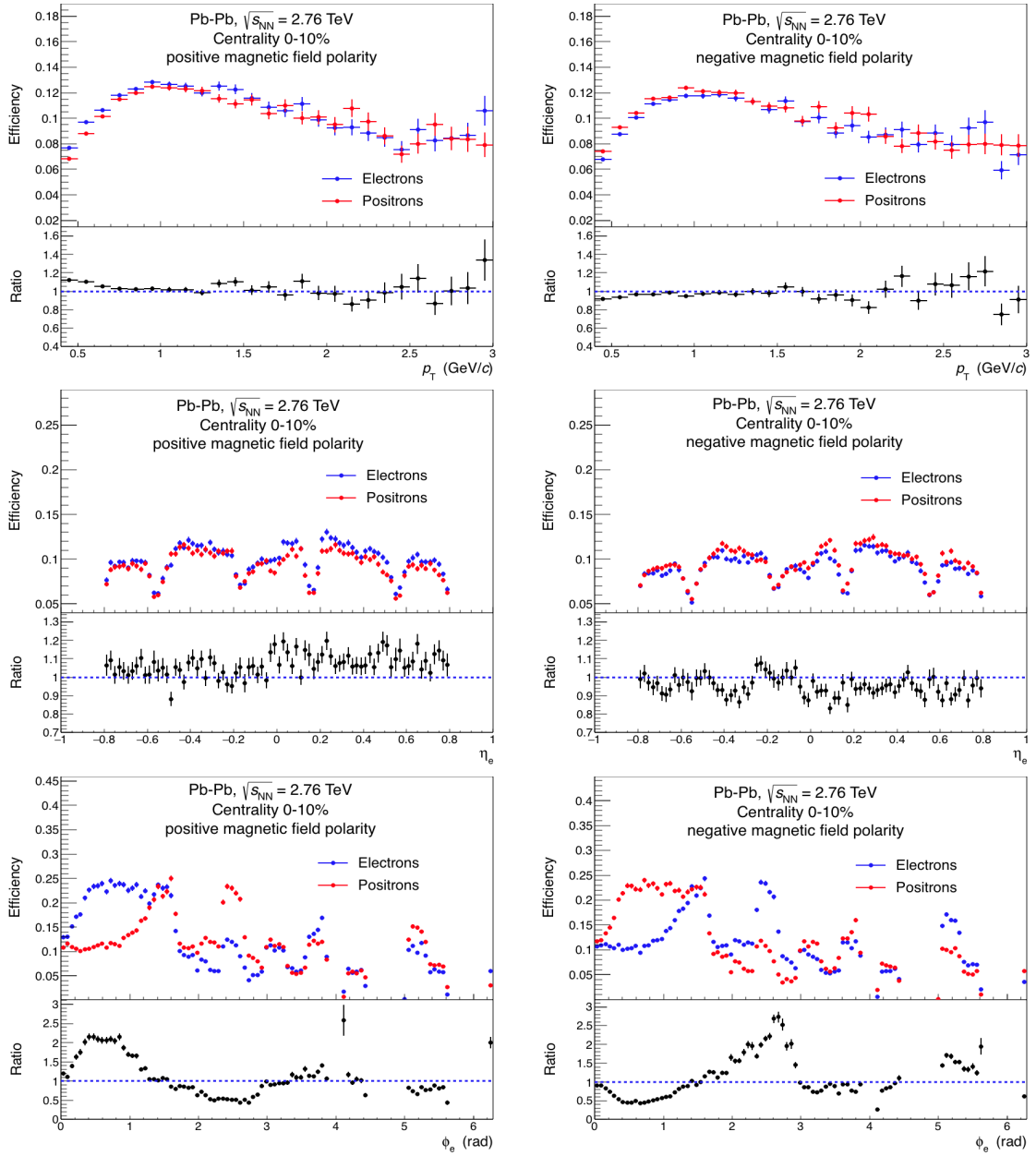


Fig. 7.8 : Comparison between single track reconstruction efficiencies of electrons and positrons in central (0-10 %) Pb-Pb collisions at $\sqrt{s_{NN}} = 2.76$ TeV as a function of p_T^e (top row), η^e (middle row) and ϕ^e (bottom row). The left and right columns refer to the opposite magnetic field orientations.

Fig. 7.9 shows the comparison between the single track efficiencies for electrons in the two centrality ranges used for this analysis: 0-10% and 10-50%.

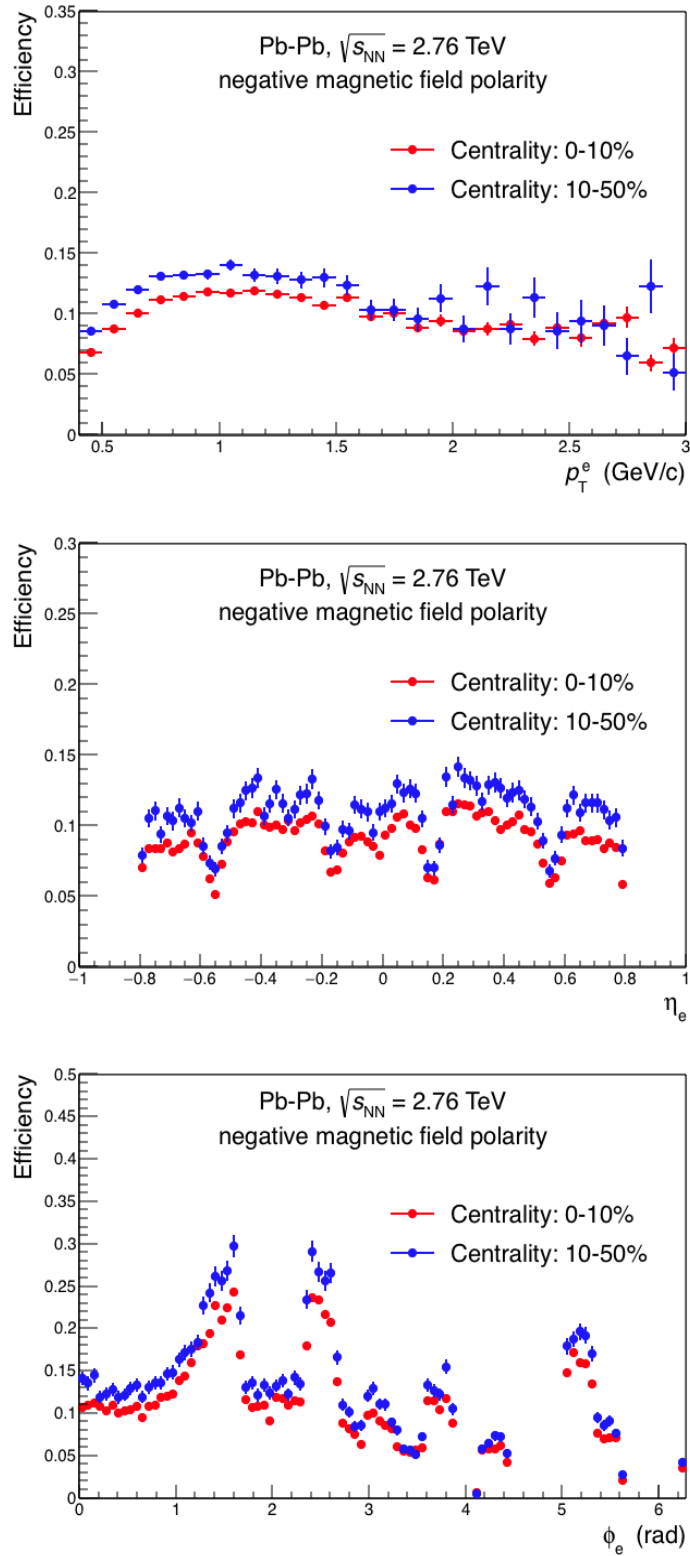


Fig. 7.9 : Comparison between single track reconstruction efficiencies for electrons in the two centrality classes used for this analysis: 0-10% and 10-50%. These graphs refer to the negative magnetic field orientation.

7.6 Pair Reconstruction Efficiency

In the calculation of the pair reconstruction efficiency only *correlated* dielectron pairs have to be used. These originated from the same particle's decay or from correlated semi-leptonic charm and beauty decays. Fig. 7.10 shows the comparison between the pair reconstruction efficiencies calculated using correlated and random pairs.

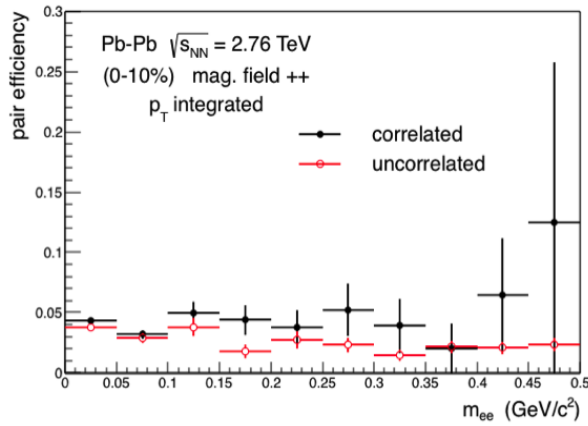


Fig. 7.10 : Comparison between pair efficiencies obtained using correlated and random pairs.

The pair efficiency using random pairs is systematically lower compared to that obtained using correlated pairs. The reason for this discrepancy is related to the different single-particle distributions of correlated and uncorrelated partners of a given electron (positron). For each mass range and for each electron (positron), the average opening angle of a random pair was larger compared to that of a real pair (Fig. 7.11).

Due to the mass constraint, this resulted in a steeper p_T distribution of the random partner compared to the real one (Fig. 7.12). In summary, for each electron (positron) and for each mass range, the average p_T of a random partner was smaller than that of the real partner. Since the single particle efficiency decreases at low p_T , the reconstruction probability of uncorrelated pairs was smaller.

7.6.1 Heavy-Flavor Electrons

The contribution from correlated semi-leptonic heavy-flavor electrons was expected to dominate the dielectron spectrum at high mass ($m_{ee} > 400 \text{ MeV}/c^2$). Electrons from charm and beauty decays have been included in the efficiency calculation in order to have a full coverage of the total phase-space ($m_{ee} - p_T^{ee}$). These particles were generated by HIJING using the default $c\bar{c}$ and $b\bar{b}$ cross sections and their input distribution

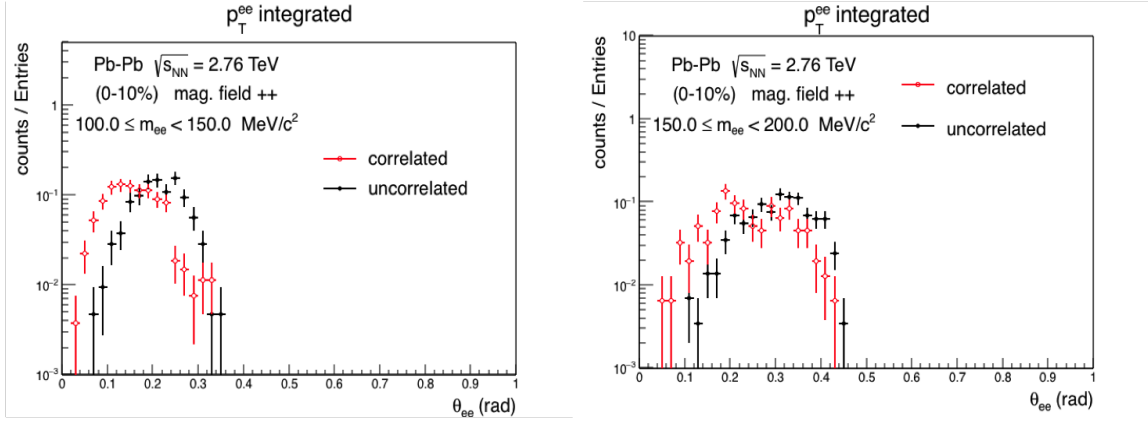


Fig. 7.11 : Opening angle distributions of correlated and random pairs for two different mass ranges.

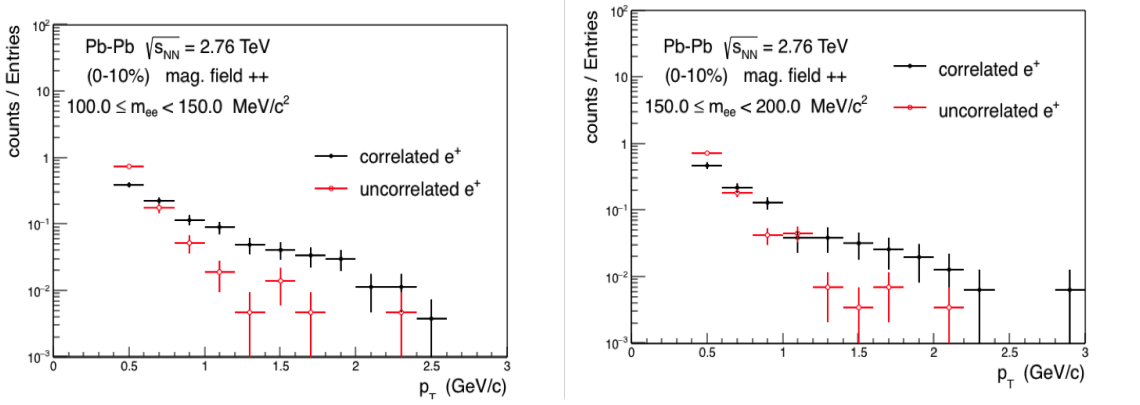


Fig. 7.12 : p_T distributions of correlated and random partners for two different mass ranges.

have not been modified. Fig. 7.13 left shows the dielectron invariant mass spectrum generated using HIJING sources, applying the proper weights for the light-flavor sources only, and the contribution from charm and beauty decays produced by the hadronic cocktail generator, which was based on the charm and beauty cross sections measured by ALICE (see Section 7.7), normalized to the total dielectron spectrum in the mass region: $1 < m_{ee} < 3 \text{ GeV}/c^2$. The overall good agreement between these distributions in the intermediate mass region $1 < m_{ee} < 3 \text{ GeV}/c^2$ (Fig. 7.13 right), which was dominated by dielectrons from heavy-flavor decays, justified the usage of the unmodified p_T spectra of heavy-flavor sources generated by HIJING for the calculation of the pair reconstruction efficiency. The agreement was valid also for different p_T ranges.

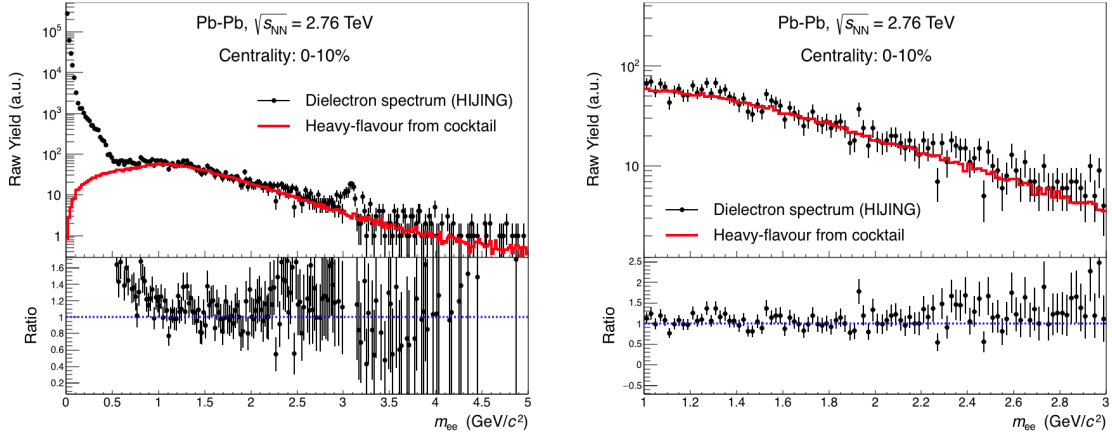


Fig. 7.13 : Dielectron invariant mass spectrum generated using HIJING sources in comparison to the heavy-flavour contribution produced by the cocktail generator.

7.6.2 Pre-filter Correction

The photon conversion rejection using the pair pre-filter could result in random rejection of primary electrons (see Chapter 5). The signal loss due to the pre-filter has been incorporated into the efficiency calculations using the number of reconstructed dielectron pairs surviving the pre-filter in the numerator of the efficiency definition. The pair reconstruction efficiency can be expressed in a factorized form to put into evidence the pre-filter correction factor:

$$\epsilon_{\text{pair}}(m_{ee}, p_T^{\text{ee}}) = \frac{[d^2 N^{\text{ee}}/dm_{ee} dp_T^{\text{ee}}]_{\text{pref}}}{[d^2 N^{\text{ee}}/dm_{ee} dp_T^{\text{ee}}]_{\text{rec}}} \cdot \frac{[d^2 N^{\text{ee}}/dm_{ee} dp_T^{\text{ee}}]_{\text{rec}}}{[d^2 N^{\text{ee}}/dm_{ee} dp_T^{\text{ee}}]_{\text{gen}}} \quad (7.6)$$

Fig. 7.14 left shows the dielectron pair reconstruction efficiency, as a function of the invariant mass, in the centrality range 0-10%, for the negative magnetic field orientation, with and without the pre-filter correction factor. The latter is shown in Fig. 7.14 right.

7.6.3 Random Rejection Probability

The random rejection of signal depends on the probability that pairs composed by signal particles and random partners satisfy the rejection criteria. This probability is proportional to the density of tracks in the sample used for tagging and to their phase space population. Fig. 7.15 shows the p_T and multiplicity distributions of tracks used for tagging in MC simulation and in real data for comparison.

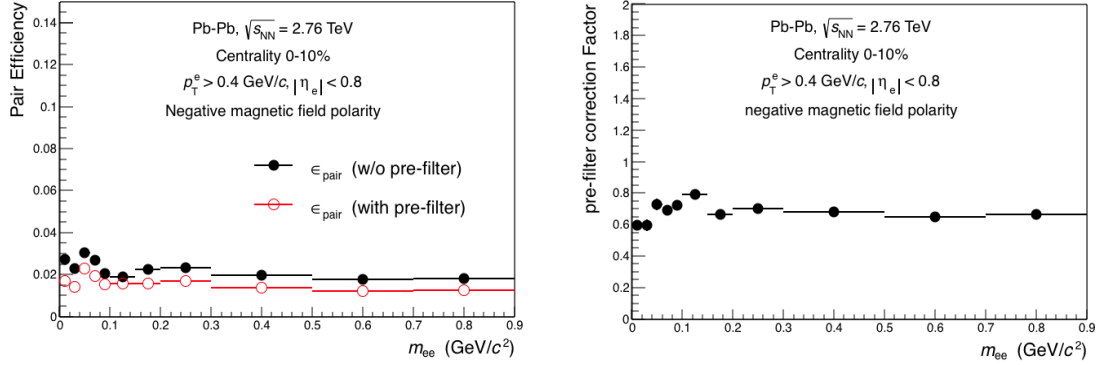


Fig. 7.14 : Dielectron pair reconstruction efficiency in central (0-10%) Pb–Pb collisions at $\sqrt{s_{\text{NN}}} = 2.76$ TeV, as a function of the invariant mass, with and without correction for random rejection due to the pre-filter (left). Pre-filter correction factor (right).

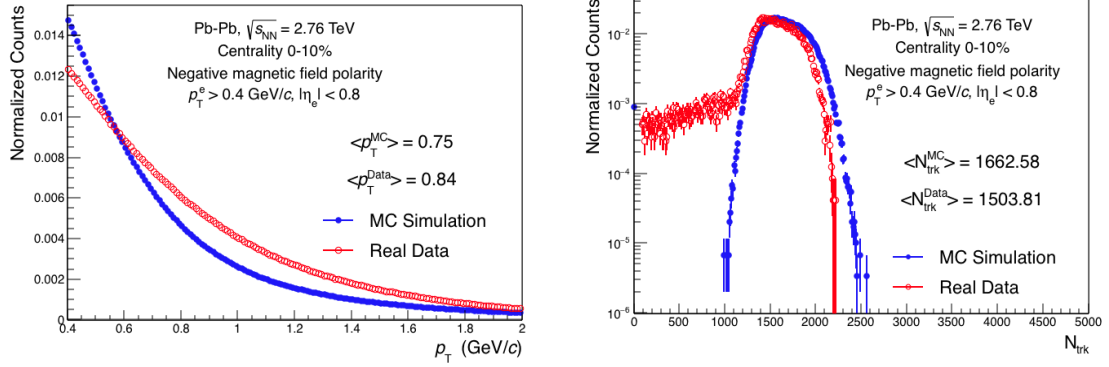


Fig. 7.15 : p_{T} distribution (left) and multiplicity distribution (right) of tracks selected with looser cuts in the MC simulation and in real data for comparison.

In the MC simulation, the average multiplicity of tracks used for tagging was slightly larger while their mean p_{T} was smaller compared to real data¹. Considering that low-momentum tracks have a larger probability of forming low-mass pairs with signal tracks and given the slightly larger track density in the simulation, this resulted in a larger random rejection probability in simulated events compared to real events. (Fig. 7.16). The pre-filter correction factor estimated based on the simulation was therefore underestimated. The correction for this effect has been obtained by comparing the pre-filter survival probability of generated pairs embedded into a simulated and real event. This correction depended on the collision centrality and on the magnetic field configuration (Fig. 7.17).

¹These properties are of course interconnected: in events with higher multiplicity the initial energy is shared by more particles, resulting in a smaller average energy per particle compared to an event with lower multiplicity.

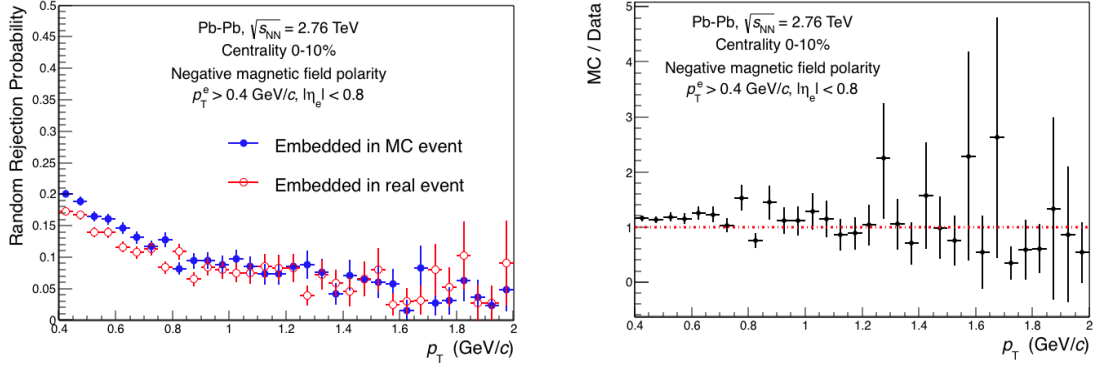


Fig. 7.16 : Comparison between the random rejection probability of injected particles in a real event and in a simulated event as a function of p_T (left) and their ratio (right).

7.6.4 Residual Conversion Contribution

The rejection efficiency of conversion electrons was $\sim 90\%$ (see Chapter 5). In consequence, there was a residual contribution to the dielectron spectrum from correlated electron-positron pairs from photon conversion in the material. This contribution has been estimated using the MC simulations by using proper p_T -dependent weights for the photon sources. Fig. 7.18 shows the total dielectron spectrum in central Pb-Pb collisions at $\sqrt{s_{NN}} = 2.76$ TeV, for the negative magnetic field polarity, and the residual contribution from photon conversions, estimated from MC simulations, with and without the usage of the pair pre-filter technique.

The invariant mass distribution of the surviving dielectrons from photon conversion in the material gave a contribution only in the very low mass range ($m_{ee} < 40$ MeV/ c^2). This was due to the very efficient suppression of late conversions which contributed to higher masses using the single-track conversion rejection methods. The correction for the residual conversion contribution has been obtained by multiplying the dielectron raw yield by the following factor before the efficiency correction:

$$F_\gamma = 1 - \frac{dN/dm_{ee}(\gamma \rightarrow e^+e^-)}{dN/dm_{ee}^{\text{incl}}} \quad (7.7)$$

where $dN/dm_{ee}(\gamma \rightarrow e^+e^-)$ represents the mass shape of electron-positron pairs from photon conversion and dN/dm_{ee}^{incl} is the inclusive dielectron spectrum. The residual contribution from photon conversion to the first mass range ($m_{ee} < 20$ MeV/ c^2) was of the order of $\sim 5\%$ when pre-filter was applied and $\sim 23\%$ when pre-filter was not applied (Fig. 7.19).

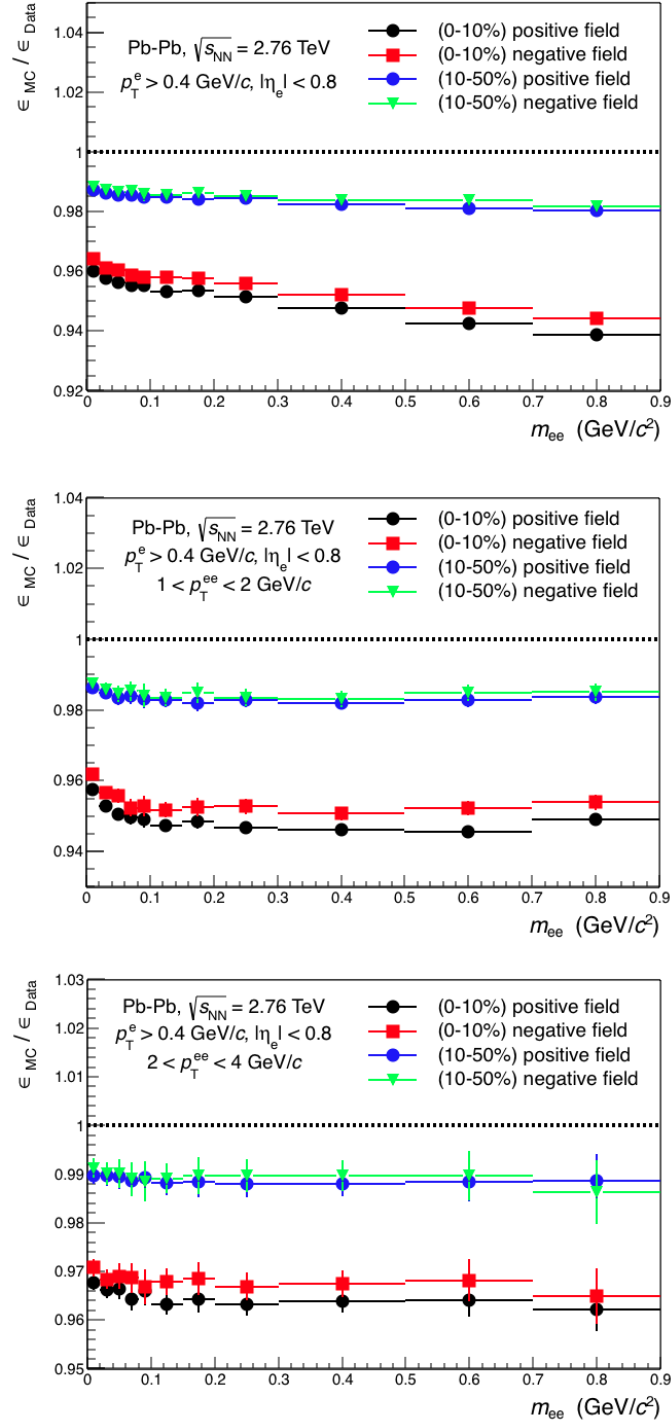


Fig. 7.17 : Ratio between the pre-filter survival probability of generated pairs embedded into a simulated and a real event for central and semi-central collisions and for the opposite magnetic field orientations.

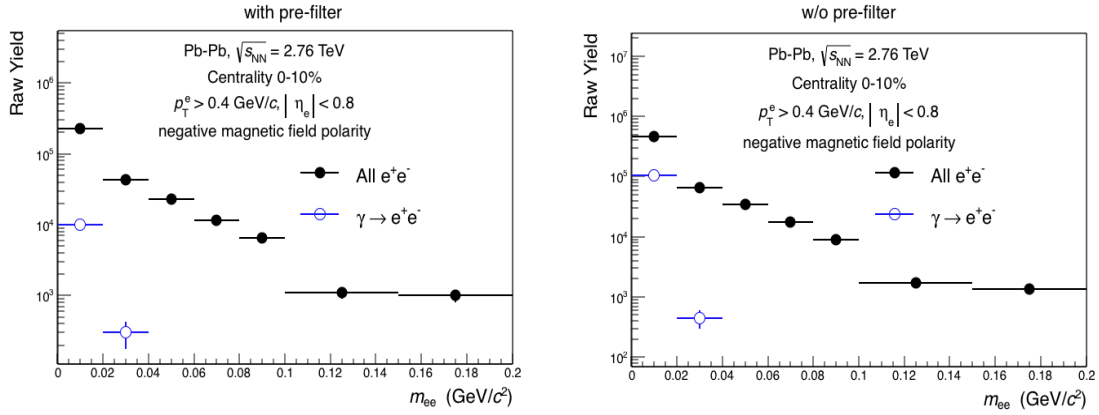


Fig. 7.18 : Residual contribution from conversion electrons to the total dielectron spectrum in central Pb–Pb collisions at $\sqrt{s_{\text{NN}}} = 2.76$ TeV, for the negative magnetic field polarity, estimated from MC simulations using proper weights for the photon sources, when pre-filter was applied (left) and when pre-filter was not applied (right).

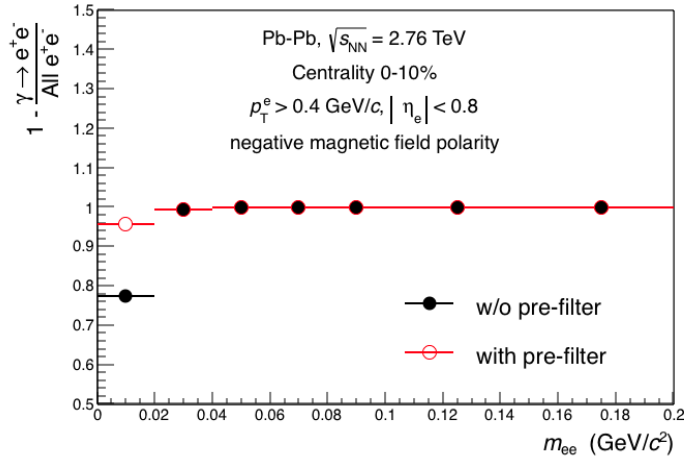


Fig. 7.19 : Correction factor for the residual contribution from conversion electrons to the total dielectron spectrum.

7.6.5 Pair Efficiency Correction

The pair reconstruction efficiency has been calculated in central (0-10%) and semi-central (10-50%) Pb–Pb collisions at $\sqrt{s_{\text{NN}}} = 2.76$ TeV, for different transverse momentum ranges and for both magnetic field orientations. The correction factors for the overestimated random rejection probability in MC simulations have been applied. The dielectron raw yields as a function of the invariant mass, obtained separately for both magnetic field orientations, have been corrected for the corresponding pair reconstruction efficiency. The total dielectron spectrum has been obtained by adding the contributions corresponding to opposite field configurations after the efficiency correction:

$$\frac{dN}{dm_{ee}} = \left[\frac{dN}{dm_{ee}} \right]_{\text{positive field}} + \left[\frac{dN}{dm_{ee}} \right]_{\text{negative field}} \quad (7.8)$$

This was done because of significant differences between the pair reconstruction efficiencies for the two magnetic field orientations both in central and semi-central collisions (Fig. 7.20).

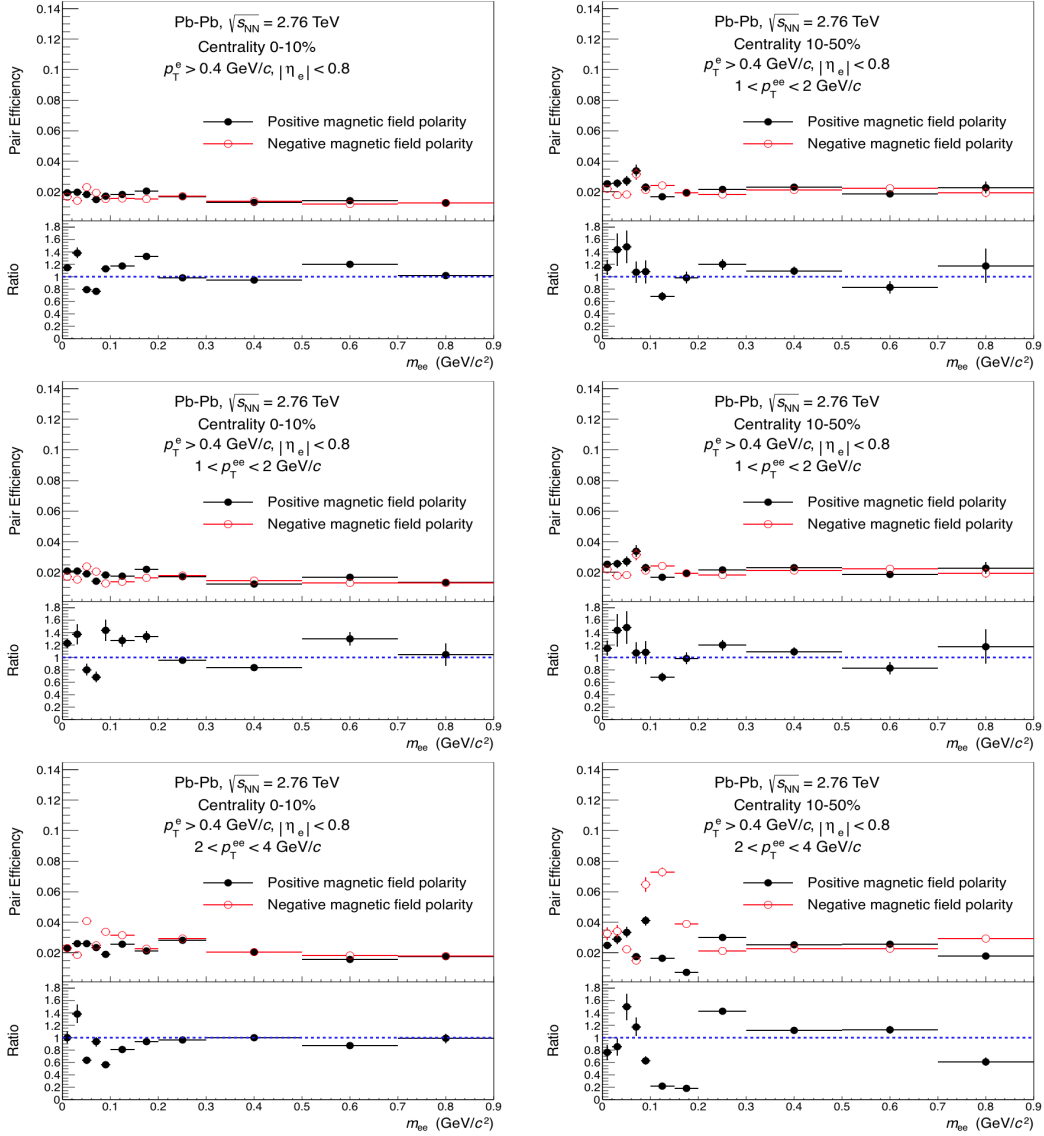


Fig. 7.20 : Comparison between the pair reconstruction efficiencies for opposite magnetic field orientations in central (left) and semi-central (right) collisions.

7.7 Hadronic Cocktail

The hadronic cocktail contains the contributions to the dielectron invariant mass spectrum coming from hadron decays. It contains two parts, one including the dielectron and Dalitz decays of light-flavor resonances and the other contains the contribution from correlated semi-leptonic charm and beauty decays. These two components have been produced using different generators and assumptions. The simulation of these two components of the hadronic cocktail is described in the following sections.

7.7.1 Light-Flavor Component: Resonance Decays

The light-flavor component of the hadronic cocktail has been generated based on the EXODUS decayer. Dielectrons from π^0 -Dalitz decay have been generated using as input to the simulation the parametrizations of the measured π^0 p_T spectra in the centrality ranges: (0-5 %), (5-10 %), (10-20 %), (20-40 %). The parametrization of the charged pion spectrum is instead used in the centrality range (40-50 %). All other contributions have been obtained from m_T -scaling using the pion spectra as a reference. This procedure consistently reflected that used in the modification of the input spectra of HIJING sources for the efficiency calculation (see Section 7.3). Regarding the systematic uncertainties on the light-flavor component of the cocktail, the upper and lower limits of the invariant mass distributions have been obtained by simulating the hadron decays using as input the parametrizations of neutral or charged pions corresponding to the upper and lower limits of their systematic uncertainties.

Regarding the η decay, which gives a sizable contribution to the low-mass region of the dielectron spectrum ($m_{ee} < 700 \text{ MeV}/c^2$), an additional systematic uncertainty has been assigned to cover the wrong estimation of its contribution by the m_T -scaling, especially at low momentum. The η/π ratio as a function of p_T in which the η spectrum was obtained from m_T scaling lied between two limits: the lower limit was defined by the η/π ratio as a function of p_T measured in pp collisions at $\sqrt{s} = 7 \text{ TeV}$, while the upper limit was defined by the K/π ratio as a function of p_T measured in Pb–Pb collisions at $\sqrt{s_{NN}} = 2.76 \text{ TeV}$. The relative differences between the η spectrum obtained via m_T scaling and η spectrum obtained from these two limits have been assigned to the upper and lower edges of the systematic uncertainties of the η contribution. These additional systematic uncertainties assigned to the η contribution are shown in table 7.1 for each transverse momentum range.

The generated momentum of electrons and positrons produced by the decayer has been transformed using the same detector response matrix used in the efficiency calculation.

p_T^{ee} range	upper syst	lower syst
p_T^{ee} -integrated	13%	26%
$1 < p_T^{ee} < 2 \text{ GeV}/c$	14%	26%
$2 < p_T^{ee} < 4 \text{ GeV}/c$	24%	13%

Table 7.1 : Additional systematic uncertainties assigned to the η contribution of the hadronic cocktail due to the wrong estimation of its contribution by m_T -scaling.

No angular smearing has been implemented in the cocktail simulation. The acceptance cut ($|\eta^e| < 0.8$) and the selection of the transverse momentum range ($0.4 < p_T^e < 5 \text{ GeV}/c$) have been done after the simulation of the radiative energy loss and momentum resolution. The contribution from the J/Ψ has been ignored due to its negligible contribution to the low-mass region ($m_{ee} < 700 \text{ MeV}/c^2$). The largest contributions to the light-flavor component of the hadronic cocktail originate from π^0 and η Dalitz decays.

7.7.2 Heavy-flavor Decays

The invariant mass spectrum of dielectrons from correlated semi-leptonic heavy-flavor decays has been obtained from simulations using PYTHIA 6. The $c\bar{c}$ and $b\bar{b}$ cross sections, as a function of the invariant mass, have been generated in pp collisions at $\sqrt{s} = 7 \text{ TeV}$, rescaled to $\sqrt{s} = 2.76 \text{ TeV}$ using the ratio between the cross sections at these energies [138, 139], and divided by the total inelastic cross section in pp collisions at $\sqrt{s} = 2.76 \text{ TeV}$ [140]. The resulting distribution has been scaled by the average number of binary nucleon-nucleon collisions $\langle N_{\text{coll}} \rangle$, obtained from MC Glauber model based on the collision centrality [137] (see Table 7.2), to obtain the heavy-flavor contribution in Pb–Pb collisions at $\sqrt{s_{\text{NN}}} = 2.76 \text{ TeV}$ for each centrality class used in this analysis. Charm and beauty suppression in the hot and dense medium have been ignored. Momentum resolution, radiative losses and kinematic cuts have been applied to heavy-flavor electrons (and positrons).

The total systematic uncertainty on the heavy-flavor contribution has been obtained by propagating the systematic uncertainties on the measured $c\bar{c}$, $b\bar{b}$ and the total inelastic cross-section in pp collisions $\sqrt{s} = 2.76 \text{ TeV}$, and that on $\langle N_{\text{coll}} \rangle$.

Fig. 7.21 shows the hadronic cocktail for central (0-10%) and semi-central (10-50%) Pb–Pb collisions at $\sqrt{s_{\text{NN}}} = 2.76 \text{ TeV}$ in the low-mass region ($m_{ee} < 900 \text{ MeV}/c^2$)

centrality (%)	$\langle N_{\text{coll}} \rangle$	RMS	syst.
(0-10)	1500.5	89	118
(10-50)	492.2	22	20.7

Table 7.2 : Average number of binary nucleon-nucleon collisions for the centrality classes used in this analysis used to rescale the charm and beauty contributions calculated for pp collisions. The numbers are taken from [137].

and the relative systematic uncertainties from each component of the hadronic cocktail. Correlated semi-leptonic heavy-flavor decays represented the dominant contribution to the total hadronic cocktail for $m_{ee} > 400 \text{ MeV}/c^2$. The charm contribution was a factor ~ 10 larger compared to beauty in the low-mass region.

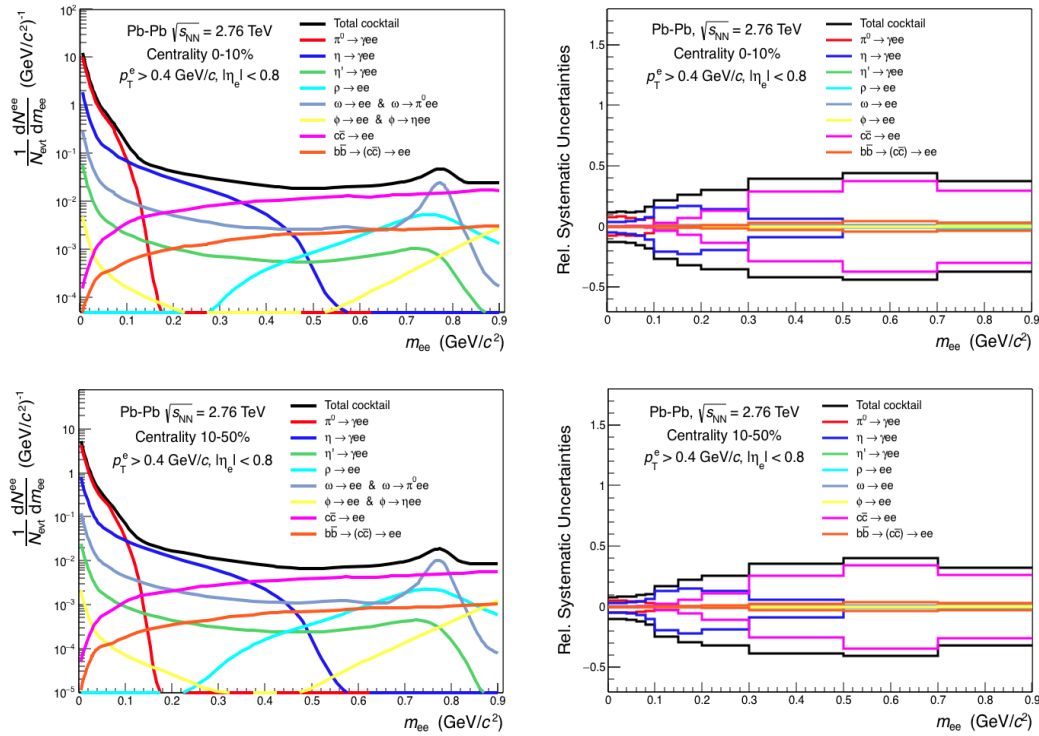


Fig. 7.21 : Hadronic cocktail in central (left) and semi-central (right) Pb–Pb collisions at $\sqrt{s_{\text{NN}}} = 2.76 \text{ TeV}$ and relative systematic uncertainties from each contribution.

Chapter 8

Systematic Uncertainties

8.1 Introduction

This chapter describes the methods used to calculate the systematic uncertainties in dielectron invariant mass spectrum.

8.2 Systematic Uncertainties Estimation

The strategy used to estimate the systematic uncertainties in the dielectron invariant mass spectrum consisted in varying the cuts used in the analysis (track selection, PID, pre-filter, etc.) and considering the corresponding variations of the data points in the efficiency corrected spectra. The corresponding pair reconstruction efficiencies have been obtained from the MC simulations using the same sets of cuts. Six different sources of systematic uncertainties have been identified and treated independently. These are listed in Table 8.1 which also illustrates the number of settings or cut variations used for the estimation of their corresponding contribution to the total systematic uncertainties.

To estimate the contribution to the systematic uncertainties originating from the p_T -dependent weights, which have been used to correct the input spectra in the MC simulation, five different settings have been used. These corresponded to different parametrizations of the input spectra in the MC simulations which have been obtained by shifting the data points of the neutral and charged pion p_T spectra by their systematic uncertainties. For each of the identified sources of systematic uncertainties, the cuts have been varied in order to produce a change in the pair reconstruction efficiencies of at least a factor ~ 2 . The systematic uncertainties for each source have been calculated as the RMS of the spread of points with respect to the measured value, except for the weights

Source of syst. uncertainty	Number of settings/ cut variations
Tracking	11
ITS PID	5
TPC PID	5
TOF PID	5
Pre-filter	5
MC tuning of input spectra	5

Table 8.1 : Sources of systematic uncertainties and number of cut variations used for the estimation of their contribution to the total systematic uncertainties.

where the maximum deviations have been considered. The total systematic uncertainties have been obtained by the quadrature sum of their individual contributions. In order to benefit from larger statistics and to obtain the maximum decoupling of statistical and systematic uncertainties, the data points have been grouped into three mass ranges: $0 < m_{ee} < 100 \text{ MeV}/c^2$, $100 < m_{ee} < 700 \text{ MeV}/c^2$ and $700 < m_{ee} < 2000 \text{ MeV}/c^2$. The relative systematic uncertainties have been calculated for each mass region and they have been assigned to the data points in the corresponding mass ranges.

Fig. 8.1 shows the relative systematic uncertainties and their individual contributions in the three mass regions for different transverse momentum ranges. The trend of the relative systematic uncertainties suggested a mass dependence. A smooth increase would have been expected rather a discontinuous trend. The partition of the mass domain into these ranges led to a slight underestimation of the systematic uncertainties on the left of the discontinuities and to an overestimation on its right. The assumption that the systematic uncertainties do not depend on centrality has been made¹.

¹This was done due to low statistics in the centrality range 10-50% which did not allow an efficient decoupling between statistical and systematic uncertainties.

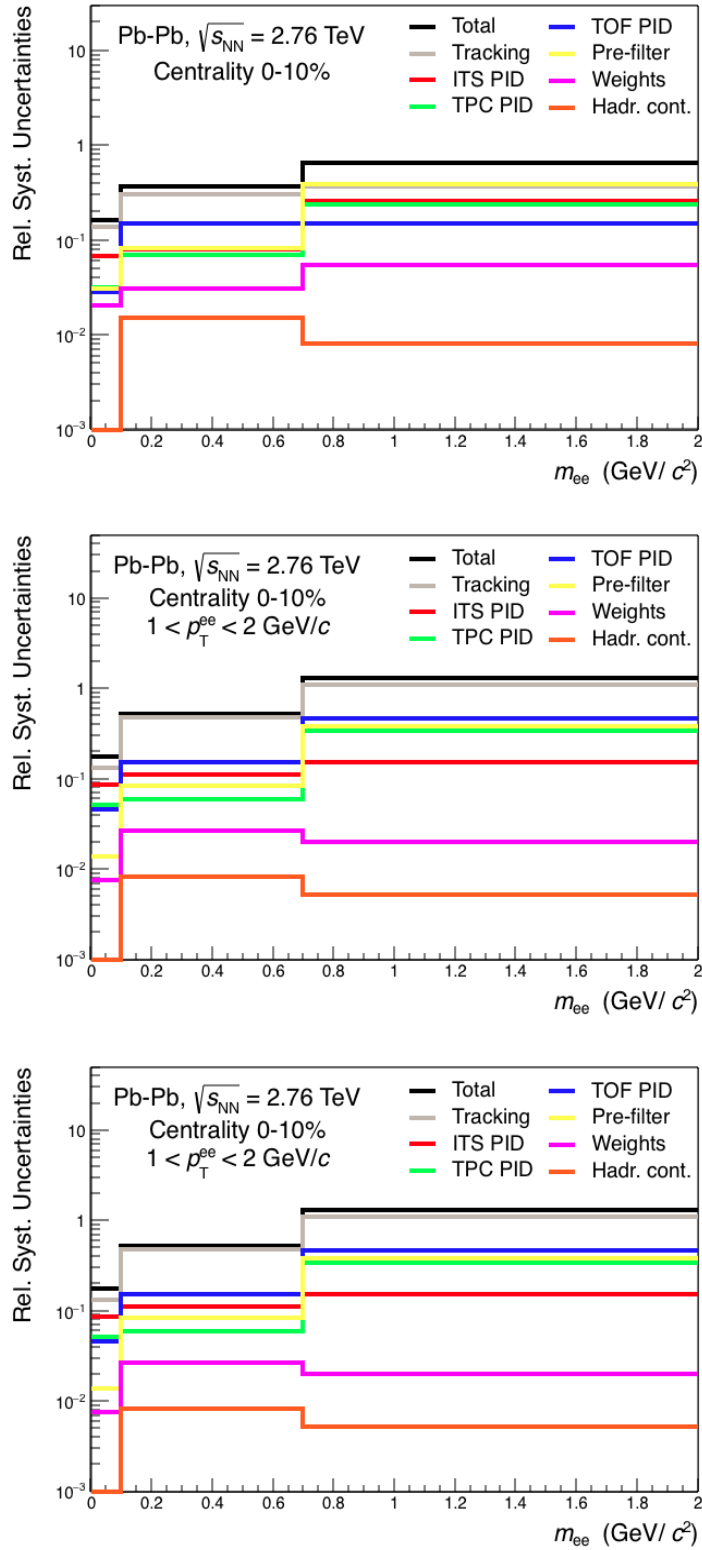


Fig. 8.1 : Relative systematic uncertainties for different pair- p_T ranges and their individual contributions.

Chapter 9

Results and Discussion

9.1 Introduction

This chapter contains the results of the dielectron measurement in Pb–Pb collisions at $\sqrt{s_{\text{NN}}} = 2.76$ TeV. The extraction of the contribution from virtual direct photons is presented and the comparison between the dielectron spectrum and theoretical model calculations, which include the contributions from thermal dileptons and in-medium modified ρ^0 and ω , is discussed.

9.2 Cocktail Comparison

The dielectron invariant mass spectra, measured in central (0-10%) and semi-central Pb–Pb collisions at $\sqrt{s_{\text{NN}}} = 2.76$ TeV, for different transverse momentum ranges, are shown in Figs. 9.1 and 9.2 in comparison with the expected contributions from hadron decays (hadronic cocktail). The downward pointing arrows in the graphs represent the upper limits at 90 % C.L. on the dielectron production in the corresponding mass ranges in the case of negative dielectron yield¹. These upper limits have been estimated using the Feldman and Cousins methodology [147] (see Appendix B).

¹The background over-subtraction was caused by upward statistical fluctuations of the like-sign spectrum whose magnitude was larger than the signal for some mass ranges in the mass region with small signal-to-background ratio.

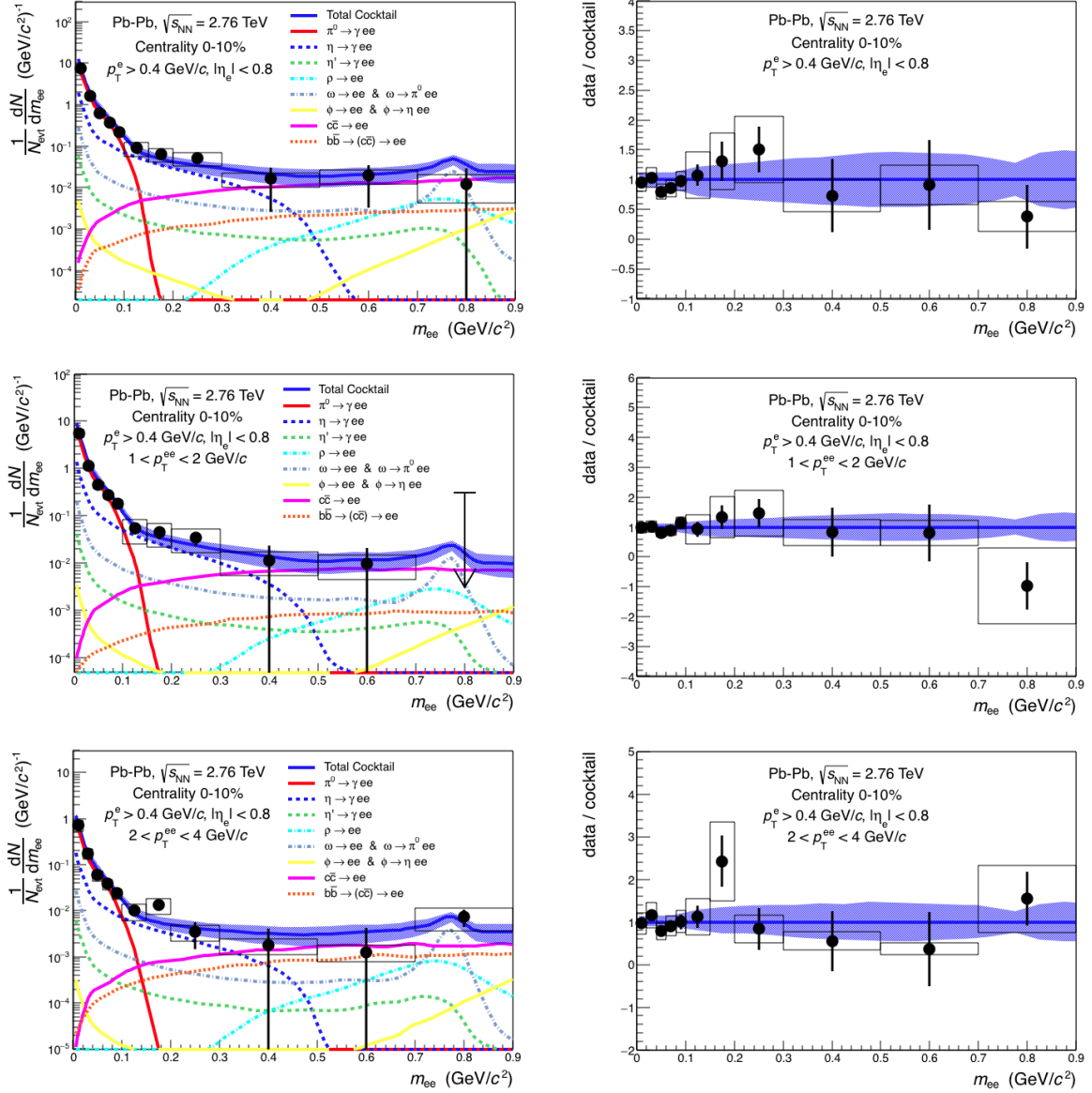


Fig. 9.1 : Dielectron invariant mass spectra measured in central (0-10%) Pb-Pb collisions at $\sqrt{s_{NN}} = 2.76$ TeV, for different transverse momentum ranges, in comparison with the expected contributions from hadron decays (left column) and data-to-cocktail ratios (right column).

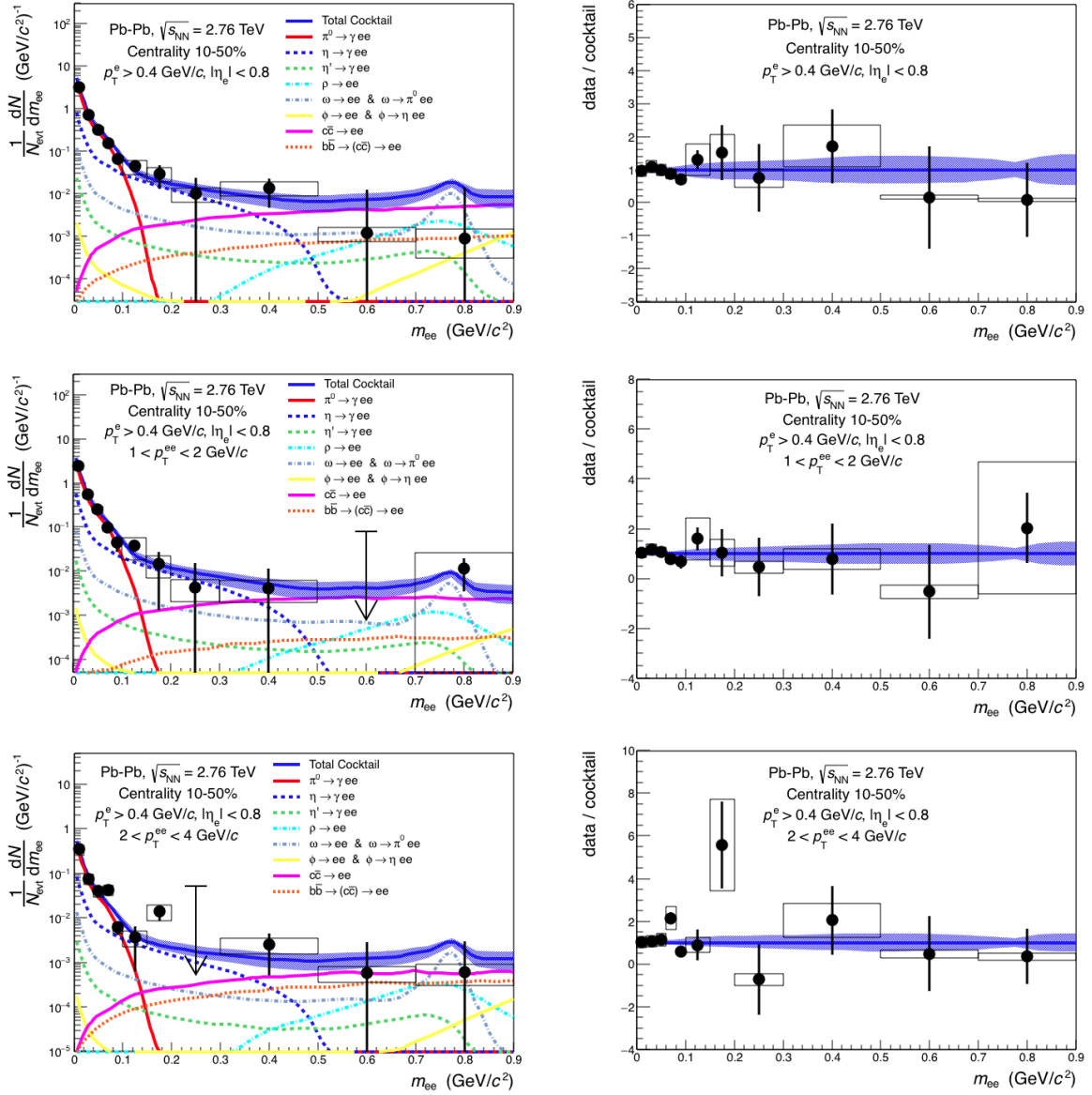


Fig. 9.2 : Dielectron invariant mass spectra measured in semi-central (10-50%) Pb-Pb collisions at $\sqrt{s_{NN}} = 2.76$ TeV, for different transverse momentum ranges, in comparison with the expected contributions from hadron decays (left column) and data-to-cocktail ratios (right column).

The data-to-cocktail ratios were consistent with unity within the statistical and systematic uncertainties in both centrality classes and for all transverse momentum ranges. This implied that the dielectron invariant mass spectra were well represented by their hadronic components only. However, additional contributions were expected in the low-mass region of the dielectron spectrum from thermal dielectrons, in the form of virtual direct photons (of the order of $\sim 10\%$ [70]), and from in-medium effects of low-mass vector mesons (to be quantified). The large uncertainties of both data and the cocktail indicated the reduced sensitivity in measuring these additional contributions. Within the limits imposed by the poor statistics and by the restricted knowledge of the hadronic components², the contribution from virtual direct photons has been extracted in the transverse momentum ranges $1 < p_{\text{T}}^{\text{ee}} < 2 \text{ GeV}/c$ and $2 < p_{\text{T}}^{\text{ee}} < 4 \text{ GeV}/c$ for both centrality classes. This is illustrated in the next session. The dielectron spectrum has also been compared to the predictions of thermal dielectrons and in-medium ρ^0/ω contributions obtained from theoretical model calculations. This is discussed in Section 9.4.

9.3 Virtual Direct Photon Measurement

The fraction of virtual direct photons has been measured in the kinematic region $p_{\text{T}}^{\text{ee}} \gg m_{\text{ee}}$ (quasi-real virtual photons). A minimized- χ^2 fit has been executed on the dielectron invariant mass spectrum in the mass domain $100 < m_{\text{ee}} < 300 \text{ MeV}/c^2$, for the transverse momentum intervals $1 < p_{\text{T}}^{\text{ee}} < 2 \text{ GeV}/c$ and $2 < p_{\text{T}}^{\text{ee}} < 4 \text{ GeV}/c$, using a three-components function:

$$f(m_{\text{ee}}) = r \cdot f_{\text{dir}}(m_{\text{ee}}) + (1 - r) \cdot f_{\text{LF}}(m_{\text{ee}}) + f_{\text{HF}}(m_{\text{ee}}) \quad (9.1)$$

In the above equation $f_{\text{dir}}(m_{\text{ee}})$ was the expected invariant mass distribution of virtual direct photons, described by the Kroll-Wada equation [74], $f_{\text{LF}}(m_{\text{ee}})$ and $f_{\text{HF}}(m_{\text{ee}})$ were the mass distributions of the light-flavor and heavy-flavor components of the hadronic cocktail, respectively. The spectra of $f_{\text{LF}}(m_{\text{ee}})$ and $f_{\text{dir}}(m_{\text{ee}})$ have been independently normalized to data in the first mass bin ($m_{\text{ee}} < 20 \text{ MeV}/c^2$) before the fit was executed. The parameter r represented the fraction of virtual direct photons:

$$r = \frac{f_{\text{dir}}}{f_{\text{dir}} + f_{\text{LF}}} = \frac{\gamma_{\text{dir}}^*}{\gamma_{\text{dir}}^* + \gamma_{\text{decay}}^*} \quad (9.2)$$

²This was due to the limited number of available measurements of hadron cross sections in Pb–Pb collisions at $\sqrt{s_{\text{NN}}} = 2.76 \text{ TeV}$, needed to simulate their contributions in the hadronic cocktail.

Fig. 9.3 shows the fit function, its individual components and the measured spectra in central (0-10%) and semi-central (10-50%) collisions for the transverse momentum ranges $1 < p_T^{ee} < 2 \text{ GeV}/c$ and $2 < p_T^{ee} < 4 \text{ GeV}/c$.

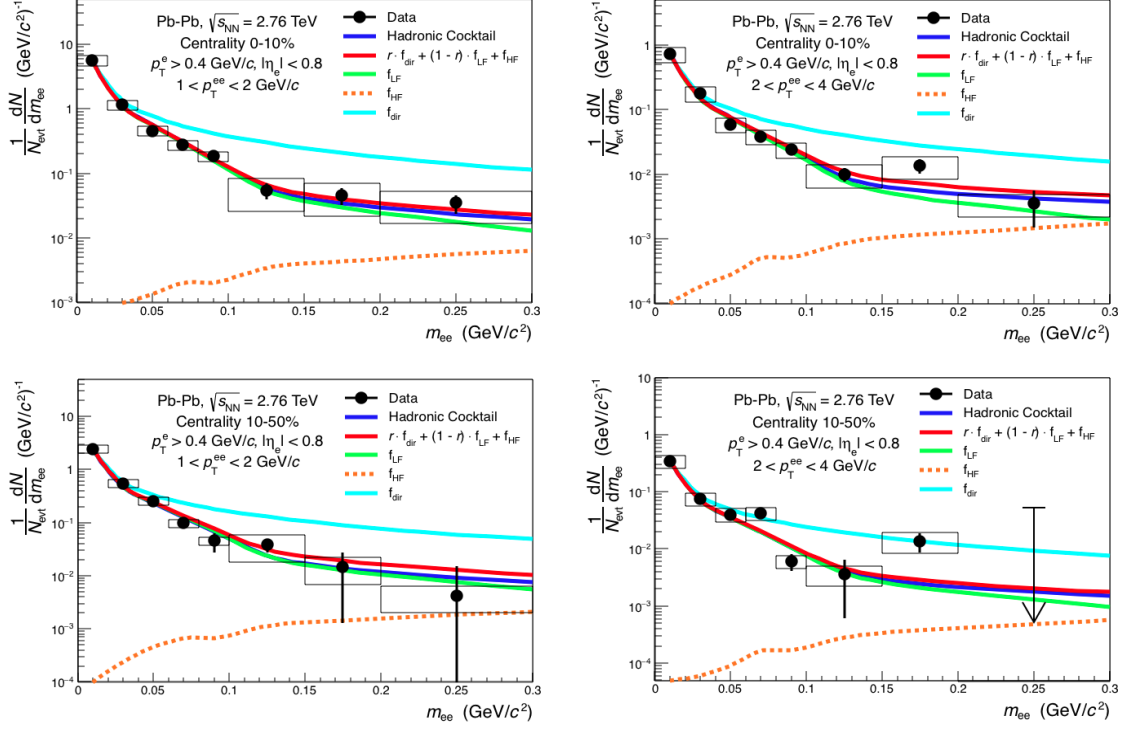


Fig. 9.3 : Fit function (equation 9.1), its individual components and dielectron invariant mass spectra measured in central (upper row) and semi-central (lower row) collisions for the transverse momentum ranges $1 < p_T^{ee} < 2 \text{ GeV}/c$ (left) and $2 < p_T^{ee} < 4 \text{ GeV}/c$ (right).

An iterative fitting procedure has been executed by varying the fit parameter r in the range $[0,1]$ and by calculating for each of these values the χ^2 , defined as:

$$\chi^2 = \sum_{i=1}^n \left[\frac{y_i(m_{ee}) - f_i(m_{ee})}{\sigma_i^{stat}} \right]^2 \quad (9.3)$$

where $y_i(m_{ee})$ and $f_i(m_{ee})$ were the data point and the fit function in the i^{th} mass bin, while σ_i^{stat} was the statistical uncertainty of the i^{th} data point. The χ^2 curve, for each centrality and transverse momentum range, has been parametrized using a parabolic function. The best estimate for the fraction of virtual direct photons, corresponding to the abscissa of the vertex of the parabola, has been determined analytically. The statistical uncertainty associated to this measurement, corresponding to a confidence level of $\approx 68.3\%$ (1σ), was given by the range $[r - r_{min}]$ corresponding to a variation

$\Delta\chi^2 = \chi^2 - \chi_{\min}^2 = 1$, which is the expected χ^2 variation for a fit with one parameter, according to the PDG table [141]. The χ^2 curves obtained for the two centrality classes in the transverse momentum ranges $1 < p_{\text{T}}^{\text{ee}} < 2 \text{ GeV}/c$ and $2 < p_{\text{T}}^{\text{ee}} < 4 \text{ GeV}/c$ are shown in Fig. 9.4, which also illustrates the procedure used for the estimation of the statistical uncertainties.

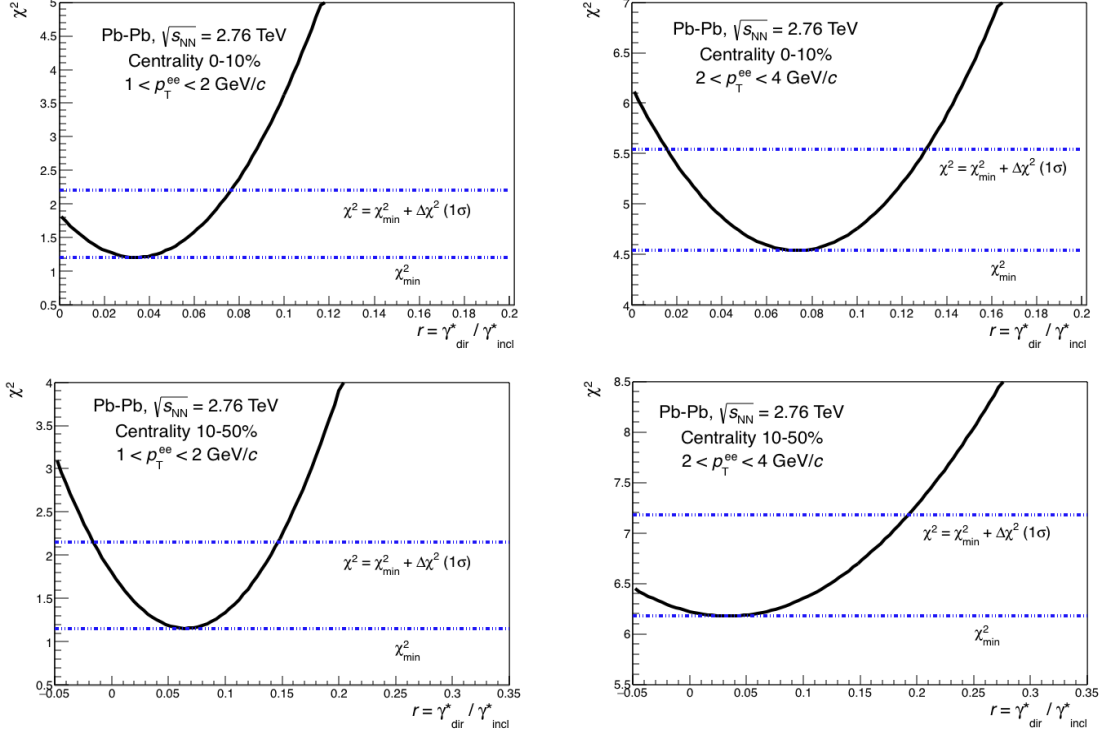


Fig. 9.4 : χ^2 curves as a function of the fit parameter r in central (upper row) and semi-central (lower row) collisions for the transverse momentum intervals $1 < p_{\text{T}}^{\text{ee}} < 2 \text{ GeV}/c$ (left) and $2 < p_{\text{T}}^{\text{ee}} < 4 \text{ GeV}/c$ (right). The χ^2 variation ranges used to extract the statistical uncertainties on the r measurement are also shown.

For the calculation of the systematic uncertainties, the contributions from data, the hadronic cocktail components and the normalization range have been considered separately. The systematic uncertainties from data have been obtained by considering the variation of the virtual direct photon measurement due to a coherent shift of all data points by their systematic uncertainties, while the hadronic cocktail and the normalization range remained unaltered. The systematic uncertainties for this contribution have been given by the RMS of the variations corresponding to the upward and downward shift of the data points, with respect to the measured virtual direct photon fraction r_0 :

$$(\Delta r)_{\text{Data}}^{\text{sys}} = \sqrt{\frac{(r_{\text{upper}} - r_0)^2 + (r_{\text{lower}} - r_0)^2}{2}} \quad (9.4)$$

The systematic uncertainties for the light-flavor and heavy-flavor components of the hadronic cocktail have been calculated similarly, while the contribution from normalization has been calculated by considering the variations of the measurement corresponding to the following normalization ranges: $0 < m_{ee} < 20 \text{ MeV}/c^2$, $0 < m_{ee} < 40 \text{ MeV}/c^2$ and $0 < m_{ee} < 60 \text{ MeV}/c^2$. The total systematic uncertainties have been obtained by summing in quadrature all individual contributions.

Tables 9.1 and 9.2 summarize the measured values of r for both centrality classes, including their statistical and systematic uncertainties.

p_T^{ee} range	r	Stat.	Data	Light-flavor	Heavy-flavor	Normaliz.	Total syst.
[1, 2] GeV/ c	0.034	0.04	0.09	0.023	0.014	0.003	0.1
[2, 4] GeV/ c	0.073	0.06	0.06	0.021	0.023	0.005	0.07

Table 9.1 : Fraction of virtual direct photons measured in central collisions.

p_T^{ee} range	r	Stat.	Data	Light-flavor	Heavy-flavor	Normaliz.	Total
[1, 2] GeV/ c	0.065	0.08	0.11	0.023	0.009	0.003	0.11
[2, 4] GeV/ c	0.0340	0.16	0.07	0.022	0.015	0.0015	0.08

Table 9.2 : Fraction of virtual direct photons measured in semi-central collisions.

Fig. 9.5 shows the values of the virtual direct photon fraction measured in central (0-10%) and semi-central (10-50%) collisions in the transverse momentum intervals $1 < p_T^{ee} < 2 \text{ GeV}/c$ and $2 < p_T^{ee} < 4 \text{ GeV}/c$. These measurements were consistent within their statistical and systematic uncertainties (Fig. 9.6).

The reduced sensitivity due to the marginal statistics and the large uncertainties was reflected in the low statistical significance of the measured virtual direct photon fractions, which was in the range 0.2 - 1.3. Since the measured fractions of virtual direct photons were consistent with zero within their uncertainties in both centrality classes, their upper limit at 90% C.L. have been estimated (Fig. 9.7). These confidence ranges were consistent with the measurement of real direct photons from ALICE in Pb–Pb collisions

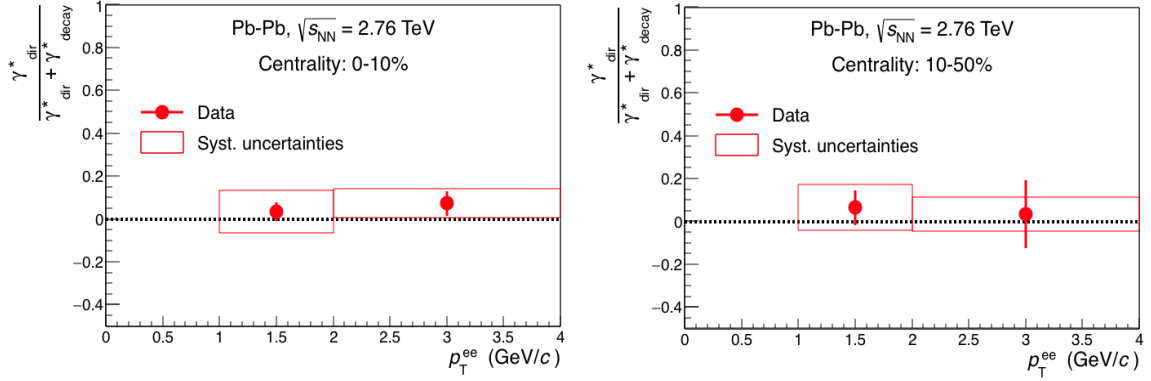


Fig. 9.5 : Fraction of virtual direct photons measured in central (left) and semi-central (right) collisions.

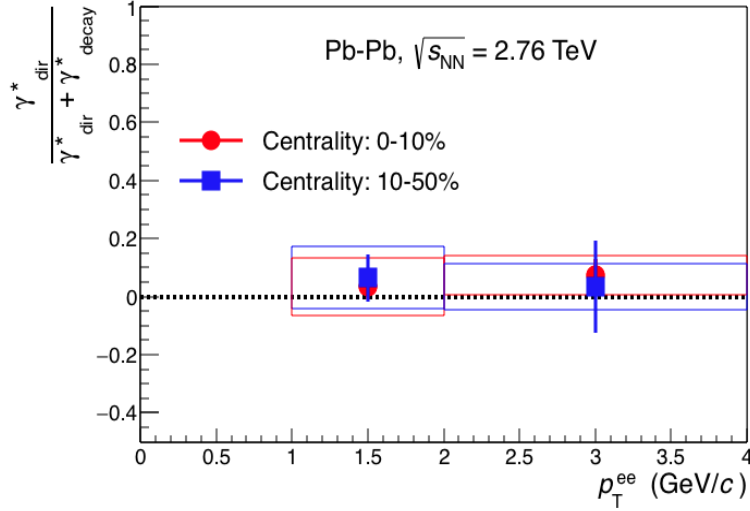


Fig. 9.6 : Comparison between the fraction of virtual direct photons measured in central and semi-central collisions.

at $\sqrt{s_{NN}} = 2.76$ TeV [70] and with existing dielectron measurements from PHENIX and STAR in Au–Au collisions at $\sqrt{s_{NN}} = 200$ GeV at the RHIC [101, 100]. Although the latter two measurements have been performed at lower center-of-mass energies compared to the measurements at the LHC, their reference was still valid considering the consistency observed in the real photon measurements at these two energy scales.

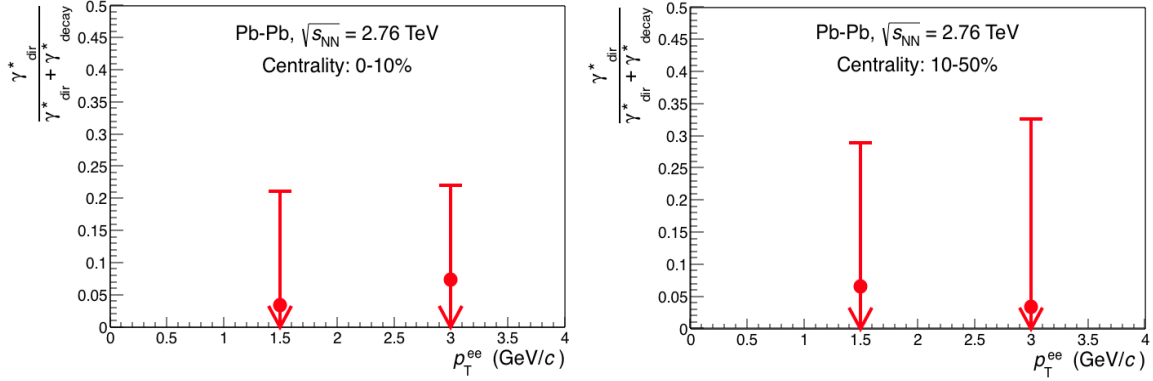


Fig. 9.7 : Fraction of virtual direct photons measured in central (left) and semi-central (right) collisions and their upper limits at 90% C.L. These have been extracted using the procedure outlined in Appendix B.

9.4 Comparison with Theoretical Predictions

The dielectron invariant mass spectrum was expected to contain additional contributions besides its hadronic component, originating from thermal dileptons and in-medium modifications of low-mass vector mesons. The latter two have been obtained from theoretical model calculations for Pb–Pb collisions at $\sqrt{s_{\text{NN}}} = 2.76$ TeV corresponding to $\langle dN_{\text{ch}}/dy \rangle = 1600$. The thermal component has been obtained from an expanding fireball model using a lattice-QCD inspired approach with an equation of state for the QGP with $T_C = 170$ MeV. The simulation of in-medium modifications of the ρ^0 and ω mesons have been obtained from an hadronic many-body theory approach, which predicted a broadening of the electromagnetic spectral functions of low-mass vector mesons [142, 143]. No contribution from Drell-Yan has been considered in the simulation. Fig. 9.8 shows the dielectron spectrum measured in central collisions in comparison with the expected contributions from hadron decays, thermal dileptons and in-medium modified ρ^0 and ω mesons.

Data were in good agreement with the expectations within the experimental uncertainties. The contributions from in-medium modified ρ^0 and ω become significantly larger compared to that of thermal dielectrons in the mass range $500 \lesssim m_{ee} \lesssim 850$ MeV/ c^2 . The sensitivity of the current measurement in studying in-medium properties of low-mass vector mesons was limited by the large uncertainties and by the intensity of the magnetic field (0.5 T) used for tracking, which has required a relatively high- p_{T} threshold in the dielectron analysis, thus rejecting a relatively large fraction of the signal. The phase-space region which is more sensitive to in-medium effects of the ρ^0 and ω mesons will be explored more accurately in Run 3 with higher statistics, reduced systematic

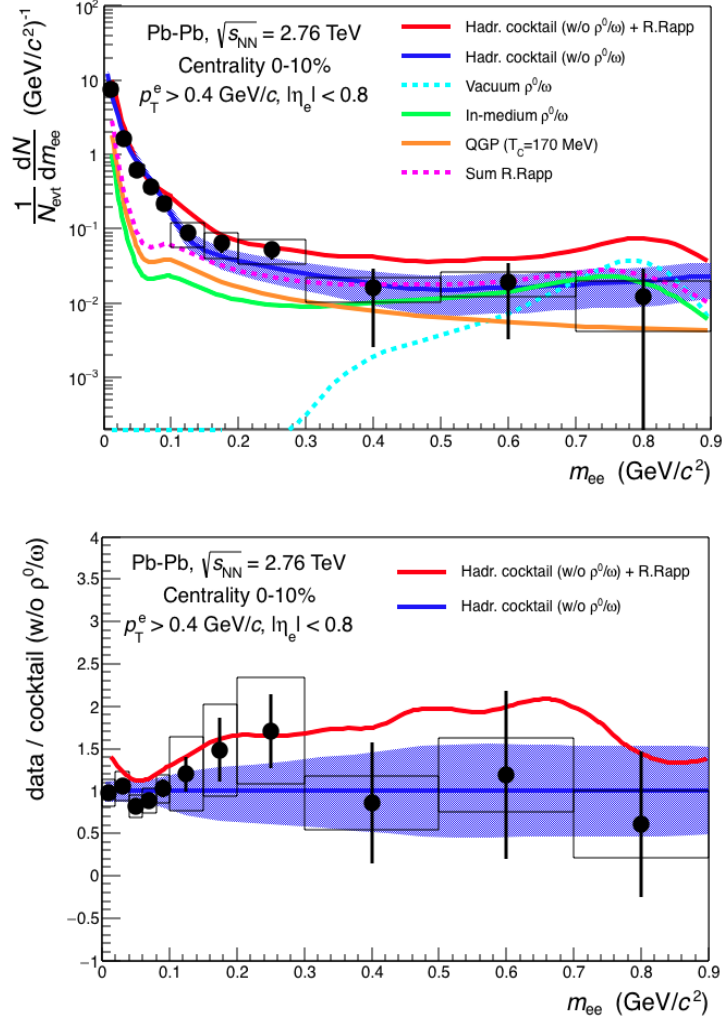


Fig. 9.8 : Dielectron invariant mass spectrum measured in central (0-10%) Pb–Pb collisions at $\sqrt{s_{NN}} = 2.76$ TeV in comparison with its expected contributions from hadron decays, thermal dileptons from QGP and in-medium modifications of the spectral functions of the ρ^0 and ω mesons [142, 143].

uncertainties and a lower intensity of the magnetic field (0.2 T instead of 0.5 T). The perspective and the expected sensitivity for the dielectron measurement in Run 3 after the ALICE upgrade are discussed in the next chapter.

Chapter 10

Perspectives for Dielectron Measurements after the ALICE Upgrade

10.1 Introduction

The ALICE upgrade program is a very complex and challenging task. It will imply major improvements of the main sub-detectors, in terms of performance and readout rates. This will be needed for the third period of data taking (Run 3) in order to handle 50 kHz of Pb–Pb event rate which will be delivered by the LHC after its luminosity upgrade. This chapter contains a brief description of the main features of the new ITS and TPC readout system and their expected performance, with a particular focus on the main advantages that these detectors will bring for the dielectron measurements. The expected scenario for the measurement of the dielectron invariant mass spectrum and the measurement of the temperature of the created matter is presented, based on simulations of the detector performance and event rates. With the expected higher statistics and improved performances of the experimental apparatus, dilepton measurement will become one of the main protagonists of the heavy-ion experimental program at the LHC after the ALICE upgrade.

10.2 Upgrade of the ITS and TPC

The new ITS will consist of 7 concentric cylindrical layers of high-resolution and low-mass monolithic pixel sensors: three layers will constitute the inner barrel, while the remaining

four layers will form the outer barrel (Fig. 10.1) [144]. The first layer of the inner tracking system, which in the current setup is located at $r = 39$ mm, will be placed closer to the interaction point ($r = 22$ mm). This will require a new beam pipe with a smaller radius (currently the beam pipe outer radius is $r = 29$ mm). The detector material budget will be significantly reduced, going from 1.14% of the radiation length in the current ITS to 0.3% for the 3 inner layers and 0.8% for the outer layers in the new ITS. The size of the pixels will also be significantly reduced: from $(50\mu\text{m} \times 425\mu\text{m})$ to $(30\mu\text{m} \times 30\mu\text{m})$. The upgraded ITS will have more than twelve billion pixels in total, complemented with a highly advanced readout system, able to handle up to 100 kHz of Pb–Pb event rate.

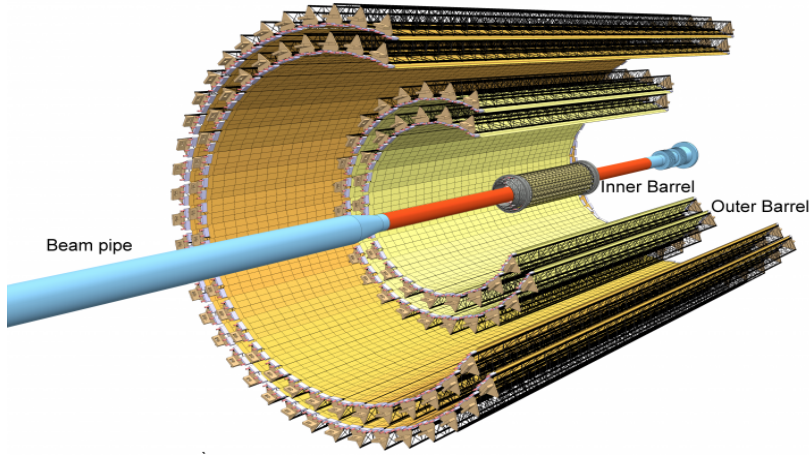


Fig. 10.1 : Schematic view of the new Inner Tracking System.

The reduced material budget will reduce the amounts of photon conversions in the detector material, which give the largest contribution to the combinatorial background, and it will increase the track reconstruction efficiency, especially at low p_T (Fig. 10.2). This will enhance the probability to detect both charged decay products of π^0 and η Dalitz decays, which can be more efficiently rejected using the pre-filter technique. To this end, ITS standalone tracks can be used for tagging the fully reconstructed tracks in the search for close pairs.

The smaller pixel size, the increased number of tracking layers and the closer position of the first layer to the interaction point will improve the momentum and secondary vertex resolutions, allowing for a better separation of electrons from heavy-flavor decays using DCA cuts. The expected suppression of correlated electron-positron pairs from semi-leptonic charm decays is by about a factor ~ 5 compared to prompt pairs [146]. The expected reduction of the combinatorial and physical background will con-

tribute to enhancing the signal-to-background ratio and the significance of the dielectron measurement.

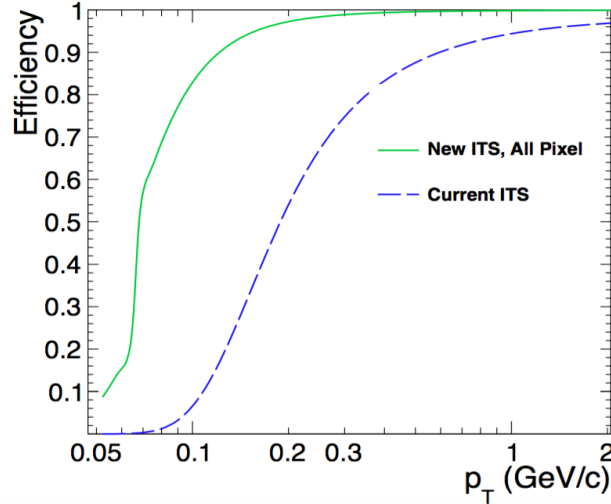


Fig. 10.2 : Comparison between the track reconstruction efficiency as a function of p_T of the new and current ITS [144].

The current TPC readout system uses Gating Grids (GG), located close to the TPC endcaps, which are used to avoid ion backflow into the drift region of the TPC. Ions, being positively charged, would drift towards the center of the TPC building up a significant space charge that would distort the TPC electric field. The drift time measurement of electrons produced by ionization is crucial to estimate the z -coordinate of the ionization event, which is necessary for the three-dimensional track reconstruction. This measurement relies on the knowledge of the electric field inside the TPC volume. The TPC readout time ($\sim 100\mu\text{s}$) and the GG closure time ($\sim 200\mu\text{s}$) impose an upper limit on the acquisition rate at $\sim 3\text{kHz}$.

The new TPC readout system will be based on GEM foils (Fig. 10.3 left), which will allow for a continuous operation. The data acquisition rate is expected to increase by a factor ~ 100 with the new TPC readout system [145]. Single GEMs have no specific intrinsic ion blocking capabilities and the ion backflow of a single GEM is $\sim 10\%$, comparable to that of MWPC with open Gating Grid. The great advantage of GEMs is that they can easily be stacked, creating a pre-amplification and main amplification stages (Fig. 10.3 right). Ions are mainly produced in the latter and, drifting backward they are blocked by the pre-amplification stage, with no need for a Gating Grid.

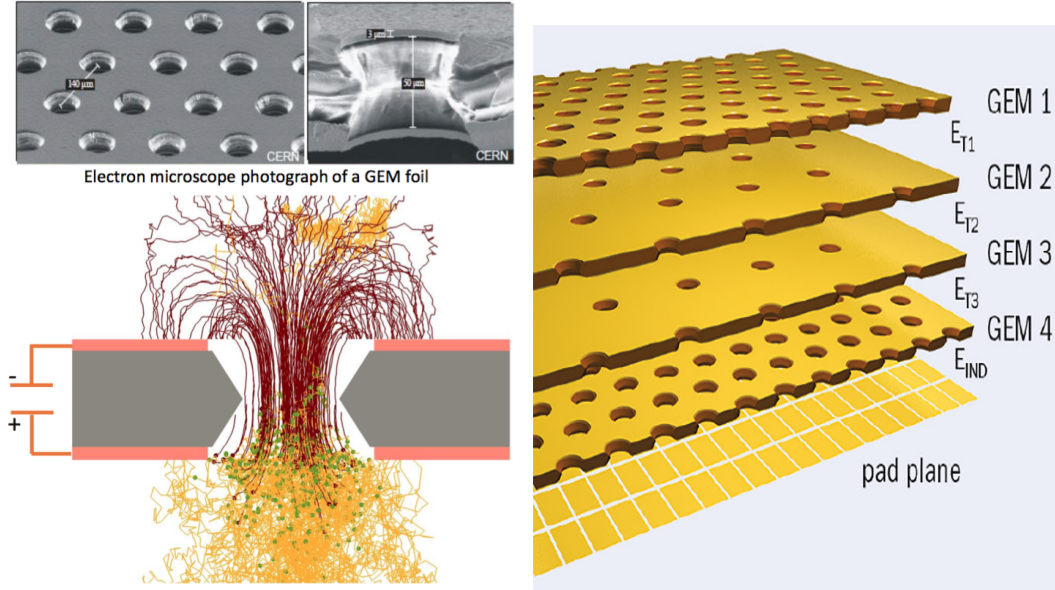


Fig. 10.3 : GEM foils photographed with electronic microscope and schematic sketch of charge amplification (left) and illustration of a stack of GEM foils, designed to create pre- and main amplification stages (right) [145].

10.3 Physics Performance Study

The expected scenario for dielectron measurements after the ALICE upgrade has been studied using MC simulations. In Run 3, after the luminosity upgrade of the LHC, the center-of-mass energy of Pb–Pb collisions will be 5.5 TeV per nucleon. The expected number of events with the new TPC readout system for the two centrality ranges used in this simulation were $2.5 \cdot 10^9$ for central (0–10%) and $5 \cdot 10^9$ for semi-central (40–60%) collisions, respectively. The simulated responses of the upgraded detectors and the parametrization of their efficiencies have been obtained based on their expected performance. The set of dielectron sources used as input in the simulation included:

- **Light-flavor cocktail:** This contained the contributions from low-mass pseudoscalar and vector mesons decays. Their yields have been adjusted based on the expected charged particle multiplicity at $\sqrt{s_{NN}} = 5.5$ TeV. Their p_T spectra and particle ratios have been obtained by extrapolation from the existing Pb–Pb data.
- **Charm:** The contribution from correlated semi-leptonic charm decays has been obtained by scaling the corresponding contribution in pp collisions at the same energy, obtained using the PYTHIA event generator, by the average number of binary nucleon-nucleon collisions $\langle N_{coll} \rangle$. The charm production cross section in pp

collisions at $\sqrt{s} = 5.5$ TeV has been obtained by interpolation of the existing data. Energy loss of heavy quarks in the hot and dense medium have been neglected.

- **Thermal dielectrons:** The contributions from thermal dileptons, produced both in the QGP and in the hot hadronic gas phase, have been obtained using perturbative emission rates. In-medium effects of low-mass vector mesons have been calculated based on the hadronic many-body theory.

All particles produced in the simulation have been propagated through the ALICE apparatus using GEANT 3, which also provided a realistic amount of conversions. The dielectron invariant mass spectrum has been obtained by subtracting the combinatorial background from the inclusive dielectron yield. The pre-filter technique has been used to reduce the contributions to the combinatorial background from conversions, π^0 and η Dalitz decays, exploiting also ITS standalone tracks. The tagging criterion for rejection of close pairs has been based on their mass and opening angle: conversion and Dalitz pair candidates have been defined by $m_{ee} < 50$ MeV/ c^2 and $\theta_{ee} < 0.1$ rad.

Fig. 10.4 shows the combinatorial background, the signal-to-background ratio and the statistical significance per event ($1/\sqrt{N_{\text{evt}}} \cdot S/\sqrt{S+B}$) obtained from the analysis of the simulated Pb–Pb collision events at $\sqrt{s_{\text{NN}}} = 5.5$ TeV for the current and new ITS. The better background rejection capabilities of the new ITS will result in a factor ~ 2 improvement in terms of S/B.

The dominant contributions to systematic uncertainties originated from the large combinatorial and physical backgrounds. The relative systematic uncertainties on the signal due to the combinatorial background was given by:

$$\frac{(\Delta S)_{\text{bkg}}}{S} = \frac{(\Delta B)}{B} \frac{B}{S} \quad (10.1)$$

The value of $\Delta B/B$ that has been used in this simulation was 0.25 %, taken from the estimate done by PHENIX in a similar analysis [97]. The relative systematic uncertainties on the signal due to the light-flavored component of the hadronic cocktail and the charm contribution have been assumed to be 10% and 20%, respectively.

10.4 Expected Scenario for Dielectron Measurements

This paragraph summarizes the main results of the physics performance study described in the previous section. Thermal radiation and in-medium modification of the ρ^0 and ω mesons can be studied from the "excess spectrum", obtained by subtracting the hadronic cocktail - except for the ρ^0 and ω mesons - from the dielectron spectrum. Fig. 10.5 shows

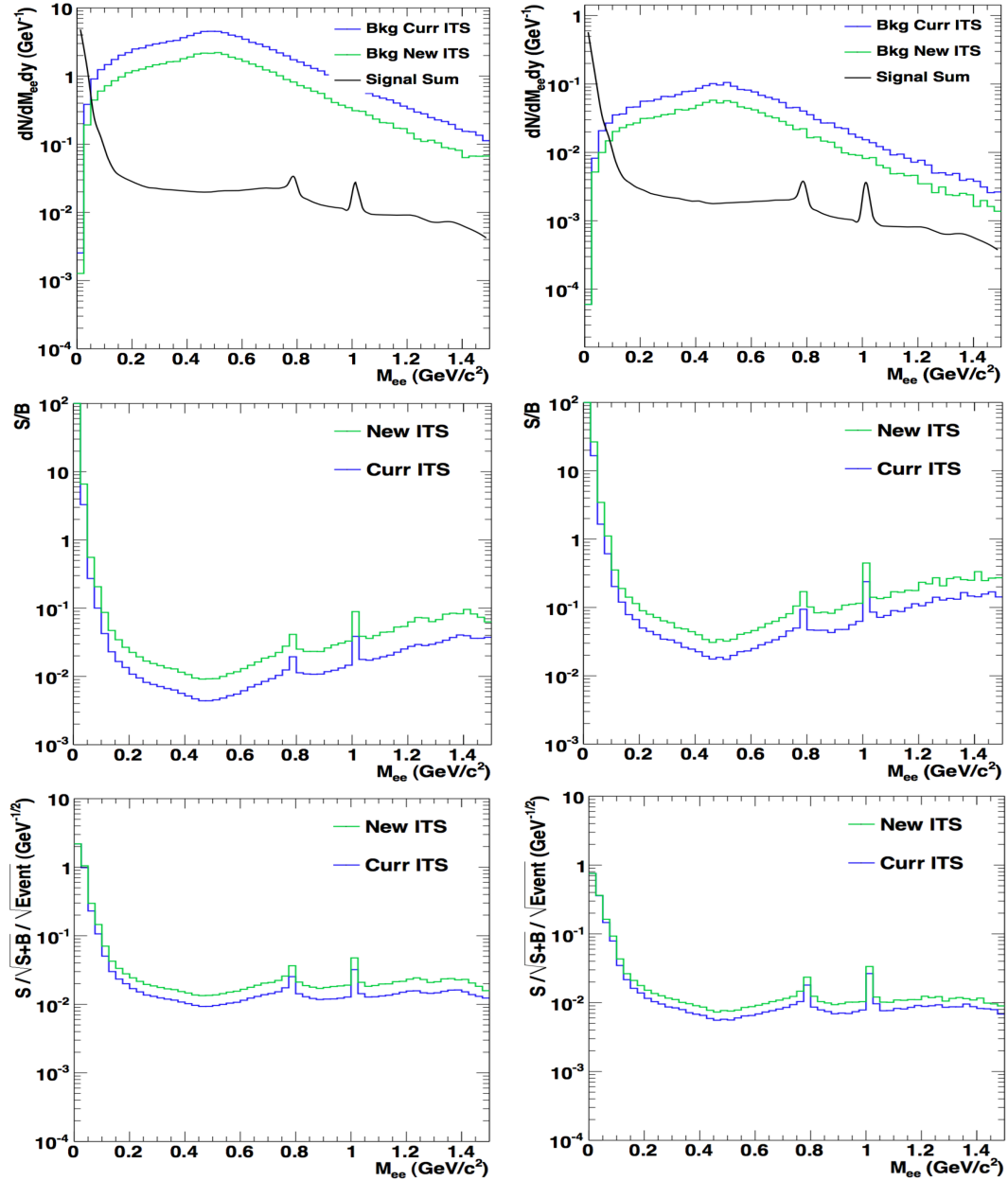


Fig. 10.4 : Expected combinatorial background and signal (top), signal-to-background ratio (middle) and statistical significance per event (bottom) for central (left column) and semi-central (right column) Pb–Pb collisions at $\sqrt{s_{NN}} = 5.5$ TeV.

the predicted excess dielectron spectra in Pb–Pb collisions at $\sqrt{s_{NN}} = 5.5$ TeV with the low acquisition rate of the current TPC for two different scenarios: for the current and the upgraded ITS.

The higher tracking efficiency at low p_T of the new ITS will enhance its rejection capabilities of the combinatorial background as compared to the current ITS. This will

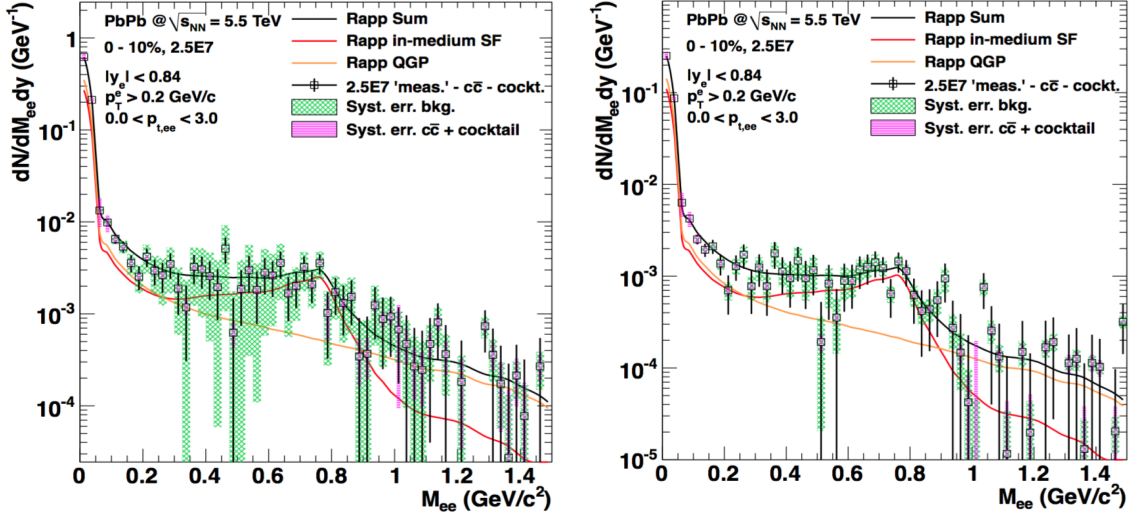


Fig. 10.5 : Expected dielectron excess spectra in Pb–Pb collisions at $\sqrt{s_{\text{NN}}} = 5.5$ TeV for the current (left) and the upgraded ITS (right).

result in a reduction of the systematic uncertainties deriving from the combinatorial background. The improved resolution of secondary vertices of the new ITS will result in a higher rejection efficiency of charm decays, thus reducing also the systematic uncertainties originating from the subtraction of dielectrons from charm decays. The limited statistics, due to low acquisition rate of the current TPC, is however not sufficient for a precise study of the thermal dielectron spectrum. The new TPC readout system will allow for a continuous data collection, leading to an improvement in the collected statistics of a factor ~ 100 . This will allow for precise measurements of the thermal radiation and detailed study of the in-medium modification of the ρ^0 and ω meson properties (Fig. 10.6).

The study of the p_T distributions for several mass regions allows the measurement of the effective temperature, which contains information on the collective flow at different stages of the collision. The differential study of the dielectron spectrum measured at high-rate with the upgraded ITS will allow a statistical precision in the measurement of the effective temperature of the order of $\sigma(T_{\text{eff}})/T_{\text{eff}} \approx 1\%$.

The temperature of the created matter in the early phases can be measured from an exponential fit to the intermediate mass region: $dn/dm_{ee} \propto \exp(-m_{ee}/T)$. Fig. 10.7 shows the ratio between the temperature extracted from an exponential fit to the mass region $1.0 < m_{ee} < 1.5$ GeV/c^2 and the input temperature of the model, in central (0-10%) and semi-central (40-60%) collisions, for the following three scenarios: current detectors, new ITS and current TPC, upgraded ITS and GEM-TPC. In the high-rate

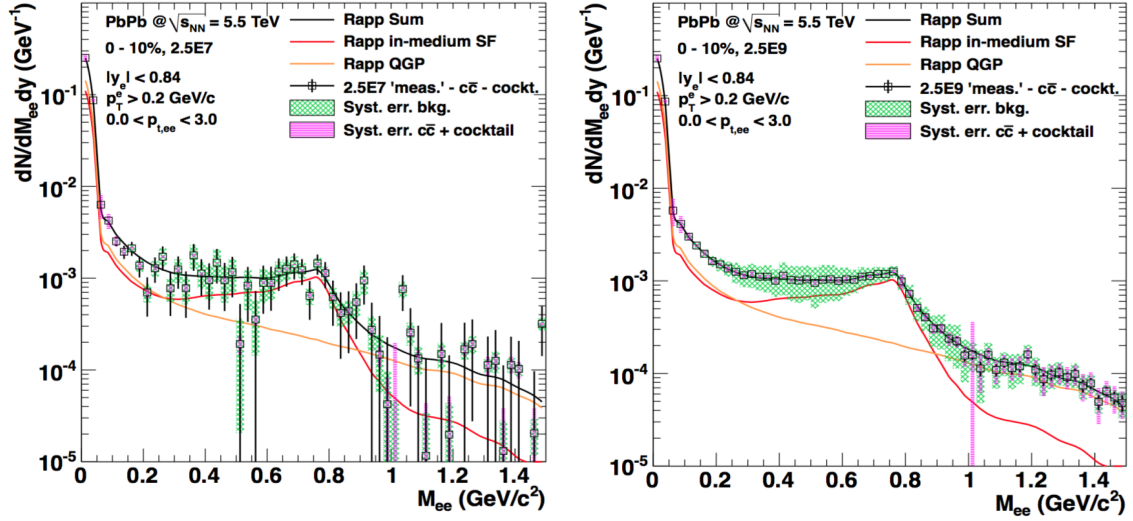


Fig. 10.6 : Expected dielectron excess spectra in Pb–Pb collisions at $\sqrt{s_{NN}} = 5.5$ TeV and for the current (left) and the new TPC readout system (right). Both scenarios refer to a detector setup including the upgraded ITS.

scenario with upgraded ITS it will be possible to precisely measure the temperature of the created matter with statistical and systematic uncertainties in the range 10-20%.

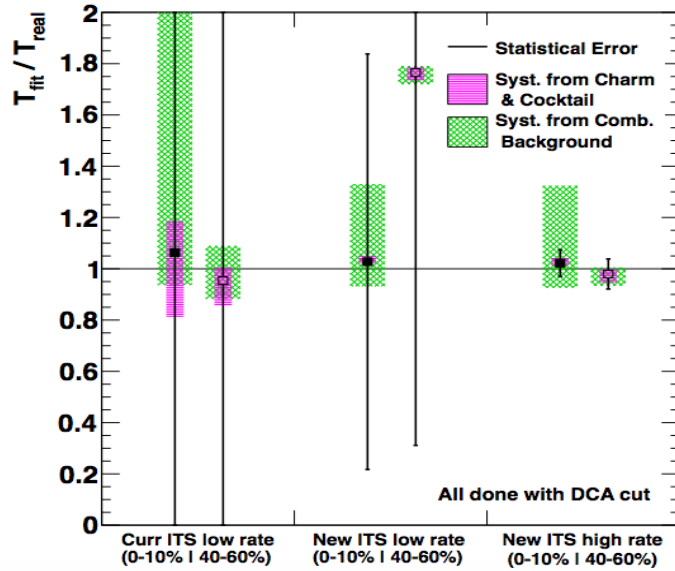


Fig. 10.7 : Expected results for the temperature measurement obtained from an exponential fit to the intermediate mass region ($1.0 < m_{ee} < 1.5$ GeV/c²) in central (0-10%) and semi-central (40-60%) collisions for three different scenarios: current detectors, new ITS and current TPC, upgraded ITS and high-rate from the GEM-TPC.

A detailed measurement of the dielectron elliptic flow coefficient as a function of mass will also be possible with high acquisition rate and upgraded ITS (Fig. 10.8). The study of the physics performance, done in semi-central Pb–Pb collisions where the elliptic flow is more pronounced, has demonstrated that the dielectron v_2 can be measured with relative statistical uncertainties of $\sim 1\text{--}2\%$. This will provide precious information on dielectron collectivity and possible access to the partonic equation of state.

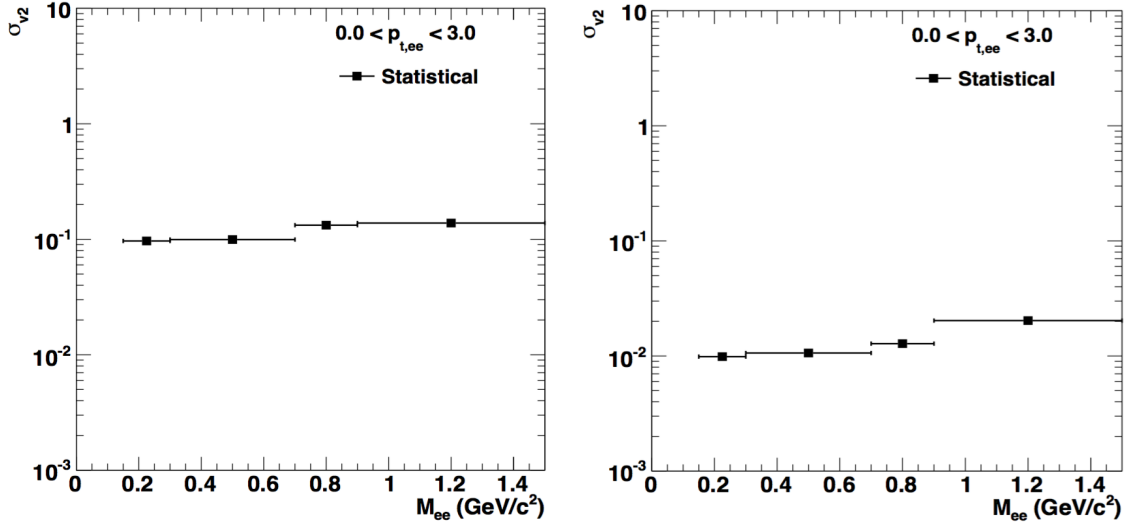


Fig. 10.8 : Expected absolute statistical uncertainties in the dielectron v_2 measurement as a function of mass in semi-central (40–60%) Pb–Pb collisions at $\sqrt{s_{NN}} = 5.5$ TeV. The scenario with current detectors and low acquisition rate is shown on the left, while the high-rate scenario with upgraded ITS is shown on the right.

In conclusion, a detailed study of the dielectron invariant mass spectrum can be done with high acquisition rate and upgraded ITS. This will allow high precision measurements of the early temperature of the system, through a fit to the intermediate mass region of the dielectron spectrum, the in-medium properties of low-mass vector mesons and the dielectron v_2 coefficient, which brings information on the dielectron collective flow. The new ITS will have enhanced background rejection capabilities, contributing to reduce the systematic uncertainties originating from the large combinatorial and physical backgrounds. The new TPC readout system, based on GEM foils, will allow continuous operation. This will contribute to increasing the collected statistics by a factor ~ 100 , with a significant improvement of the statistical precision of dielectron measurements.

Chapter 11

Summary and Conclusions

The dielectron invariant mass spectrum has been measured in central (0-10%) and semi-central (10-50%) Pb–Pb collisions at unprecedented energies with ALICE at the LHC. Dielectrons are electromagnetic probes which carry unaffected information on the evolution of the hot and dense matter created in heavy-ion collisions. These are rare probes, whose production is governed by the electromagnetic interaction. The measurement of electromagnetic probes is an extremely challenging task, due to the small signal and huge background. The analysis was mainly focused on the low-mass region of the dielectron spectrum ($m_{ee} < 900 \text{ MeV}/c^2$), where the contributions from thermal dielectrons from the partonic and hadronic phase were expected. This mass region was also interesting to study the modifications of the electromagnetic spectral functions of low-mass vector mesons in the hot hadron gas phase. These in-medium effects have been proposed since a long time as signatures for chiral symmetry restoration at high temperature. Moreover, the measurement of quasi-real virtual direct photons, in the low-mass region for $p_T^{ee} \gg m_{ee}$, provided a complementary and independent measurement to that of real direct photons.

This delicate analysis has required a careful choice of the track selection criteria, the particle identification and of the background rejection methods.

Track selection cuts have been optimized to ensure a good quality of the reconstructed tracks and to reject secondary tracks. The particle identification strategy has been studied to have a track sample with high electron purity. This was done to reduce the impact of the hadron contamination on the dielectron invariant mass spectrum, originating from correlated electron-hadron or hadron-hadron pairs (hadronic background), which would have produced a fake signal due to the electron mass assignment to all reconstructed tracks. The contribution from this hadronic background, which was of the order of $\sim 2\%$,

has been estimated using the MC simulations with properly tuned input distributions and subtracted from the dielectron spectrum. Electrons produced by photon conversion in the detector material were about 70% of all electrons in the selected track sample, thus representing the largest contributors to the combinatorial background. A substantial effort has been dedicated to the development of very efficient conversion rejection methods in order to reduce the combinatorial background and improve the signal-to-background ratio in the mass region of interest. Photon conversion rejection on a single-track basis, which conveniently exploited some features of the tracking algorithm and the properties of secondary tracks, has been complemented with pair rejection methods, which were based on the correlations between electron-positron pairs produced by photon conversion in the material and the orientation of the plane defined by their momentum vectors with respect to the ALICE magnetic field. The latter approach has been used to tag conversion candidates, which were rejected from the selected track sample, thus removing their contribution to the combinatorial background (active background rejection). The combination of these two methods gave a suppression efficiency of conversion electrons reaching $\sim 90\%$. This resulted in an improvement of the signal-to-noise ratio of a factor ~ 2 in the low-mass region. The residual contribution to the dielectron spectrum from surviving conversion electrons has been estimated using the MC simulations and subtracted from the spectrum. The combinatorial background in the dielectron invariant mass spectrum has been estimated using the invariant mass distribution of same-sign dielectron pairs, which simultaneously incorporated the uncorrelated and correlated background. Small distortions in the like-sign distribution were produced by a charge asymmetry originating from some detector inhomogeneities. These geometric effects, which created a different acceptance for opposite-sign and same-sign dielectron pairs, have been corrected using the event-mixing technique. The two magnetic field configurations used during the data taking in Run 1, gave opposite charge asymmetries which resulted in a difference between the corresponding correction factors of the order of $\sim 2\%$. Given the high level of precision required in the background estimation, the events corresponding to opposite magnetic field orientations have been analyzed separately and the final spectra have been combined after the pair efficiency correction. These detector geometrical asymmetries were correctly reproduced by the simulations. The pair reconstruction efficiency has been estimated using the MC simulations, in which the effects of the radiative energy loss, the momentum resolution and angular smearing for electrons have also been included using two-dimensional detector response matrices.

The fully corrected dielectron spectra, measured in central (0-10%) and semi-central

(10-50%) Pb–Pb collisions, for all transverse momenta and for $1 < p_{\text{T}}^{\text{ee}} < 2 \text{ GeV}/c$ and $2 < p_{\text{T}}^{\text{ee}} < 4 \text{ GeV}/c$, have been compared to the expected contributions from hadron decays in the mass range $m_{\text{ee}} < 900 \text{ MeV}/c^2$. Data were consistent with the so-called "hadronic cocktail" within their statistical and systematic uncertainties. This indicated a reduced sensitivity in measuring the additional contributions to the dielectron spectrum which were expected in the low-mass region (thermal dileptons and in-medium modified ρ^0 and ω). Within the limits imposed by the low statistics and the large systematic uncertainties due to the reduced knowledge of all hadronic components, the contribution from virtual direct photons has been measured. This was done by fitting the dielectron spectrum with a three-component function in the mass range $100 < m_{\text{ee}} < 300 \text{ MeV}/c^2$ for the transverse momentum intervals: $1 < p_{\text{T}}^{\text{ee}} < 2 \text{ GeV}/c$ and $2 < p_{\text{T}}^{\text{ee}} < 4 \text{ GeV}/c$. The three components of the fit function were the mass distribution of the light flavor and heavy flavor contributions of the hadronic cocktail and the mass shape of virtual direct photons, given by the Kroll-Wada equation. The fractions of virtual direct photons measured in central (0-10%) and semi-central (10-50%) collisions were consistent within their statistical and systematic uncertainties. Due to the small statistical significance of these measurements, their upper limits at 90% C.L. have been extracted in both centrality ranges based on the Feldman and Cousins methodology. The estimated confidence intervals were compatible with the measurement of real direct photons from ALICE and with existing dielectron measurements from PHENIX and STAR at RHIC. The dielectron spectrum measured in central (0-10%) Pb–Pb collisions has been compared to expectations from theoretical model calculations including thermal dielectrons from QGP and hadron gas and in-medium effects of low-mass vector meson decays, obtained using an approach based on the hadronic many-body theory. The measured spectrum was consistent with the expectations within the experimental uncertainties.

The perspectives for dielectron measurements and the expected scenario after the ALICE upgrade have been studied with MC simulations, based on the expected performance of the new detectors. The new ITS, with reduced material budget and improved secondary vertex resolution, will give higher rejection capabilities of the main background sources (conversions, Dalitz decays, charm and beauty) while the new TPC readout system, based on GEM foils, will enable to handle the higher event rate expected after the LHC luminosity upgrade. This will result in a factor > 100 more statistics which, together with the reduced systematic uncertainties (due to reduced contribution from charm and beauty) will allow for precise measurement of the temperature of the created matter from an exponential fit to the intermediate mass region ($1 < m_{\text{ee}} < 1.5 \text{ GeV}/c^2$). The higher

statistical precision, smaller systematic uncertainties and reduced contributions from Dalitz and heavy flavor decays in the low-mass region will give the necessary sensitivity for a detailed study of in-medium effects of the spectral properties of low-mass vector mesons.

The dielectron measurement in Run 1 can be considered a pioneering work, in which the analysis techniques have been optimized and the detector effects have been understood. A better knowledge of the global picture will be reached in Run 2, with slightly higher statistics, while a high precision dielectron measurement will be done only in Run 3, after the upgrade of the main sub-detectors of the ALICE experimental apparatus.

Samenvatting

Het massaspectrum van dielectrons is gemeten in ultra-relativistische zware-ionen botsingen met ALICE bij de Large Hadron Collider (LHC). Het begin van het dielectron spectrum is gevoelig voor thermische straling van de partonische en hadronische fase en modificaties aan de lage-massa vector mesonen.

De meting van deze zeldzame elektromagnetische sondes zijn zeer uitdagend door de kleine hoeveelheid signaal en grote hoeveelheid achtergrond. Innovatieve en efficiënte technieken zijn gebruikt om de dominante bijdrage van de achtergrond in de meting te onderdrukken. De bijdrage van virtuele directe fotonen is vooral aanwezig aan het begin van het dielectron massaspectrum. Daardoor is de meting een aanvulling en onafhankelijke bijdrage op de bestaande metingen van directe fotonen. De meting van de virtuele directe fotonen is in overeenstemming met de directe fotonen uitgevoerd door ALICE, en met de bestaande dielectron metingen van experimenten aan de relativistische Heavy-Ion Collider (RHIC) bij lagere energie. De gemeten dielectron spectrum is vergeleken met de voorspellingen van theoretische modellen, die bijdragen bevatten van hadronische vervallen, thermische dileptons en middelgrote modificaties van de ρ^0 en ω mesonen in de hete hadronische fase. De resultaten komen, binnen de experimentele onzekerheid, goed overeen met de theoretische voorspellingen. De vooruitzichten voor dielectron metingen is onderzocht voor de ALICE detector upgrade. De simulaties geven aan dat de temperatuurmeting verbeterd met daarbij een verhoogde gevoeligheid voor middelgrote effecten van lage-massa vector mesonen met verbeterde detectoren en statistieken Run 3 van de LHC.

Appendix A

Reconstruction of Secondary Tracks: Features of the Tracking Algorithm

This section is dedicated to the description of some particular effects produced by the tracking algorithm which affected the reconstructed momentum of secondary tracks. The largest majority of secondary electrons were produced by photon conversion in the detector material and in the Dalitz decay of neutral pions originating from K_S^0 decay, while semi-leptonic heavy flavor decays gave a minor contribution. The momentum modification of these tracks was responsible for a mass shift in the unlike-sign and like-sign dielectron invariant mass distributions. The magnitude of this effect has been significantly reduced using the photon conversion rejection methods (see Section 5.3).

A.1 Shift in the Track Momentum

The track reconstruction algorithm, during the inward track propagation towards the primary vertex, searched for compatible clusters in the inner layers of the detector. Tracks were assumed to be primary if the inward propagation could be extended down to the primary vertex. The momentum of primary tracks was estimated at the point of closest approach (*PCA*) to the primary vertex: its direction was tangent to the reconstructed helicoidal trajectory at the *PCA* while its magnitude was corrected for energy loss in the crossed elements of the detector. Radiative energy loss (Bremsstrahlung) due to the bending of particle trajectories in the magnetic field were also taken into account.

This procedure had some unwanted effects for secondary tracks in the case of a successful inward propagation to the primary vertex. The latter was possible due to wrong cluster associations and to the relatively large fraction of isolated clusters in the ITS ($\sim 60\%$ in Pb–Pb collisions). As a consequence, secondary tracks were tagged as primary

tracks, with a consequent wrong estimation of their momentum. This was calculated at a point which was different from the true production vertex and its magnitude was biased by corrections for the energy loss in the detector material that actually was never crossed. Moreover, a longer path length in the magnetic field was assumed with consequent overestimated radiative energy loss corrections.

The net result of this procedure was to shift the particle momentum to larger values and to modify its azimuthal angle. This effect has been studied using the MC simulation and its magnitude for electrons has been quantified by comparing the generated and reconstructed momentum of electrons. Fig. A.1 shows the relative difference between the reconstructed and generated transverse momentum of electrons in different ranges of p_T^{gen} and for three different ranges of radial distance R of the true production vertex.

Besides the left tail and the width of the distributions, which were caused by Bremsstrahlung and the finite momentum resolution respectively, a momentum shift to higher values of the order of $\sim 3 - 5\%$ was clearly visible. This effect was stronger at lower particle momenta and for larger radial distances of the production vertex, as expected. Fig. A.2 shows the effect of the inward propagation of secondary tracks down to the primary vertex on their azimuthal angle. A systematic shift of the order of $\sim 1 - 2\%$, in either direction depending on the particle charge, was observed in the reconstructed azimuthal angle due to the wrong point used to estimate the particle momentum. This is illustrated in the sketch depicted in Fig. A.3. This effect was stronger for larger radial distances of the particle production vertex and at lower momenta. For particles with a given charge, the shift $\Delta\phi = \phi_{gen} - \phi_{rec}$ was the opposite when the magnetic field was reversed.

This bias in the measurement of the particle momentum had some consequences on the invariant mass and opening angle distributions of opposite-sign and same-sign dielectron pairs. This is discussed in details in the next paragraph.

A.2 Mass and Opening Angle Shift

Fig. A.4 shows the comparison between the invariant mass distributions obtained using the generated and reconstructed momentum, for unlike-sign and like-sign dielectron pairs. A mass shift was visible, in the very low-mass region of the spectrum ($m_{ee} < 100 \text{ MeV}/c^2$), towards larger values for the unlike-sign spectrum and in the opposite direction for like-sign pairs. In the latter, this effect caused the appearance of a unphysical peak at zero mass.

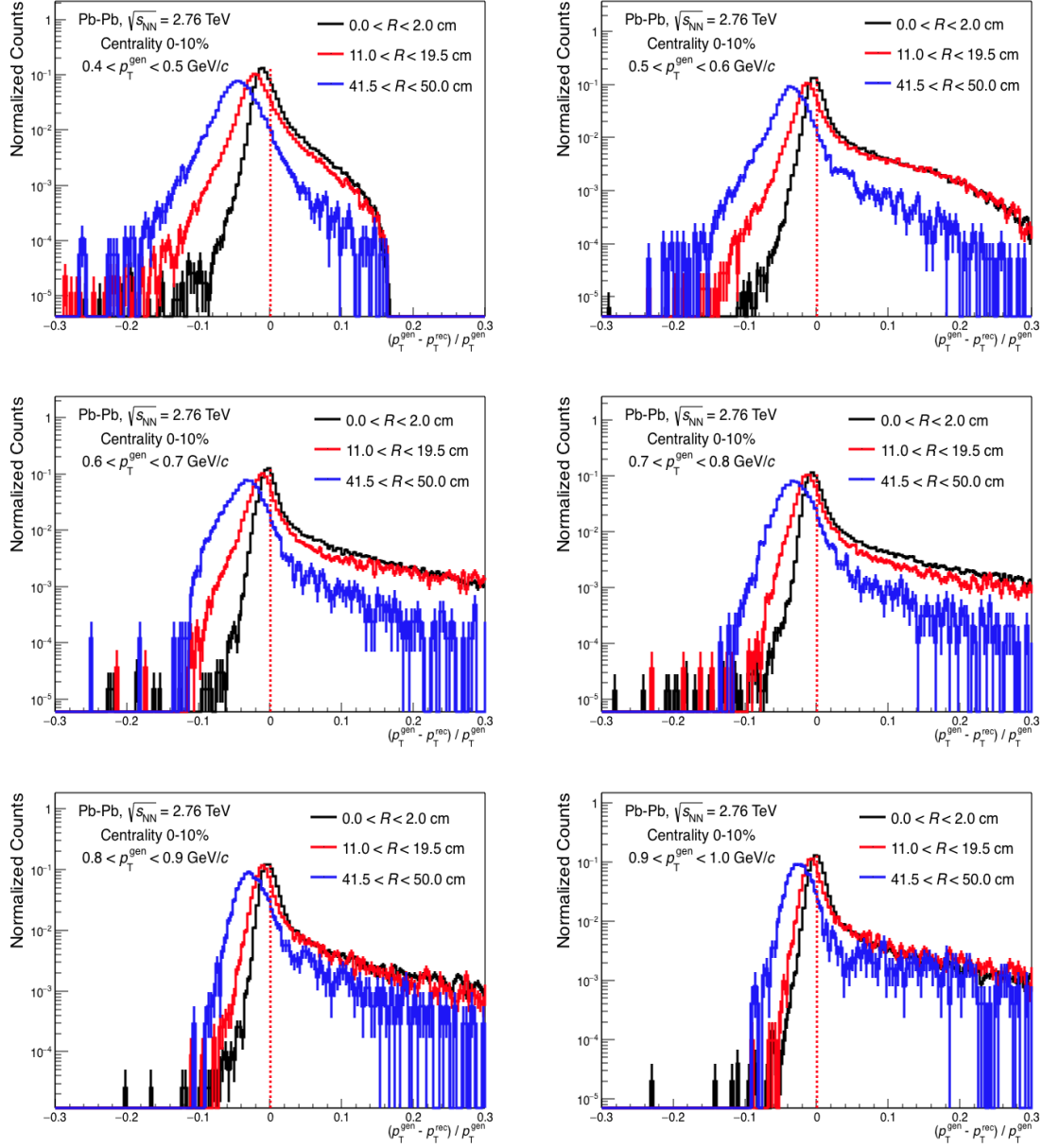


Fig. A.1 : Relative difference between the reconstructed and generated transverse momentum of electrons in different ranges of p_T^{gen} and for three different ranges of radial distance of the true production vertex.

In the case of unlike-sign pairs, this mass shift was caused by the overestimate of the momentum magnitude of secondary electrons, which had the opposite effect of Bremsstrahlung, and to the larger opening angle of these pairs when measured at the PCA to the primary vertex. The larger mass due to a larger opening angle can be

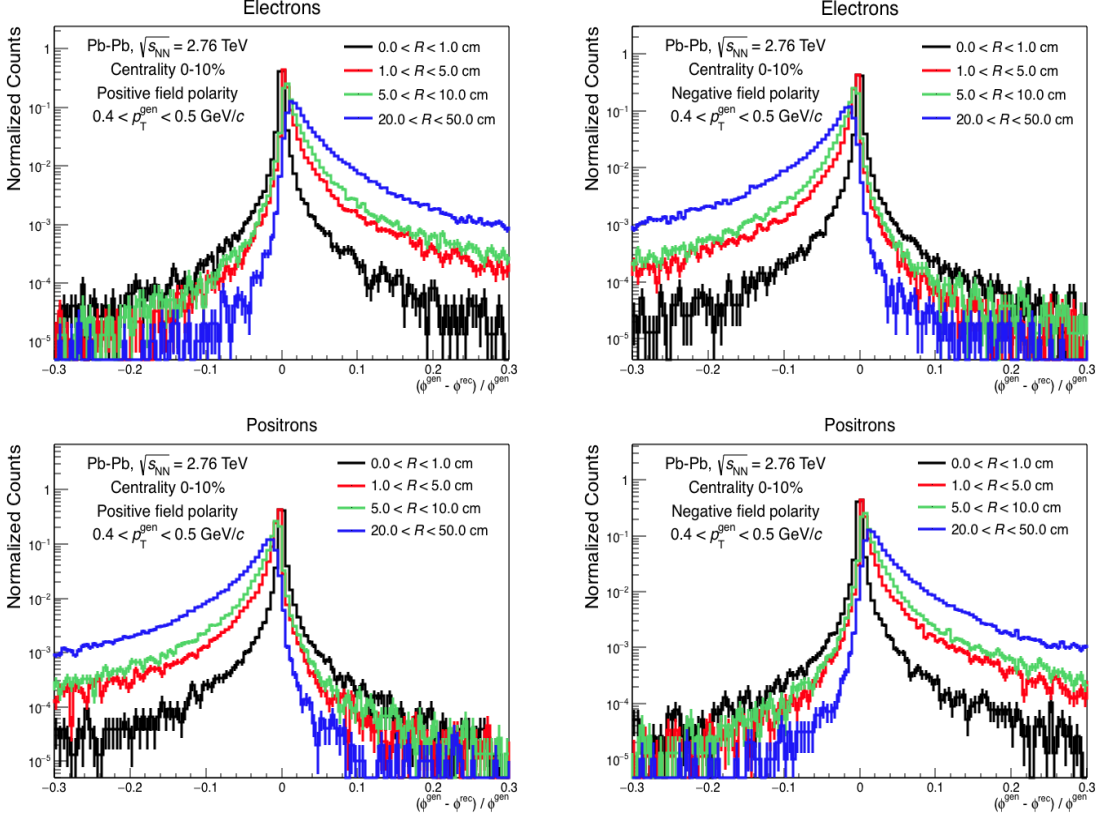


Fig. A.2 : Relative difference between the azimuthal angle of reconstructed and generated momentum of electrons (upper row) and positrons (lower row) for positive (left column) and negative (right column) magnetic field orientations. Different colors refer to different ranges of radial distance of the particle production vertex.

explained by the approximately linear relationship between these two variables for small opening angles:

$$m_{ee} \approx 2 \cdot \sqrt{p_1 p_2} \cdot \sin(\theta_{ee}/2) \approx \sqrt{p_1 p_2} \cdot \theta_{ee} \quad (\text{A.1})$$

The mass shift in the like-sign spectrum originated instead from small track distortions due to the track matching with clusters which did not belong to it. Two close like-sign tracks were stretched and pushed towards each other, sharing one or more clusters in the innermost layers of the SPD: their opening angle was reduced causing a mass shift to smaller values. The effects of the tracking algorithm on the opening angle of unlike-sign and like-sign dielectron pairs are illustrated in the Fig. A.5.

The magnitude of this effect has been significantly reduced using the photon conversion rejection methods. These are extensively discussed in Chapter 5.3. Fig. A.6 shows the effect of the cuts used to reject secondary tracks on the unlike-sign and like-sign

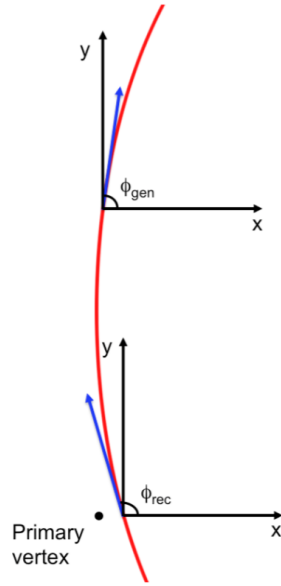


Fig. A.3 : Illustration of the inward propagation of secondary tracks: the angular shift is a consequence of the wrong point used to estimate the particle momentum.

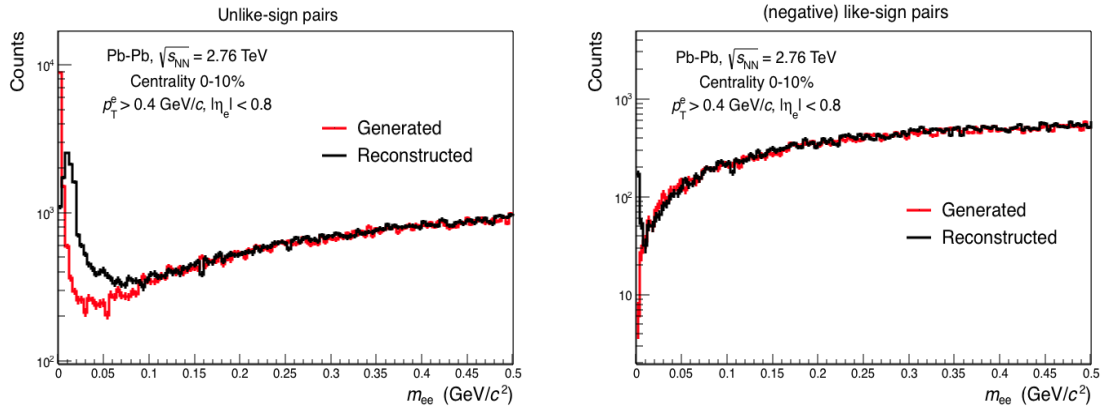


Fig. A.4 : Comparison between invariant mass distribution obtained using the generated and reconstructed momentum for unlike-sign (left) and like-sign (right) dielectron pairs.

invariant mass distributions. The peak in the like-sign spectrum at zero mass was no longer visible while the mass shift in the unlike-sign spectrum was present only in the very low-mass range ($m_{ee} < 1 \text{ MeV}/c^2$). This had no effect in the raw yield extraction in the present analysis since the width of the mass bins used in the low-mass region was $\Delta m_{ee} = 20 \text{ MeV}/c^2$.

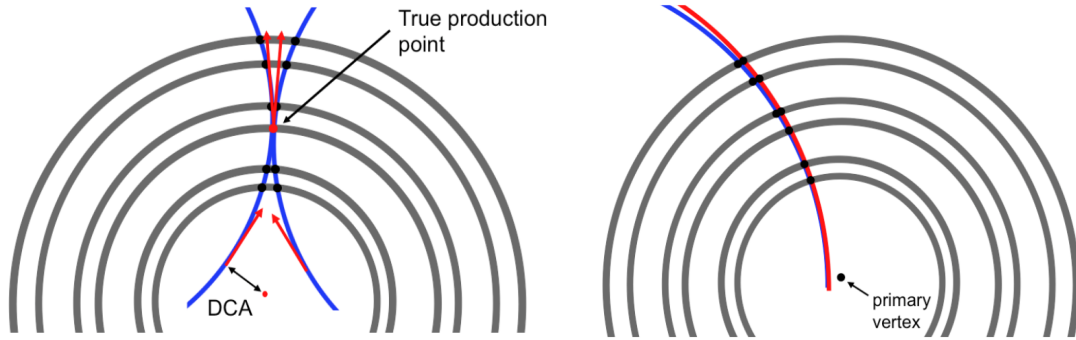


Fig. A.5 : Effects of the tracking algorithm on the opening angle of unlike-sign (left) and like-sign (right) dielectron pairs.

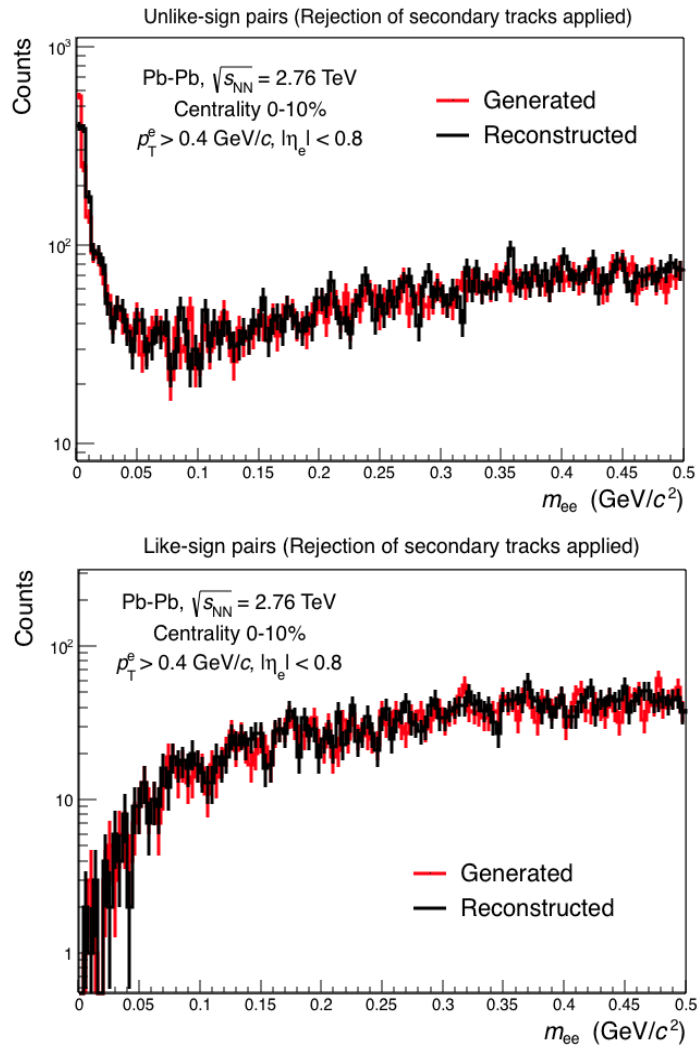


Fig. A.6 : Comparison between invariant mass distribution using generated and reconstructed momentum for unlike-sign (top) and like-sign (bottom) dielectron pairs obtained after applying the rejection methods of secondary tracks.

Appendix B

Upper Limit Estimation

This section describes the procedure used for the extraction of the upper limits on the negative dielectron yield, due to over-subtraction of the combinatorial background in some of the mass ranges, and on the measurement of the fraction of virtual direct photons. The methodology used is based on the Feldman and Cousins approach. More details can be found in [147].

B.1 Confidence Belts: Neyman's Construction

The Feldman and Cousins method is a *unified approach* for the estimation of confidence intervals which provides a smooth transition from two-sided intervals (measurements) to one-sided intervals (upper limits). The Feldman and Cousins method will be illustrated using the example of a Gaussian PDF for the measured variable x , with non-negative true mean μ and variance σ given by the experimental uncertainty ($\sigma = 0.1$ in this example):

$$P(x|\mu) = \frac{1}{\sigma\sqrt{2\pi}} \exp\left(-\frac{(x-\mu)^2}{2\sigma^2}\right) \quad (\text{B.1})$$

For each value of the true mean μ , a confidence interval is considered with a given coverage probability (90% C.L. is used in this example). The confidence intervals are determined using the Neyman's construction, which is also called the method of *confidence belts*. The Feldman and Cousins approach uses a *Likelihood Ratio* in order to determine which values of x should become part of the confidence interval. This ratio R is given by:

$$R(x) = \frac{P(x|\mu)}{P(x|\mu_0)} \quad (\text{B.2})$$

where μ_0 denotes the μ value which maximizes $P(x|\mu)$ and is physically allowed (non-negative in this case). For a given $x = x_0$, $P(x_0|\mu)$ is maximized by $\mu_0 = x_0$ when $x_0 \leq 0$ and by $\mu_0 = 0$ if the measured value is negative. The likelihood ratio is then given by:

$$R(x) = \begin{cases} \exp\left(-\frac{(x-\mu)^2}{2\sigma^2}\right) & \text{if } x \geq 0 \\ \exp\left(-\frac{(x-\mu)^2 - x^2}{2\sigma^2}\right) & \text{if } x < 0 \end{cases} \quad (\text{B.3})$$

Fig. B.1 shows the likelihood ratio $R(x)$ for $\mu = 0.1, 0.2$ and 0.5 .

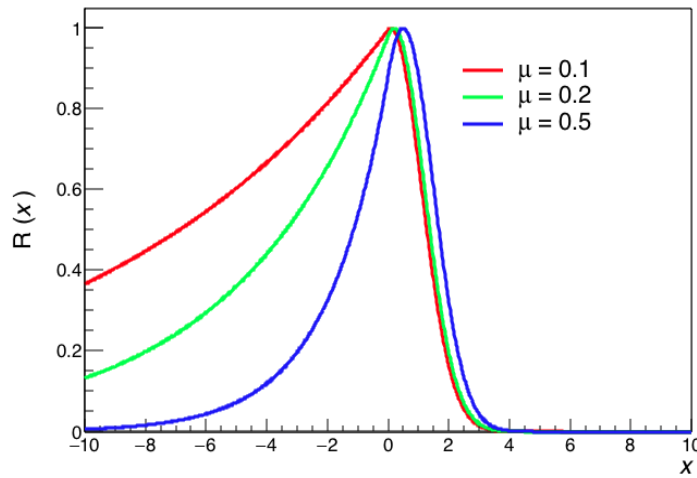


Fig. B.1 : Likelihood Ratio, given by Eq. (B.3), for a Gaussian PDF corresponding to non-negative values of the true mean $\mu = 0.1, 0.2$ and 0.5 .

For a given μ value, the corresponding confidence interval with 90% coverage probability is obtained by including the x values with the biggest R first and repeating the procedure until the two extremes of this interval, x_1 and x_2 , satisfy:

$$\int_{x_1}^{x_2} R(x) dx = 0.9 \cdot \int_{-\infty}^{\infty} R(x) dx \quad (\text{B.4})$$

This is done iteratively by determining the intersections x_1 and x_2 between $R(x)$ and a horizontal line $y = \text{const}$:

$$x = \begin{cases} \frac{\mu^2 + 2\sigma^2 \ln(y)}{2\mu} & \text{if } x < 0 \\ \mu \pm \sqrt{-2\sigma^2 \ln(y)} & \text{if } x \geq 0 \end{cases} \quad (\text{B.5})$$

The initial value of y is R_{max} , that is iteratively shifted downward, thus increasing the confidence range, until the two extremes reach the desired confidence level. The set

of confidence intervals, one for each μ value, gives a *confidence belt*, which is shown in Fig. B.2.

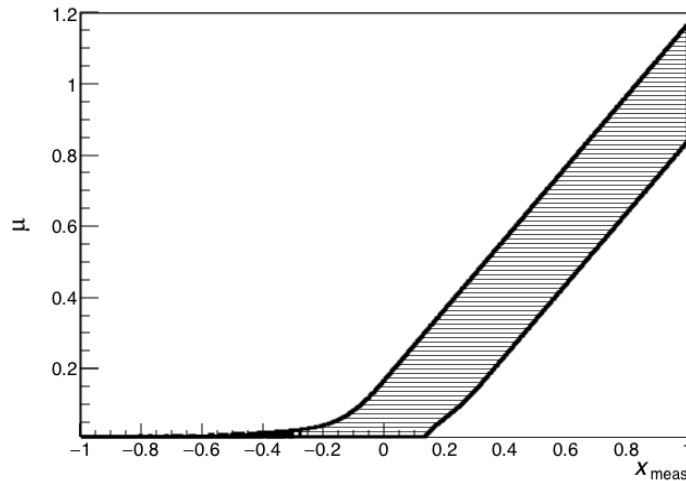


Fig. B.2 : Example of a confidence belt. For each μ value a confidence interval is constructed with the desired coverage probability.

B.2 Extraction of Confidence Intervals

The confidence belt, constructed following Neyman's procedure, is used to extract the confidence interval to be associated with a given measured x value. A vertical line with equation $x = x_{meas}$ is drawn which intersects the boundaries of the confidence belt in one or two points. In the case of two intersections, the ordinates y_1 and y_2 of these two points represent the extremes of the confidence interval associated to x_{meas} corresponding to the same coverage probability used in the construction of the belt. In the case of a single intersection, its ordinate represents the upper limit for the given measurement. This procedure is illustrated in Fig. B.3 in the case of one-sided and two-sided intervals.

The inclusion of systematic uncertainties in the estimation of the confidence intervals requires some knowledge of their distribution and of their degree of correlation to the statistical uncertainties. In the present example, the systematic uncertainties (10% in this example) are assumed to follow a Gaussian PDF and to be independent of the statistical uncertainties. The total uncertainty used to construct the confidence belt is then given by the quadratic sum of the statistical and systematic uncertainties: $\sigma^2 = \sigma_{stat}^2 + \sigma_{syst}^2$. The effect of the inclusion of systematic uncertainties into the construction of the confidence belt is to increase the upper limit or the width of the two-sided confidence interval (Fig. B.4).

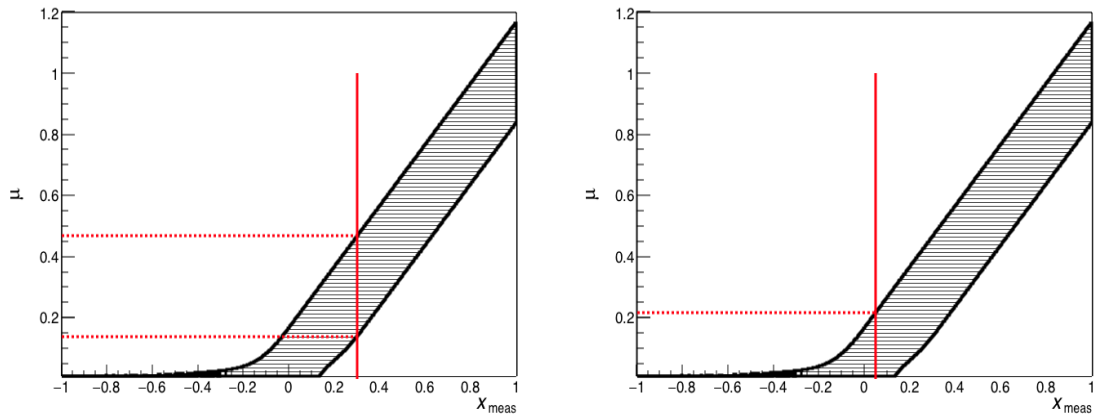


Fig. B.3 : Illustration of the procedure used for the extraction of a two-sided (left) and one-sided (right) confidence intervals to be associated with a given measured x value.

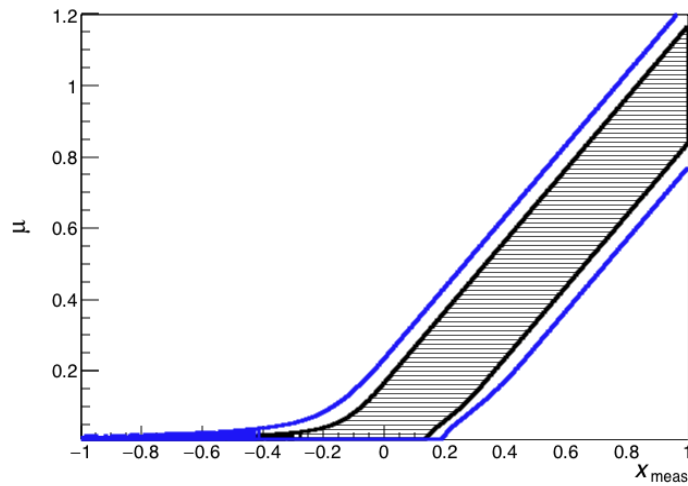


Fig. B.4 : Example of a confidence belt with (blue) and without (black) the inclusion of systematic uncertainties.

References

- [1] C. Quigg, "Gauge Theories of the Strong, Weak and Electromagnetic Interactions", Benjamin-Cummings, Reading (1983).
- [2] P. W. Higgs, "Broken Symmetries and the Masses of Gauge Bosons", Phys. Rev. Lett. **13**, 16, pp. 508-509 (1964).
- [3] H. Yukawa, "On the Interaction of Elementary Particles", PTP, 17, 48 (1935).
- [4] An extensive bibliography on the quark model is given by O.W. Greenberg, American Journal of Physics **50**, 12, pp. 1074-1089 (1982).
- [5] K.A. Olive *et al.* (Particle Data Group), Chinese Physics C38, 090001 (2014).
- [6] B. Andersson *et al.*, "Parton Fragmentation and String Dynamics", Phys. Rep. **97**, 2 & 3, pp. 31-145 (1983).
- [7] <http://pdg.lbl.gov/2014/tables/rpp2014-sum-quarks.pdf>
- [8] R. Hagedorn, "Statistical thermodynamics of strong interactions at high energies", Nuovo Cimento Supplemento **3**, p. 147 (1965).
- [9] W. Broniowski, W. Florkowski and L. Ya. Glozman, "Update of the Hagedorn mass spectrum", Phys.Rev. **D70**, 117503 (2004).
- [10] C. Caso *et al.*, (Particle Data Group), Eur. Phys. J. **C3**, 1 (1998).
- [11] L.Ya. Glozman, Phys. Lett. **B 539**, 257 (2002).
- [12] L.Ya. Glozman, Phys. Lett. **B 587**, 69 (2004).
- [13] H.D. Politzer, "Reliable Perturbative Results for Strong Interactions?", Phys. Rev. Lett. **30**, 26, p. 1346 (1973).

-
- [14] D.J. Gross and F. Wilczek, "Ultraviolet Behavior of Non-Abelian Gauge Theories", Phys. Rev. Lett. **30**, 26, p. 1343 (1973).
- [15] J.C. Collins and M.J. Perry, "Superdense Matter: Neutrons or Asymptotically Free Quarks?", Phys. Rev. Lett. **34**, p. 1353 (1975).
- [16] N. Cabibbo and G. Parisi, "Exponential hadronic spectrum and quark liberation", Phys. Lett. **B59**, p. 67 (1975).
- [17] E. V. Shuryak, "Quark Gluon Plasma and Hadronic Production of Leptons, Photons and Psions", Phys. Lett. **B78**, p. 150 (1978).
- [18] M. A. Stephanov, "QCD phase diagram: an overview", PoS LAT2006:024 (2006).
- [19] A. Chodes *et al.*, "New extended model of hadrons", Phys. Rev. **D9**, 3471 (1974).
- [20] C.Y. Wong, "Introduction to High-Energy Heavy-Ion Collisions", ISBN: 978-981-02-0263-7
- [21] S. Gupta, *et al.*, "Scale for the Phase Diagram of Quantum Chromodynamics", Science **332**, 1525 (2011).
- [22] M. G. Alford, K. Rajagopal, T. Schaefer and A. Schmitt, "Color superconductivity in dense quark matter", Rev. Mod. Phys. **80**, pp. 1455-1515 (2008).
- [23] F. Karsch, "Lattice QCD at High Temperature and Density", Lecture Notes of Physics, 583, (2002).
- [24] F. Karsch, "Lattice Results on QCD Thermodynamics", Nucl. Phys. **A698** (2002).
- [25] J.D. Bjorken, "Highly relativistic nucleus-nucleus collisions: The central rapidity region", Phys. Rev. **D27**, p. 140 (1983).
- [26] F. Gelis, "Color Glass Condensate and Glasma", Nucl. Phys. **A854**, pp. 10-17 (2011).
- [27] F. Becattini, "An introduction to the Statistical Hadronization Model", Lecture Notes, arXiv:0901.3643 (2009)
- [28] R. Hagedorn, "Thermodynamics of strong interactions", CERN lectures (1970)
- [29] R. Stock, "The parton to hadron phase transition observed in Pb+Pb collisions at 158 GeV per nucleon", Phys. Lett. **B456**, pp. 277-282 (1999).

- [30] R. Nouicer, "New State of Nuclear Matter: Nearly Perfect Fluid of Quarks and Gluons in Heavy Ion Collisions at RHIC Energies", *Eur. Phys. J. Plus* **131**, 3, 70 (2016).
- [31] P. F. Kolb *et al.*, "Hydrodynamic description of ultrarelativistic heavy-ion collisions", arXiv:nucl-th/0305084 (2003)
- [32] J. Stachel, A. Andronic, P. B. Munzinger and K. Redlichar, "Confronting LHC data with the statistical hadronization model", arXiv:1311.4662 [nucl-th] (2013)
- [33] M. Floris *et al.* (The ALICE Collaboration), "Identified particles in pp and Pb–Pb collisions at LHC energies with the ALICE detector", *J. Phys.* **G38**, 124025 (2011).
- [34] C. Shen *et al.*, "Radial and elliptic flow in Pb+Pb collisions at the Large Hadron Collider from viscous hydrodynamic", *Phys. Rev.* **C84**, 044903 (2011).
- [35] K. Aamodt *et al.* (The ALICE Collaboration), "Elliptic Flow of Charged Particles in Pb–Pb Collisions at $\sqrt{s_{NN}} = 2.76$ TeV", *Phys. Rev. Lett.* **105**, 252302 (2010).
- [36] J. Rafelski, R. Hagedorn, CERN-TH-2969, C80-08-24-4 (1980).
- [37] F. Antinori *et al.* (The NA57 Collaboration), "Enhancement of hyperon production at central rapidity in 158 A GeV/c Pb–Pb collisions", *J.Phys. G.* **32**, pp. 427-442 (2006).
- [38] A.R. Timmins *et al.* (The STAR Collaboration), "Overview of strangeness production at the STAR experiment", *J. Phys.* **G36**:064006 (2009).
- [39] T. Matsui and H. Satz, "J/Ψ suppression by quark-gluon plasma formation", *Phys. Lett.* **B178**, p. 416 (1986).
- [40] H. Stocker, F. Jundt and G. Guillaume. *Toute la physique*. DUNOD (1999).
- [41] P. Braun-Munzinger, J. Stachel, "Charmonium from Statistical Hadronization of Heavy Quarks - a Probe for Deconfinement in the Quark-Gluon Plasma", arXiv:0901.2500 [nucl-th] (2009).
- [42] K. Aamodt *et al.* (The ALICE Collaboration), "Suppression of Charged Particle Production at Large Transverse Momentum in Central Pb–Pb Collisions at $\sqrt{s_{NN}} = 2.76$ TeV", *Phys. Lett.* **B696**, 30 (2011).

- [43] S. Chatrchyan *et al.* (The CMS Collaboration), "Study of high- p_T charged particle suppression in PbPb compared to pp collisions at $\sqrt{s_{NN}} = 2.76$ TeV", *Eur. Phys. J.* **C72**, 1945 (2012).
- [44] J. Adams *et al.* (The STAR Collaboration), "Evidence from d+Au measurements for final-state suppression of high p_T hadrons in Au+Au collisions at RHIC", *Phys. Rev. Lett.* **91**, 072304 (2003).
- [45] S. S. Adler *et al.* (The PHENIX Collaboration), "A Detailed Study of High- p_T Neutral Pion Suppression and Azimuthal Anisotropy in Au+Au Collisions at $\sqrt{s_{NN}} = 200$ GeV", *Phys. Rev.* **C76**, 034904 (2007).
- [46] The CMS Collaboration, "Suppression of non-prompt J/ Ψ , prompt J/ Ψ , and Y(1S) in PbPb collisions at $\sqrt{s_{NN}} = 2.76$ TeV", *JHEP* 05, 063, (2012).
- [47] J. Adam *et al.* (The ALICE Collaboration), "Production of charged pions, kaons and protons at large transverse momenta in pp and Pb–Pb collisions at $\sqrt{s_{NN}} = 2.76$ TeV", *Phys. Lett.* **B736**, pp. 196-207 (2014).
- [48] J. Adam *et al.* (The ALICE Collaboration), "Transverse momentum dependence of D-meson production in Pb–Pb collisions at $\sqrt{s_{NN}} = 2.76$ TeV", *JHEP* 1603, 081 (2016).
- [49] G. Aad *et al.* (The ATLAS Collaboration), "Observation of a Centrality-Dependent Dijet Asymmetry in Lead-Lead Collisions at $\sqrt{s_{NN}} = 2.76$ TeV with the ATLAS Detector at the LHC", *Phys. Rev. Lett.* **105**, 252303 (2010).
- [50] K. Aamodt *et al.* (The ALICE Collaboration), "Two-pion Bose-Einstein correlations in central Pb–Pb collisions at $\sqrt{s_{NN}} = 2.76$ TeV", *Phys. Lett.* **B696**, pp. 328-337 (2011).
- [51] M. A. Lisa *et al.* (The E895 Collaboration), "Bombarding energy dependence of piminus interferometry at the Brookhaven AGS", *Phys. Rev. Lett.* **84**, pp. 2798-2802 (2000).
- [52] C. Alt *et al.* (The NA49 Collaboration), "Bose-Einstein correlations of $\pi^-\pi^-$ pairs in central Pb+Pb collisions at A-20, A-30, A-40, A-80, and A-158 GeV", *Phys. Rev.* **C77**, 064908 (2008).
- [53] S. V. Afanasiev *et al.* (The NA49 Collaboration), "Energy dependence of pion and kaon production in central Pb + Pb collisions", *Phys. Rev.* **C66**, 054902 (2002).

-
- [54] D. Adamova *et al.* (The CERES Collaboration), "Beam energy and centrality dependence of two pion Bose-Einstein correlations at SPS energies", Nucl. Phys. **A714**, pp. 124-144 (2003).
- [55] B. I. Abelev *et al.*, (The STAR Collaboration), "Pion interferometry in Au+Au and Cu+Cu collisions at $\sqrt{s_{\text{NN}}} = 62.4$ and 200 GeV", Phys. Rev. **C80**, 024905 (2009).
- [56] B. B. Back *et al.* (The PHOBOS Collaboration), "Transverse Momentum and Rapidity Dependence of HBT Correlations in Au+Au Collisions at $\sqrt{s_{\text{NN}}} = 62.4$ and 200 GeV", Phys. Rev. **C73**, 031901 (2006).
- [57] B. B. Back *et al.*, (The PHOBOS Collaboration), "Charged-particle pseudorapidity distributions in Au+Au collisions at $\sqrt{s_{\text{NN}}} = 62.4$ GeV", Phys. Rev. **C74**, 021901 (2006).
- [58] B. B. Back *et al.* (The PHOBOS Collaboration), "Significance of the Fragmentation Region in Ultrarelativistic Heavy-Ion Collisions", Phys. Rev. Lett. **91**, 052303 (2003).
- [59] J. Adams *et al.* (The STAR Collaboration), "Pion interferometry in Au+Au collisions at $\sqrt{s_{\text{NN}}} = 200$ GeV", Phys. Rev. **C71**, 044906 (2005).
- [60] B. I. Abelev *et al.* (The STAR Collaboration), "Systematic measurements of identified particle spectra in pp, d+Au, and Au+Au collisions at the STAR detector", Phys. Rev. **C79**, 034909 (2009).
- [61] G. Aad *et al.* (The ATLAS Collaboration), "Measurement of the centrality dependence of the charged particle pseudorapidity distribution in lead-lead collisions at $\sqrt{s_{\text{NN}}} = 2.76$ TeV with the ATLAS detector", Phys. Lett. **B710**, pp. 363-382 (2012).
- [62] K. Aamodt *et al.* (The ALICE Collaboration), "Charged-Particle Multiplicity Density at Midrapidity in Central Pb-Pb Collisions at $\sqrt{s_{\text{NN}}} = 2.76$ TeV", Phys. Rev. Lett. **105**, 252301 (2010).
- [63] J.e. Alam, S. Raha, and B. Sinha, "Electromagnetic probes of quark gluon plasma", Phys. Rep. **273**, 5-6, pp. 243-364 (1996).
- [64] A. Adare *et al.* (The PHENIX Collaboration), "Centrality dependence of low-momentum direct-photon production in Au+Au collisions at $\sqrt{s_{\text{NN}}} = 200$ GeV", Phys. Rev. **C91** 064904 (2015).

- [65] J.F. Paquet, C. Shen, G. S. Denicol, M. Luzum, B. Schenke, S. Jeon, and C. Gale, "Production of photons in relativistic heavy-ion collisions", *Phys. Rev.* **C93**, 4, 044906 (2016).
- [66] S.D. Drell, T.M. Yan, "Massive Lepton-Pair Production in Hadron-Hadron Collisions at High Energies", *Phys. Rev. Lett.* **25**, 5, pp. 316-320 (1970).
- [67] J. H. Christenson, G. S. Hicks, L. M. Lederman, P. J. Limon, B. G. Pope, and E. Zavattini, "Observation of Massive Muon Pairs in Hadron Collisions", *Phys. Rev. Lett.* **25**, 21, pp. 1523-1526 (1970).
- [68] S. Ryu, J. F. Paquet, C. Shen, G. S. Denicol, B. Schenke, S. Jeon, C. Gale, "Importance of the Bulk Viscosity of QCD in Ultrarelativistic Heavy-Ion Collisions", *Phys. Rev. Lett.* **115**, 13, 132301 (2015) .
- [69] F. M. Steffens, "The temperature dependence of the QCD running coupling", *Braz. J. Phys.* **36**, no. 2b, pp.582-585. ISSN 0103-9733 (2006).
- [70] J. Adam *et al.* (The ALICE Collaboration), "Direct photon production in Pb–Pb collisions at $\sqrt{s_{NN}} = 2.76$ TeV", *Phys. Lett.* **B754**, pp. 235-248 (2016).
- [71] H.van Hees, C. Gale, R. Rapp, "Thermal Photons and Collective Flow at the Relativistic Heavy-Ion Collider", *Phys. Rev.* **C84**, 054906 (2011).
- [72] D. Lohner *et al.* (for the ALICE Collaboration), "Measurement of Direct-Photon Elliptic Flow in Pb-Pb Collisions at $\sqrt{s_{NN}} = 2.76$ TeV", arXiv:1212.3995 [hep-ex] (2013).
- [73] S. Campbell (for the PHENIX Collaboration), "Thermal and direct photons in PHENIX", *Journal of Physics: Conference Series* **422**, 012020 (2013).
- [74] N. Kroll, W. Wada, "Internal Pair Production Associated with the Emission of High-Energy Gamma Rays", *Phys. Rev.* **98**, p. 1355 (1955).
- [75] L.G. Landsberg, "Electromagnetic decays of light mesons", *Phys. Rep.* **128**, 6, pp. 301-376 (1985)
- [76] R. D. Pisarski, "Phenomenology of the Chiral Phase Transition", *Phys. Lett.* **110B**, pp. 155-158 (1982).
- [77] G. Q. Li, C. M. Rho and G. E. Brown, "Enhancement of Low-Mass Dileptons in Heavy Ion Collisions", *Phys. Rev. Lett.* **75**, 4007 (1995).

- [78] G. Chanfray, R. Rapp and J. Wambach, "Medium Modifications of the Rho Meson at CERN Super Proton Synchrotron Energies (200 GeV/nucleon)", *Phys. Rev. Lett.* **76**, 368 (1996).
- [79] T. Akesson *et al.*, (The HELIOS-1 Collaboration), *Z. Phys.* **C68**, 47 (1995).
- [80] G. Agakishiev *et al.* (The CERES Collaboration), "Neutral meson production in pBe and pAu collisions at 450-GeV beam energy", *Eur. Phys. J.* **C4**, pp. 249-257 (1998).
- [81] J. D. Bjorken and H. Weisberg, "Direct lepton production and the Drell-Yan mechanism", *Phys. Rev.* **D13**, 1405 (1976).
- [82] M. C. Abreu *et al.* (The NA38 Collaboration), "J/ Ψ , Ψ' and muon pair production in p-W and S-U collisions", *Nucl. Phys.* **A566**, pp. 77-85 (1994).
- [83] G. Agakishiev *et al.* (The CERES Collaboration), "Enhanced Production of Low-Mass Electron Pairs in 200 GeV/Nucleon S-Au Collisions at the CERN Super Proton Synchrotron", *Phys. Rev. Lett.* **75**, 1272 (1995).
- [84] Quark Matter Bielefeld 1982, (World Scientific, Singapore).
- [85] G. Agakishiev *et al.* (The CERES Collaboration), "Low-mass e^+e^- pair production in 158 A GeV Pb-Au collisions at the CERN SPS, its dependence on multiplicity and transverse momentum", *Phys. Lett.* **B422**, pp. 405-412 (1998).
- [86] M. Masera *et al.* (The HELIOS-3 Collaboration), "Dimuon production below mass 3.1 GeV/ c^2 in p-W and S-W interactions at 200 GeV/c/A", *Nucl. Phys.* **A590**, 1-2, pp. 93-102 (1995).
- [87] A. L. S. Angelis *et al.*, "Excess of continuum dimuon production at masses between threshold and the J / Psi in S-W interactions at 200-GeV/c/nucleon", *Eur. Phys. J.* **C13**, pp. 433-452 (2000).
- [88] R. Arnaldi *et al.* (The NA60 Collaboration), "First Measurement of the rho Spectral Function in High-Energy Nuclear Collisions", *Phys. Rev. Lett.* **96**, 162302 (2006).
- [89] S. Damjanovic *et al.* (The NA60 Collaboration), "NA60 results on the ρ spectral function in In-In collisions", *Nucl. Phys.* **A783**, 1-4, pp. 327-334 (2007).
- [90] R. Arnaldi *et al.* (The NA60 Collaboration), "Thermal Dimuon Emission in In-In at the CERN SPS", arXiv:0806.0577v1 [nucl-ex] (2008).

-
- [91] R. Arnaldi *et al.* (The NA60 Collaboration), "Proceedings of the INPC07", Tokyo (2007).
- [92] J. Ruppert and T. Renk, "Dimuon transverse momentum spectra as a tool to characterize the emission region in heavy-ion collisions", *Phys. Rev.* **C77**, 024907 (2008).
- [93] J. Ruppert, C. Gale, T. Renk, P. Lichard and J. I. Kapusta, "Low Mass Dimuons Produced in Relativistic Nuclear Collisions", *Phys. Rev. Lett.* **100**, 162301 (2008).
- [94] A. Adare *et al.* (The PHENIX Collaboration), "Dilepton mass spectra in p+p collisions at $\sqrt{s_{NN}} = 200$ GeV and the contribution from open charm", *Phys. Lett.* **B670**, pp. 313-320 (2009).
- [95] D. Sharma (for the PHENIX Collaboration), "Dielectrons in d+Au collisions measured by PHENIX and its implications on heavy flavor", *Nucl. Phys.* **A932**, pp. 235-240 (2014).
- [96] S. Kelly (for the PHENIX Collaboration), "The PHENIX measurement of Heavy Flavor via Single Electrons in pp, d-Au, and Au-Au collisions at $\sqrt{s_{NN}} = 200$ GeV", *J.Phys.* **G30**, S1189-S1192 (2004).
- [97] A. Adare *et al.* (The PHENIX Collaboration), "Detailed measurement of the e^+e^- continuum in p+p and Au+Au collisions at $\sqrt{s_{NN}} = 200$ GeV and implications for direct photon production", *Phys. Rev.* **C81**, 034911 (2010).
- [98] S. S. Adler *et al.* (The PHENIX Collaboration), "Centrality Dependence of Direct Photon Production in $\sqrt{s_{NN}} = 200$ GeV Au+Au Collisions", *Phys. Rev. Lett.* **94**, 232301 (2005).
- [99] S. S. Adler *et al.* (The PHENIX Collaboration), "Measurement of Direct Photon Production in p+p Collisions at $\sqrt{s_{NN}} = 200$ GeV", *Phys. Rev. Lett.* **98**, 012002 (2007).
- [100] L. Adamczyk *et al.* (The STAR Collaboration), "Dielectron Mass Spectra from Au+Au Collisions at $\sqrt{s_{NN}} = 200$ GeV", *Phys. Rev. Lett.* **113**, 049903 (2014).
- [101] A. Adare *et al.* (The PHENIX Collaboration), "Dielectron production in Au+Au collisions at $\sqrt{s_{NN}} = 200$ GeV", *Phys.Rev.* **C93**, 014904 (2016).
- [102] L. E. Gordon and W. Vogelsang, *Phys. Rev.* **D48**, 3136 (1993).

-
- [103] A. Adare *et al.* (The PHENIX Collaboration), "Enhanced Production of Direct Photons in Au+Au Collisions at $\sqrt{s_{NN}} = 200$ GeV and Implications for the Initial Temperature", *Phys. Rev. Lett.* **104**, 132301 (2010).
- [104] The ALICE Collaboration, " ϕ -meson production at forward rapidity in p-Pb collisions at $\sqrt{s_{NN}} = 5.02$ TeV and in pp collisions at $\sqrt{s} = 2.76$ TeV", arXiv:1506.09206 [nucl-ex]
- [105] K. Aamodt *et al.* (The ALICE Collaboration), "The ALICE experiment at the CERN LHC", *JINST* **3** S08002 (2008).
- [106] A. Fernandez, S. Kartal, C. Pagliarone, "ACORDE - A Cosmic Ray Detector for ALICE", arXiv:physics/0612051 [physics.ins-det]
- [107] The ALICE Collaboration, "ALICE Technical Design Report of the Inner Tracking System (ITS)", CERN / LHCC 99-12, ALICE TDR 4 (1999).
- [108] The ALICE Collaboration, "ALICE Technical Design Report of the Time Projection Chamber", CERN / LHCC 2000-001, ALICE TDR 7 (2000).
- [109] The ALICE Collaboration, "ALICE Technical Design Report of the Time of Flight System (TOF)", CERN / LHCC 2000-012, ALICE TDR 8 (2000).
- [110] The ALICE Collaboration, "ALICE Technical Design Report on Forward Detectors: FMD, T0 and V0", CERN / LHCC 2004-025, ALICE TDR 011 (2004).
- [111] The ALICE Collaboration, "ALICE Technical Design Report of the Zero Degree Calorimeter (ZDC)", CERN / LHCC 99-005, ALICE TDR 3 (1999).
- [112] The ALICE Collaboration, "ALICE Technical Design Report of the Transition Radiation Detector", CERN / LHCC 2001-021, ALICE TDR 9 (2001).
- [113] The ALICE Collaboration, "ALICE Technical Design Report of the High Momentum Particle Identification Detector", CERN / LHCC 98-19, ALICE TDR 1 (1998).
- [114] The ALICE Collaboration, "ALICE Electromagnetic Calorimeter Technical Design Report", CERN / LHCC 2008-014, ALICE-TDR-014 (2008).
- [115] The ALICE Collaboration, "ALICE Technical Design Report of the Photon Spectrometer (PHOS)", CERN / LHCC 99-4, ALICE TDR 2 (1999).
- [116] The ALICE Collaboration, "ALICE Technical Design Report of the Muon Forward Tracker", CERN / LHCC 2015-001, ALICE TDR 018 (2015).

- [117] X. N. Wang, M. Gyulassy, "HIJING: A Monte Carlo model for multiple jet production in pp, p-A and A-A collisions", Phys. Rev. **D44**, pp. 3501-3516 (1991).
- [118] <https://home.cern/about/computing>
- [119] F. Carminati and Y. Schutz (on behalf of the ALICE Collaboration), "ALICE Computing Model", CERN / LHCC 2004-038, G-086 (2005).
- [120] H. Tilsner, T. Alt, K. Aurbakken *et al.*, "The high-level trigger of ALICE", Eur. Phys. J. **C33**, pp. s1041-s1043 (2004).
- [121] D. Huffman, "A Method for the Construction of Minimum-Redundancy Codes", Proceedings of the IRE. 40, 9, pp. 1098-1101 (1952).
- [122] The ALICE Collaboration, "Performance of the ALICE Experiment at the CERN LHC", Int. J. Mod. Phys. **A29**, 1430044 (2014).
- [123] M. Miller, K. Reygers, S. J. Sanders, and P. Steinberg, "Glauber Modeling in High Energy Nuclear Collisions", Ann. Rev. Nucl. Part. Sci. **57**, 205 (2007).
- [124] R. J. Glauber, "Cross Sections in Deuterium at High Energies", Phys. Rev. **100**, 242 (1955).
- [125] R. Glauber, ed WE Brittin and LG Dunham 1 (1959).
- [126] R. Glauber, "Quantum Optics and Heavy Ion Physics", J. Nucl.Phys. **A774**, 3-13 (2006).
- [127] R. D. Woods, D. S. Saxon, "Diffuse Surface Optical Model for Nucleon-Nuclei Scattering", Phys. Rev. **95**, 2, pp. 577-578 (1954).
- [128] H. De Vries, C. W. De Jager, and C. De Vries, Atom. Data Nucl. Data Tabl. 36, **495** (1987).
- [129] D. Kharzeev, E. Levin, and M. Nardi, "Color glass condensate at the LHC: hadron multiplicities in pp, pA and AA collisions", Nucl. Phys. **A747**, 609 (2005).
- [130] W. Deng, X. Wang, and R. Xu, "Hadron production in p+p, p+Pb and Pb+Pb collisions with the HIJING 2.0 model at energies available at the CERN Large Hadron Collider", arXiv:1008.1841 [hep-ph] (2010).
- [131] The ALICE Collaboration, "Technical Proposal for A Large Ion Collider Experiment at the CERN LHC", CERN / LHCC 95-71, LHCC / P3 (1995).

- [132] M.Ivanov, K.Safarik, Y.Belikov and J.Bracinik, "TPC tracking and particle identification in high-density environment", arXiv:physics/0306108 [physics.data-an] (2003).
- [133] C. Patrignani *et al.* (Particle Data Group), "The Review of Particle Physics", Chin. Phys. **C40**, 100001 (2016).
- [134] B. Abelev *et al.* (The ALICE Collaboration), "Neutral pion production at midrapidity in pp and Pb–Pb collisions at $\sqrt{s_{NN}} = 2.76$ TeV", Eur. Phys. J. **C74**, 10, p. 3108 (2014).
- [135] M. Biyajima, T. Mizoguchi, N. Nakajima, N. Suzuki and G.Wilk, "Modified Hagedorn formula including temperature fluctuation - Estimation of temperatures at RHIC experiments", Eur. Phys. J. **C48**, pp. 597-603 (2006).
- [136] R. Albrecht *et al.* (The WA80 Collaboration), "Production of η mesons in 200 AGeV/c S+S and S+Au reactions", Phys. Lett. **B361**, 1-4, pp. 14-20 (1995).
- [137] D. d'Enterria, "Hard scattering cross sections at LHC in the Glauber approach: from pp to pA and AA collisions", arXiv:nucl-ex/0302016v3 (2003).
- [138] B. Abelev *et al.* (The ALICE Collaboration), "Measurement of charm production at central rapidity in proton-proton collisions at $\sqrt{s_{NN}} = 2.76$ TeV", arXiv:1205.4007 [hep-ex] (2012).
- [139] B. Abelev *et al.* (The ALICE Collaboration), "Beauty production in pp collisions at $\sqrt{s_{NN}} = 2.76$ TeV measured via semi-electronic decays", Phys. Lett. **B738**, p. 97 (2014).
- [140] B. Abelev *et al.* (The ALICE Collaboration), "Measurement of inelastic, single- and double-diffraction cross sections in proton–proton collisions at the LHC with ALICE", Eur. Phys. J. **C73**, 2456 (2013).
- [141] <http://pdg.lbl.gov/2015/reviews/rpp2015-rev-statistics.pdf>
- [142] R. Rapp, "Signatures of Thermal Dilepton Radiation at RHIC", Phys. Rev. **C63**, 054907 (2001).
- [143] R. Rapp, "Dilepton Spectroscopy of QCD Matter at Collider Energies", Adv. High Energy Phys. 2013, 148253 (2013).

-
- [144] The ALICE Collaboration, "Technical Design Report for the Upgrade of the ALICE Inner Tracking System", CERN / LHCC 2013-024, ALICE-TDR-017 (2013).
- [145] The ALICE Collaboration, "Technical Design Report for the Upgrade of the ALICE Time Projection Chamber", CERN / LHCC 2013-020, ALICE-TDR-016 (2014).
- [146] B. Abelev *et al.* (The ALICE Collaboration), "Upgrade of the ALICE Experiment: Letter of Intent", J. Phys. G: Nucl. Part. Phys. **41** 087001 (2014).
- [147] G.J. Feldman and R.D. Cousins, "Unified approach to the classical statistical analysis of small signals", Phys. Rev. **D57**, 3873 (1998).

Curriculum Vitae

Ph.D. candidate

Utrecht University, Institute of Subatomic Physics and FOM, Utrecht (The Netherlands).

Thesis: Low-mass dielectron measurement in Pb–Pb collisions at $\sqrt{s_{\text{NN}}} = 2.76$ TeV with ALICE at the LHC

M.Sc. Physics (Nuclear and Subnuclear Physics)

University of Catania and INFN, Catania (Italy)

Thesis: Reconstruction of the charged K^* resonance in pp collisions at $\sqrt{s} = 7$ TeV with ALICE at the LHC

BSc. Physics

University of Palermo, Palermo (Italy)

Thesis: The Majorana Neutrino and the Neutrinoless Double Beta Decay

